Therapeutic applications of DNA origami-based programmable nanoparticles

A DISSERTATION SUBMITTED
BY
OLIVIA JANE YOUNG ARNOLD
TO
HARVARD-MIT PROGRAM IN HEALTH SCIENCES AND TECHNOLOGY

IN PARTIAL FULFILLMENT OF THE REQUIREMENTS
FOR THE DEGREE OF
DOCTOR OF PHILOSOPHY
IN THE SUBJECT OF
MEDICAL ENGINEERING AND MEDICAL PHYSICS

MASSACHUSETTS INSTITUTE OF TECHNOLOGY
CAMBRIDGE, MASSACHUSETTS
MAY 2024

AUTHORED BY: OLIVIA JANE YOUNG ARNOLD
HARVARD-MIT DEPARTMENT OF HEALTH SCIENCES AND TECHNOLOGY
JANUARY 29, 2024

CERTIFIED BY: WILLIAM M. SHIH
FOUNDING CORE FACULTY, WYSS INSTITUTE AT HARVARD UNIVERSITY
PROFESSOR, DEPARTMENT OF BIOLOGICAL CHEMISTRY AND MOLECULAR PHARMACOLOGY, HARVARD MEDICAL SCHOOL
PROFESSOR, DEPARTMENT OF CANCER BIOLOGY, DANA-FARBER CANCER INSTITUTE

ACCEPTED BY: COLLIN STULTZ
DIRECTOR, HARVARD-MIT PROGRAM IN HEALTH SCIENCES AND TECHNOLOGY
NINA T. AND ROBERT H. RUBIN PROFESSOR IN MEDICAL ENGINEERING AND SCIENCE
PROFESSOR OF ELECTRICAL ENGINEERING AND COMPUTER SCIENCE

Thesis advisor: Professor Dr. William Shih Olivia Jane Young Arnold

Therapeutic applications of DNA origami-based programmable nanoparticles

Abstract

DNA origami utilizes the complementary Watson and Crick base pairing of DNA to self-assemble highly programmable nanoparticles. These nanoparticles have distinct advantages over other nanoparticle delivery platforms, including polymeric and lipid nanoparticles, in that they offer precise nanoscale resolution control over the attachment of therapeutic cargo, while other nanoparticle platforms only offer control over average ligand density. In this thesis, we demonstrate the therapeutic utility of DNA origami for cancer and infectious diseases. First, we demonstrate that modulating the nanoscale arrangement of an adjuvant enhances the efficacy of cancer vaccines. Second, we demonstrate that this DNA origami nanoparticle can be used as a modular delivery vehicle for infectious disease associated antigens, enabling rapid response during pandemic situations. Third, we demonstrate the conjugation of CD40 ligand, an immune-activating molecule, onto the DNA origami nanoparticle, and describe initial investigations into the diverse spatial arrangements of CD40L and preliminary effects on the immune response. Collectively, these studies illustrate the potential of DNA origami as a therapeutic for various disease areas, as well as its potential as a tool for investigating biological receptor-ligand interactions.

Table of Contents

List of Tables and Figures

I dedicate this dissertation to my family.

To my dad, my mom and my sister — for your unwavering encouragement to work hard and pursue my dreams, along with your steadfast support throughout this journey.

And to Austin — my husband and my forever love — for being by my side for every day of my PhD and for every day of the rest of our lives.

Acknowledgments

This PhD thesis is the product of many people who walked this journey with me. I could not have accomplished the academic milestone without their endless support.

First, I must thank my thesis advisor, Dr. William Shih, for constantly challenging me to ask questions and frame my scientific experiments in a systematic way. William has taught me to think critically about each and every hurdle that I faced during my PhD, and in doing so, has made me into the scientist that I am today. Additionally, I am beyond grateful that William allowed me to pursue an internship outside of my area of research – an internship that eventually led to a full-time role. I also want to thank my thesis committee, Dr. Dan Anderson, Dr. Cathy Wu and Dr. Dave Mooney for the insightful and productive conversations that we had throughout the journey of this thesis.

Second, I would like to thank all the fellow lab members who contributed to this degree. I would like to thank the Shih Lab therapeutics team, especially Claire Zeng, Hawa Dembele, Anjali Ragwar, and Giorgia Isinelli who shared many late nights and many weekends with me in the lab. Many of the results published here are a product of a team effort. I want to thank Claire especially for teaching me all the techniques that were critical to my PhD and answering endless clarifying questions. I believe that DNA origami is an amazing tool to both understand immune cells at the nanoscale and to deliver therapeutics. I am confident that the Shih lab therapeutics team is establishing the foundation for a future where DNA origami nanoparticles will enhance patients' lives. I look forward with excitement to witness the team's future accomplishments.

Third, there are many other colleagues who helped me throughout my PhD research. In no particular order, I would like to thank: (I) Anastasia Ershova, Dionis Minev and Chris Wintersinger for being fantastic examples of successful graduate students and answering my questions about committee meetings, qualification exams, thesis writing, and everything in between. (II) Pascal and Julia Lill – I hope you realize how much of a lifeline you were for me during a very difficult time in my PhD. Thank you for the coffee breaks which truly restored my belief in myself.(III) Michael Carr, Maurice Perez and all the Wyss operations staff – thank you so much for all you do in keeping the Wyss running. (IV) Madison Adamwaithe – thank you for bearing with me for my first foray into mentoring. (V) Amanda Graveline, Andyna Vernet, Melinda Sanchez-Ventura – thank you for all that you taught me regarding animal studies and all your help along the way. We could not have done these experiments without you. (VI) Catherine Wu, Dave Mooney, and Dan Anderson – thank you for being supportive committee members and for asking questions which pushed me to be a better scientist and to think critically. (VII) Katie Mulligan, Devon Yu, Michele Rosso, Qiancheng Xiong, Michal Walczak – thank you for your contributions to the therapeutics team. There were many experiments which could not have been done without you. (VIII) Mette Malle, Fabian Schnitter, Stella Wang and many others – thank you for the daily Shih lab lunches. (IV) The rest of my HST cohort, especially Morgan Janes, for commiserating when the PhD seemed never ending. (V Luis Barros for helping me learn the business side of the biotech industry, as a mentor for the MIT Sloan Healthcare Certificate.

Fourth, I am incredibly grateful for my time in Matthew DeLisa's lab at Cornell University for setting the groundwork for my PhD. I was mentored by Thapakorn (Tommy) Jaroentomeechai, who fostered a love for science and persistence through the challenges of research. I am so grateful that Dr. Delisa and Tommy encouraged me to apply for a National Science Foundation Fellowship and to graduate school. I would not be where I am today without them. I am also incredibly grateful for some fantastic high school teachers and coaches who taught me that I could tackle anything that I set my mind to: Carrie Dickmann and Mark Lacianca.

Fifth, I would be remiss to not highlight my Boston community, especially Sydney Brannan and the South End community group, who have supported me through the ups and downs of my PhD. Even though they may not have understood the nuances of my PhD life ('what is a gel?'), they showed me that they would support and encourage me through this challenge and any future challenge. I also need to thank my best friend, Brenna Remick, who endured countless conversations with me about my failed experiments. I am so grateful that we got to pursue our PhDs at the same time, even if it was on opposite coasts. With Brenna, I knew that I always had someone to call to commisserate in the struggles of a PhD that no one else understood.

Finally, I need to thank my family. My parents initially fostered a love for science for me. I have many memories of working with my dad at our 'workbench', performing scientific experiments in preparation for the yearly school science fair. My sister and my mom were there for almost daily calls, where I lamented the failed experiments of that day. My grandparents and my extended family have cheered me on every step of the way. I also need to thank my godparents, Dan and Lori, who have celebrated every milestone along the way with me and sent me little pick-me-ups to get me through the tougher weeks. Finally, My husband, Austin, has been by my side through all the challenges of my PhD. He encouraged me on the days

WHEN IT FELT LIKE NONE OF MY EXPERIMENTS WERE WORKING AND WHEN GRADUATION FELT LIKE IT WOULD NEVER COME.

1

Introduction

1.0.1 Motivation

In this chapter, we present an introduction to DNA nanotechnology, with a specific focus on DNA origami and its applications in biological systems. Many studies have been published which suggest the therapeutic utility of DNA origami in model systems; however, DNA origami has never been tested in the clinic with human patients. As such, we discuss the challenges in clinical translation of DNA origami-based therapeutics. Finally, we outline the scope of the thesis which seeks to validate the efficacy of DNA origami-based therapeutics in pre-clinical models, and also demonstrate the modularity of the platform for conjugation of diverse cargo for various disease applications.

1.0.2 Structural DNA nanotechnology

The building block of life is deoxyribose nucleic acid, more commonly referred to as DNA. The structure of DNA was first elucidated in 1953 by James Watson and Francis Crick with insight from Rosalind Franklin and Maurice Wilkins[216]. With this structural data, they discovered that DNA is a polymer composed of four nucleotide base pairs, namely adenine (A), thymine (T), cytosine (C), and guanine (G). Adenine tends to bind to thymine in an interaction with two hydrogen bonds, while cytosine tends to bind to guanine via three hydrogen bonds in a highly predictable and programmable pattern. These base pairs come together in a double helix, typically found in nature in the "B-form", where each strand of DNA is wound in a right-handed helix around the same center axis. The discovery of the double helix structure and the so-called Watson and Crick base-pairing principles provided the critical foundation for structural DNA nanotechnology.

Even though the principles of DNA were well understood, it was not until several decades later that the idea of using DNA as a building material (rather than a genetic material) was conceived and the field of structural DNA nanotechnology was born. Nadrian (Ned) Seeman is credited with founding the field. In 1982, Seeman proposed the idea of using DNA to create nanoscale structures by exploiting the Watson and Crick complementary base-pairing property of DNA (Fig. 1.1)[170]. DNA, unlike other nanoscale materials, had a precise language that could be programmed to enable self-assembly of the DNA into nanoscale shapes. In his work, Seeman designed DNA junctions with sequence-specific 'sticky ends' (a few nucleotides of an oligonucleotide which extend beyond the structure and encourage self-assembly with complementary unpaired nucleotides) which self-assembled into DNA arrays[170]. Seeman further demonstrated the feasibility of this idea by designing and fabricating several higher-order nanoscale shapes, including cubes, arrays and other geometries (Fig. 1.1)[219,32].

Seeman's work soon gave rise to a method for self-assembly of DNA structures, the DNA tile technique[127]. With this method, DNA tiles were developed with several overhang 'arms' that enabled the fabrication of highly periodic and symmetric structures. The DNA tensegrity triangle tile was assembled in 2009, marking a milestone in the field, as it was the first designed three-dimensional nanostructure crystal that was well-ordered enough to diffract to atomic resolution[236]. Complementary to the DNA tiles technique, Peng Yin developed a special kind of single-stranded DNA tile called

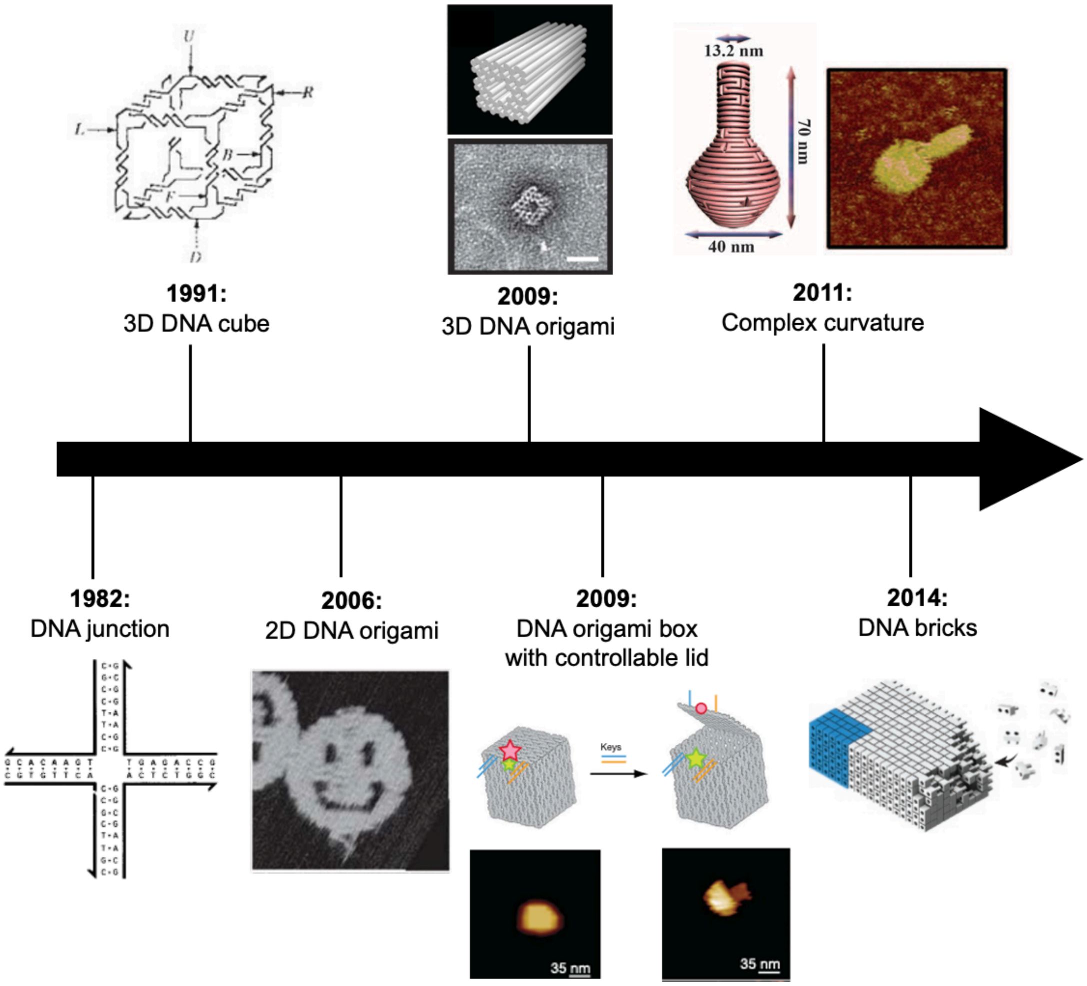

Figure 1.1: Brief timeline of discoveries in the DNA origami field. Figures were adapeted from the following publications: DNA junction [170]; 3D DNA cube [32]; 2D DNA origami [162]; 3D DNA origami [49]; DNA origami box with controllable lid (Fig. 1.1) [8]; Complex curvature [73]; DNA bricks [91]. Use of these figures is covered under the fair use provisions of U.S. copyright law.

a DNA brick (Fig. 1.1)[91] . Each DNA brick has a unique single-stranded DNA sequence which can interact with other bricks, creating two- or three-dimensional objects. With these discoveries, DNA cemented itself as a viable building material for nanoscale structures.

1.0.3 DNA ORIGAMI

In 2006, Paul Rothemund introduced the technique called DNA origami, which is the technique utilized to build the nanostructures in this thesis work[162] (Fig. 1.1). DNA origami is a novel nanofabrication tool that enables specific folding of a long 'scaffold' DNA strand into a 3D nanostructure via complementary base pairing of short 'staple' (20-80 bp) oligonucleotides. The source of the long DNA scaffold is typically the M13 bacteriophage genome, as synthesis of oligonucleotides that are thousands of base pairs in length is extremely inefficient[95], even though this could change as novel technologies enable efficient synthesis of long DNA strands. Self-assembly of these DNA origami nanostructures requires the presence of positive cations (typically Mg^{2+}) to counteract the repulsive force due to the close packing of the negatively charged DNA backbone. This breakthrough discovery of DNA origami allowed for the fabrication of more complex two- and three-dimensional nanostructures. Despite these advances in the field, DNA origami nanostructures are limited by the length of the scaffold strand and by the chosen lattice (square lattice or honeycomb) for templating the design.

The first DNA origami nanostructures were two-dimensional structures. Douglas and colleagues in the Shih lab first demonstrated the development of complex three-dimensional nanostructures (Fig. 1.1)[49]. Douglas also designed a software program, cadnano, which now facilitates design of such complex structures, encouraging adoption of the technology by many labs worldwide[50]. Other advances in the field include introducing curvature into the DNA origami (Fig. 1.1), unlocking a wider array of structures[44,73], and the development of hollow structures via 'wire-frame' origami, which are not constrained to any lattice, and thus are better able to approximate any desired shape[49,213]. Nevertheless, these 'wire-frame' structures are less rigid than solid DNA origami structures, which can limit their

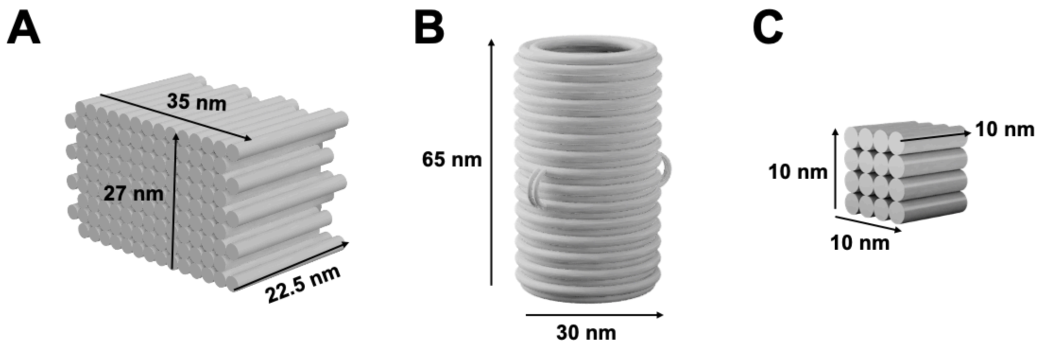

Figure 1.2: Representative three-dimensional renderings of various DNA origami nanostructures, showcasing the diversity of structures which can be formed using the DNA origami technique. A. This three-dimensional structure is a DNA origami square lattice block, as described by Ke et al.[90], and utilized in the subsequent chapters of this thesis. **B.** This three-dimensional structure is a 30 nm barrel structure, as described by Wickham et al.[218]. **C.** This three-dimensional structure is a nanocube, as described by Scheible et al.[166].

range of applications. Researchers have also developed methods for fabricating higher-order superstructures, expanding beyond the nanoscale[195,208,223].

1.0.4 Functionalizing DNA origami

In contrast to other nanoparticle strategies which only offer control over average ligand density, DNA origami offers precise structural control at the nanoscale level and the capability to act as a modular billboard for various cargos[162,49,44,73,90]. The diameter of the DNA double helix is approximately 2.5 nm with 10.5 base pairs per turn of the helix and a rise of 0.335 nm per base pair in physiological salt and temperature conditions; the exact dimensions of the DNA double helix depend on the environmental conditions, as well as the form of the nanoscale assembly. The dimensions of the double helix dictate the resolution of the DNA origami nanostructure; because the width of a DNA double helix is 2.5 nm, the minimum ligand spacing on the DNA origami nanostructure is 2.5 nm between neighboring ligands.

More recent studies have imparted additional dynamicity onto DNA origami, by programming in specific motifs which react to environmental stimuli. For example, studies have demonstrated the feasibility of DNA walkers, which are capable of motion via the hybridization and displacement of 'fuel' strands[225,178,143]. Responsive containers for cargo delivery have been developed which rely on i-motifs and open and close in response to changes in pH[55,176,125]. Imparting DNA origami with specific functions suggests the potential of DNA origami as nanoscale molecular machines.

With the development of DNA origami, researchers began designing more functional nanostructures for specific applications, including but not limited to drug delivery systems, biosensors, nanorobots and molecular machines[31,139,17,66]. Recent discoveries in the field have uncovered new methods to improve the stability, complexity and functionality of DNA nanostructures for practical applications. For example, researchers have identified coating methods to extend the half-life of DNA origami in serum-containing media, by protecting the structure from serum nucleases[152,7], and have also identified coating methods to promote endosomal escape inside a target cell[182]. These advances are critical for the translation of DNA origami for biological applications.

1.0.5 UNCOVERING BIOLOGY WITH DNA ORIGAMI

More recently, DNA origami has been used as a tool to study biology at the nanoscale level and understand how nanoscale spatial arrangement affects downstream signaling processes[211,77,46]. In fact, numerous reviews have been written about how DNA origami can be utilized to investigate biological systems[98,57,130,56]. With DNA origami, researchers can probe biological processes at a resolution that is unattainable by even super-resolution light microscopy[46]. Cargo number, spacing and stoichiometry can be varied in a systematic fashion to uncover the optimal configuration for a desired biological response. Furthermore, researchers can vary the shape of the nanostructure, as well as the structure's rigidity and curvature to understand the effect on downstream cell signaling pathways.

Although DNA origami has been used as a tool to study many varied biological responses, including apoptosis, viral capsid arrangement, coagulation and enzyme activities[16,234,185,161,96,212], many studies focus on improved understanding of immune processes[77,46,198,173,188,59,94]. DNA origami is a powerful tool to investigate how the spatial arrangement of activating ligands plays a role in human immune response, especially as increasing lines of evidence suggest that the nanoscale spacing of immune stimulating molecules affect the subsequent immune polarization, via multimerization and cross linking of the corresponding receptors. As such, several studies have investigated how the copy number, position and spatial arrangement of biological cargo affects biological responses.

There are many other studies that validate that nanoscale spacing matters in inducing a biological response. For example, Veneziano et al. and Wamhoff et al. demonstrates how antigen spacing on a wireframe DNA origami nanostructure affects B cell activation and ultimately the neutralizing antibody response[198,211]. Many studies also focused on TCR-MHC interactions, as the immunological synapse is known to have a precise nanoscale arrangement. Sun et al. showed how spacing of MHC complexes on artificial antigen presenting cells (APCs) affects T cell activation before therapeutic infusion[188]. Dong et al. showed that TCR patterning affects both the sensitivity and kinetics of downstream signaling[46]. Zhang et al. focused on the effect of receptor binding domain organization on SARS-CoV-2 immunity[230]. Furthermore, one chapter of this thesis will focus on investigating the biological effect of CpG adjuvant spacing in the context of cancer vaccines[228], while another chapter will focus on better understanding the biological effect of CD40 ligand spatial arrangement on adaptive immune responses.

DNA origami is a valuable tool for understanding biology. Many researchers have taken it a step further and have applied DNA origami nanostructures for biosensing, detection and diagnostics. For example, Sun et al. showed how the arrangement of pMHC multimers can be tuned to detect CD8+ T cells[189]. Other studies demonstrated that the rational arrangement of DNA probes on DNA origami nanoparticles improved the recognition efficiency of such probes, enabling the detection of disease-specific microRNA[74,118]. These studies and others highlight some of the translational applications of DNA origami.

1.0.6 DNA ORIGAMI AS A THERAPEUTIC

Beyond biosensors and diagnostics, researchers have also utilized DNA origami nanoparticles to deliver therapeutic cargo. DNA origami is highly addressable and offers precise control over the shape and size of the nanoparticle, as well as the arrangement of the associated cargo.

Many studies demonstrate the utility of DNA origami nanostructures for drug delivery. The first cargo to be delivered to cells via DNA origami are intercalating chemotherapy drugs, such as doxorubicin [235,84]. These drugs can intercalate into the DNA duplexes of the nanostructure, enabling simple loading and tunable release of the cargo without requiring chemical conjugation [235]. This delivery strategy was validated in a living murine model in 2016 with daunorubicin, a similar intercalating chemotherapeutic [72].

Chemical conjugation of therapeutic cargo to oligonucleotides unlocks many more therapeutic possibilities for delivery via DNA origami nanoparticles, beyond just intercalating drugs. DNA origami has been demonstrated to deliver therapeutically relevant DNA, RNA, peptides, and proteins to target cells, including dendritic cells and tumor cells, inducing downstream signaling processes [215,114,117]. Several studies have focused on delivery of CpG, a single-stranded DNA sequence that serves as an adjuvant [144,169,228,52], as it is readily integrated into the DNA-based nanoparticle.

DNA origami can also be used to deliver DNA or siRNA directly for gene editing applications [229,192,222]. In 2019, Zhang et al. demonstrated siRNA-induced gene silencing in mature plants via DNA origami delivery [229]. Tang et al. demonstrated efficient in vivo gene editing of a tumor-associated gene by delivering Cas9 protein and an associated guide RNA [192].

Additionally, DNA origami has also been used to deliver therapeutically relevant proteins and peptides. Zhao et al. demonstrated the delivery of RNase A to kill targeted tumor cells [233]. Wagenbauer et al. demonstrated delivery of single chain antibody fragments (scFvs) to engage and activate T cells [207]. Several other studies conjugate neoantigen peptides as the relevant antigen for immune activation[188,228,87].

Furthermore, DNA origami has demonstrated potential as a stimuli-responsive therapeutic, delivering cargo to an acidic environment or only after binding of a specific "key" DNA strand[114,47]. The majority of initial studies of DNA origami therapeutics have relied on cancer as the disease of interest, likely due to the widespread availability of model cell lines and murine models.

However, the COVID-19 pandemic has renewed interest in using DNA origami as a vaccine delivery strategy. One study examined the spatial arrangement of the receptor binding domain (RBD) protein in a DNA origami-based SARS-CoV-2 vaccine[144], while another designed DNA origami nanostructures to trap SARS-CoV-2, among other viruses[134,180]. Additionally, DNA origami is not just limited to applications in cancer and infectious diseases. Studies also investigated DNA origami in the context of autoimmune disorders and thrombosis, respectively[234,123], suggesting that DNA origami nanoparticles could serve as a viable delivery strategy for a host of diseases.

In summary, this brief section showcases the wide diversity of therapeutically relevant cargo which can be delivered via DNA origami and highlights two disease areas, which will be further explored in the remaining chapters of this thesis, where DNA origami has demonstrated promising initial efficacy via pre-clinical studies.

1.0.7 Therapeutic nanoparticles

Nanotechnology as a field was founded in 1959, when Richard P. Feynman presented a paper termed, "There's Plenty of Room at the Bottom: an invitation to enter a new field of physics"[60]. By 1991, the term "nanomedicine" had been published for the first time in the book "The Nanotechnology Revolution"[51]. As such, nanoparticles, defined as particles with one dimension less than 100 nm[156], have been used for several decades to deliver therapeutic cargo to target cells. The first therapeutic nanoparticle, Doxil, a liposomal formulation of the chemotherapy doxorubicin, was approved by the FDA in 1995[9], and since then, more than 30 therapeutic nanoparticles have been approved by the

FDA[11].

Many review articles have compared different nanoparticle platforms[9,10,11,5]. For the purpose of this article, we will not summarize their work and encourage readers to refer to the above cited review articles. Lipid nanoparticles have become especially notable recently for their utility in the mRNA SARS-CoV-2 vaccines in 2021[194]. Even though nanoparticles have been clinically approved for certain diseases[9], they have faced challenges in translation for many other disease areas. These challenges encompass both biological issues (e.g. biodistribution, trafficking to disease site) and technological issues (e.g. manufacturing scale-up, efficacy prediction, optimization of critical parameters)[9]. These challenges are similar to the challenges that DNA origami nanoparticles will face on the path to clinical translation.

The main difference between these nanoparticle platforms and DNA origami nanoparticles is that other nanoparticles can only control the homogenous density of cargo (e.g. loading high or low amounts of therapeutic cargo) on the entire surface or encapsulated within the nanoparticle, while DNA origami can precisely control the distance between neighboring cargo in a heterogenous fashion. This difference has proven to be critical in cell studies and murine models, which directly compare irregular cargo spacing with precise nanoscale cargo spacing, as controlled by DNA origami[228,38,198,211]. However, we have not identified any study that directly compares DNA origami nanoparticles with clinically-approved nanoparticle platforms. We believe that this direct comparison is necessary to critically evaluate whether DNA origami can outperform other nanoparticle delivery strategies.

In summary, therapeutic nanoparticles have been validated in the clinic for several decades. They have faced challenges on the path to clinical translation, just as DNA origami nanoparticles will face challenges. Finally, DNA origami needs to be directly compared to clinically-approved nanoparticle platforms in order to gain traction as a viable therapeutic delivery strategy for clinical use.

1.0.8 Advantages of DNA origami in therapeutics

DNA origami offers several advantages in therapeutics compared to other nanoparticle delivery platforms. We have identified some of these advantages as follows: (1) precise nanoscale delivery of multiple cargo; (2) modular, highly programmable design; (3) well-established fabrication and (4) minimal cold-chain storage requirements.

First and most notably, DNA origami offers precise control over cargo spatial arrangement at nanoscale resolution. This control allows for optimization of the ideal spacing to elicit a desired biological response; ideal spacing of immunostimulatory cargo has been demonstrated to enhance immune polarization in murine models[228]. Additionally, multiple different cargo (for example, antigens and adjuvants) can be conjugated onto the same particle with precise stoichiometry and spacing, allowing for co-delivery of multiple cargo to the same cell.

Second, DNA origami has a modular, highly programmable design. This modularity is a distinct advantage for diseases where rapid fabrication of a therapeutic is desirable. For example, in the later chapters, we will demonstrate the utility of DNA origami for personalized cancer medicine as a neoantigen vaccine. The highly modular DNA origami is ideal for the purpose of personalized medicine because the nanoparticle with the associated adjuvant can be fabricated in advance, and then patient-specific neoantigens can be identified, rapidly synthesized and fabricated onto the nanoparticle via Watson and Crick base pairing chemistry in a minimum amount of time. This modularity is also a distinct advantage for pandemic preparedness, as the adjuvant-conjugated nanoparticle can be stored until a viral variant of concern is identified; then, the variant associated-antigen can be synthesized and fabricated onto the nanoparticle for rapid dissemination. Additionally, this modularity means that virtually any cargo can be conjugated onto the DNA origami, as long as the cargo is amenable to oligonucleotide conjugation.

Third, DNA origami fabrication is well-established and efficient at bench-top scales. DNA origami is self-assembled during an overnight annealing temperature ramp, then purified, conjugated with appropriate cargo via simple base-pairing hybridization, and further processed for biological applications. Self-assembly tends to have a greater than 90% yield (data not shown), while polyethylene glycol (PEG) purification has a recovery yield of at least 50%[172], depending on the DNA origami structure.

Fourth, DNA origami nanostructures are stable at 4°C, contrasting with mRNA vaccines needing -20°C to -80°C cold chain storage[205]. As such, DNA nanostructures do not have the cold-chain storage requirements that hampered worldwide delivery of mRNA vaccines.

In summary, DNA origami has several distinct advantages as a therapeutic platform, most notably, in its precise control over the nanoscale arrangement of cargo, which has demonstrated increase therapeutic efficacy in murine models[228]. Beyond this initial advantage, DNA origami is also highly modular, and has robust manufacturing at bench-top scales and minimal cold-chain storage requirements, suggesting that it is well-suited for applications in personalized medicine and pandemic response, where modularity and speed of fabrication are highly desired.

1.0.9 Challenges of DNA origami in therapeutics

DNA origami faces several barriers on the path to clinical translation. The key challenges that we and others have identified are as follows: (1) in vivo stability, (2) targeting, (3) cost, (4) manufacturing scale-up and (5) demonstration of safety[2,45]. All of these challenges will likely have to be addressed before a DNA origami-based therapeutic is approved for clinical use. The first challenge of DNA origami translation is the stability of the structures in vivo[45]. Our body harbors many nucleases to degrade foreign DNA. DNA origami is no exception, as it is recognized by our immune system as foreign DNA. As such, researchers have developed several post-fabrication processing methods to improve the stability of DNA in physiological conditions[18]. One method is oligolysine coating, where cationic lysines coat the negatively charged nanoparticle, and PEG groups shield the DNA origami structure from degradation[152]. Furthermore, another study showed that glutaldehyde-crosslinking of the oligolysines imparts further stability[7]. However, no long-term in vivo studies have been performed with DNA origami, so we do not know the extent of this stability in vivo. The major innovation that led to mRNA becoming a therapeutic modality was the identification of pseudouridine as a modified base that imparted significant stability to the mRNA molecule while also diminishing its in vivo immunogenicity[88]. A similar innovation may be necessary for DNA to persist in vivo and to ultimately achieve clinical translation.

The second major challenge of DNA origami translation is targeting and in vivo distribution. DNA origami is readily taken up by cells in vitro[120]; however, only a few studies have investigated how the nanoparticles distribute within animal models[231,116]. These studies have highlighted that in vivo distribution is highly dependent on the shape of the DNA origami nanoparticle[231], although the kidney is the primary organ where these nanoparticles accumulate[45]. Researchers have tried to impart additional targeting capacity via conjugation of DNA aptamers, which are DNA sequences with secondary structures that bind to markers on the surface of specific target cells[31,155,82,147,65]. However, more studies are needed to understand and manipulate the trafficking of DNA origami nanoparticles.

The third major challenge is the cost of DNA. With current prices for DNA synthesis, DNA origami is expensive compared to other nanoparticle modalities. However, the price of DNA decreases every year as companies scale up production and competition increases, with consistent decreases by a factor of 1.5 each year, in a manner similar to Moore's law[136]. Several studies have highlighted advances in single-stranded DNA synthesis, suggesting further improvements are on the horizon for commercial scale synthesis[95,15,153,133,111,146]. Dobrovolskaia et al. estimate that the cost per milligram of DNA origami as 141.39 USD, compared to an estimated 141.50 for PEGylated liposomes, suggesting that the cost of DNA origami is on par with liposomal formulations, although it remains to be seen if this holds true with manufacturing scale-up[45]. Additionally, the decreasing cost of DNA synthesis is expected to continue, suggesting that DNA origami could become more cost-competitive with other nanoparticle technologies in the future.

The fourth major challenge of translating DNA origami to the clinic is the manufacturing novelty and complexity. One particularly challenging material is the scaffold DNA, which is several thousand base pairs in length. We typically harvest the M13 bacteriophage genome in-house to use as the scaffold strand and design the DNA origami with this sequence as a template[25]. However, for manufacturing consistency and ultimate approval by the FDA, it would be ideal to synthesize this DNA enzymatically. To date, the longest single stranded DNA produced by enzymatic synthesis is 15000 bp[199], which is longer than the scaffold strand of 8634 base pairs used in the studies detailed in later chapters. Nevertheless, even though synthesis of these long lengths is possible, the yield of DNA synthesis is incredibly low, making production of a high quantity of DNA prohibitively expensive. Kano Therapeutics is one start-up that is tackling this challenge and claims to have developed a more robust method for synthesis of long single-stranded DNA products[58]. More than just the synthesis of the scaffold DNA, scale-up of the entire DNA origami manufacturing process could present challenges, as parts of the protocol are highly specialized and have been optimized for the lab environment. For example, to purify the DNA origami, we rely on a procedure called polyethylene glycol (PEG) purification, which requires adding a specific percentage of PEG to each sample, spinning down the mixture, and then carefully removing the supernatant via pipette. This protocol may be difficult to scale-up for larger scale studies. However, several other purification methods have been validated with DNA origami and may be more appropriate for large-scale DNA origami synthesis[172]. Finally, Afonin et al. highlighted how the ability to conjugate these nanostructures with peptides, nanobodies, antibodies, small molecules and other cargos leads to more complex therapeutics and ultimately a more convoluted path to regulatory approval, as each type of cargo is reviewed by a different center within the FDA[2]. In summary, DNA origami is a novel technology and requires a novel manufacturing procedure which must be scaled up and carefully validated by the FDA. As such, we expect that manufacturing may be a hurdle on the path to clinical translation.

The final major challenge that we have identified is the safety of DNA origami nanoparticles in humans. Even though the immunogenicity and toxicity have been studied in the short-term in murine models and non-toxicity was confirmed[120], the long-term immunogenicity and side effects of DNA origami therapeutics must be studied in clinical trials. For example, even with the oligolysine coating[152], the DNA origami nanoparticles will degrade over time in the presence of serum. The degradation products of the DNA origami nanostructures need to be characterized for safety. Afonin et al. highlighted that there are many open questions about how nucleic acid nanotechnologies interact with the immune system and these questions must be answered in order to tailor formulations for effective therapeutics, while also minimizing undesirable immune stimulation and adverse effects[2]. Additionally, if M13 phage DNA is used as the DNA origami scaffold, as it is used in our pre-clinical studies, then we need to confirm that the foreign phage DNA does not have immunogenic properties, especially as there are many toll-like receptors and other innate immune receptors which are activated by DNA[45]. Furthermore, prior clinical studies with DNA oligonucleotides have been led to significant side effects, including decreases in immune cell counts, splenomegaly, plasma coagulation inhibition, activation of TLR9 and other pattern recognition receptors, and others, which highlight the need to carefully examine the safety of DNA origami[45]. Future studies must extensively characterize the pharmacokinetics, pharmacodynamics, immunogenicity and toxicology profiles of these therapeutic DNA origami-based nanoparticles, before moving to a clinical trial and eventually obtaining FDA approval.

This list of challenges is not an exhaustive list, but rather key hurdles that we have identified that must be overcome for DNA origami to reach the clinic. We believe that all of these hurdles are surmountable, but should not be treated lightly, as they are all critical considerations in the path to clinical translation. Afonin et al. recommend that a nucleic acid nanotechnology consortium, where translational efforts can be consolidated, would expedite the translation of DNA nanotechnology from bench-to-bedside[2]. We agree that combined efforts would dramatically accelerate this process and may be necessary to overcome all of the above hurdles in a timely fashion.

1.0.10 CONCLUSION

In the field of DNA nanotechnology, there are now several methods to create precisely defined nanoscale structures in a robust and generalizable way. DNA origami is particularly notable for its ability to generate rigid nanostructures from a single long ‘scaffold’ strand of DNA. Advances in coatings for the DNA nanostructures, which protect the DNA from degradation by serum nucleases, unlocked the application of these DNA origami nanostructures in biological systems.

Studies from the past decade have applied these rigid DNA origami nanostructures to understand biological signaling, to detect biomarkers and most recently, to treat disease. As a therapeutic, DNA origami has the unique advantage of being highly programmable for modular conjugation of diverse cargo, while also offering precise control over the nanoscale spacing of cargo. Furthermore, studies have suggested that the nanoscale spacing of cargo plays a critical role in subsequent biological signaling, suggesting that this level of control over cargo spacing is valuable in therapeutics design.

Nevertheless, we believe that prior studies have not highlighted the full potential of DNA origami as a therapeutic platform. The reminder of this thesis will focus on demonstrating the diverse applications of DNA origami as a modular, highly programmable, disease-agnostic therapeutic platform.

1.0.11 SCOPE OF THE THESIS

In this thesis, we describe four studies which validate the utility of DNA origami for therapeutic applications. First, we present a study where CpG, an immune adjuvant, is conjugated onto the DNA origami nanoparticle in various nanoscale arrangements, and the optimal CpG arrangement is identified and validated in extensive in vivo and in vitro studies, with a focus on cancer models. Second, we describe how this CpG-conjugated DNA origami nanoparticle can be repurposed for infectious disease applications, highlighting the modularity and programmability of DNA origami. Third, we describe conjugation of CD40L, an immune activating molecule, in various spatial arrangements onto the DNA origami nanoparticle and detail why an optimal arrangement of CD40L was not uncovered. Taken together, these works highlight the potential of DNA origami as a therapeutic platform for various cargo and disease areas, as well as a tool for understanding biological receptor-ligand interactions.

2

Fine tuning of CpG spatial distribution with DNA origami for cancer vaccination

2.1 Author Contributions

The contents of Chapter 2 are reproduced from Zeng, Y.C., Young, O. J., Wintersinger, C. M., Anastassacos, F.M., MacDonald, J. I. , Isinelli, G., Dellacherie, M.O., Sobral, M., Bai, H., Graveline, A.R., Vernet, A., Sanchez, M., Mulligan, K., Choi, Y., Ferrante, T.C., Fell, G.G., Neuberg, D., Wu, C.J., Mooney, D.J., Kwon, I.C., Ryu*, J.H., Shih*, W.M., (2022). Fine tuning of CpG spatial distribution with DNA origami for improved therapeutic cancer vaccination. *Biorxiv.*

*Co-corresponding authors

Y.C.Z. developed and planned the experiments, carried out the vaccine fabrication and validation, and wrote the manuscript. J.H.R. and W.M.S provided experimental and theoretical guidance and edited the manuscript. O.J.Y. assisted Y.C.Z. in performing experiments, analyzing data and manuscript editing. C.M.W., F.M.A., J.I.M. and GI assisted with the DNA origami design, modeling and fabrication. H.B. performed the RNA sequencing analyzing. M.O.D, M.S, M.S, A.R.G., A.V. and M.S. helped with animal study design, modeling and sampling. T.C.F assisted with confocal experiment. Y.C. assisted with 3D modeling and manuscript editing. G.G.F and D.N. guided statistical analysis. C.J.W. guided the experiment design and offered manuscript editing. D.M. and I.C.K. provided project support and manuscript editing.

2.2 Abstract

Multivalent presentation of ligands often enhances receptor activation and downstream signaling. DNA origami offers precise nanoscale spacing of ligands, a potentially useful feature for therapeutic nanoparticles. Here, we use a square block DNA origami platform to explore the importance of spacing of CpG oligonucleotides. CpG engages Toll-like receptors (TLRs) and thereby acts to activate dendritic cells. Through in vitro cell-culture studies and in vivo tumor-treatment models, we demonstrate that square blocks induce Th1 immune polarization when CpG is spaced at 3.5 nm. We observe that this DNA origami vaccine enhances DC activation, antigen cross-presentation, CD8+ T cell activation, Th1-polarized CD4+ activation and natural killer cell activation. The vaccine also synergizes effectively with anti-PD-L1 for improved cancer immunotherapy in melanoma and lymphoma models and induces long-term T cell memory. Our results suggest that DNA origami may serve as a platform for controlling adjuvant spacing and co-delivering antigens in vaccines.

2.3 Introduction

Therapeutic personalized cancer vaccine technologies have made tremendous strides in recent years[164]. Successful vaccination requires immune activation via engagement of pattern-recognition receptors such as Toll-like receptors (TLRs) expressed by antigen-presenting cells (APCs). One class of TLR ligands is CpG oligodeoxynucleotides (termed CpGs here) containing unmethylated cytosine-phosphate-guanosine present in bacteria and viruses [14,19]. Recognition of CpGs by TLR9 in APCs can be exploited to boost the antigen-specific immune response [19]. Nanoparticles that display multiple copies of CpGs represent promising candidates for cancer vaccine adjuvants [97,169]. However, limited knowledge exists on optimizing specific spatial arrangements of CpGs on nanoparticles to influence the magnitude, duration, and polarization of immune responses, which could be critical for designing future vaccines targeting cancer or infectious diseases.

The nanoscale distribution of ligands on therapeutic nanoparticles is believed to impact which signaling pathways are activated in targeted cells, as subtle differences in ligand spacing can be translated into diverse cellular responses [26,174,104]. The adjuvant CpG is well known to provoke differential Th1 or Th2 immune responses, depending on the context of CpG presentation [154]. In particular, the spacing between multiple CpGs presented by therapeutic nanoparticles may determine immune polarization. The crystal structure of CpG-bound TLR9 shows two CpG molecules binding to dimeric TLR9 with a spacing of 2.9 nm [142]. Studies on poly (lactic-co-glycolic acid) (PLGA) nanoparticles revealed that a higher density of CpGs induced a Th1-polarized immune response, while a lower density provoked a Th2-polarized response [112]. Another study suggested that CpGs at an optimum spacing of 3.5 nm can interlock with multiple TLR9s like a zipper, resulting in amplified immune responses [168,110]; however, these CpGs were presented in a double-stranded DNA context, whereas TLR9 is thought to bind to single-stranded DNA [142]. Recently, CpG dimers were fabricated on DNA origami with 7 nm and 38 nm spacing [37], where only the former strongly activated RAW264.7 cells. Most recently, another study found that both CpG copy number and spatial organization could contribute to the magnitude of TLR9 signaling when CpG was fabricated on a wireframe DNA origami structure [52]. These studies collectively indicate that CpG spacing at the nanoscale can impact receptor activation and subsequent immune polarization. For cancer therapy, a Th1-polarized APC response would be beneficial, leading to Th1-polarized CD4 and cytotoxic CD8 T lymphocyte activation and secretion of antitumor cytokines[85]. Additionally, nanoparticles with optimally spaced CpGs could enable significant Th1 immune polarization with a minimal adjuvant dose, potentially reducing adjuvant-associated side effects[224]. However, many currently investigated nanomaterials (excluding DNA origami) control only the average spacing, potentially resulting in mixed induction of Th1 and Th2 responses.

DNA origami, recognized for its rigid compact structure, controlled drug release, and precise stoichiometric loading with multiple cargos[102,197,114,117] is explored in cancer therapy. It facilitates the display of nanoscale ligand arrangements[37,52,94,16] such as CpGs and co-deliver tumor antigens. Employing Watson-Crick complementary base-pairing, a long single-stranded DNA (ssDNA) scaffold, and short staple strands self-assemble into custom three-dimensional (3D) nanoscale shapes[162,49,115,177,44]. CpGs can be specifically incorporated into DNA origami via linking to staple strands, and antigens are co-delivered for enhanced presentation and cross-presentation[175,131,34]. Methods have been developed to stabilize DNA nanostructures against denaturation and degradation via electrostatic formulation with PEGylated oligolysine[152,7]. Furthermore, DNA origami is well tolerated when administered systemically[120,210]. This study introduces square block DNA origami (SQB) to investigate CpGs with finer-tuned nanospacings (2.5 to 7 nm) for inducing a Th1-polarized immune response (Fig. 2.1A,B) in our DNA origami vaccine, referred to as DoriVac.

2.4 Results

2.4.1 Fabrication of DoriVac with different CpG spacings

SQB DNA origami, with a rigid structure and dense modification sites, achieves precise ligand spacing as small as 2.5 nm. Unlike other CpG-conjugated nanoparticles, CpG-functionalized DNA origami allows versatile modification with additional cargos (e.g., antigens for co-delivery), maintaining CpG

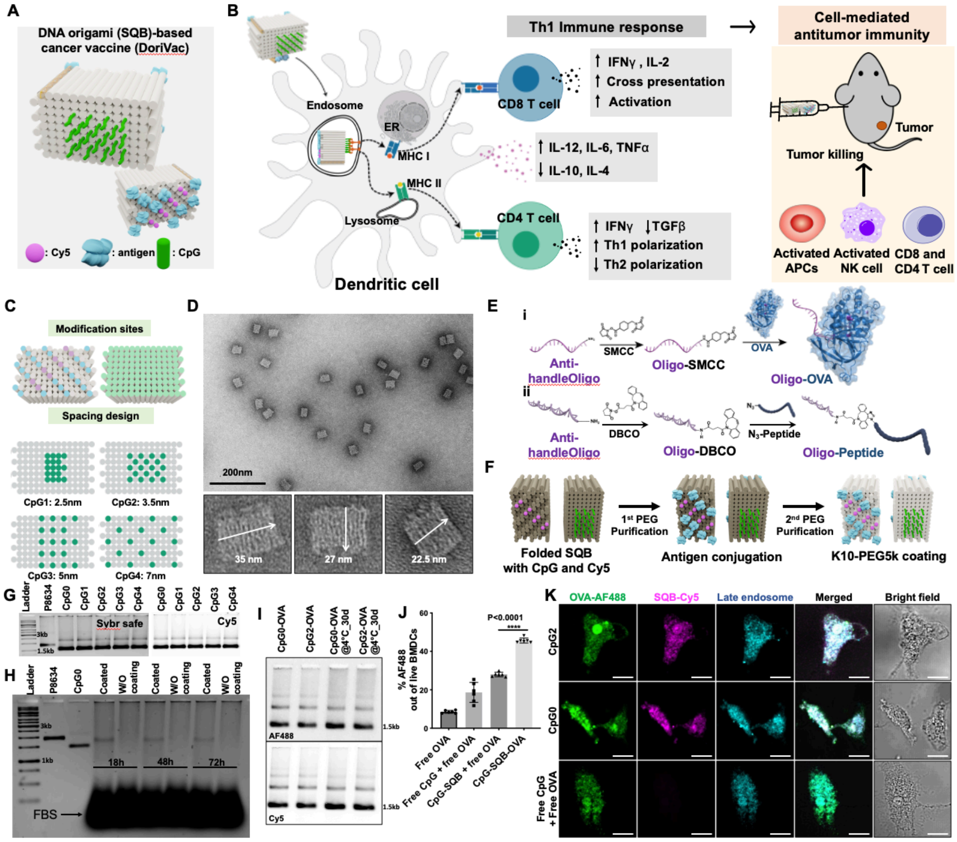

Figure 2.1: DNA origami square blocks (SQBs)-based vaccines (DoriVac) were fabricated with different spacings of CpG adjuvant. A. Proposed schematic of the DoriVac containing CpG (green) as adjuvant, OVA protein (blue) as model antigen and Cy5 dye (pink) as tracer. **B.** Schematic figure showing DoriVac co-delivering antigen and adjuvant at optimal spacing induces improved Th1-polarized immune response. **C.** The modification sites and CpG array on DNA origami SQB. Different CpG (green dots indicate the positions for a single CpG strand) spacings were designed to arrange CpGs on specific helix ends of the SQB. CpG1, 2, 3, and 4 refer to four versions of DoriVac with different CpG spacings. **D.** Representative TEM images of the 3D SQB nanostructure. White arrows indicate dimensions of SQB. **E.** Schematic figure showing **i.** conjugation strategy between OVA and anti-handle via an SMCC linker. **ii.** Conjugation strategy between neoantigen (short peptide) and anti-handle via azide-DBCO click chemistry. **F.** Schematic of the DoriVac composition, purification with polyethylene glycol (PEG) and coating with PEGylated oligolysine (K10-PEG5k). **G.** Agarose gel results showing the SQB folded with different CpG spacing imaged for SYBR Safe (left) and Cy5 (right) (no antigen included). **H.** Agarose gel results of SQB with and without K10-PEG5k coating after incubation with 10% FBS culture medium for 18, 48 and 72 hours. **I.** Agarose gel results of DoriVac (CpG0-OVA, CpG2-OVA) freshly prepared or stored at low temperature (4 °C) for 30 days. Model antigen OVA is conjugated with Alexa Fluor 488 (AF488) and SQB is attached with Cy5. **J.** Quantification on uptake of DoriVac by BMDCs. Model antigen OVA is conjugated with Alexa Fluor 488 (AF488) and SQB is attached with Cy5. DoriVac is treated at 1 nM SQB or equivalent amounts of free CpG and/or OVA as loaded on the SQB for the controls. n=6 replicates of a single prep of BMDC cells randomly distributed into separate wells. **K.** Confocal images of BMDCs treated with DoriVac for 1 day. The scale bar represents 10 µm. Data are presented as mean values +/- SEM in figure 1j. One-way ANOVA was applied for statistical analysis.

spatial distribution. Optimizing adjuvant spacing and stoichiometry enables tailored dosing for maximum efficacy with minimal toxicity[224]. Designed using CaDNAno software, SQB couples an M13-based ssDNA scaffold (Supplementary Table 1) with hundreds of complementary staple strands (Supplementary Table 2)[50] (Supplementary Figure 1–3). Featuring 126 double helices, these structures allow facile modification on both ends of the helices, where ssDNA docking handles can be programmed for precise, addressable spacing of cargos. With one face flat and the other with extruding helices (Fig. 2.1C), these monodispersed structures have dimensions of 35 × 22.5 × 27 nm and exhibit minimal aggregation, as evidenced by TEM imaging (Fig. 2.1D, Supplementary Figure 3).

We explored various CpG spatial patterns on the SQB flat face (Fig. 2.1C, Supplementary Figure 4). CpG-functionalized staple strands were initially incorporated during SQB folding, with subsequent purification using polyethylene glycol (PEG) precipitation (Fig. 2.1E, F). Eighteen phosphorothioate-modified CpG strands (20 mer) were introduced with controlled distances (2.5, 3.5, 5, and 7 nm) corresponding to CpG1, CpG2, CpG3, and CpG4 (Supplementary Table 3, Supplementary Figure 5-10). All CpGs were oriented with the 5′ end extruding from SQB, except for CpG1, which used a mix of ten 5′ and eight 3′ extensions, or a 3′-3′ linkage via DBCO-azide click chemistry for 2.5 nm spacing (see Methods, Supplementary Figure 5). CpG conjugation efficiency exceeded 90% for DoriVac with 18 CpGs and 80-90% for over 18 CpGs (Supplementary Figure 10). CpG0, lacking conjugated CpG strands, served as an origami control. For investigating CpG spacing's impact in the vaccine setting, model antigen protein or neoantigen peptides were modified onto the DNA origami through SMCC linkage or DBCO-Azide click chemistry (Fig. 2.1E, Supplementary Figure 6, 7). DoriVac fabrication included two PEG purification steps and K10-PEG5k coating for stability against nuclease and low salt[152,7]. SQB coated with K10-PEG5k survived in 10% FBS culture for at least 72 hours (Fig. 2.1H). DoriVac remained monodispersed and stable after storage at 4°C for one month (Fig. 2.1I).

To explore CpG spacing's impact on Th1-polarized immune responses, we conducted sequential immune cell co-culture experiments, analyzed using flow cytometry and ELISA (Supplementary Figure 11). SQBs (CpG0 – CpG4) uptake by HeLa cells, 293T cells, and mouse BMDCs was confirmed in several leading cell culture studies (Supplementary Figure 12). BMDCs exhibited greater apoptosis when exposed to free CpG than CpG-SQBs, indicating cytotoxicity of free CpG compared to the same molar amount in SQBs (Supplementary Figure 13A–E). Co-delivery of antigen and adjuvant by SQB notably enhanced antigen uptake (Fig. 2.1J). DoriVac efficiently entered BMDCs, colocalizing with late endosomes in confocal imaging (Fig. 2.1K, Supplementary Figure 14A).

2.4.2 Enhanced Th1 polarization from 3.5 nm CpG spacing

Subsequently, we assessed the impact of CpG spacing on various DC cell types, including mouse BMDCs, human plasmacytoid DCs (pDCs), monocyte-derived DCs (moDCs), and mouse RAW264.7 macrophages. The population of mature BMDCs (indicated by CD86 and MHC II double-positive) significantly increased in the CpG2 group with 3.5 nm CpG spacing (Fig. 2.2A, Supplementary Figure 13G–J). CD40 can bind to the ligands on T helper cells as a costimulatory signal for Th1-polarized immune response[140]. Moreover, DEC205 has been reported as a receptor of CpG on the cell surface and also a marker of activated DCs involved in antigen uptake[107]. The CD40+DEC205+ cell population notably increased in all DoriVac-treated groups, especially in the CpG2 group (Fig. 2.2B, Supplementary Figure 14B). The CpG2 group exhibited the highest increase in SIINFEKL MHC I+ and TLR9+MyD88+ populations (Supplementary Figure 14C, D). ELISA assays demonstrated that DoriVac stimulated BMDCs to produce more Th1-polarizing cytokines (IL-12, TNFα, and IL-6) and fewer Th2-polarizing cytokines (IL-10 and IL-4) compared to free CpG and free OVA administration (bolus vaccine) (Supplementary Figure 14E, G, J, K, Supplementary Figure 14F, H, L). The marked increase in IL-12/IL-10 ratio indicated that CpG delivered at a spacing of 3.5 nm (CpG2) induced greater Th1 polarization compared to delivery through other spatial configurations (Fig. 2.2C, Supplementary Figure 13K–M, Supplementary Figure 14I)[226,78,167]. Of note, the SQB alone (CpG0) generated only minimal IL-12 and IL-10 secretion, indicating the low immunogenicity of

DNA origami (Supplementary Figure 14E-H). The CpG2 group consistently induced the strongest Th1 polarization on human pDCs and moDCs (Fig. 2.2D, E, Supplementary Figure 15). Notably, moDCs exhibited a more vigorous response to DoriVac stimulation compared to pDCs, aligning with a recent study indicating preferential internalization of DNA origami by CD11b+ myeloid cells (Supplementary Figure 15)[120]. Further verification on mouse RAW264.7 macrophages revealed a significant increase in CD11c+, SIINFEKL MHC I+, and CD40+DEC205+ populations (Fig. 2.2F, G, Supplementary Figure 16A). When compared with liposome nanoparticles, commonly used in vaccine formulation, DoriVac demonstrated significantly enhanced stimulation of CD11c, CD40, CD11b, PD-L1, and CD103 expression, along with twelve times more expression of SIINFEKL MHC I+ on RAW264.7 cells (Fig. 2.2H, I, Supplementary Figure 16B, C, Fig. 2.2J, Supplementary Figure 16D).

To understand the gene profiling of immune polarization, we performed mRNA sequencing (RNAseq) analysis on the BMDC samples, which corroborated (Fig. 2.2K, Supplementary Figure 17) the ELISA results and demonstrated upregulation of IL-12, IL-1, and IL-6 gene expression (Th1-polarizing cytokines) and downregulation of IL-10, IL-4, and IL-18 gene expression (Th2-polarizing cytokines) in the context of CpG2 with 3.5 nm spacing compared to bolus vaccine and other spacing configurations. DC maturation markers (CD40, CD80, CD86, and DEC205), and MHC I molecules (H2-K1 and H2-K2) were upregulated in the CpG2 group compared to others. Furthermore, we found that TLR13 is significantly increased in DoriVac groups in the TLR signaling pathway (Fig. 2.2L. Supplementary Figure 17G). A previous study showed that chicken TLR21 is an innate CpG receptor distinct from human TLR9[93], and showed similarity to mouse TLR13. We suspect that TLR13 might also be a receptor for CpGs delivered by SQB in our study, although a different study showed mouse TLR13 recognizes RNA[145]. Based on the gene sequencing results, this pathway might not rely on MyD88 activation (Fig. 2.2L). It coincides with the previous study that TLR9 was activated by plasmid DNA even in MyD88-deficient mice[183]. Some other pathways that may participate in DC

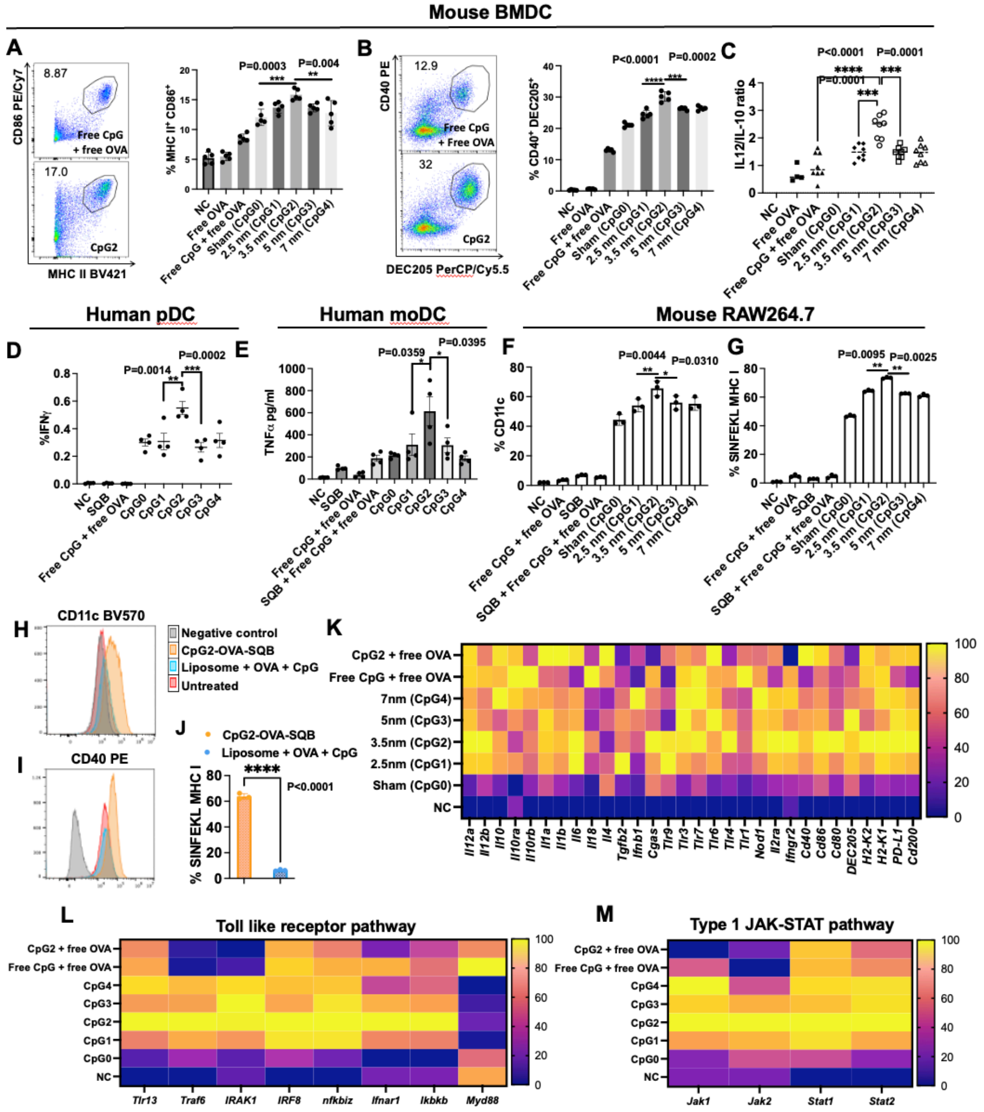

Figure 2.2: CpG, delivered at a spacing of 3.5 nm on DNA origami SQB, provides enhanced dendritic cell (DC) activation for Th1-polarized immune response. A, B. Representative scatter plots (left) and percentages (right) of double-positive CD86+MHCII+ and CD40+DEC205+ populations detected in mouse BMDCs by flow cytometry. **C.** The ratio of IL-12 to IL-10 detected by ELISA after one-day stimulation with various vaccine groups treated to mouse BMDCs. **D.** IFNγ expression in human plasmacytoid DCs (pDCs) treated with various vaccine groups as determined by flow cytometry. **E.** TNFα secretion in human monocyte-derived DCs (moDCs) treated with various vaccine groups as determined by Luminex. **F, G.** Percentages of CD11c+ and SINFEKL MHC I+ population detected in mouse RAW264.7 cell lines by flow cytometry. **H, I.** CD11c and CD40 expression on RAW264.7 cells treated with DoriVac or liposome carrying the same amount of CpG and OVA. NC is unstained flow control. **J.** Percentages of SINFEKL MHC I+ population detected in mouse RAW264.7 cells treated with DoriVac or liposome carrying the same amount of CpG and OVA by flow cytometry (n=3 cell numbers). **K.** Heatmap of the expression patterns of BMDC genes across all the treated groups. The scale bar represents the normalized expression intensity. **L, M.** Heatmap of the expression patterns of BMDC genes related to potential signaling pathways. Sham (CpG0) refers to SQB conjugated with OVA antigen but without CpG. Various DNA origami vaccine constructs (based on the concentration of 1 nM SQB), free OVA (4 nM for A-C, K-M or 10 nM for D-J) or free CpG (18 nM) was treated. In the graphs, "n" represents replicates of a single prep of BMDC cells (A, B: n=5, C: n=8), pDCs (D: n=4), moDCs (E: n=4) or Raw264.7 (F, G, J: n=3) randomly distributed into separate wells. Data are presented as mean values +/- SEM. One-way ANOVA was applied for statistical analysis of Figure 2A-G with Tukey's post hoc multiple comparisons test. Two-tailed student T test was applied for Figure 2J. '*' refers to P ≤ 0.05; '**' refers to P ≤ 0.01; '***' refers to P ≤ 0.001; '****' refers to P ≤ 0.0001.

activation include but are not limited to: Type1 JAK-STAT pathway (Fig. 2.2M, Supplementary Figure 17D), BMP-SMAD pathway (Supplementary Figure 17E), and STING pathway (Supplementary Figure 17F), based on the gene sequencing analysis. Of note, CpG2 showed the highest immune stimulation. Altogether, these data demonstrate that the spatial distribution of CpG has potent biological effects to direct Th1 polarization, and that adjuvant spacing can impact vaccine effectiveness.

2.4.3 Distinct anti-tumor effects from varied CpG spatial patterns

We next queried whether antigen-specific CD4 and CD8 T cell responses could be triggered by DoriVac-pulsed DCs co-cultured with OVA-specific OT-I and OT-II T cells. Flow cytometry results revealed that both CD8 and CD4 T cell activation were increased by CpG2 (3.5 nm spacing) pulsed DCs (Supplementary Figure 18A–D). Interferon (IFN)γ-expressing Th1-polarized CD4 T cells were significantly increased in the CpG2 group when the antigen was co-delivered (Fig. 2.3A). IL-2 secretion by CD4 T cells showed negligible differences among different spacings (Supplementary Figure 18E). TGFβ secretion by CD4 T cells was downregulated in all the DoriVac groups (Supplementary Figure 18F). IFNγ and IL-2 secreted by OT-I CD8 T cells were markedly increased in the CpG2 group (Fig. 2.3B, C), corresponding to increased proliferation of CD8 cells (Fig. 2.3D, E), while CpG-SQBs without co-delivery of antigen showed a similar trend but limited secretion of IFNγ and IL-2. In addition, CpG2 led to increased tumor cell killing by activated CD8 T cells compared to other spacings (Fig. 2.3F, Supplementary Figure 19). These data indicate that (1) spacing of CpG at 3.5 nm enhances the Th1-polarized immune response; and (2) simultaneous presentation of antigen and adjuvant through DoriVac strongly stimulates DCs and preferentially increases cross-presentation via MHC I for improved CD8 T cell activation.

A previous study showed that when two CpGs were conjugated together as a dimer at the 3′ end, the DC stimulation could be enhanced[227]. This study motivated us to explore whether a spatial configuration of CpG dimers might affect receptor multimerization. To this end, we conceptualized adjacent

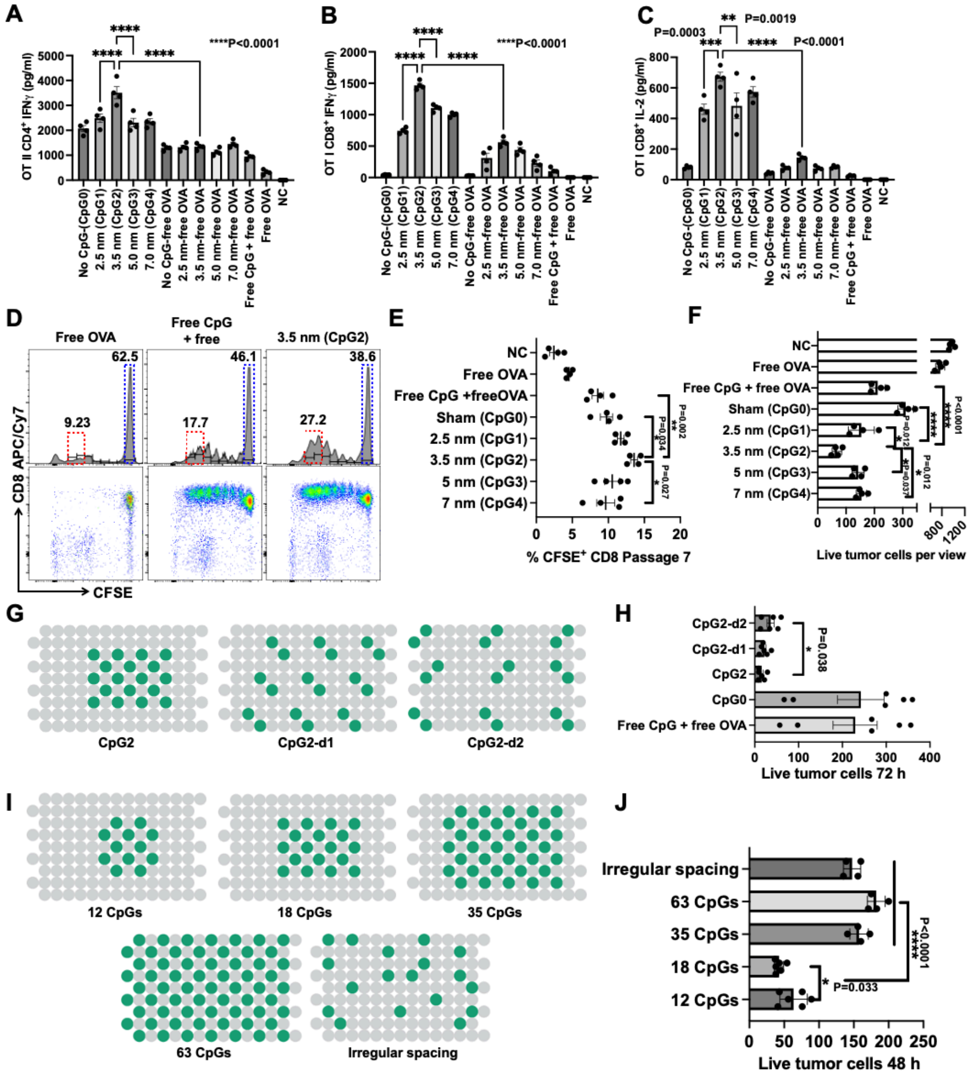

Figure 2.3: T cell activation by DCs instructed by DoriVac bearing varying CpG spatial patterns and densities revealed distinctive anti-tumoral effects. A, B. Quantification of IFNγ in the co-culture supernatant of OT-II CD4 and OT-I CD8 T cells by ELISA. **C.** Quantification of IL-2 in the co-culture supernatant of OT-I CD8 T cells by ELISA. **D.** Representative scatter plots of CFSE fluorescent dye labeled OT-I CD8 T cells in three groups. Red frame, passage 6 and 7 proliferated cells. Blue frame, non-proliferating cells. **E.** The frequency of OT-I CD8 T cells at passage 7. **F.** Quantification of live tumor cells after 48 hours co-culture of OT-I CD8 T cells activated with various DoriVac constructs and B16-OVA melanoma cells. **G.** Designs with different spacings of CpG dimer on SQB. Two CpG oligonucleotide strands were placed as a dimer unit and distributed with three different spacings (CpG2, CpG2-d1, CpG2-d2). **H.** Quantification of live tumor cells after 72 hours co-culture of OT-I CD8 T cells activated with various DoriVac constructs and B16-OVA melanoma cells. **I.** Designs with 12–63 CpGs spaced at 3.5 nm, and one with 18 irregularly spaced CpGs. **J.** Quantification of live tumor cells after 48 hours co-culture of OT-I CD8 T cells activated with various DoriVac constructs and B16-OVA melanoma cells. NC represents negative control without treatment. Various DoriVac constructs (1 nM SQB), free OVA (4 nM for A–F, 6 nM for G–J) or free CpG (18 nM) were tested. In the graphs, "n" represents replicates of a single prep of OT-II CD4 T cells (A: n=4), OT-I CD8 (B, C, E: n=4), or B16OVA tumor cells (F, J: n=4, H: n=6) randomly distributed into separate wells. Data are presented as mean values +/- SEM. One-way ANOVA was applied for statistical analysis of all the figures with Tukey's post hoc multiple comparisons test. '*' refers to P ≤ 0.05; '**' refers to P ≤ 0.01; '***' refers to P ≤ 0.001; '****' refers to P ≤ 0.0001.

CpGs (with 3.5 nm spacing between the two monomers) as a dimer unit and spaced them apart on the SQB with decreasing densities (CpG2-d1 and CpG2-d2 in Fig. 2.3G). Interestingly, we found that both IL-12 and IL-10 were elevated as spacing of the dimer increased even though we did not observe an associated change in the IL-12/IL-10 ratio (Supplementary Figure 20A–C). However, CD8 and CD4 T cell activation (indicated by IFNγ secretion) decreased as the dimer spacing increased (Supplementary Figure 20D, E), and the tumor-killing effects showed a corresponding decrease (Fig. 2.3H, Supplementary Figure 20K¬–M). These data suggest that spatial configuration of CpGs could impact receptor activation and subsequent immune polarization through higher-order receptor multimerization (i.e. beyond dimerization). Furthermore, DNA origami may provide an informative tool to further study the role of multimerization in TLR activation and other receptor activation.

Another study previously demonstrated that increasing the molar ratio of CpG on a DNA duplex induced increasing secretion of IL-12[132]. To investigate if the number of CpGs influences the immune polarization, we kept constant the CpG 3.5 nm spacing, antigens per DNA origami particle, and number of particles, but only increased the number of CpGs per particle from 12 to 63 (Fig. 2.3I). Irregularly spaced CpGs (CpGi) were also designed as a control with 18 CpGs. IL-12 and IL-10 secretion both increased when there were more CpGs (Supplementary Figure 20F, G). However, IL-10 secretion was greatly induced with 35 and 63 CpGs (Supplementary Figure 20G). The IL-12/IL-10 ratio was higher with 12 or 18 CpGs than with 35, 63, or irregularly spaced CpGs (Supplementary Figure 20H). We found that 12 to 18 CpGs showed no difference in terms of IFNγ secretion from CD4 OT-II T cells, but 12 CpGs induced less IFNγ secretion from CD8 OT-I T cells (Supplementary Figure 20I, J). However, 35, 63, and irregularly spaced CpGs induced less IFNγ expression in both CD4 OT-II and CD8 OT-I T cells, consistent with elevated IL-10 leading to inhibition of CD8 T cell function[181]. The tumor-killing effects were most notable in the 18 CpGs group (Fig. 2.3J, Supplementary Figure 20N). These data suggest that both optimal CpG stoichiometry and uniform CpG spacing may be beneficial for Th1 immune response.

2.4.4 DoriVac distribution and immune stimulation in vivo

To explore the potential of DoriVac as a vaccine, its biodistribution was first evaluated through in vivo fluorescence imaging. DoriVac primarily accumulated in the nearest draining lymph nodes (LNs) from the injection site with minimal increase in other LNs (Fig. 2.4A, Supplementary Figure 21). The DoriVac persisted in the draining LN for at least 48 hours and the antigen maintained high intensity even after 48 hours as evidenced by AF488 conjugated on OVA (Fig. 2.4A, B). The SQB was cleared by both the liver and kidney within two days, as the Cy5 fluorescent signal was barely detectable at this time point (Fig. 2.4A-C). Lung and spleen only showed minimal Cy5 signal increase at two and four hours (Fig. 2.4C). Administration of the DoriVac in naïve mice verified that optimized spatial configurations (CpG2; 3.5 nm spacing and 18 CpGs) could greatly increase DC activation and improve the CD8+ tetramer+ population without increasing the immunosuppressive regulatory T cells (Tregs) (Fig. 2.4D–H, Supplementary Figure 22). Encouraged by the preferential Th1 immune response, two doses of the DoriVac treatment were subcutaneously injected on days 0 and 7 as a prophylactic treatment, and then the mice were inoculated with B16-OVA tumor cells on day 14 (Fig. 2.4I). On day 28, measurable tumors were observed in control groups and in 40% of the bolus vaccine group (Fig. 2.4J). No tumors were observed in DoriVac-treated group until day 42. While all mice in the untreated group and 60% of mice in the bolus vaccine group died by the conclusion of the study, only one mouse in the CpG2 group died but with a much longer life span compared to other groups (Fig. 2.4K). These results verified the prophylactic efficacy of the DoriVac in an aggressive murine melanoma model.

2.4.5 Therapeutic DoriVac treatment in mouse melanoma models

We assessed DoriVac's therapeutic antitumor effect in a melanoma mouse model, treating tumor-bearing mice with 10, 20, 40, or 80 pmoles of DoriVac, each with optimized spatial configurations

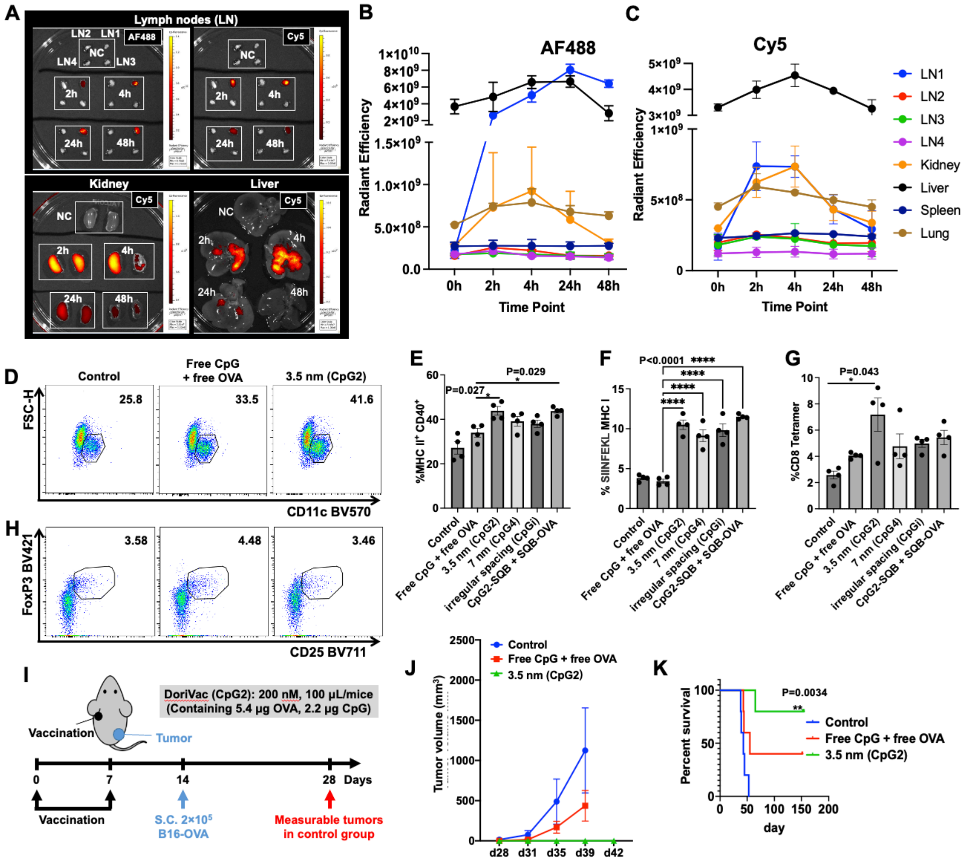

Figure 2.4: DoriVac distribution, in vivo immune-cell stimulation and prophylactic-vaccination effects. A. Representative ex vivo images showing the organ distribution of the DoriVac within 48 hours after subcutaneous injection on left shoulder analyzed by IVIS machine detecting the fluorescence carried on the vaccine nanoparticles. The images showed the AF488 (OVA) or Cy5 (SQB) in different organs. LN1: left brachial; LN2: right brachial; LN3: left inguinal; LN4: right inguinal. **B, C.** Radiant efficiency of AF488 and Cy5 in different organs corresponding to in vivo accumulation. **D-H.** Before applying the vaccine in a tumor model, we vaccinated naïve C57BL/6 mice and detected DC activation and T cell response in the draining lymph node on day 1 and day 8 post vaccination. n=4 lymph node samples from independent mice. **D.** Representative scatter plots showing CD11c+ DC cells in the lymph nodes on day 1 post vaccination. **E.** Flow results showing MHC II+ CD40+ population on DCs. **F.** Flow results showing SIINFEKL MHC I expression on DCs. **G.** Flow results showing CD8 T cell population bound with SIINFEKL MHC I tetramer on day 8 in the lymph node. **H.** Representative scatter plots showing CD4+CD25+FoxP3+ Treg cells in the lymph nodes on day 1 after vaccination. **I.** Schematic showing prophylactic vaccination treatment plan and tumor challenge protocol in C57BL/6 mice. **J.** Tumor growth graph. Note that only one mouse in the DoriVac-treated group demonstrated tumor growth, after a remarkably delayed tumor onset (4 weeks after tumor inoculation). **K.** Mouse survival curve (n=5 mice). Control refers to untreated group. ** in this graph refers to comparison with the control. Data are presented as mean values +/- SEM. One-way ANOVA was applied for statistical analysis of graphs E, F and G with Tukey's post hoc multiple comparisons test. Two-way ANOVA was applied for statistical analysis of graph J with Tukey's post hoc multiple comparisons test. Survival curves were analyzed by Kaplan-Meier method and log-rank test for graph K. '*' refers to P ≤ 0.05; '**' refers to P ≤ 0.01; '***' refers to P ≤ 0.001; '****' refers to P ≤ 0.0001.

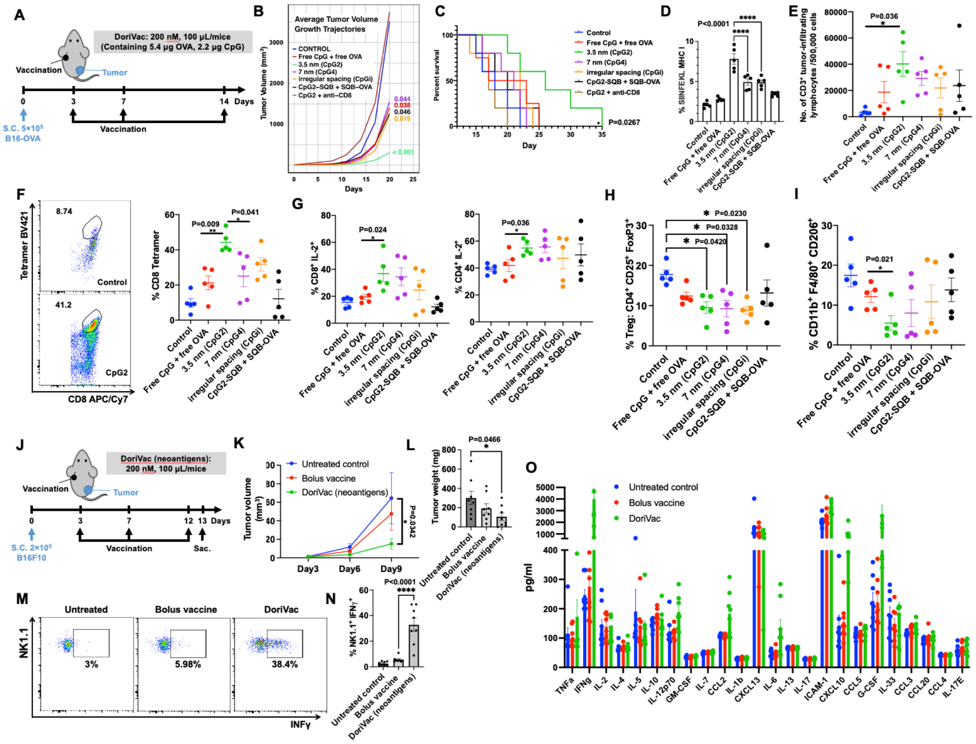

Figure 2.5: Immune cell profiling revealed a Th1-polarized immune response after therapeutic DoriVac treatment in mouse melanoma models. **A.** Schematic delineating mouse tumor model setup and therapeutic vaccination treatment plan in C57BL/6 mice. **B.** Average tumor volume growth trajectories (n=5 mice). **C.** Mouse survival curve (n=5 mice). * refers to comparison with the control. B16-OVA tumor-bearing C57BL/6 mice were treated with vaccines on days 3, 7 and 11, and then sacrificed on day 15. The draining lymph nodes (D) and tumor tissue (E–I) were processed for flow cytometry (n=5 mice). **D.** Percentages of SIINFEKL MHC I+ cells in the CD11c+ population in draining lymph node. **E.** Number of intratumoral CD3+ tumor-infiltrating lymphocytes (TILs) out of 500,000 cells in various treatment groups. **F.** Representative scatter plots (left) and percentages (right) of SIINFEKL MHC I tetramer+ cells in intratumoral CD8+ T cells. **G.** Representative IL-2+ scatter plots on CD8+ cells (left) and percentages of IL-2+ cells in CD8+ and CD4+ T cells (right). **H,I.** Quantification of CD25+FoxP3+CD4+ Treg cells and CD11b+F4/80+CD206+ immunosuppressive type 2 macrophages population in tumor tissue. **J.** Mouse tumor model setup and therapeutic vaccination treatment plan with DoriVac bearing neoantigen in C57BL/6 mice. **K.** B16F10 tumor growth graph (n=8 mice). **L.** B16F10 tumor weight on day 13 (n=8 tumor tissues from individual mice). **M, N.** Representative scatter plots and percentage of double-positive IFNγ+NK1.1+ populations detected in NK1.1+CD3- population by flow cytometry (n=8 mice). **O.** Cytokine expression profile of the plasma samples analyzed by multiplexed Luminex after sacrificing the mice on day 13 (n=8 plasma samples from independent tumor-model mice). Data are presented as mean values +/- SEM. Two-way ANOVA was applied for statistical analysis of graphs B and K with Tukey's post hoc multiple comparisons test. One-way ANOVA was applied for statistical analysis of graphs D–I, L and N with Tukey's post hoc multiple comparisons test. Survival curves were analyzed by Kaplan-Meier method and log-rank test for graph C. '*' refers to P ≤ 0.05; '**' refers to P ≤ 0.01; '***' refers to P ≤ 0.001; '****' refers to P ≤ 0.0001.

of CpG (CpG2). Results showed that 10 or 20 pmoles efficiently inhibited tumor growth and increased survival (Supplementary Figure 23A, B). Notably, 20 pmoles of DoriVac contained only 5.4 μg OVA and 2.2 μg CpG, significantly less than other pre-clinical CpG studies [113]. When applying 20 pmoles of DoriVac with different spacings or corresponding bolus controls, CpG2 with optimal CpG configuration (3.5 nm spacing) significantly delayed tumor growth compared to other spacings (Fig. 2.5A, B, Supplementary Table 5). The median survival of CpG2 DoriVac (26 days) was higher than other groups (18-21 days) (Fig. 2.5C, Supplementary Figure 23C, D). Anti-CD8 antibody treatment abolished therapeutic effects in CpG2, suggesting DoriVac strongly relies on CD8 activation (Fig. 2.5B, C). Immune cells from LNs and tumor tissues showed increased DC accumulation, improved DC maturation and cross-presentation, decreased myeloid-derived suppressor cells, increased monocytes in CpG2 (Fig. 2.5D, Supplementary Figure 24A–J). Th1-polarized CD4 and CD8 T cells were more activated in CpG2 than bolus vaccine (Supplementary Figure 25). Notably, 3.5 nm spacing induced significantly increased CD8 activation compared to other spacings (7 nm or irregular spacing) (Supplementary Figure 25A, C). In the tumor tissue, infiltrated CD3 T cells accumulated notably in the CpG2 group (Fig. 2.5E, Supplementary Figure 26A–D). CpG2 group showed increased effector memory cells and effector cells in both CD4 and CD8 T cell populations (Supplementary Figure 26E–H). A large portion of infiltrated CD8 T cells were OVA-specific in CpG2-treated group, significantly more than CpG4 group where CpG spacing was at 7 nm (Fig. 2.5F). More IL-2+ CD8+ and CD4+ T cells were found in CpG2 group (Fig. 2.5G). Tregs, myeloid-derived suppressor cells, and M2 macrophages in tumor tissue were not increased in DoriVac-treated groups, with a further decreased trend in CpG2 group (Fig. 2.5H, I, Supplementary Figure 26I-M). Furthermore, 35 CpGs (3.5 nm spacing) did not show enhanced therapeutic effect compared to 18 CpGs (CpG2, 3.5 nm spacing), most likely due to decreased CD8 activation (Supplementary Figure 27. Supplementary Figure 20F–J). These results indicate that DoriVac CpG2, with optimal CpG configurations (3.5 nm spacing and 18 CpGs), directed a Th1-polarized immune response in the treated tumor through a cohort of immune-cell regulation.

We further assessed DoriVac's therapeutic efficacy applying neoantigens (Fig. 2.5J). For targeting neoantigens in the murine B16F10 melanoma model, DoriVac was fabricated with B16F10 neoantigen peptides, M27 and M33 (CD8+ responsive) and M30 and M47 (CD4+ responsive)[113,101] (Supplementary Figure 28). DoriVac bearing neoantigen induced significant tumor suppression compared to the untreated control, with one mouse in the DoriVac group showing no tumor after three treatments on day 3, 7, and 12 (Fig. 2.5K, L, Supplementary Figure 29A). Additionally, DoriVac significantly increased NK cell activation detected by IFNγ expression (indicated by NK1.1+IFNγ+), without an obvious increase in NK cell number in the LN (Fig. 2.5M, N, Supplementary Figure 29B-E). Additional immune cell profiling on DC and T cells revealed similar activation phenotypes as shown in Fig. 2.4 and Supplementary Figure 24 and 25. Plasma analysis by multiplex Luminex for cytokine profiling on day 13 showed a massive increase in Th1-polarized cytokines in DoriVac-treated groups, including TNFα, IFNγ, IL-12, CCL-2, IL-6, CXCL10, and G-CSF, with no increase in Th2-polarized cytokines compared to bolus vaccine or untreated groups (Fig. 2.5O). Evaluation of anti-dsDNA antibodies and anti-PEG antibodies disclosed that the increase in anti-dsDNA antibodies is associated with effective anti-tumor effects[196] instead of DNA origami nanoparticles themselves (Supplementary Figure 30A, B). There was also no significant elevation of anti-PEG IgG observed in mouse serum (Supplementary Figure 30C). These results indicate that DoriVac may serve as a safe, effective, and modular platform for presenting various neoantigens to induce therapeutic anti-tumor efficacy.

2.4.6 Synergistic efficacy from DoriVac combined anti-PD-L1

Having observed elevated PD-L1 expression on DCs in the draining LN of DoriVac-treated groups (Fig. 2.6A), we speculated that combining DoriVac with immune checkpoint inhibition would further enhance therapeutic effects (Fig. 2.6B). Indeed, combining with αPD-L1 (but not αPD-1) signif-

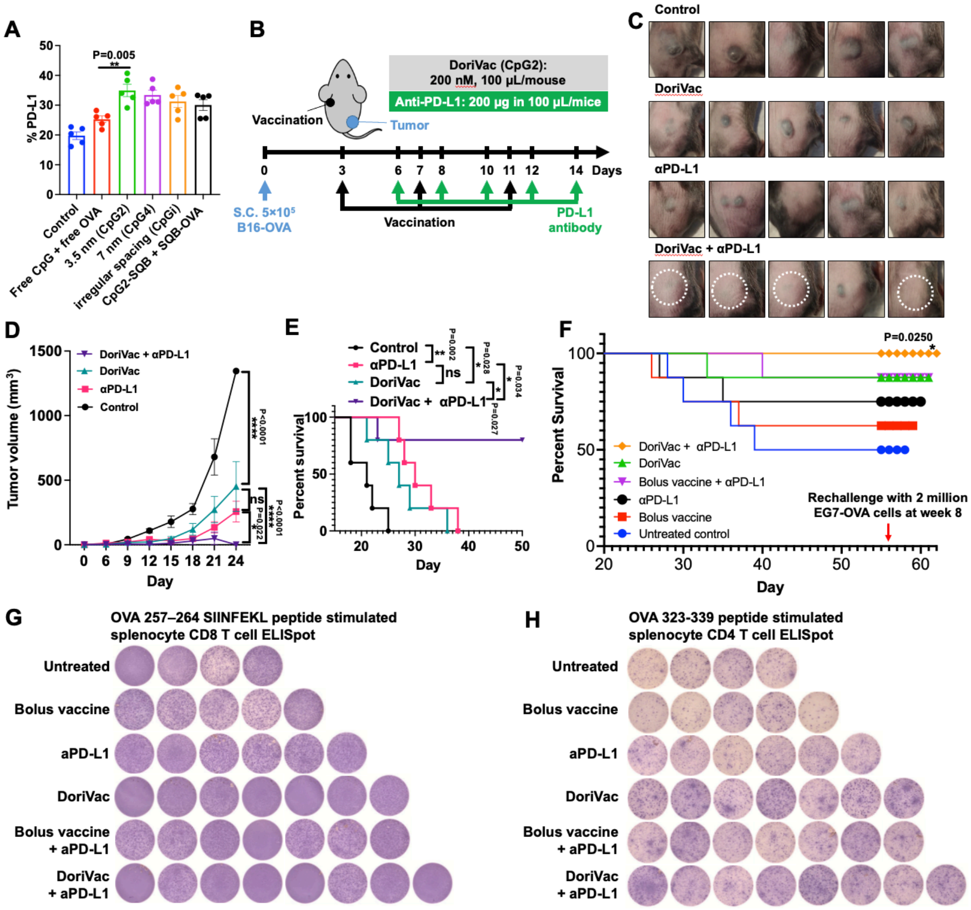

Figure 2.6: DoriVac combined with immune checkpoint inhibitor anti-PD-L1 exhibited synergistic, durable T cell responses. A. Percentages of PD-L1+ cells on dendritic cells (DCs) in the lymph node (n=5 lymph node samples from independent tumor-model mice). PD-L1 expression was increased on the DCs in the DNA origami vaccine-treated groups, correlating with the increase in the activated DC population, which provided a rationale for combination with anti-PD-L1 immune checkpoint inhibitor. **B.** Experimental design schematic for the combination treatment with anti-PD-L1 antibody (αPD-L1). CpG2 DoriVac (200 nM) was subcutaneously administrated on days 3, 7, and 11 and anti-PD-L1 (200 μg/mice) was administered on the days 6, 8, 10, 12, and 14 to B16-OVA tumor-bearing mice. **C, D.** The tumor photos (white circle indicates faded tumor) and associated graph of subcutaneous tumor growth in C57BL/6 mice (n=5 mice). The combination therapy significantly inhibited tumor growth and induced tumor regression in 80% (4 out of 5) of mice. **E.** Percent survival of B16-OVA tumor-bearing mice in various treatment groups (n=5 mice). All four mice with demonstrated tumor regression survived with no sign of recurrence and survived a tumor rechallenge administered at four months. **F.** Percent survival of EG7-OVA tumor-bearing mice in various treatment groups (n=8 mice). All the mice survived from the DoriVac treatment in combination with αPD-L1. **G, H.** IFNγ ELISpot results on the splenocytes of the survived mice at 6 months showed more CD8 and CD4 T cell spots (as indicated by the purple color) in all the DoriVac applied groups. Data are presented as mean values +/- SEM. One-way ANOVA was applied for statistical analysis of graph A with Tukey's post hoc multiple comparisons test. Two-way ANOVA was applied for statistical analysis of graph D with Tukey's post hoc multiple comparisons test. Survival curves were analyzed by Kaplan-Meier method and log-rank test for graph E and F. '*' refers to $P \leq 0.05$; '**' refers to $P \leq 0.01$; '***' refers to $P \leq 0.001$; '****' refers to $P \leq 0.0001$.

icantly inhibited tumor growth and induced regression in 4 out of 5 mice in the B16-OVA melanoma model (Fig. 2.6C, D, Supplementary Figure 31). All four mice with tumor regression survived and exhibited no signs of recurrence (Fig. 2.6E). Rechallenging the surviving mice with 2×10^5 B16-OVA tumor cells four months later resulted in complete tumor remission (Supplementary Figure 31D). ELISpot assays conducted one year after the initial tumor cell inoculation revealed that only DoriVac-included groups could induce SIINFEKL-specific CD8 T cell activation (Supplementary Figure 31E). Beyond the B16-OVA model, DoriVac demonstrated enhanced therapeutic efficacy compared to bolus vaccine groups in the EG7-OVA lymphoma tumor model (Supplementary Figure 32A). All mice treated with DoriVac in combination with αPD-L1 survived (Fig. 2.6F). ELISpot results on the splenocytes and peripheral blood mononuclear cells (PBMCs) of the surviving mice at 6 months disclosed long-term durable CD4 and CD8 T cell memories in the DoriVac-applied groups (Fig. 2.6G, H, Supplementary Figure 32B-D). These results highlight DoriVac's ability to induce both innate and adaptive immune cell activation with a durable T cell response. Moreover, the antigen-specific immune response induced by DoriVac synergized with immune checkpoint inhibition for improved cancer immunotherapy.

2.5 Conclusion

In this study, we utilized a square-block DNA origami architecture to compare the spacing of CpG ligands within the range of 2.5 nm to 7 nm, alongside co-delivery of antigen, resulting in Th1-polarized immune responses. DNA origami serves as a versatile delivery platform for various cargos, offering precise nanospacing control. Its advantages include easy fabrication and purification, high stability, substantial drug loading capacity, and low immunogenicity. These attributes empower DoriVac to elicit effective immune responses with minimal adjuvant quantities. We envision the rapid and convenient loading of patient-specific antigens/neoantigens onto prefabricated, adjuvant-containing DNA origami to create personalized cancer vaccines easily combinable with FDA-approved immune checkpoint inhibitors. This technology platform also holds promise for investigating other cellular ligand-receptor interactions where nanoscale ligand spacing critically influences receptor signaling and subsequent immune polarization. Our findings suggest that the DoriVac platform may extend beyond cancer applications to address infectious diseases, given its capacity to generate robust and durable CD4 and CD8 memory T cell responses.

2.6 Acknowledgements

We thank Qi Yan, Zhao Zhao, Tian Zhang, Pascal Lill, Pranav Prabhala, Leo Chou, Jaeseung Han, Dionis Minev, Benjamin Everhart, Jie Deng, David Zhang, Kwasi Adu-Berchie, Hawa Dembele, Anjali Rajwar, and Kow Simpson for aiding in labor support, experimental design, exploring experiments, or manuscript proof-reading. We also thank Maurice Perez, Michael Carr, and Eric Zigon for their assistance in the lab management and facility usage. We thank Maartje Bastings and Aileen Li for exploration, before the current project initiated, of CpG-functionalized DNA-origami barrels for immune stimulation.

2.7 Funding

This work was funded by Barr Award granted by Claudia Adams Barr Program (Y.C.Z) in Dana-Farber Cancer Institute and by Wyss validation funding (Y.C.Z.) at Wyss Institute for Biologically Inspired Engineering at Harvard. This study was supported by the Korean Fund for Regenerative Medicine (J.H.R., KFRM; 21A0504L1) funded by the Korea government (the Ministry of Science and ICT, and the Korean Ministry of Health & Welfare), and the Intramural Research Program of KIST (J.H.R., No. 2E30840). This project was also supported by an NIH U54 grant (W.M.S., CA244726-01).

2.8 MATERIALS AND METHODS

Our research complies with all relevant ethical regulations at Harvard University, Dana Farber Cancer Institute, and Wyss Institute. Biosafety protocols were approved by the Harvard Committee on Microbiological Safety. All animal studies (Protocol No. IS00003369) were approved by the Institutional Animal Care and Use Committee (IACUC) of Harvard Medical School.

2.8.1 FABRICATION OF SQBS

SQBs were designed using square-lattice CaDNAno and assembled using previously published methods for folding of 3D DNA origami[90]. Construction plans for SQB, scaffold and staple sequences are listed in Figs. S1–2 and Tables S1–3, respectively. Short synthetic DNA staple strands were purchased on a 100 nmole or 10 nmole scale from Integrated DNA Technologies, Inc. Scaffold p8634 was produced in-house using previously published protocols[48], and purified from endotoxins by extraction with 2% Triton-X114[71]. To assemble the structures, DNA staple strands were mixed to a final concentration of 100 nM or 500 nM per strand (as higher concentrations are better for large scale folding as needed for in vivo applications). The optimized folding conditions used were 5 mM Tris, 1 mM ethylenediaminetetraacetic acid (EDTA; pH 8.0), 12 mM MgCl2, 20–100 nM scaffold, 5 times excess core staple strands (in excess compared to the scaffold concentration), 10 times excess handle conjugated staples and 20 times excess CpG-containing staples. Folding was performed in a thermocycler with the following program: denaturing at 80°C for 15 minutes, and then annealing from 50°C to 40°C decreasing at -0.1°C every 10 minutes and 48 seconds for a total folding time of 18 hours. All constructs were purified using PEG-8000 purification (below). The quality of SQBs was analyzed via agarose gel electrophoresis and negative-stain transmission electron microscopy (TEM).

2.8.2 Fluorescent labeling of SQBs

SQBs were labeled with Cy5 fluorophores. DNA oligonucleotides /5AmMC6/GGGATAAGTTGATTGCAGAGC-3′(anti-handle) were modified with a 5′ amine and covalently coupled to Cy5 fluorophores via N-hydroxysuccinimide (NHS) ester coupling (Lumiprobe). DNA oligonucleotide (1 mM in ddH2O) was mixed with 10 times excess of Cy5-NHS (10 mM in DMSO) and supplemented with 10% of $NaHCO_3$ (1M, buffer at pH 8.0). The reaction was carried out in the dark overnight at room temperature shaking at 400 rpm. Zeba size-exclusion and desalting columns (7K MWCO; Thermo Scientific, Waltham, MA) were used to remove unreacted dye through centrifugation at 1000 g for 2 minutes. The columns were washed with 400 µL of ddH2O three times before use, according to manufacturer's protocol. The Cy5 conjugated oligonucleotides were added to the SQB folding pool with 5 times excess to ensure complete conjugation. Eight staples linked with complementary handle strands (5′-GCTCTGCAATCAACTTATCCC-3′) were used to capture the Cy5-linked strands.

2.8.3 CpG-containing staple strands attachment to DNA origami SQB

CpG-containing staple strands were appended on one end of double helices on the flat side of the SQBs. For most of the staples on the flat face of the SQB, 10 thymine residues were added to the end of the staples on the flat face of the SQB (known as a poly-thymine modification) to minimize aggregation of origami. The CpG oligonucleotides with nuclease resistant phosphorothioate (PS) backbone (5′-tccatgacgttcctgacgtt-3′) replaced the poly T at designed positions for nanoscale patterning as described. The CpG strands were added to the 5′ ends of the staples (Supplementary Table 3), except for where indicated below (Supplementary Figure 5). The CpG-containing staples were either ordered from IDT or made in-house by a splint guided T4 ligation (Supplementary Figure 5A–D). For CpG1, to ensure that the CpG orientation was uniform, 3′-3′ linkage of CpG with some staples were applied by dibenzocyclooctyne (DBCO)-azide (Sigma, US) click chemistry (Supplementary Figure 5E–H). When folding the SQBs, the CpG-containing staple strands were 20 times in excess compared to the scaffold concentration to ensure complete conjugation of the CpG-containing strands.

2.8.4 Ovalbumin (OVA) conjugation and quantification

For OVA conjugation, 24 sites on the extruding site of SQB were replaced with 5′-CGTCCCCTTTTAACCCTAGAA-3′ handle oligo at poly T positions. The complementary anti-handle oligo 5′-TTCTAGGGTTAAAAGGGGACG-3′ was modified with an amine group at the 5′ end. This oligo was conjugated with succinimidyl 4-(N-maleimidomethyl)cyclohexane-1-carboxylate (SMCC) linker through NH2-NHS ester reaction. The SMCC-linked oligo was purified through Nap column (GE Healthcare Life Sciences). The purified SMCC-linked oligo was conjugated with OVA through cysteine (thiol)-maleimide group coupling. The maleimide group of SMCC-modified anti-handle can be attached to 4 cysteine residues on OVA (Fig. 2.1D, Supplementary Figure 6). SMCC-linked oligo that was not conjugated with OVA was washed away through 30K Amicon filter (Sigma) filtration for up to 7 times. The conjugated OVA-oligo was incubated with the DNA origami SQB at 37°C for 2 hours at 3 times excess. Free OVA-oligo was removed by PEG precipitation, as described below. To quantify the OVA protein conjugation, a standard curve of fluorophore intensity versus the molar concentration of the AF488-OVA (ThermoFisher, O34781) was made. Briefly, we tested the different AF488 reading by Nanodrop after diluting the protein to a range of concentration that is close to the theoretical concentration of conjugated OVA. The linear curve correlates the OVA molar concentration and the fluorophore intensity. Three individual experiments were executed to get a repeatable equation for calculation. After OVA was fabricated to the SQB and the vaccine was purified, the AF488 intensity was detected by using the equation to calculation the OVA molar concentration. By dividing the concentration of SQB, the number of OVA per SQB is estimated (Supplementary Figure 7).

2.8.5 SQB purification by PEG precipitation

After annealing, SQB monomers or OVA or peptide conjugated CpG-SQBs were purified from excess staples or excess OVA via PEG precipitation. Typically, 1 × TE buffer (5 mM Tris, pH 8.0 and 1 mM EDTA) containing 15% (w/v) PEG-8000 (Fisher Scientific, BP2331), and 510 mM NaCl was added to the origami sample at 1:1 volume in an Eppendorf tube and mixed gently. Note that it is essential to use PEG-8000 containing less than 5% water. The concentration of MgCl2 was adjusted by adding high concentration MgCl2 stock to the PEG buffer to obtain 10 mM MgCl2 concentration in the final mixture. The mixture was centrifuged at 16,000g for 25 minutes at room temperature. The supernatant was carefully removed, and the pellet was re-suspended in 1 × TE buffer supplemented with 10 mM MgCl2. This purification procedure was either carried out once or twice, depending on the desired purity level. This procedure is also used to concentrate the SQB monomer when high concentration is desired. The final SQB concentration after PEG precipitation was determined by NanoDrop.

2.8.6 K10PEG5 coating of SQBs

SQBs with or without OVA was mixed with oligolysine-PEG5k, in short K10-PEG5k (methoxy-poly(ethylene glycol)-block-poly(L-lysine hydrochloride); n=113, x=10) (Alamanda polymers) such that nitrogen in amines: phosphates in DNA ratio was 1:1, according to the published method[152]. Samples were incubated at room temperature for 1 hour. After coating, the concentration of SQB was calculated based on the volume increase. K10-PEG5k coating does not affect vaccine efficacy (Supplementary Figure 14M). To remove K10-PEG5k for agarose gel verification in Fig. 2.1H, the nuclease was inactivated by 5 mM EGTA and 10% β-mercaptoethanol in 10 mM MgCl2 incubating at 37°C for 1 hour and then the K10-PEG5k shell was removed by incubating the samples with chondroitin sulfate 31 at 37°C for 2 hours.

2.8.7 DNase I degradation assay

SQBs (1 μg) were incubated with 1.0 U/μL DNase I (NEB) with 10 × DNase I buffer diluted in water (Gibco). Samples were incubated at 37°C for 30 minutes and then analyzed using 15% denaturing polyacrylamide (PAGE) gel to observe the CpG loading efficiency comparing to the calculated theoretical CpG oligos. Denaturing PAGE gel (15%) was made in-house using 9 mL urea concentrate, 4.5 mL urea diluent, 1.5 mL urea buffer (all three from Fisher Scientific), 10 μL tetramethylethylenediamine (TEMED) and 150 μL 10 wt% ammonium persulfate (APS) casting into mini-cassette (ThermoFisher Novex). Loading wells were generated by inserting the comb into the cassette.

2.8.8 Confocal imaging

Localization of OVA and SQB in the BMDCs was imaged using a Zeiss 710 confocal microscope equipped with 405 diode (405 nm), Ar (458, 488, 514 nm), and white light (633 nm) lasers for live cell tracking. For staining of late endosomes, cells were exposed to CellLight™ Late Endosomes-RFP (Life technologies, Catalog no. C10589) one day before. The cells were cultured with different version of vaccines, and the AF488 from OVA and Cy5 conjugated on SQB were detected for their colocalization with late endosome.

2.8.9 BMDC isolation and stimulation

C57BL/6 mice at the age of 6–8 months were sacrificed, and the femurs and tibias were obtained. The muscle and connective tissues were removed from the femurs and tibias. A 25G syringe needle was used to flush the inner bone and collect the marrow. The solution was pipetted to release marrow; the marrow clot was then filtered through 40 μm cell strainer. The cells were spun down at 300 g for 5 minutes. The cells were resuspended at a density of 3 million cell per mL in RPMI1640 medium supplemented with 10% low endotoxin FBS (Gibco), 50 μM β-mercaptoethanol, 20 ng/mL granulocytemacrophage colony-stimulating factor (GM-CSF; R&D Systems) and penicillin–streptomycin. Note that red blood cells were not removed. Fresh culture medium was added at day 3 and day 5. On day 7, the floating immature bone marrow derived dendritic cells (BMDCs) were collected for stimulation. BMDCs were seeded in 96 well with the density of 0.1 million in 100 or 200 μL medium. 0.01–1 nM of different DNA origami vaccine and controls were applied for BMDC stimulation for 1–2 days, depending on the experiment set-up. In the majority of our in vitro cell culture studies (Fig. 1-3, Supplementary Figure 13-S20), we have applied 1 nM SQB origami. For the control bolus vaccine, we have used an equivalent amount of CpG (usually 18 nM CpG if not specified otherwise) and antigens (4-10 nM of antigens). The supernatant was collected and stored in -80°C freezer for later ELISA analysis. The cells were collected for antibody staining and flow cytometry analysis or for downstream T cell co-culture. For cell culture study, there are usually 5 replicates in each group. For each n=5 in vitro cell-culture study, a single preparation of cells was harvested from several animals, combined, and then split into 5 replicate wells. Furthermore, for each of these studies, we have repeated 3–4 times with 3–6 replicates each.

2.8.10 Isolation of OT-I and OT-II T cells and co-culture with BMDCs

The transgenic T cell receptors of OT-I and OT-II mouse were designed to recognize OVA residues 257–264 in the context of H2-Kb (MHC I) and residues 323–339 in the context of I-Ab (MHC II). 6–8 week C57BL/6-Tg(TcraTcrb)1100Mjb/J OT-I mice and B6.Cg-Tg(TcraTcrb)425Cbn/J OT-II mice were purchased from Jackson Laboratory. Mice were sacrificed according to established procedures and the spleens were obtained. The spleens were processed into single cell suspension by mashing the spleen using the top of the plunger of a syringe in a 70 μm cell strainer. CD8 OT-I cells and CD4 OT-II were isolated by MojoSort kit purchased from BioLegend (480035, 480033) according to the manufacturer protocol. Approximately 2–5 million cells were isolated from each spleen. The isolated cells were labeled with carboxyfluorescein succinimidyl ester (CFSE; Biolegend 423801), incubated in 37°C for 20 minutes. Then the CFSE was bleached by the T cell culture medium, RPMI1640 supplemented with 10% FBS and penicillin–streptomycin. For co-culture, the culture medium for the BMDCs was removed completely. OT-I and OT-II T were added into the wells in fresh T cell culture medium at the number of 0.3-0.5 million based on the yield of isolation (BMDC versus T cells, 1:3-5), and allowed to culture together for 2 days. After 2 days of co-culture, the supernatant was collected and stored in -80°C freezer for ELISA and the cells were collected for antibody staining and flow cytometry analysis. Some T cells were applied for a tumor cell killing assay.

2.8.11 Tumor cells and in vitro tumor cell killing assay

B16-OVA melanoma cells are a kind gift from Dr. David Mooney (Harvard University). B16-OVA cells were cultured at 37°C in DMEM supplemented with 10% heat-inactivated FBS (Thermo Fisher Scientific), 100 U/mL penicillin and streptomycin (Mediatech), 2 mM L-glutamine (Thermo Fisher Scientific). For in vitro tumor cell killing experiment, 3,000 tumor cells in 100 μL medium were seeded in 96 well plate one day before CD8 T cell co-culture. The next day, 30,000 of the previously activated OT-I CD8 T cell suspension from the BMDC co-culture was added into the tumor cell wells and supplemented with 70 μL additional culture medium. The ratio of tumor cell and OT-I CD8 T cells was 1:10 and cells were cultured together for up to three days, depending on the experimental protocol. The live tumor cells were quantified via confocal microscopy on day 2 or day 3.

2.8.12 Vaccine distribution

The in vivo distribution of DoriVac was assessed in healthy C57BL/6 mice. Mice were subcutaneously injected with DoriVac (200 μg/kg, one injection) at the left shoulder. After a 2, 4, 24 and 48 hour post-injection period, respectively, mice were sacrificed, followed by extraction of major organs (LNs, kidney, liver, spleen, and lung). Fluorescence intensities for Alexa Fluor488 (AF488) conjugated on

OVA and Cy5 conjugated on SQB from organs were analyzed using an IVIS Lumina Series III system (PerkinElmer) and quantified using Living Image software (PerkinElmer).

2.8.13 Flow cytometry

BMDCs or cell suspensions collected from LN, blood, or tumors were washed with PBS and stained with Zombie UV viability dye (BioLegend, 423108) and then washed with cell staining buffer (BioLegend, 420201). The cells were then stained with cell surface antibodies conjugated with various fluorophores (Supplementary Table 4 and 5). Intracellular staining was initiated by fixation and/or permeabilization reagents (BioLegend, 424401). Cells were then stained with antibodies conjugated with various fluorophores. Antibodies (Supplementary Table 4) were arranged into different panels, appropriate compensations were set up to compensate for fluorescent emission overlap, and the stained cells were analyzed on Fortessa X-20 (BD Biosciences). Storage events were gated on the population of interest. Flow data was analyzed using FlowJo V10. We followed a generic way to gate on all the cells excluding debris, then singlets and live cells. The gating for single maker or double-marker positive population was out of the live cell population or other mother populations.

2.8.14 ELISA

Cytokines IL-12, IL-10, IL-6, TNFα, IL-4, TGFβ, IL-2, and IFNγ were evaluated in the culture supernatant, in the serum or the LN tissue by Quantikine ELISA kit (R&D Systems). Following the manufacturer's instructions, the samples were diluted according to protein concentration, reacted with the appropriate antibodies and the intensity determined via a microplate reader.

2.8.15 LUMINEX

The samples for Luminex experiments are either from human cell culture supernatant or from blood plasma. Blood samples collected from mice were collected into heparin-lined tubes and put on ice until processed. Blood was then centrifuged at 4°C, 350 x g for 5 minutes. The top plasma layer was then collected and transferred to tubes and stored at -80°C until ready to be used. Cytokines were detected using either Bio-Plex Pro™ Mouse Cytokine Th1/Th2 Assay (Bio-Rad, M60000003J7) or the Mouse Magnetic Luminex Assay (RD Systems, LXSAMSM20) by following methods provided by manufacturer. Human cytokines were detected using the Human Th1/Th2 11-plex Luminex Performance Assay (RD Systems, LKTM008) by following the manufacturer's methods.

2.8.16 RNA SEQUENCING AND DATA ANALYSIS

The BMDCs were treated with different vaccines for 1 day and collected by TRIzol (Invitrogen). RNA sequencing (RNA-seq) was carried out by Genewiz using an ultra-low input RNA-seq package that includes polyA selection and sequencing on an Illumina HiSeq with 150-bp pair-ended reads. Sequence reads were trimmed to remove possible adapter sequences and nucleotides with poor quality using Trimmomatic v.0.36. The trimmed reads were mapped to the Mouse GRCm38 reference genome using the STAR aligner v.2.5.2b. Unique gene hit counts were calculated by using feature Counts from the Subread package v.1.5.2 followed by differential expression analysis using DESeq2. Gene ontology analysis was performed using Database for Annotation, Visualization, and Integrated Discovery (DAVID). Principal component analysis (PCA) analysis and transcriptomic heat maps were graphed using R4.0.2.

2.8.17 Animal model and treatment

C57BL/6J female mice (5–6 weeks) were purchased from the Jackson Laboratory and maintained in the Harvard Medical School animal facility. For therapeutic vaccination, after one-week accommodation in the animal facility, 5×10^5 B16-OVA, 2×10^5 B16F10 or 1×10^6 EG7-OVA cells (kindly given from Dr. David Mooney's lab at Harvard) were administered subcutaneously (s.c.) on the right flank of the mice. The establishment of the tumor model was identified by visualization of tumor mass after the tumor cell inoculation. All tumor-bearing mice were randomly divided into multiple groups (n=5-8 in each group) and received appropriate vaccine treatment on day 3, 7 and 14 (or otherwise stated). Tumor growth and mouse survival were recorded. For CD8 depletion, mice were intraperitoneally (i.p.) given 100 μg of anti-CD8 antibody (BioXCell, BP0004-1) diluted in 100 μl of PBS every other day for three total injections, starting the day before vaccination. For sampling, the last treatment was moved to day 11 and the mice were sacrificed on day 15 to make sure the sampling could be completed before the mice in control group started to die. For prophylactic vaccination, mice were treated on day 0 and 7 and then inoculated with 2×10^5 B16-OVA tumor cells on day 14. For anti-PD-L1 (BioXCell, BE0101) or anti-PD-1 (BioXCell, BE0146) combination study, the mice were given 5 doses subcutaneously close to vaccine site at 200 μg per dose diluted in 100 μL PBS on day 6, 8, 10, 12, and 14 in addition to vaccine administration as outlined in the vaccine schedule in Figure 4. The animal housing facility maintained a 12-hour light and 12-hour dark cycle, with room temperature set at 71°F and a relative humidity of 50%. These conditions are continuously monitored using an electronic building monitoring system with on-site response personnel available 24/7.

2.8.18 Tumor growth and mouse survival

Tumor growth was evaluated by calculating the tumor volume using caliper measurements of length, width, and height of the tumor every 3–4 days after tumor inoculation. Survival time was calculated as life span from the day of tumor inoculation (day 0). The mice were euthanized in the cases of large tumor size (more than 20 mm in any single dimension) and/or poor body condition were observed. The life spans of the mice were recorded at the day of euthanasia.

2.8.19 IFNr ELIspot

After splenocytes or PBMDCs were harvested and processed according to protocols above, the cells were plated into a 96-well round-bottom plate, with each well containing cells from an individual mouse in 200 μL of media. We stimulated each well with 2 μg/mL of the associated peptide. The MHC I OVA peptide epitope (OVA peptide (257-264), sequence: SIINFEKLC, ThermoFisher) was used to probe antigen-specific CD8+ T cell responses, while the MHC II OVA peptide epitope (OVA peptide (323-339), sequence: ISQAVHAAHAEINEAGR, Thermo Fisher) was used to probe antigen-specific CD4+ T cell responses. After 48 hours of stimulated pre-incubation at 37°C, we collected the cells (1200 rmp, 5 minutes, 4°C) and resuspended in 100 μL of sterile splenocyte media. We incubated the cells for 36 hours at 37°C and then process the ELIspot plate according to the manufacturer's instructions (RND Systems, Mouse IFNγ ELIspot kit, 505841). Any wells that were dry after the incubation steps were removed from the analysis. The plate was analyzed via an ELIspot plate reader by Dana Farber Cancer Institute's Center for Immuno-oncology (CIO) Translational Immunogenics Laboratory (TIGL). The number of spot forming units (SFUs) per initial number of cells plated was quantified.

2.8.20 Statistical analyses

GraphPad Prism 9 and 10 were used to make graphs, analyze the statistics, and calculate P values. One-way ANOVA was applied for flow cytometry data and ELISA data with Tukey's post hoc multiple comparisons test. The analysis of mouse tumor volume trajectory was performed using a generalized linear mixed effect model, fit to a log transformed response looking at tumor volume growth rate across days. This analysis was executed using R version 4.04 and utilizing the lme4 package version 1.1-26 for all mixed modeling estimation. Survival curves were analyzed by Kaplan-Meier method and log-rank test. A two-tailed student t-test was applied to analyze the significance between two groups. P value ≤ 0.05 was considered statistically significant. '*' refers to $P \leq 0.05$; '**' refers to $P \leq 0.01$; '***' refers to $P \leq 0.001$; '****' refers to $P \leq 0.0001$. Error bars represent standard error of the mean (SEM).

2.9 Data and Code Availability

Data supporting the findings of this study are presented in the paper and the supplementary materials. The RNA sequencing data for stimulated BMDCs generated and analyzed in this publication have been deposited in NCBI's Gene Expression Omnibus under accession No. GSE251850. Source data is available for Figures 1–6 and Supplementary Figures 7, 10, 12–16, 18–20, 22–27, and 29–32 in the associated source data file. No custom code or mathematical algorithms were used in this study.

3

DNA origami vaccine (DoriVac) nanoparticles improve both humoral and cellular immune responses to infectious diseases

3.1 AUTHOR CONTRIBUTIONS

The contents of Chapter 3 are reproduced from Zeng*, Y.C., Young*, O.J., Si, L.*, Ku, M.W.*, Isinelli, G., Rajwar, A., Jiang, A., Wintersinger, C.M., Graveline, A.R., Vernet, A., Sanchez, M., Ryu, J.H., Kwon, I.C., Goyal #, G., Ingber #, D.E., Shih #, W.M., (2024). DNA origami vaccine (DoriVac) nanoparticles improve both humoral and cellular immune responses to infectious diseases. *Biorxiv.*

*These authors contributed equally to the work. #Co-corresponding authors

Y.C.Z. and L.S. developed the idea. Y.C.Z., O.J.Y., L.S., and M.W.K. planned experiments. O.J.Y. fabricated and tested the vaccine. Y.C.Z. and O.J.Y. led the animal studies and immune-cell profiling. L.S. led the HR2 design and neutralization study. M.W.K. and A.R. fabricated the protein vaccine and tested via organ-on-a-chip. O.J.Y. drafted the manuscript with the guidance of Y.C.Z. and L.S. and supported by M.W.K. and A.R. in figure and writing preparation. Y.C.Z., O.J.Y., G.I., L.S., M.W.K., A.R., and A.J. performed experiments. O.J.Y. modeled the SQB in Fusion with C.M.W. providing assistance. A.R.G., A.V. and M.S. assisted animal study design, model set-up, and sampling. J.H.R. and I.C.K. supported the project and manuscript editing. W.M.S., Y.C.Z., D.E.I., and G.G. provided overall guidance for the project, and edited the manuscript.

3.2 Abstract

Current SARS-CoV-2 vaccines have demonstrated robust induction of neutralizing antibodies and CD4+ T cell activation; however CD8+ responses are variable, and the duration of immunity and protection against variants are limited. Here we repurposed our DNA origami vaccine nanotechnology, DoriVac, for targeting infectious viruses, namely SARS-CoV-2, HIV, and Ebola. The DNA origami nanoparticle, conjugated with infectious-disease-specific heptad repeat 2 (HR2) peptides, which act as highly conserved antigens, and CpG adjuvant at precise nanoscale spacing, induced neutralizing antibodies, Th1 CD4+ T cells, and CD8+ T cells in naïve mice, with significant improvement over a bolus control. Pre-clinical studies using lymph-node-on-a-chip systems validated that DoriVac, when conjugated with antigenic peptides or proteins, induced promising cellular immune responses in human cells. These results suggest that DoriVac holds potential as a versatile, modular vaccine nanotechnology, capable of inducing both humoral and cellular immunities. The programmability of this nanoparticle underscores its potential utility in addressing future pandemics.

3.3 Introduction

The coronavirus disease 2019 pandemic highlighted the need for swift vaccine development. Initial focus on rapid vaccine design for pandemics[12,62,151,163,92] led to the novel mRNA vaccines, mRNA-1273 (manufactured by Moderna) and BNT162b2 (manufactured by Pfizer), which rely on lipid nanoparticle delivery of mRNA encoding an early variant of the spike protein. Despite their success, the emergence of SARS-CoV-2 variants like B.1.351 (Beta)[193], B.1.617.2 (Delta)[33], and B.1.529 (Omicron)[21] raised concerns about the vaccine efficacy as variants demonstrated the ability to evade immunity[68,67,80,124,214,217,221]. The immune evasion observed with current vaccines necessitates interventions effective against mutations.

Current SARS-CoV-2 vaccines focus on the receptor binding domain (RBD) of the spike protein. Viruses rely on RBD to bind to cells and initiate infection, and then heptad repeat 1 (HR1) and heptad repeat 2 (HR2) to fuse the viral and cell membranes. HR1 and HR2, conserved across various viruses, self-assemble into α-helical coils, and then assemble into superhelical structures to facilitate fusion[179,29,75,30,86,126]. While the RBD region and other viral regions are subject to viral evolution, HR1 and HR2 sequences remain highly conserved, providing a conserved antigen for vaccines[122]. Only three amino acids differ between the original SARS-CoV-2 HR1 sequence and the Omicron variant (Supplementary Table 1). HR1 and HR2 also harbor T cell epitopes and may induce neutralizing antibodies, serving as viable antigens for vaccine design[54,70]. HR2, with a simpler structure than HR1, has been successfully targeted by vaccines,[122,76] and was selected as the antigen for delivery via our vaccine nanotechnology for SARS-CoV-2, HIV, and Ebola (Supplementary Table 2).

While the vaccine community traditionally prioritized neutralizing antibody responses[105], there is now growing acknowledgement of the essential role of cellular immune responses (dendritic cells, CD4+ and CD8+ T cells) for broad viral protection[68,70,138,160,191,42,109,22,128]. Functional T cells prevent immune escape of mutated strains[68]. SARS-CoV-2 mutated strains have been demonstrated to escape neutralizing antibody responses, but not T cell responses[158]. CD4+ T cells support antibody generation[135], and studies show that CD4+ T cell transfer can protect against viral challenge[232]. Mild SARS-CoV-2 infections exhibit robust CD8+ T cell reactivity[150,171] contributing to rapid viral clearance[191]. Depleting CD8+ T cells in non-human primates increases susceptibility to SARS-CoV-2 re-infection[129]. In HIV and Ebola, CD8+ T cells are crucial for long-term control and vaccine-induced protection. CD8+ depletion led to failure in controlling simian immunodeficiency virus in non-human primates[64,35]. In Ebola, CD8+ cells were essential for immune protection in non-human primates, while antibody transfer failed to protect[187]. An ideal vaccine should induce both humoral and cellular immune responses, including neutralizing antibodies and long-term memory T cells[68]. mRNA vaccines demonstrate robust CD4+ responses, but variable CD8+ responses; both influence long-term immunity[220,13,141,103,38].

Multiple vaccine candidates have been developed to induce neutralizing antibodies and cellular responses against the SARS-CoV-2 spike protein, including over 60 different nanoparticle formulations[205,148]. Despite the success of lipid nanoparticle-based mRNA vaccines, these vaccines face challenges like manufacturing complexity, cold-chain requirements, limited stability, high cost, poor cargo loading efficiency, limited control over cargo stoichiometry, and off-target effects[205,81]. Here, we introduce DoriVac, a DNA origami vaccine nanoparticle, as a versatile nanotechnology for infectious disease. While previous studies have demonstrated vaccine delivery with DNA origami for cancer[228,52,117] and individual infectious diseases[144,198,230], this study aims to demonstrate its broad applicability for infectious diseases. DoriVac induced robust humoral and T cell immune responses against SARS-CoV-2, HIV, and Ebola viruses in mouse models, demonstrating the nanotechnology's programmability for various infectious-disease HR2 antigens. This approach may broadly apply to pathogen vaccine development by conjugating the respective antigens to the DNA origami.

3.4 RESULTS

3.4.1 FABRICATION OF MODULAR DORIVAC NANOPARTICLES

We previously developed a DNA origami nanoparticle, termed square block (SQB), for its square-lattice architecture for precise spatial presentation of CpG adjuvants[228]. Formed through self-assembly of a long scaffold strand with corresponding short 'staple' strands, DoriVac is easy to manufacture and highly stable without cold-chain requirements, exhibits high cargo-loading efficiency due to the robustness of DNA hybridization, and offers precise control over cargo attachment. This nanotechnology facilitates optimized spatial arrangement of immune-activating adjuvants, resulting in robust cellular immune responses in various cancers, as previously published[228]. The SQB flat face, modified with 18 CpG strands at 3.5 nm spacing, induces type I (Th1) skewed immune activation (Fig. 3.1Ai)[228].

We applied DoriVac technology to create vaccines for SARS-CoV-2, HIV, and Ebola viruses by linking highly conserved viral HR2 peptides to the extruding face of the SQB nanoparticles (Fig. 3.1Aii). HR2 peptides contain MHC-I and MHC-II epitopes, which are crucial for broadly activating cellular immunity. To this end, we designed peptide-oligonucleotide conjugates with the appropriate "anti-handle" strand through DBCO-Azide click chemistry for specific attachment onto 24 specific "handle" sites of the extruding face of the SQB (Fig. 3.1A, B). The SQB nanoparticle co-delivers CpG adjuvant and disease-specific HR2 antigens to antigen presenting cells. B cells produce neutralizing antibodies, which can block the membrane fusion of the virus with the host cell (Fig. 3.1C). Dendritic cells (DCs) present and cross-present the antigens to activate both CD4+ and CD8+ T cells (Fig. 3.1D). The oligonucleotide-HR2-peptide conjugates were purified via PAGE purification (Fig. 3.1E). The agarose-gel electrophoresis band shift demonstrates successful fabrication of peptide-functionalized SQB (Fig. 3.1F). To confirm peptide conjugation efficiency to the SQB, we digested the DNA origami via DNase I and estimated peptide occupancy of greater than 95% of the

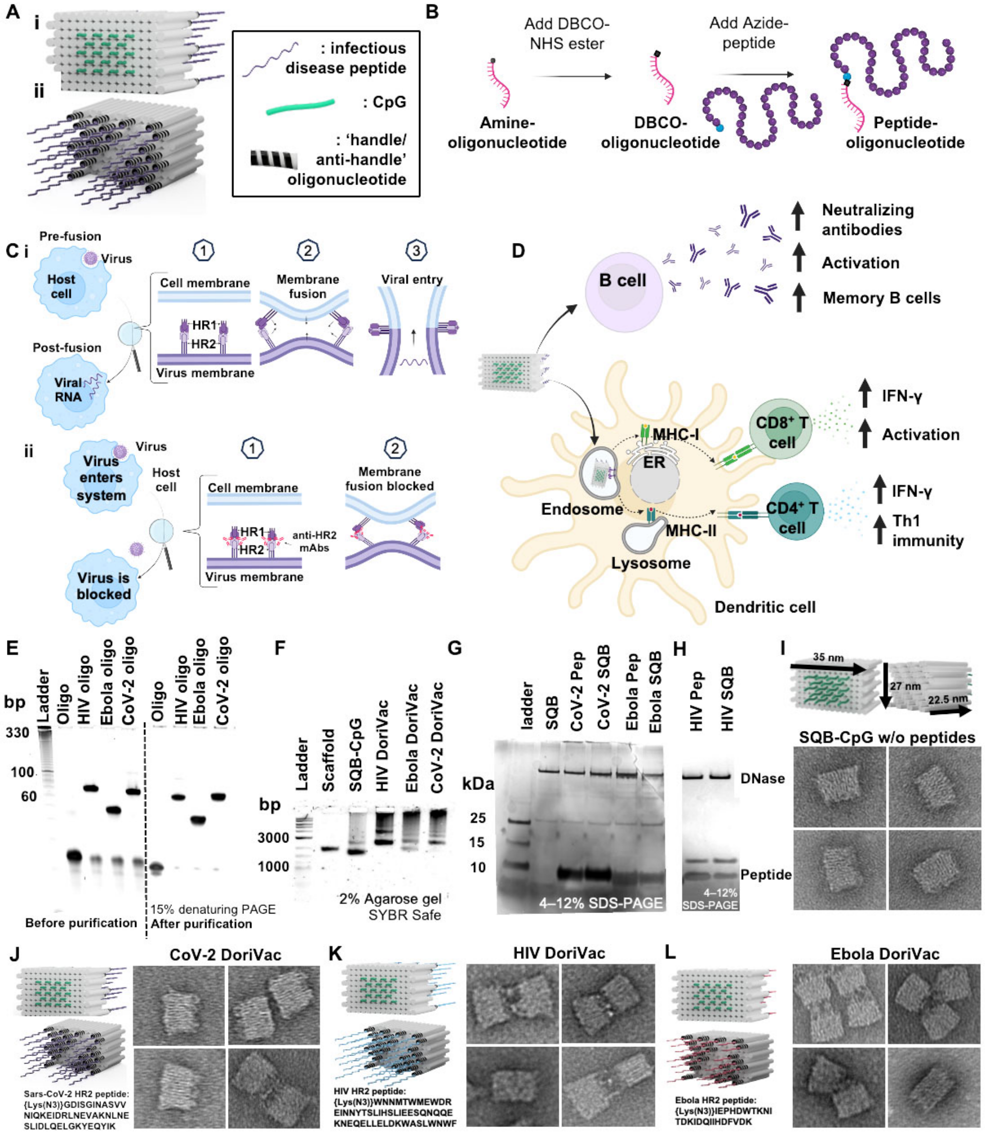

Figure 3.1: DNA origami vaccines (DoriVac) were fabricated with infectious-disease-specific peptides. **A.** Schematic of DoriVac, consisting of a DNA origami square block (SQB) nanoparticle conjugated with CpG at precise spacing of 3.5 nm and with infectious disease-specific peptides. **B.** Schematic demonstrated conjugation of DBCO-modified-oligonucleotide to an azide-modified peptide via copper-free click chemistry. **C. i.** A schematic showing how HR2 protein mediates virus-host fusion; HR2 can serve as a conserved target for infectious-disease vaccines. **ii.** Schematic showing how production of anti-HR2 antibodies (mAbs) prevents virus-host cell-membrane fusion and thereby inhibits viral infection. **D.** Schematic of DNA origami SQB nanoparticles delivering antigen and adjuvant at a precise spacing to antigen presenting cells, eliciting both humoral and cellular immune responses. **E.** Denaturing PAGE gel demonstrating successful conjugation and purification of infectious-disease-specific HR2 peptides to anti-handle oligonucleotides ("oligo"). **F.** Agarose gel demonstrating successful conjugation of oligo-HR2 peptides to the SQB DNA origami nanoparticle. **G, H.** SDS-PAGE gel demonstrating the results after DNase I digestion of infectious disease-specific HR2 peptides alone or conjugated with SQBs. DNase I digestion of the SQBs, followed by the analysis of the conjugated peptides using silver staining, confirms the successful peptide conjugation on the SQBs. **I - L.** Proposed schematics of the SQBs conjugated with CpGs (SQB-CpG) and SQBs conjugated with CpGs and HR2 peptides (CoV-2-HR2 DoriVac, HIV-HR2 DoriVac, Ebola-HR2 DoriVac), respectively, and their representative TEM images. The specific HR2 peptide sequences associated with each infectious disease are listed.

conjugation sites via silver stain (Fig. 3.1G-H, Supplementary Table 3). Fabrication of SARS-CoV-2-HR2, HIV-HR2, and Ebola-HR2 DoriVac was verified via TEM (Fig. 3.1I-L, Supplementary Figure 1). Aggregation was observed via agarose gel, especially in the case of the HIV and Ebola SQBs of which the majority are dimers, possibly due to hydrophobic peptide interactions.

3.4.2 DoriVac induces robust humoral immune responses

Having successfully fabricated the vaccine, we evaluated DoriVac's efficacy for induction of both humoral and cellular immune responses in vivo. Naïve mice were administered 20 pmol of HR2-fabricated DoriVac, comprising 0.36 nmol (2.2 μg) of CpG and 0.48 nmol of antigen (1.5 – 3.2 μg) (Fig. 3.2A). Two subcutaneous doses of DoriVac were given on day 0 and day 20, compared to bolus vaccine consisting of free CpG adjuvant and HR2 peptide. Blood samples were collected on day 14 and 28 for peripheral blood mononuclear cells (PBMCs) and plasma processing. On day 21, half of the mice from each group were sacrificed for immune cell profiling (Supplementary Table 4-6). On day 35, the remaining mice were sacrificed for immune cell profiling.

On day 21, B cells from PBMCs exhibited increased CD40 expression, a marker of activation and antigen-presentation capacity, in all three DoriVac treatment groups (Fig. 3.2B), surpassing the bolus vaccine, suggesting that DoriVac is superior in inducing B cell activation. Day 35 revealed a heightened plasma memory B cell population in the bone marrow, as evidenced by an increased CD19^{low} CD38^{low} CD27^{high} subpopulation after DoriVac treatment (Fig. 3.2C), despite unchanged overall B cell numbers (Supplementary Figures 2–4). SARS-CoV-2-HR2-DoriVac treatment induced elevated HR2 peptide-specific IgG1 antibody responses, as quantified via ELISA, compared to the bolus vaccine (Fig. 3.2D, Supplementary Figure 4). Neutralizing antibodies harvested from SARS-CoV-2-HR2-DoriVac groups significantly reduced infection in a SARS-CoV-2 pseudovirus (SARS-CoV-2pp) assay (Fig. 3.2E). In contrast, we did not observe neutralization of the pseudovirus for HIV and Ebola in our assay, possibly due to the weak immunogenicity of the antigens associated with these

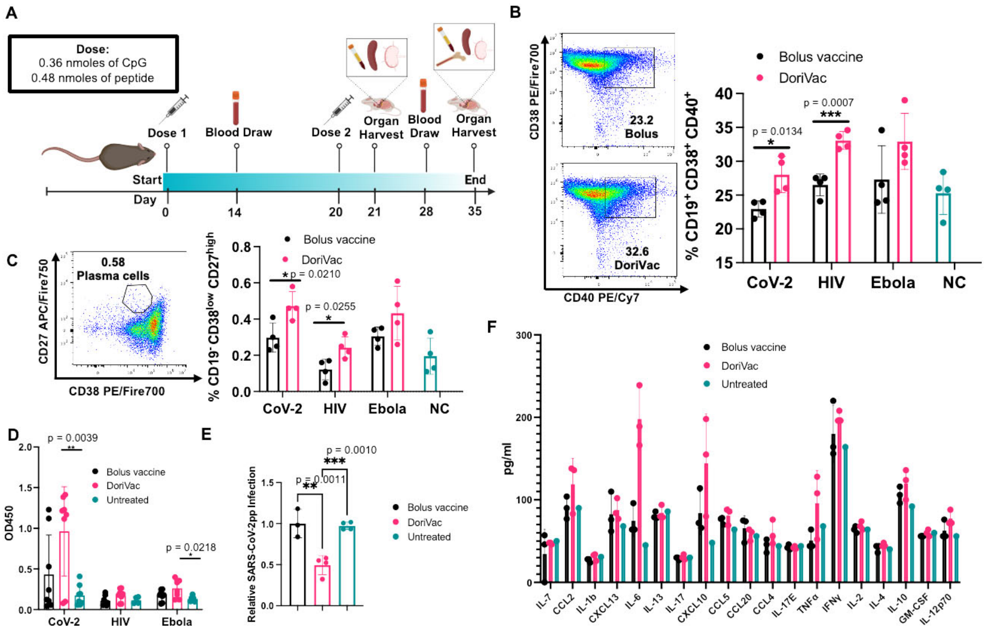

Figure 3.2: Immune profiling reveals the DoriVac elicits improved neutralizing antibody responses compared to a bolus vaccine. A. Schematic delineating the vaccine administration protocol for naïve C57BL/6 mice and the data collection timeline. Lymph nodes (LNs) and spleens were collected on day 21 and day 35 after sacrificing the mice for flow cytometry and ELISpot analysis. Plasma was collected on Days 14 and 28 for anti-HR2 antibody quantification and pseudovirus neutralization assays. Bone marrow and heart blood was collected at the conclusion of the study, day 35, to analyze B cell markers. **B.** B cells collected from the blood demonstrated increased markers of activation and antigen-presentation capabilities (CD40) and memory capacity (CD38) after two doses of DoriVac treatment (n=4) as determined by flow cytometry on day 21. NC refers to negative control. **C.** B cells collected from the blood on Day 21 demonstrated increased plasma-memory-cell population as evidenced by the increased CD19- CD38low CD27high subpopulation as determined by flow cytometry (n=4). **D.** DoriVac treatment enhanced HR2-specific IgG antibody production as evidenced via ELISA assay, after two doses of DoriVac (on Day 35) compared to a bolus vaccine of free peptide and free CpG. Samples were diluted 1:100 before quantification. Data has been normalized (n=8). **E.** SARS-CoV-2 pseudovirus (SARS-CoV-2pp) neutralization assay (n=3-4, 1:10 dilution, Day 28) in model cell line ACE2-293T (n=4). **F.** Plasma was collected four hours after the first treatment dose on Day 0. The inflammatory cytokine response was quantified via Luminex ELISA assay (Bio-Plex Pro Mouse Cytokine 20-plex Assay (Bio-Rad)) (n=3 for treated groups; n=1 for negative (i.e. untreated) control). Data are represented as mean ± SD. The pseudovirus and ELISA data were analyzed by one-way ANOVA (with correction for multiple comparisons using a Tukey test) and significance was defined as a multiplicity-adjusted p value less than 0.05. The flow data were analyzed by multiple unpaired t-tests and significance was defined as a two-tailed p value less than 0.05. '*' refers to p≤ 0.05; '**' refers to p≤ 0.01; '***' refers to p ≤ 0.001.

viruses (Supplementary Tables 7–10). We did observe modest antigen-specific IgG1 responses for HIV and Ebola after HIV-HR-DoriVac and Ebola-HR2-DoriVac treatment, respectively (Fig. 3.2D, Supplementary Figure 4). We examined initial cytokine responses four hours post the first vaccine dose to naïve mice (Fig. 3.2F). Type 1 cytokines (TNFα, IL-2, IFNγ, IL-12) were slightly elevated, while type 2 cytokines (IL-4, IL-10) exhibited no obvious elevation after DoriVac treatment compared to the bolus vaccine group and the untreated mice[89]. Overall, these findings affirm DoriVac's superior induction of humoral immune responses compared to those induced by a bolus vaccine, demonstrating its effectiveness in reducing the infection rate of SARS-CoV-2 pseudovirus.

3.4.3 DoriVac induces DC activation

To ensure enduring immune protection against viral variants, a vaccine should stimulate both humoral and cellular immune responses. We first checked the DCs, which serve as a link between innate and adaptive immune responses. On day 21 — one day after the second vaccine dose— half of the mice were sacrificed, and the draining lymph nodes near the injection site were collected for flow (Supplementary Figure 5). DoriVac increased the overall DC population (Fig. 3.3A) and activated DCs (CD11c+ CD86+) compared to the bolus vaccine (Fig. 3.3B). Plasmacytoid DCs (pDCs) are crucial in the anti-viral response in humans, secreting abundant type-1 interferon, fostering T cell activation and recruiting other immune cells[61]. The human pDC-like population (CD11c+ Gr-1+) significantly increased after DoriVac treatment (Fig. 3.3C), suggesting an increased anti-viral response. Activation markers MHC-II, PD-L1 and CD40 also increased after DoriVac administration (Fig. 3.3D–F). A notable rise was observed in the CD40+ DEC205+ DC population, indicating an increase in the activated, endocytic DC population (Fig. 3.3G). These results demonstrated DoriVac induced robust activation of DCs in healthy mice (Supplementary Figure 6). Furthermore, co-delivery of SQB and HR2 peptide did not elicit the same level of DC activation as observed with the delivery of HR2 peptide-conjugated SQBs (Supplementary Figure 7). This observation is consistent with the

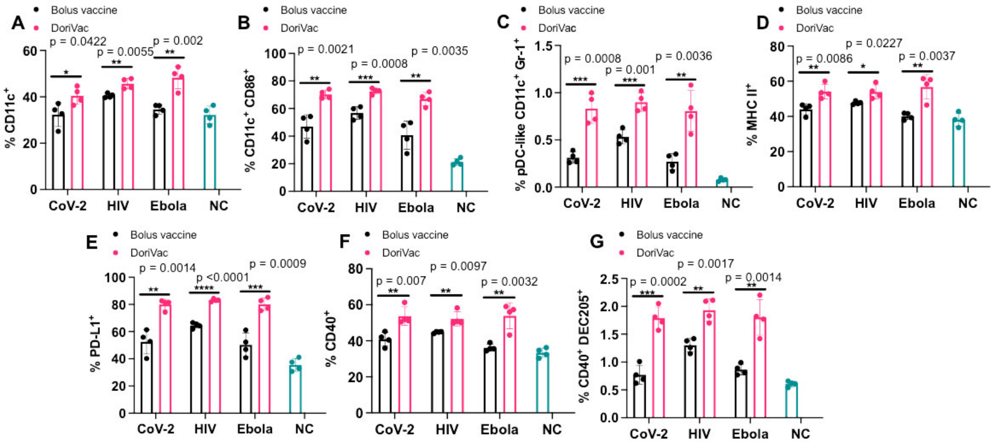

Figure 3.3: Immune profiling reveals DoriVac elicits superior antigen presenting cell responses compared to a bolus vaccine. C57BL/6 mice were treated with DoriVac (20 pmol) on Day 0 and Day 20. The mice were sacrificed on Day 21 and the draining lymph nodes (LNs) were processed into single-cell suspensions and analyzed by flow cytometry. **A.** Percentages of CD11c+ cells in the draining LNs (n=4) were quantified. NC means negative (i.e. untreated) control. **B.** Percentages of CD11c+ CD86+ DCs in the draining LNs (n=4) as determined by flow cytometry. **C.** Percentages of human plasmacytoid DC (pDC)-like (CD11c+ Gr-1+) DCs in the draining LNs (n=4) as determined by flow cytometry. **D.** Percentages of MHC-II+ DCs in the draining LNs (n=4) as determined by flow cytometry. **E.** Percentages of PD-L1+ population in the draining LNs (n=4) as determined by flow cytometry. **F.** Percentages of CD40+ population in the draining LNs (n=4) as determined by flow cytometry. **G.** Percentages of CD40+ DEC205+ population in DCs in the draining LNs (n=4) as determined by flow cytometry. DoriVac demonstrated a significant increase in DC activation compared to bolus-vaccine treatment. Data are represented as mean ± SD. The flow data were analyzed by multiple unpaired t-tests and significance was defined as a two-tailed p value less than 0.05. '*' refers to P ≤ 0.05; '**' refers to P ≤ 0.01; '***' refers to P ≤ 0.001; '****' refers to P ≤ 0.0001.

outcomes previously noted in DoriVac studies involving tumor-bearing mice[228], further supporting the notion that the enhanced efficacy of the conjugated delivery system in activating DCs.

3.4.4 DoriVac demonstrates activation of CD4$^+$ T cells

In our previous study involving DoriVac in mouse cancer models[228], we showed that DC activation by DoriVac leads to broad T cell activation. We aimed to confirm T cell induction by DoriVac in the context of viral antigens. Antigen-specific T cell activation was assessed via IFNγ ELISpot assay on splenocytes; our results demonstrated a significant increase in antigen-specific T cells after SARS-CoV-2-HR2 DoriVac administration (Fig. 3.4A, B). In contrast, HIV-HR2 DoriVac administration led to only a modest increase, and Ebola-HR2 DoriVac showed no apparent effect (Fig. 3.4A, B; Supplementary Figure 8). We attribute this to the limited immunogenicity of the HR2 peptides used for HIV and Ebola, validated by their weaker predicted binding to MHC-I and MHC-II in both mice and humans via NetMHCpan-4.1[157]. In contrast, the SARS-CoV-2 HR2 peptide exhibited stronger binding predictions with six epitopes classified as strong binders, compared to zero to two epitopes for HIV and Ebola (Supplementary Tables 7–10). These findings underscore the importance of antigen selection in achieving effective antigen-specific T cell activation. Notably, these results confirmed that SARS-CoV-2-HR2 DoriVac induces significantly more antigen-specific T cells compared to the bolus vaccine.

Beyond overall T cell responses, we confirmed the presence of activated Th1 CD4+ T cells via flow cytometry (Supplementary Figure 9 for gating strategy). CD107a notably increased in the CD4+ T cell population, indicating enhanced CD4+ T cell activation and increased cytotoxic potential (Fig. 3.4C)[190]. PD-1 was also upregulated in the CD4+ T cell population, demonstrating increased activation (Fig. 3.4D). The T regulatory cell (Treg) population significantly decreased after treatment with DoriVac, suggesting reduced immunosuppression (Fig. 3.4E). Antigen-specific CD4+ T cell activation (CD8+ T cells depleted by positive sorting) was quantified via IFNγ ELISpot, revealing a

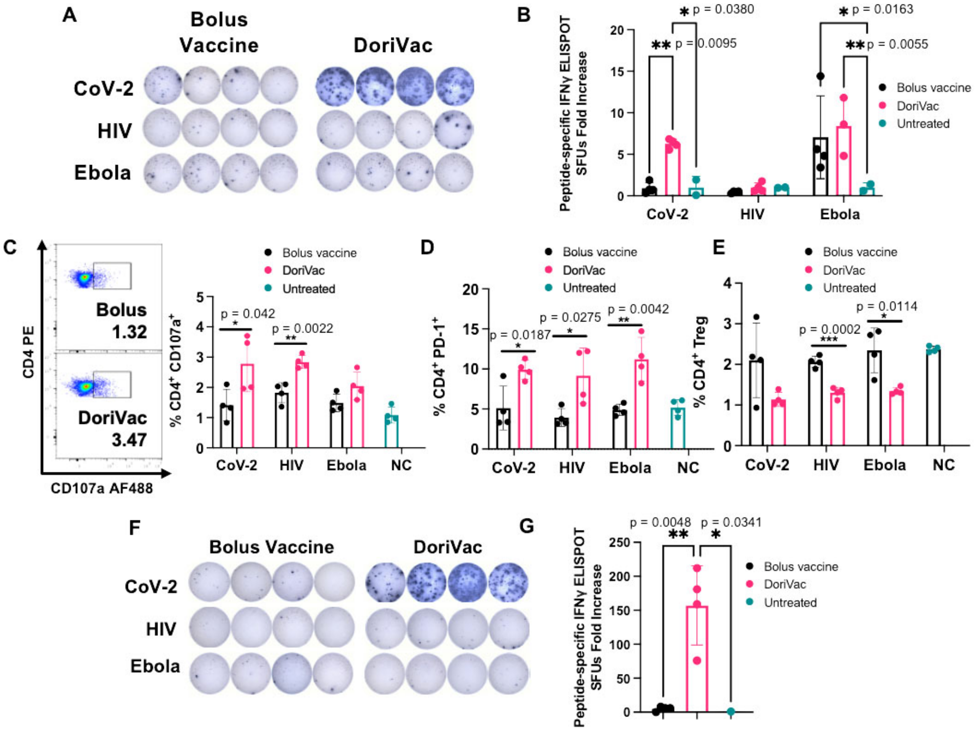

Figure 3.4: DoriVac induces enhanced Th1 CD4+ T cell activation in mice. **A.** IFNγ ELISpot demonstrating frequency of antigen-specific T cells in splenocytes on day 35 (n=4) after treatment with DoriVac compared with the bolus vaccine. **B.** Quantification of IFNγ ELISpot spot forming units (SFUs) demonstrates significant increase in SARS-COV-2 antigen-specific T cell frequency after treatment with DoriVac compared with the bolus vaccine and negative (i.e. untreated) control. **C.** Percentages of CD4+ CD107a+ T cells in the LN (n=4) as determined by flow cytometry and representative flow plots on day 35. NC means negative (i.e. untreated) control. **D.** Percentages of the LN CD4+ PD-1+ population (n=4) as determined by flow cytometry on day 21. **E.** Percentages of LN CD4+ T regulatory cell (Treg) population (n=4) as determined by flow cytometry on day 21. **F.** IFNγ ELISpot demonstrating frequency of CD4+ enriched antigen-specific splenocytes (n=4, day 35) after treatment with SARS-CoV-2-HR2 DoriVac. **G.** Corresponding quantification of IFNγ ELISpot spot forming units (SFUs). Data are represented as mean ± SD. The ELIspot data in **B** were analyzed by two-way ANOVA (with correction for multiple comparisons using Tukey's test). The ELISpot data in **G** were analyzed by one-way ANOVA (with correction for multiple comparisons using Tukey's test). In both analyses, statistical significance was defined as a multiplicity-adjusted p value less than 0.05. The flow data were analyzed by multiple unpaired t-tests and significance was defined as a two-tailed p value less than 0.05. '*' refers to $P \le 0.05$; '**' refers to $P \le 0.01$.

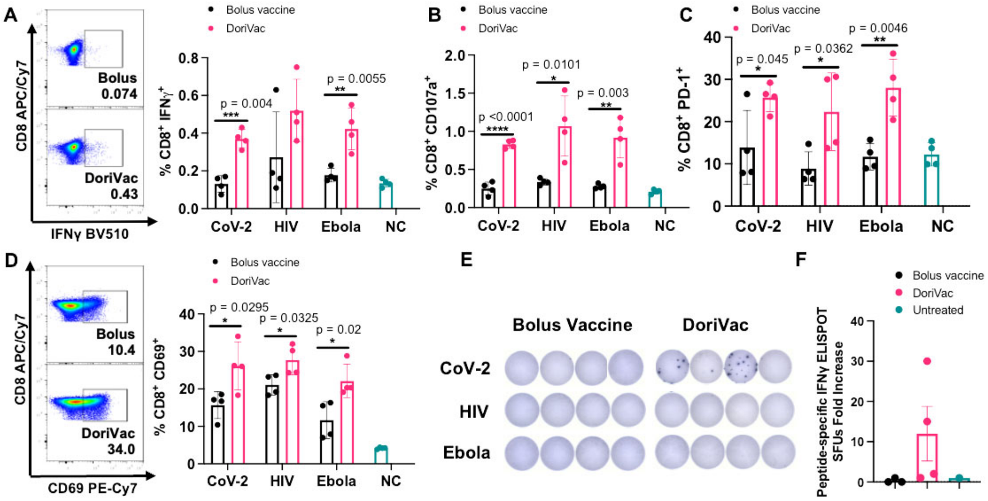

Figure 3.5: DoriVac induces enhanced antigen-specific CD8+ T cell activation in mice compared to bolus vaccine. A. Percentages of CD8+ IFNγ+ T cells in the lymph node (LN; n=4) on Day 21 as determined by flow cytometry and representative flow plots from the SARS-CoV-2 data. NC means negative (i.e. untreated) control. **B.** Percentages of CD8+ CD107a+ T cells in the LN (n=4) on Day 21 as determined by flow cytometry. **C.** Percentages of CD8+ PD-1+ T cells in the LN (n=4) on Day 21 as determined by flow cytometry. **D.** Percentages of CD8+ CD69+ T cells in the LN (n=4) on Day 21 as determined by flow cytometry and representative flow plots. **E-F.** IFNγ ELISpot demonstrating frequency of CD8+ enriched antigen-specific splenocytes (n=4, day 35) and accompanying quantification of IFNγ ELISpot SFUs demonstrates an increase significant difference in SARS-COV-2 antigen-specific CD8+ T cell frequency after treatment with DoriVac compared with the bolus vaccine. Data are represented as mean ± SD. The flow data were analyzed by multiple unpaired t-tests and significance was defined as a two-tailed p value less than 0.05. The ELISpot data were analyzed by one-way ANOVA (with correction for multiple comparisons using Tukey's test). Statistical significance was defined as a multiplicity-adjusted p value less than 0.05. '*' refers to $p \leq 0.05$; '**' refers to $p \leq 0.01$; '***' refers to $p \leq 0.001$; '****' refers to $p \leq 0.0001$.

significant increase in antigen-specific activation after SARS-CoV-2 vaccination (Fig. 3.4F, G). These results verified activation of CD4+ T cells, demonstrating an antigen-specific immune response critical for immune memory.

3.4.5 DoriVac induces an antigen-specific CD8$^+$ T cell activation

Furthermore, after two vaccine doses, we confirmed activation of cytotoxic CD8+ T cells. DoriVac increased the population of IFNγ secreting cytotoxic CD8+ T cells (Fig. 3.5A) and degranulating CD107a+ CD8+ T cells (Fig. 3.5B) in the LNs. PD-1 and CD69 were upregulated in the CD8+

T cell population (Fig. 3.5C-D), indicating increased activation. On Day 35, after the second dose, we quantified antigen-specific CD8+ enriched T cells (CD4+ T cell depleted by positive sorting) in the spleen via IFNγ ELISpot, showing increased antigen-specific CD8+ T cells after SARS-CoV-2 DoriVac (Fig. 3.5E, F). Co-delivery of SQB, free HIV-HR2 peptide, and free CpG did not induce similar level of T cell activation as observed with the delivery of DoriVac (Supplementary Figure 10).

3.4.6 Human immune-cell validation of peptide-conjugated DoriVac

Beyond murine models, we assessed DoriVac immunogenicity using a human LN organ-on-a-chip model. This model mimics the human LN for rapid prediction of vaccine responses in humans[69]. Analyzing the impact of SARS-CoV-2-HR2 DoriVac on human monocyte-derived DCs, we observed increased CD86, CD40, HLA-DR, and CD83 expression, indicating DoriVac can activate human DCs (Fig. 3.6A, Supplementary Table 11, Supplementary Figure 11). DoriVac treatment also elevated inflammatory cytokines secreted by DCs compared to the bolus (Fig. 3.6B). Analyzing effector T cell responses on the human LN organ-on-a-chip model after nine days of vaccination, DoriVac displayed a substantial increase in CD4+ and CD8+ T cell activation in two of the three donors, as evidenced by TNFα+ and IL-2+ staining (Fig. 3.6C, Supplementary Table 12, Supplementary Figure 12) Polyfunctionality analysis (examining T cells that express IFNγ, TNFα and IL-2) revealed significantly more CD4+ polyfunctional cells induced by DoriVac than the bolus vaccine, and an overall increase CD8+ polyfunctional cells (Fig. 3.6D). Inflammatory cytokine analysis indicated similar levels induced by bolus and DoriVac across three donors (Fig. 3.6E). These findings suggest that DoriVac induces a robust immune response in an in vitro human immune system that closely predicts human vaccine response.

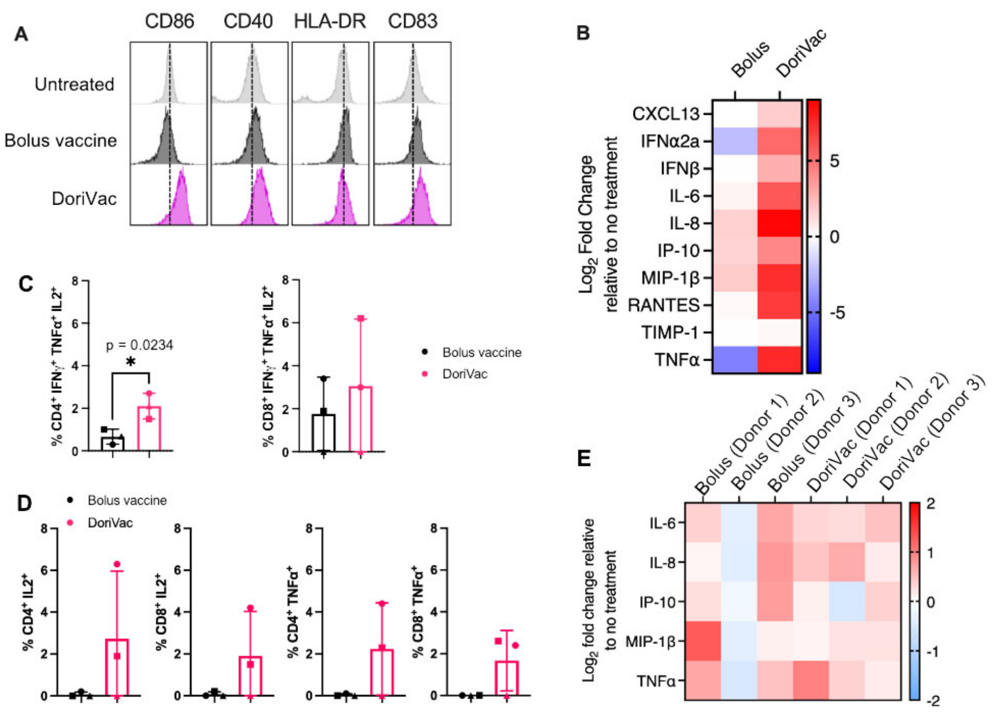

Figure 3.6: Peptide-conjugated (SARS-CoV-2-HR2) DoriVac effectively stimulates human dendritic cells (DCs) and induce enhanced immunogenicity compared to bolus vaccine on lymph node (LN) organ-on-a-chip model. A. Human monocyte-derived DCs were stimulated for 24 hours with bolus or DoriVac, and the DC activation markers were analyzed using flow cytometry. **B.** Relative fold changes in cytokines and chemokines after 24 hours of human monocyte-derived DCs with bolus or DoriVac. Fold change relative to no treatment is shown. **C.** Graph quantifying polyfunctional T cells, as determined by their ability to co-secrete IFNγ, TNFα and IL-2 as determined via intracellular cytokine staining and flow cytometry. **D.** LN organ-on-a-chips (n = 3) were vaccinated with bolus or the SARS-CoV-2-HR2 DoriVac. Nine days after vaccination, T cell responses were assessed via intracellular cytokine staining and flow cytometry after ex vivo stimulation with SARS-CoV-2 HR2 peptide and PMA/Ionomycin. Graph quantifying the average cytokine-producing CD8+ and CD4+ T cell populations at 9 days after vaccination in three different donors. Each symbol represents one donor. **E.** Relative fold changes in IL-6, IL-8, IP-10, MIP-1β and TNFα at 9 days after transduction either of the bolus or DoriVac on the LN organ-on-a-chip. Fold change relative to no treatment is shown. Data are represented as mean ± SD. The flow data were analyzed by unpaired t-test and significance was defined as a two-tailed p value less than 0.05. '*' refers to $p \leq 0.05$.

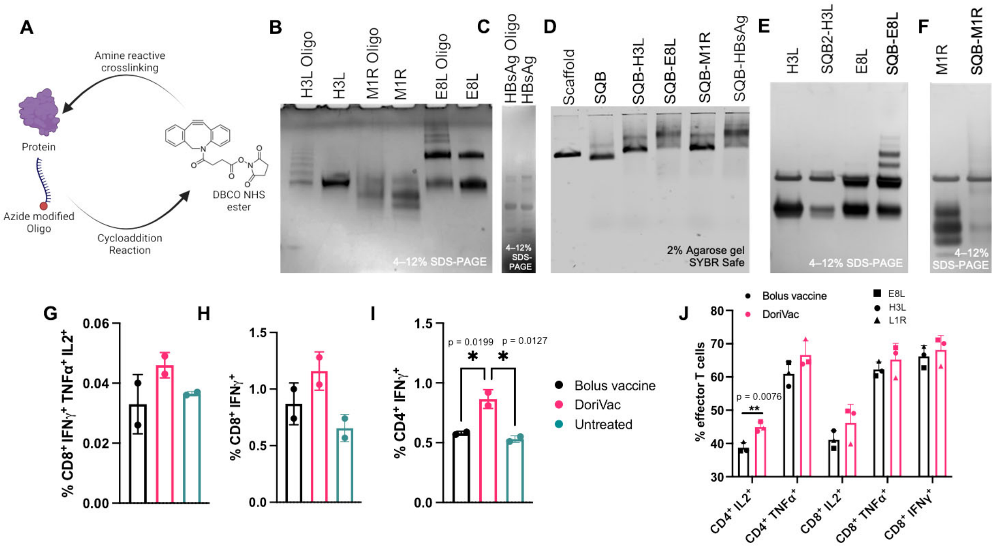

Figure 3.7: Preclinical validation of protein antigen-conjugated DoriVac immunogenicity in a human lymph node organ-on-chip model and a tonsil organoid model. A. Schematic representation of protein-oligonucleotide conjugation, demonstrating the utilization of DBCO-NHS ester crosslinker to link an azide-modified oligonucleotide to the protein via free amine groups on lysines. **B.** SDS-PAGE gel demonstrating the successful conjugation of monkeypox-specific proteins to oligonucleotides. **C.** SDS-PAGE gel demonstrating the successful conjugation of Hepatitis B surface antigen (HBsAg) proteins to oligonucleotides. **D.** Agarose gel demonstrating the successful conjugation of infectious-disease protein onto the SQB DNA origami. **E-F.** Confirmation via SDS-PAGE gel of successful protein conjugation after DNase degradation of the DNA origami scaffold and staple strands and analysis of the remaining protein via silver stain. **G-I.** LN chips (n = 2) were vaccinated with bolus or DoriVac harboring CpG and full-length HBsAg. The T cell responses were assessed using intracellular cytokine staining and flow cytometry after ex vivo stimulation with autologous DC-pulsed HBsAg (1:10 effector :target ratio), nine days after vaccination. Graph quantifies the **G** CD8+ polyfunctionality after nine days of vaccination in two different donors. Polyfunctionality is defined by T cells producing IFNγ, TNFα, and IL-2, **H** IFNγ+ CD8+ populations, and **I** IFNγ+ CD4+ populations. **J.** Tonsil organoids from one donor were vaccinated with bolus or DoriVac harboring CpG and full length monkeypox antigens (E8L, H3L or M1R). T cell responses were assessed using intracellular cytokine staining and flow cytometry after ex vivo stimulation with 15-mer monkeypox antigenic peptides (overlapping by 11-mer) and PMA/Ionomycin stimulation for the last 4 hours of incubation. Graph quantifies the cytokine-producing effector CD8+ and CD4+ populations, nine days after vaccination (n = 3 cell samples obtained from one preparation, treated with DoriVac fabricated with three different monkeypox antigens). Data are represented as mean ± SD. The flow data were analyzed by one-way ANOVA (with correction for multiple comparisons using Tukey's test). Significance was defined as a multiplicity-adjusted p value less than 0.05. The grouped flow data was analyzed by multiple unpaired t-tests. Significance was defined as a p value less than 0.05. '*' refers to p≤ 0.05.

3.4.7 Human immune-cell validation of protein-conjugated DoriVac

We further expanded our investigation to showcase the versatility of DoriVac, enabling the conjugation of full-length viral protein antigens. Protein vaccines historically faced limitations in presenting antigens on MHC-I and inducing CD8+ T cell responses[159]. As a proof-of-concept, we selected hepatitis B surface antigen (HBsAg) and three monkeypox antigens (E8L, H3L and M1R), validated for prior immunogenicity in their respective diseases (Supplemetary Table 13)[36,40]. This study demonstrates DoriVac versatility in eliciting both CD4+ and CD8+ T cell responses against protein antigens.

The protein-'anti-handle'-oligonucleotide conjugate was synthesized using DBCO-azide click chemistry, where azide-modified oligonucleotide was conjugated to a protein via a DBCO-NHS ester linker (Fig. 3.7A). Successful conjugation was confirmed by SDS-PAGE gel (Fig. 3.7B, C). The protein-'anti-handle'-oligonucleotide conjugate was hybridized to the corresponding 'handle' strands on the SQB via Watson-Crick base-pairing. Protein-conjugated DoriVac exhibited reduced mobility in agarose gel electrophoresis compared to unconjugated DNA origami (Fig. 3.7D). Successful protein conjugation was observed via SDS-PAGE gel analysis after DNase I digestion (relative to a protein-only control) (Fig. 3.7E,F).

Initially, we assessed T cell responses to HbsAg-conjugated DoriVac and bolus vaccine in the human LN organ-on-a-chip system nine days post-vaccination. DoriVac-stimulated DCs, pulsed with HBsAg, induced IFN-γ secretion in both CD4+ and CD8+ subsets, demonstrating antigen-specific T cell activation (Fig. 3.7G-I, Supplementary Table 12, Supplementary Figure 12). Polyfunctionality of T cells, measured by CD8+ T cells secreting IFNγ, TNFα and IL-2, was higher for DoriVac than the bolus (Fig. 3.7I). Additionally, we evaluated the immunogenicity of monkeypox antigens using a tonsil organoid model[206], observing increased CD4+ IL-2+ and TNFα+ effector T cells, as well as a higher percentage of IL-2+, TNFα+ and IFNγ+ CD8+ T cells (Fig. 3.7J). These findings illustrate the capability of DoriVac to induce cellular immunity against protein antigens of various infectious diseases.

3.5 CONCLUSION

Enduring immune memory and protection against variants rely on cellular immune responses, particularly CD8 T cells that target less mutable viral proteins. SARS-CoV-2 vaccines with greater than 90% protection demonstrated Th1-skewed immunity[119,41,106,83,209], emphasizing the importance of Th1 CD4 and CD8 T cell responses for protection. In recent decades, DNA origami has achieved crucial milestones, indicating its potential as a modular therapeutic nanoparticle. Its programmability makes it a versatile 'plug-and-play' vaccine nanotechnology, particularly relevant for emerging infectious diseases. In this proof-of-concept study, HR2-DoriVac, conjugated with infectious-disease-associated peptides and proteins, successfully elicited robust neutralizing antibodies and antigen-specific CD4 and CD8 T cell activation in healthy mice, a notable contrast to some SARS-CoV-2 vaccines with limited T cell responses. DoriVac presents four distinct advantages: (1) precise nanoscale arrangement of antigen and adjuvant for their co-delivery on each nanoparticle; (2) well-established, simple, and scalable fabrication; (3) modular, programmable design adaptable for various antigens via DNA hybridization; (4) stability at 4°C, contrasting with mRNA vaccines needing -20°C to -80°C cold chain storage[205].

While robust antigen-specific T cell activation was observed with SARS-CoV-2-HR2 DoriVac, the same level of activation was not observed for HIV and Ebola. However, significant activation of B cells, DCs, CD4 and CD8 T cells for HIV and Ebola, suggested a strong immune response, albeit possibly insufficient for protection from infection. The chosen antigens for HIV and Ebola are also predicted to be weakly immunogenic in humans (Supplementary Table 14-17), so future studies could focus on identifying more immunogenic peptides for HIV and Ebola for human HLA, potentially enhancing antigen-specific activation. Viral rechallenge studies, contingent on availability of BL3 facilities, could further assess the effectiveness of DoriVac-induced immune activation against live viruses. Additionally, a direct comparison with mRNA-based vaccines would be beneficial; however, differences in dosing regimens and experimental setups may present challenges in making direct comparisons.

This proof-of-concept study suggests the potential of DoriVac, when conjugated with antigens associated with emerging infectious diseases, to rapidly manufacture vaccines capable of offering protection against variants and future outbreaks. The unique programmable modularity of DoriVac allows for the creation of multiplexed nanoparticles, each carrying a different antigen. This feature holds the promise of developing a universal vaccine, adaptable to a wide range of pathogens, by targeting multiple antigens simultaneously. Such versatility and adaptability establish DoriVac as a noatble advancement in the field of vaccine technology, especially in the context of rapidly evolving infectious threats.

3.6 Acknowledgements

We appreciate the support and experimental input from Shih Lab members. Special thanks to Kathleen Mulligan, Maurice Perez, Michael Carr, Thomas Ferrante, and Eric Zigon for their expertise with instrumentation. Figures 1b-d and Figure 2a were generated using BioRender (https://biorender.com/).

3.7 Materials and Methods

3.7.1 SQB fabrication

SQB fabrication is detailed in a previous publication, including scaffold and staple sequences[228,90]. Scaffold p8634 was produced in-house, as previously published[48]. DNA staple strands were purchased from IDT. Folding concentrations were 5 mM Tris base, 1 mM ethylenediaminetetraacetic acid (EDTA; pH 8.0), 12 mM MgCl2, 20–100 nM scaffold, 5 times excess of the basic staple strands (relative to scaffold concentration), 10 times excess of handle-conjugated staple strands (for attachment of relevant infectious-disease antigens) and 20 times excess CpG-staple strands. An 18-hour thermocycler program was used to fabricate SQBs: denaturation at 80°C for 15 minutes, then annealing via a temperature ramp from 50°C to 40°C decreasing at -0.1°C every 10 minutes and 48 seconds. Most staple strands include ten thymidine residues at the end of the double helices to minimize aggregation. The CpG-containing strands were appended on the flat face of the SQB. The CpG oligonucleotides with nuclease-resistant phosphorothioate backbones (5′ – TCCATGACGTTCCTGACGTT-3′, IDT) replaced the corresponding thymine residues in a 3.5 nm nanoscale pattern as determined previously[228]. CpG was appended to the 5′ ends of designated strands.

3.7.2 HR2 PEPTIDE CONJUGATION WITH 'ANTI-HANDLE' OLIGONUCLEOTIDE

An 'anti-handle' oligonucleotide, which corresponds to 24 sites of 'handle' oligonucleotide on the extruding face of the SQB, was ordered from IDT with an 5' amine (aminoC6-TTCTAGGGTTAAAAGGGGACG). HR2 peptides were ordered from GenScript with an azide-modified N-terminal lysine (Fig. 3.1 I–L; Supplementary Table 2) for DBCO-Azide copper-free click chemistry reaction between the peptide and oligonucleotide. The oligonucleotide was prepared at 1 mM with phosphate buffer (pH 8.0). The dibenzocyclooctyne-N-hydroxysuccinimidyl ester (DBCO-NHS ester; Millipore, 761524) (diluted in DMSO to 2 mM) was incubated with the oligonucleotide (diluted in phosphate buffer pH 8.0 to 100 uM) in 1:1 volume ratio and 1: 20 oligonucleotides to DBCO ratio (with final concentration of DBCO >1 mM) and incubated overnight at ambient temperature. The oligonucleotide-DBCO was purified via Illustra NAP column (GE Healthcare Life Sciences, 17-0852-02), eluted with sterile water, and concentrated via 3K Amicon Ultra Centrifugal Filter Unit (Millipore; UFC500324). DBCO incorporation was confirmed via OD310 peak. Concentration measured via A260 with the NanoDrop. The Azide-modified HR2 peptides, representing SARS-CoV-2, HIV and Ebola, were dissolved in DMSO to 5 mM. The peptide-Azide was mixed with the oligonucleotide-DBCO at a ratio of 1.5: 1 and incubated overnight at room temperature in 1 × PBS.

3.7.3 Denaturing PAGE (dPAGE) verification and purification of peptide-conjugated oligonucleotide

15% denaturing PAGE (dPAGE) was used to confirm peptide-oligonucleotide conjugation. dPAGE gel (15%) was prepared using 9 mL urea concentrate (Fisher Scientific EC-833), 4.5 mL urea dilutant, 1.5 mL urea buffer, 10 µL tetramethylethylenediamine (TEMED) and 150 µL 10 wt% ammonium persulfate in a casette (ThermoFisher Novex NC2010)[228]. 5 picomoles of the sample were mixed in a 1:1 ratio with formamide loading buffer (FLB) and denatured at 80°C for 10 minutes before loading into wells. Electrophoresis was carried out in 0.5 × TBE buffer at 250V for 45 minutes, followed by staining with SYBR Gold and imaging using the Typhoon Gel Scanner. For purification, the mixture was combined with formamide loading buffer (FLB), loaded into an 8% dPAGE gel in a large well formed using a taped comb, and run at 250V for 50 minutes. The peptide-oligonucleotide was observed through UV shadowing on a thin layer chromatography plate, excised, crushed, and immersed in 1× TE buffer. After overnight shaking at 25°C, purification was performed using Freeze 'N Squeeze DNA Gel Extraction Spin Columns (Bio-Rad; 7326165) and ethanol precipitation. The resulting peptide-oligonucleotide was resuspended in 1× PBS, and its concentration was determined using NanoDrop. Confirmation of purification was achieved via dPAGE.

3.7.4 Protein conjugation with 'anti-handle' oligonucleotide

We generated protein-oligonucleotides by conjugating azide-modified DNA handles to the protein (obtained from Sino Biologic or Advanced ImmunoChemical, Supplementary Table 13) via the amino group present on lysine residues using DBCO-Azide click chemistry. The reaction was incubated in phosphate buffer with a pH of 8.0 overnight 4°C and was subsequently agitated at 37°C for 30 minutes. At higher pH levels (> 8.0), NHS reactivity towards the ε-amino groups of lysines is enhanced compared to the α-amino group[137]. The protein was simultaneously labeled with NHS-Cy3 dye. DTT was also added to the reaction to reduce any disulfide bonds.

3.7.5 SILVER STAIN VERIFICATION AND PURIFICATION OF PROTEIN-CONJUGATED OLIGONUCLEOTIDE

Silver stain confirmed protein-oligonucleotide conjugation. The sample, mixed with 4× NuPAGE LDS sample buffer (ThermoFisher; NP0008), underwent incubation at 95°C for 2 minutes before loading onto 4–12% NuPAGE Bis-Tris gels (ThermoFisher; NP0322) and electrophoresis at 150V for 45 minutes in 1× MES SDS running buffer (ThermoFisher; NP0002). Gel analysis followed Pierce's (24612) silver staining protocol using Image Lab 6 on a Gel Doc EZ Imager (Bio-Rad). Purification utilized a 10K Amicon filter; the reaction sample, supplemented with phosphate buffer, was centrifuged at 14000rcf for 30 minutes until the flow-through reached a DNA concentration of less than 1 ng/µl, indicating removal of all unconjugated DNA. Buffer exchange was carried out to 1xTE 10mM $MgCl_2$.

3.7.6 PEPTIDE- OR PROTEIN-CONJUGATED OLIGONUCLEOTIDE HYBRIDIZATION WITH SQB

The peptide-oligonucleotides or protein-oligonucleotides were hybridized to the SQB DNA origami in a 2× excess, maintaining 10 mM $MgCl_2$ and 1× TE by adding stock 10× TE and 100 mM $MgCl_2$. SQBs were added last to ensure a consistent buffer environment. The resulting conjugated SQBs were incubated at 37°C for 1–2 hours with shaking, followed by purification through PEG precipitation. Analysis was performed using agarose gel electrophoresis, TEM, and a DNase I degradation assay.

3.7.7 Agarose gel electrophoresis

SQBs were analyzed via 2% native agarose gel electrophoresis. Gel was prepared with 0.5 × TBE buffer with 11 mM MgCl2 and 0.005% v/v SYBR Safe (ThermoFisher S33102), run at 70V for 2 hours, and imaged via a Typhoon Gel Scanner.

3.7.8 Transmission electron microscopy (TEM) analysis

Transmission electron microscopy (TEM) was utilized to assess structural integrity and SQB aggregation using negative-stain techniques. Formar-coated, carbon-stabilized grids, either self-prepared or obtained from Electron Microscopy Services (FCF200-CU-TA), were plasma-discharged for 30 seconds for passivation. Subsequently, 4–10 nM SQBs were deposited on the grids for 45 seconds, followed by blotting with filter paper. Uranyl-formate solution (0.75% w/v in H2O) was applied to the grid, blotted off, and a second application lasted for 2 minutes before blotting. Imaging of the grids occurred using a JEOL JEM-1400 TEM in brightfield mode at 120 kV.

3.7.9 SQB purification via PEG precipitation

CpG-SQBs or peptide- or protein-conjugated CpG-SQBs were purified via PEG precipitation. 1 × TE buffer (5 mM Tris base, pH 8.0 and 1 mM EDTA acid) containing 15% w/v PEG-8000 (Fisher Scientific, BP2331) and 510 mM NaCl was added to the SQB sample at 1:1 volume and mixed gently via pipetting. MgCl2 stock was added to the PEG solution to achieve 10 mM MgCl2 final concentration. As described previously, the solution was incubated for 30 min on the benchtop, centrifuged at 16000 g for 25 minutes and the supernatant was removed[228]. This procedure purifies and concentrates the sample, as a high concentration is often required for further studies. The concentration was determined via Nanodrop; the sample purity and integrity were confirmed via agarose gel electrophoresis and TEM.

3.7.10 DNase I degradation and silver stain analysis of peptide conjugation efficiency

One µg of SQBs was incubated with 1.0 U/µL DNase I (NEB) with 10 × DNase I buffer diluted in water (New England Biolabs M0303S). Samples were incubated in the thermocycler for 30 minutes at 37°C. The silver stain was performed as described above. ImageJ was used to quantify band intensities and determine peptide or protein loading efficiencies.

3.7.11 K10-PEG5k coating of SQBs

PEG-purified SQBs were mixed with oligolysine-PEG5k (K10-PEG5k; methoxy-poly(ethylene glycol)-block-poly(L-lysine hydrochloride); n=113, x=10; Alamanda Polymers (mPEG20K-b-PLKC10) based on the calculated number of phosphates in the SQB sequence. An appropriate quantity of K10-PEG5k was added to match the number of nitrogens in its amines with the SQB phosphates, following a previously published method[152]. The mixture underwent incubation at 37°C for at least 30 minutes, and concentration was determined based on dilution.

3.7.12 Animal model and treatment

C57BL/6 mice (6–8 weeks old) were obtained from Jackson Laboratory and housed at the Harvard Medical School (HMS) animal facility. Eight groups of eight mice each underwent the following treatments: (1) SARS-CoV-2-HR2 DoriVac, (2) SARS-CoV-2 HR2 bolus, (3) HIV-HR2 DoriVac, (4) HIV-HR2 bolus, (5) Ebola-HR2 DoriVac, (6) Ebola-HR2 bolus, (7) SQB-CpG + free HIV-HR2 peptide, and (8) untreated. The bolus contained an equivalent dose of CpG and HR2 peptide in PBS. Following one-week acclimation, mice received the first treatment dose (100µL of DoriVac containing 0.36 nmoles of CpG, 0.48 nmoles of HR2 peptide) subcutaneously on days 0 and 20. Blood was drawn via submandibular vein puncture four hours after dosing and also on days 14, 20, and 28. On days 21 and 35, four mice from each group were sacrificed; heart blood, LNs, spleens, and femurs were collected. All procedures were approved by the HMS Institutional Animal Care and Use Committee.

3.7.13 Lymph-node-on-a-chip and tonsil organoid vaccination

Lymph-node-on-a-chip (LN chip) was fabricated as previously described[69]. Tonsil organoids was seeded according to a prior publication[206]. Human patient-derived apheresis collars and tonsil were obtained from the Crimson Biomaterials Collection Core Facility under approval of Harvard University's Institutional Review Board. Chips and organoid culture were treated with 1 nM of vaccine. In LN chip experiments, medium (RPMI supplemented with 10% FBS, 1% antibiotics, IL-2 and IL-4 as previously described[69]) was circulated for 4 days of treatment (i.e., effluents were added back to the inlet perfusion reservoir), and at day 4, a 1:1 mix of effluent and fresh medium was used for perfusion to maintain the cytokine milieu. In the tonsil organoid experiment, fresh media was added in a 1:1 ratio at day 4. At the study's conclusion, cells were harvested by blocking one port of the basal channel and manually pipetting Cell Recovery Medium (Corning, 354253, 200 μL per chip) through the other port to extract the ECM and cells. The ECM was incubated in Cell Recovery Medium for 1 hour at 4 °C to depolymerize it and release associated cells. The released cells were centrifuged at 300 × g for 5 minutes and resuspended in PBS.

3.7.14 Processing blood cells

Blood was collected either via heart extraction or through a submandibular cheek draw into heparin-coated tubes. Plasma and blood cells were separated via centrifugation at 800g and 4°C for 5 minutes. The collected plasma was stored at -80°C until analysis, while the blood cells underwent treatment with red blood cell lysis buffer (10×) from BioLegend (420301) three times, following the manufacturer's protocol. Peripheral blood mononuclear cells (PBMCs) were subsequently analysed using

ELISpot and/or flow cytometry (Cytoflex LX).

3.7.15 LUMINEX MULTIPLEX ELISA ANALYSIS

The customized Bio-Plex Pro Mouse Cytokine Standard 23-plex kit from Bio-Rad included the following cytokines: IL-1α, IL-1β, IL-2, IL-3, IL-4, IL-5, IL-6, IL-9, IL-10, IL-12p40, IL-12p70, IL-13, IL-17A, Eotaxin, G-CSF, GM-CSF, IFNγ, MCP-1, MIP-1α, MIP-1β, RANTES, TNFα, following the manufacturer's protocol. Data collection was performed using the Bio-Plex 3D Suspension Array System (Bio-Rad).

3.7.16 PROCESSING LYMPH NODES (LNS)

Following euthanasia, the upper axillary and superficial cervical LNs from the mouse were harvested and stored in cold PBS, as previously outlined[228]. These LNs were processed into single-cell suspensions for flow cytometry analysis (Cytoflex LX) by gently mashing them through a 40 μm cell strainer using a sterile syringe plunger into a petri dish. Cells were collected into 1.5 mL Eppendorf tubes, centrifuged at 400g for 5 minutes at 4°C, and the supernatant was discarded. The cell pellet was resuspended in 700 μL of PBS and distributed into 96-well plates for flow cytometry analysis.

3.7.17 PROCESSING SPLEENS

Following euthanasia, mouse spleens were harvested, washed with PBS, and mashed through a 40 μm cell strainer into a 60 mm petri dish using a sterile syringe plunger. The resulting single-cell suspension was washed with complete RPMI-1640 media (containing 10% fetal bovine serum and 1% penicillin-streptomycin), collected into a Falcon tube, and subjected to two treatments with red blood cell lysis buffer (BioLegend; 420301) following the manufacturer's protocol. The cell pellet was resuspended in 2 mL of complete RPMI media, and the cell count was determined. These splenocytes were used for flow cytometry or ELISpot assays.

3.7.18 PROCESSING BONE MARROW

Following euthanasia, femurs were repeatedly washed with PBS. Muscle fibers and connective tissues were extracted using forceps. Marrow extraction involved flushing the bone with a syringe into a PBS-filled dish. The collected marrow clot was pipetted, filtered through a 40 μm cell strainer, and gathered into a Falcon tube. The resulting single-cell suspension underwent centrifugation at 300 × g for five minutes. After discarding the supernatant, the pellet was treated with red blood cell lysis buffer (BioLegend 420301) following the manufacturer's instructions. The suspension was centrifuged at 300 × g for five minutes and subsequently resuspended in culture media for flow cytometry (Cytoflex LX).

3.7.19 FLOW CYTOMETRY

Single cell suspensions of LNs, PBMCs, spleens, and bone marrow were obtained. The suspensions were washed with PBS, stained with Zombie UV (BioLegend; 423108) or ViaKrome 808 (Beckman Coulter C36628) viability dye and washed with cell staining buffer (BioLegend, 420201). The cells were stained with fluorophore-conjugated cell surface antibodies (Supplementary Table 4-6, 11-12). Intracellular staining was performed using permeabilization and fixation reagents (BioLegend; 424401). Antibodies were arranged into appropriate panels, compensations were set up to minimize fluorescent emission overlap, and the cells were analyzed on a Cytoflex LX flow cytometer. Storage events were gated on the population of interest, based on protocols published previously[228], and according to the gating in Supplementary Figures 2, 5, 9, 11 and 12. Flow data was analyzed using FlowJo V10.

3.7.20 CD8 and CD4 enrichment of splenocytes

Splenocytes were depleted for CD4 or CD8 T cells using CD8 DynabeadsTM (Thermofisher, 11145D) or CD4 Microbeads (Miltenyi Biotec, 130-117-043), according to manufacturer's instructions. The remaining sample was enriched for CD4 T cells (via CD8 T cell depletion) or enriched for CD8 T cells (via CD4 T cell depletion). Splenocytes were maintained in 4°C for 36 hours before processing for CD8 T cell enrichment. For CD8 depletion, the Dynabeads$_{TM}$ were washed in isolation buffer and placed in the magnet. At the same time, cells were prepared at a concentration of 1×10^7 cells per mL in isolation buffer. The prewashed beads were added, and the solution was incubated for 30 minutes at 4°C with gentle tilting. After, the tubes were placed in the magnet for 2 minutes and the supernatant was transferred to a new tube for further analysis. The beads and associated cells were discarded. Regarding CD4 depletion via Microbeads, the cells were incubated with the microbeads for 10 minutes at 4°C and then processed through an LD column, yielding the CD8-enriched (CD4-depleted) population in the flow-through for subsequent analysis.

3.7.21 IFNΓ ELISpot

Samples were processed into single-cell suspensions, followed by plating PBMCs or splenocytes into a 96-well round-bottom plate, each containing cells from an individual mouse in 200 µl of media. The cell quantities utilized were: two and a half million cells for splenocytes on day 21, three million cells for splenocytes on day 35, two million cells for PBMCs, and eight and a half million cells for CD4 and CD8 enriched samples. Each well was stimulated with 2 µg/mL of HR2 peptide. After 48 hours of incubation, cells were collected, resuspended in 100 µl of sterile splenocyte media, and plated onto an ELISpot plate (RND systems, Mouse IFNγ ELISpot kit, 505841). The plate was incubated for 36 hours at 37°C, processed as per the manufacturer's guidelines, and analyzed using an ELISpot plate reader at Dana Farber Cancer Institute's Center for Immuno-oncology Translational Immunogenics Laboratory to determine the fold increase in cells for DoriVac treated groups compared to bolus groups.

3.7.22 Enzyme-linked Immunosorbent Assay (ELISA)

Plasma IgG from vaccinated mice was quantified using an ELISA method. Nunc Maxisorp ELISA plates (ThermoFisher, USA 44-2404-21) were coated with HR2 peptide at a concentration of 2–20 μg/mL in 100 μL of coating buffer (100 mM bicarbonate/carbonate buffer, pH 9.5) and incubated overnight at 4°C. After washing three times with washing buffer (PBS containing 0.05% Tween 20), 150 μL of blocking buffer (2% bovine serum albumin (Sigma, USA 9048-46-8) in washing buffer) was applied for 1 h at 37°C. After removing the blocking buffer, 100 μL of plasma samples diluted in blocking buffer (1:100, 1:200, 1:400 dilutions) were added and incubated for 1 h at 37°C. After washing three times with washing buffer, 150 μL of blocking buffer was applied for 1 h at 37°C. After removing the blocking buffer, 100 μL of HRP-conjugated anti-mouse IgG antibody (Cell Signaling Technology, USA 7076) diluted in blocking buffer was applied for 1 h at 37°C. After washing five times with washing buffer, 50 μL of 3,3',5,5'-tetramethyl benzidine substrate (Sigma 54827-17-7) for detection was added, and the reaction was stopped after 15 min by the addition of 50 μL of 1 M H2SO4. Absorbance at 450 nm was measured using an automated plate reader (BioTek).

3.7.23 Pseudovirus assay

Plasma was isolated by collecting the clear supernatant post-centrifugation. Samples were diluted in 1× PBS at varying ratios (1:10, 1:100, 1:1000) and cultured with the corresponding pseudovirus and ACE2-293 T cells. Data in the figures represents the optimal 1:100 dilution. Relative pseudovirus infection level was assessed as the ratio of infected cells in each group to those in the bolus group, which was assigned a relative infection level of 1.0.

3.7.24 STATISTICAL ANALYSES

One-way or two-way ANOVA or unpaired t-test(s) with appropriate corrections for multiple comparisons as detailed in the figure captions was applied to determine the statistical significance of all flow, ELISpot, and ELISA data in Figures 2–7. GraphPad Prism 10 was used to make graphs, analyze statistics, and calculate p values. A p value ≤ 0.05 was considered statistically significant. '*' refers to $p \leq 0.05$; '**' refers to $p \leq 0.01$; '***' refers to $p \leq 0.001$; '****' refers to $p \leq 0.0001$. Error bars represent standard deviation (SD).

4

Constructing DNA origami nanoparticles with immunostimulatory CD40 ligands as a novel adjuvant

4.1 Author Contributions

This work was performed in collaboration with William M. Shih and Yang C. Zeng. O.J.Y, W.M.S and Y.C.Z. conceived of this project and developed the idea. O.J.Y planned and carried out experiments with the assistance of W.M.S amd Y.C.Z. Peter Sulc and Matthew Sample from Arizona State University performed the molecular dynamics simulations, with feedback from O.J.Y and W.M.S.

4.2 ABSTRACT

CD40 ligand (CD40L) is a critical co-stimulatory molecule that is required for effective dendritic cell (DC) licensing, enabling DC interactions with CD8+ T cells and ultimately, inducing a robust adaptive immune response. Moreso, crosslinking of the CD40 receptor is critical for DC licensing, requiring many CD40L complexes to interact with many CD40 receptors at once. Previous CD40 agonists have been tested clinically, where they have shown robust immune responses, but have been hindered by severe adverse events caused by off-target immune activation. Here, we demonstrate the design, fabrication and characterization of a CD40L-conjugated DNA origami nanoparticle and model the expected molecular dynamics of the nanoparticle. This nanoparticle offers precise control over ligand spacing down to a pitch of 2.5 nm, a level of spatial control that cannot be achieved with other nanoparticles. We hope that future studies will test and optimize this nanoparticle as a novel immune adjuvant with potential therapeutic applications in cancer, as well as chronic infectious diseases.

4.3 INTRODUCTION

Cancer is the leading cause of premature death in the US and in many countries world-wide[23]. Cancer immunotherapy is a powerful treatment modality that activates the patient's own immune system to eradicate cancer cells. Cancer immunotherapies have improved patient survival, but the overall success rate has been less than 25%, suggesting that there is much room for improvement[200]. Many studies aim to improve the efficacy of immunotherapy by presenting antigen, adjuvant, and other immunomodulatory cues as a 'cancer vaccine' to dendritic cells, which play a critical role in directing the immune response[34,3,4]. However, most technologies cannot reproduce the nanoscale organization at which these cues are naturally presented, leading to suboptimal DC activation. One such cue, CD40L, which is endogenously presented by CD4+ T helper cells, interacts with the receptor CD40 on activated DCs. CD40 activation induces subsequent upregulation of critical immune-

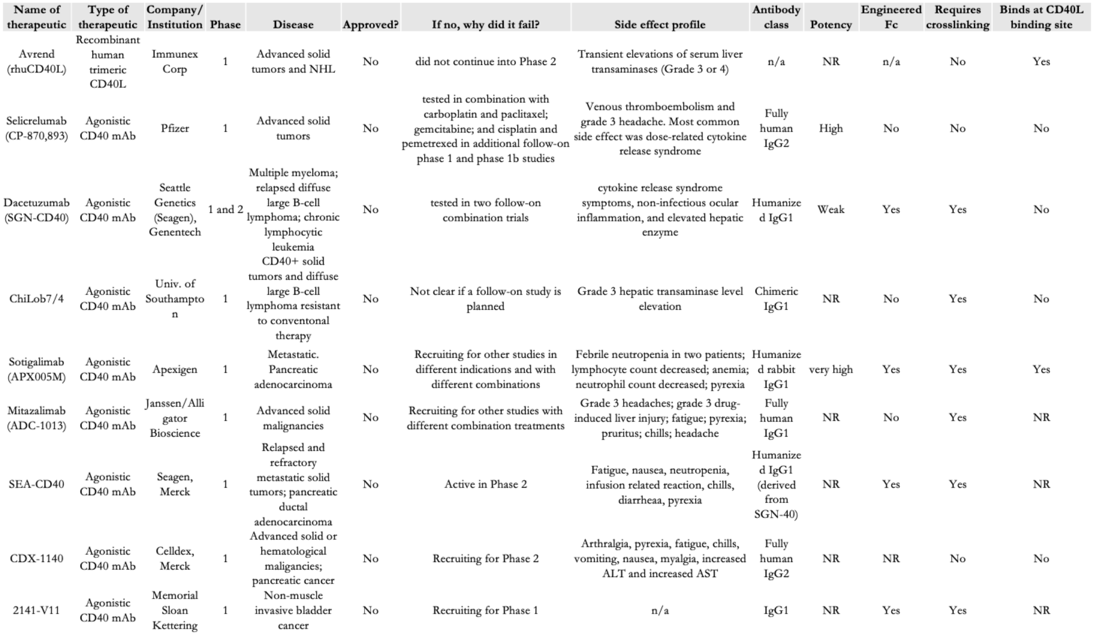

Name of therapeutic	Type of therapeutic	Company/ Institution	Phase	Disease	Approved?	If no, why did it fail?	Side effect profile	Antibody class	Potency	Engineered Fc	Requires crosslinking	Binds at CD40L binding site
Avrend (rhuCD40L)	Recombinant human trimeric CD40L	Immunex Corp	1	Advanced solid tumors and NHL	No	did not continue into Phase 2	Transient elevations of serum liver transaminases (Grade 3 or 4)	n/a	NR	n/a	No	Yes
Selicrelumab (CP-870,893)	Agonistic CD40 mAb	Pfizer	1	Advanced solid tumors	No	tested in combination with carboplatin and paclitaxel; gemcitabine; and cisplatin and pemetrexed in additional follow-on phase 1 and phase 1b studies	Venous thromboembolism and grade 3 headache. Most common side effect was dose-related cytokine release syndrome	Fully human IgG2	High	No	No	No
Dacetuzumab (SGN-CD40)	Agonistic CD40 mAb	Seattle Genetics (Seagen), Genentech	1 and 2	Multiple myeloma; relapsed diffuse large B-cell lymphoma; chronic lymphocytic leukemia	No	tested in two follow-on combination trials	cytokine release syndrome symptoms, non-infectious ocular inflammation, and elevated hepatic enzyme	Humanized IgG1	Weak	Yes	Yes	No
ChiLob7/4	Agonistic CD40 mAb	Univ. of Southampton	1	CD40+ solid tumors and diffuse large B-cell lymphoma resistant to conventonal therapy	No	Not clear if a follow-on study is planned	Grade 3 hepatic transaminase level elevation	Chimeric IgG1	NR	No	Yes	No
Sotigalimab (APX005M)	Agonistic CD40 mAb	Apexigen	1	Metastatic. Pancreatic adenocarcinoma	No	Recruiting for other studies in different indications and with different combinations	Febrile neutropenia in two patients; lymphocyte count decreased; anemia; neutrophil count decreased; pyrexia	Humanized rabbit IgG1	very high	Yes	Yes	Yes
Mitazalimab (ADC-1013)	Agonistic CD40 mAb	Janssen/Alligator Bioscience	1	Advanced solid malignancies	No	Recruiting for other studies with different combination treatments	Grade 3 headaches; grade 3 drug-induced liver injury; fatigue; pyrexia; pruritus; chills; headache	Fully human IgG1	NR	No	Yes	NR
SEA-CD40	Agonistic CD40 mAb	Seagen, Merck	1	Relapsed and refractory metastatic solid tumors; pancreatic ductal adenocarcinoma	No	Active in Phase 2	Fatigue, nausea, neutropenia, infusion related reaction, chills, diarrheaa, pyrexia	Humanized IgG1 (derived from SGN-40)	NR	Yes	Yes	NR
CDX-1140	Agonistic CD40 mAb	Celldex, Merck	1	Advanced solid or hematological maligancies; pancreatic cancer	No	Recruiting for Phase 2	Arthralgia, pyrexia, fatigue, chills, vomiting, nausea, myalgia, increased ALT and increased AST	Fully human IgG2	NR	NR	No	No
2141-V11	Agonistic CD40 mAb	Memorial Sloan Kettering	1	Non-muscle invasive bladder cancer	No	Recruiting for Phase 1	n/a	IgG1	NR	Yes	Yes	NR

Figure 4.1: Relevant clinical trials for both CD40 ligand and anti-CD40 agonists. CD40 ligand and anti-CD40 agonists have been tested extensively in clinical trials. Some early CD40 agonists failed in clinical trials due to their severe toxicity, often attributed to the high doses required for therapeutic efficacy. Currently, there are several active trials in various types of cancers, often in combination with the standard of care. All data is updated as of March 2023.

activating signals[121,28,27]. Soluble CD40L and anti-CD40 agonists have demonstrated significant anti-tumor effects in pre-clinical studies. To date, no clinical candidates have received FDA approval, even though this could change in the near future with several promising clinical candidates undergoing testing[100,99,108,24,140,186,203,204,202] (Figure 4.1).

Even though CD40 ligand has been demonstrated to have robust immune effects in pre-clinical studies and clinical trials via DC licensing (Fig. 4.2A), the efficacy in human patients was at times severely limited by the adverse events caused by a high dose. However, studies suggest that higher order nanoscale multimerization of CD40 is critical for activation, as the density of CD40L on the surface of T helper cells varies dramatically during inactivated and activated states, ranging from approximately 200 complexes/μm^2 in naïve T cells to 600 or more complexes/μm^2 in activated T helper cells[165,1].

This higher order multimerization has not been reproduced with prior CD40L clinical candidates. As such, our hypothesis based on the literature and prior clinical trials is that a dense CD40L pattern will engage more CD40 receptors on the DC, leading to CD40 multimerization and subsequent DC activation (Fig. 4.2B)[121,28,27,165,1].

DNA origami offers a new method to present CD40L with dense patterning. DNA origami is a novel nanofabrication tool that enables specific folding of a long scaffold DNA strand into a 3D nanostructure. Unlike other nanofabrication strategies, DNA origami offers structural control at the nanoscale level and the capability to act as a modular billboard for various cargos[44,49,73,90,162]. This chapter will demonstrate precise patterning of CD40L onto the DNA origami nanoparticles and will simulate the behavior of these nanoparticles in physiological conditions using molecular dynamics.

4.4 Results

4.4.1 Design of CD40 ligand (CD40L)-conjugated DNA origami nanoparticles

Pioneering studies in the Shih lab in the field of DNA 3D nanostructures have fabricated and validated DNA-origami square-lattice block nanoparticles (SQBs) that control cargo spacing[44,49,228]. With this technology, we can precisely pattern CD40L onto the flat surface of the SQB with a range of copy numbers and spatial arrangements (Fig. 4.2C). DNA origami SQB nanoparticles were folded by combining the p8634 scaffold DNA and staple strands at an appropriate temperature ramp, according to previously published protocols[228]. We designed custom ssDNA 'handles' to decorate each position for CD40L conjugation on the SQB independently. These handles can be partnered in a sequence-specific fashion with the CD40L protein that is linked to ssDNA complementary 'anti-handles'. Unfortunately, there are no rigorous studies on the natural spatial arrangement of CD40L on the T cell surface, as the nanoscale spacing is below the resolution limit for many relevant imaging techniques.

Additionally, it is difficult to predict the optimal DNA origami spacing based on the endogenous spacing. However, 5.3 nm spacing is observed between neighboring CD40L residues in the CD40L-CD40 crystal structure, suggesting that this spacing may be physiologically relevant[6]. Therefore, we constructed CD40L patterns with spacing of 5, 7, 10 and 20 nm between each complex and and with varying numbers of complexes on the DNA origami nanoparticles (Fig. 4.2D). We aimed to enhance the activation of the CD40 receptor by precisely delivering CD40L through the DNA origami SQB, ideally surpassing the potency of the natural endogenous interaction.

4.4.2 Conjugation of CD40L to oligonucleotide

Two crucial parameters dictate CD40 activation. First, the trimeric organization of the CD40L complex promotes activation. CD40L trimers, and even CD40L dimers, lead to significantly more activation of a single CD40 receptor than a CD40L monomer[79]. Second, the higher order arrangement of CD40L complexes plays a pivotal role, as increased CD40L complex density is associated with increased CD40 activation[165,1]. Research indicates that multimerization of multiple CD40L complexes, and crosslinking of the corresponding CD40 receptor, is essential for CD40 pathway activation. Certain therapeutics leverage multiplexed CD40L complexes (linked via chemical conjugation), which show promising outcomes compared to the use of a single CD40L molecule[100,99,53]. Even though peptide mimics[63], minimal peptide epitopes, and monomers of CD40L were considered for the following experiments, recent studies have raised questions about the validity of these peptide mimics[20] and have suggested that monomers are less effective as therapeutics (Supplemental Figure 1 showcases some of the alternative CD40L designs considered). With this in mind, we decided to move forward with a CD40L protein dimer with a single-stalk, which enabled the conjugation of a single oligonucleotide to a single CD40L protein for single-point attachment of each CD40L protein-oligonucleotide to the DNA origami nanoparticle (Supplementary Table 1-2, Supplementary Figure 2)[79]. The chosen CD40L protein dimer is based on murine CD40L, which works well for the pur-

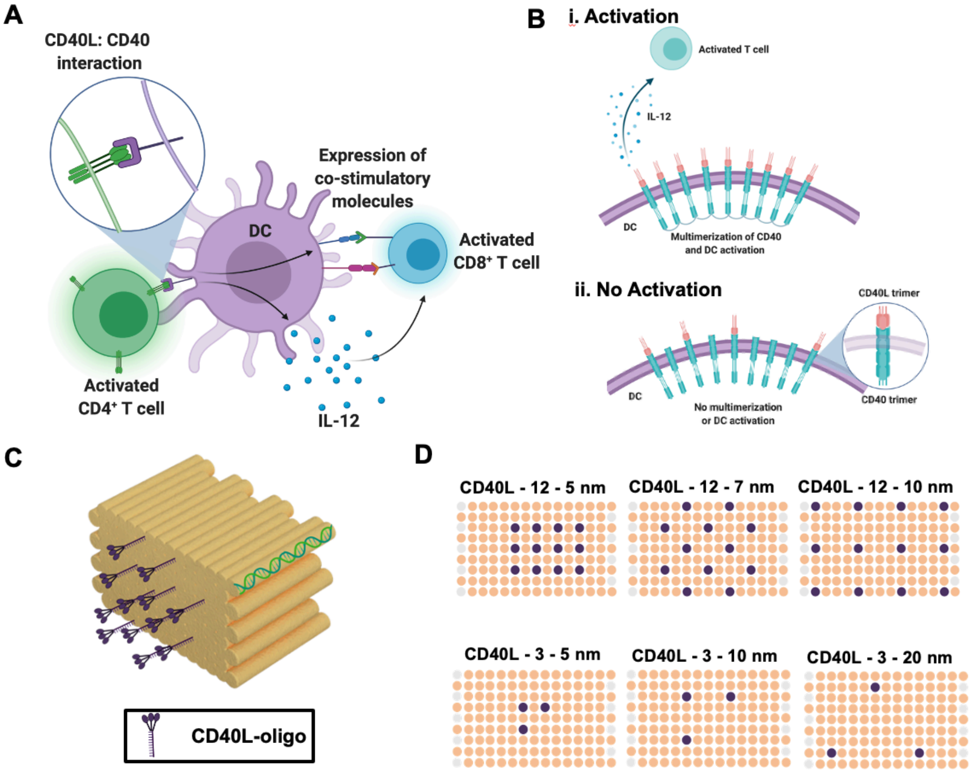

Figure 4.2: Design of CD40 ligand (CD40L)-conjugated DNA origami nanoparticles. A. Schematic demonstrating the mechanism of action of CD40 ligand in activating and licensing dendritic cells. **B.** Schematic demonstrating how CD40 multimerization leads to dendritic cell (DC) and T cell activation. **i.** Multimerization of CD40 leads to a cascade of immune effects, including IL-12 production, which is critical to T cell activation. **ii.** Without CD40 multimerization, there is no immune signaling cascade. **C.** Schematic of CD40L-conjugated DNA origami nanoparticles, consisting of a DNA origami square block (SQB) conjugated with CD40L protein on the flat face. **D.** Schematic of the various copy number and spatial arrangements of CD40L which were designed for the SQB structure.

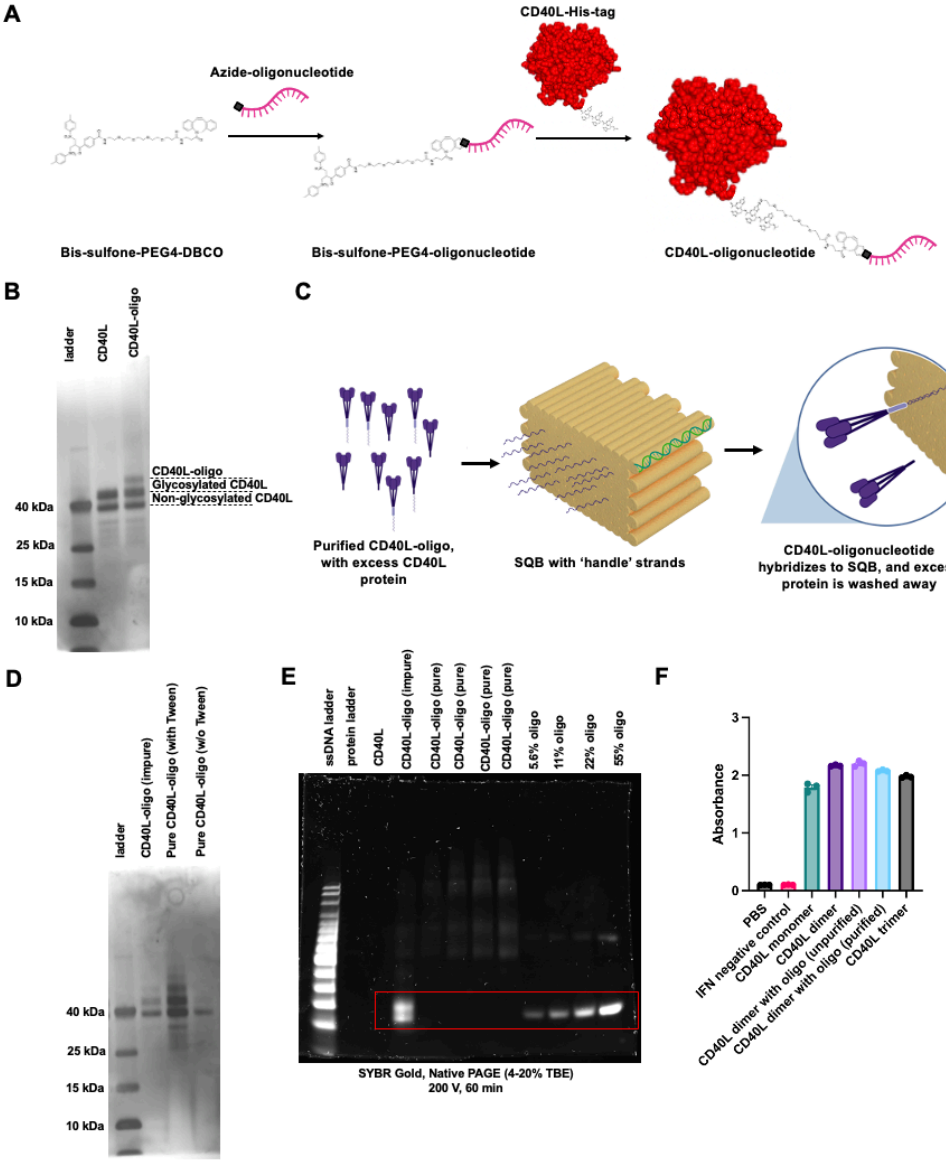

Figure 4.3: Conjugation of CD40L to the oligonucleotide. **A.** Schematic demonstrating the bis-sulfone-PEG4-DBCO reaction to a desired oligonucleotide via DBCO-azide click chemistry and then the reaction of the bis-sulfone conjugated oligonucleotide to the His-tag of the CD40L protein. **B.** Silver stain SDS-PAGE gel demonstrating successful conjugation of the CD40L protein with an oligonucleotide. **C.** Schematic showing the desired purification of the CD40L-oligonucleotide, ensuring that all unconjugated oligonucleotide is removed. **D.** Silver stain SDS-PAGE gel demonstrating the purification of the CD40L-oligonucleotide via Amicon filtration and highlighting the increased yield after precoating the Amicon filter with Tween. **E.** Native PAGE gel demonstrating the purity of the CD40L-oligonucleotide, as less than 5% of the sample is unconjugated oligonucleotide. **F.** SEAP absorbance measured from HEK-CD40 reporter cell assay demonstrates that the CD40L-oligonucleotide retains its CD40 stimulating activity and is not hindered by the conjugation of the oligonucleotide.

poses of our experiments as murine CD40L activates human CD40 in a similar manner as human CD40L due to the fact that they share 78% of their sequence[184]. We implemented and optimized a bis-sulfone conjugation chemistry to attach the oligonucleotide to adjacent histidine residues in the His-tag region of the CD40L protein (Fig. 4.3A,B, Supplementary Figure 3-4). This chemical conjugation strategy was chosen as it was one of the few site-selective methods to attach an oligonucleotide to a protein. Other methods, including lysine labeling or SMCC chemistry to cysteines, would result in a heterogenous mixture of protein-oligonucleotides, where the oligonucleotide is conjugated to different sites on the protein (Supplementary Table 3). The CD40L protein-oligonucleotide was then purified via 10K Amicon filtration, which removed the unconjugated oligonucleotide, as confirmed by SDS-PAGE gel (Fig. 4.3C-E, Supplementary Figure 5). The CD40L protein-oligonucleotide was confirmed to activate the CD40 receptor by inducing activation of HEK-CD40 reporter cells (Fig. 4.3).

4.4.3 Fabrication of CD40L-conjugated SQBs

We successfully fabricated the CD40L protein-oligonucleotide on the SQB with spacing of 5, 7, 10 and 20 nm via Watson and Crick base-pairing hybridization. Agarose gel verified successful fabrication and purification of the CD40L-SQBs as evidenced by a bandshift after conjugation and minimal low-molecular weight staple strands on the gel (Fig. 4.4A). We then characterized the conjugated DNA origami constructs via agarose gel electrophoresis, TEM, dynamic light scattering and silver stain. TEM demonstrated that the DNA origami nanoparticles were well-formed and exhibited minimal aggregation after CD40L conjugation (Fig. 4.4B). Dynamic light scattering was further used to validate the size change after CD40L conjugation and to confirm minimal aggregation, as demonstrated by a polydispersity index under 0.3 for all samples, which is considered the metric for a homogenous population (Fig. 4.4C)[43]. DNase degradation of the DNA origami SQB, followed by subsequent silver stain of the remaining protein product was used to validate that CD40L proteins were successfully

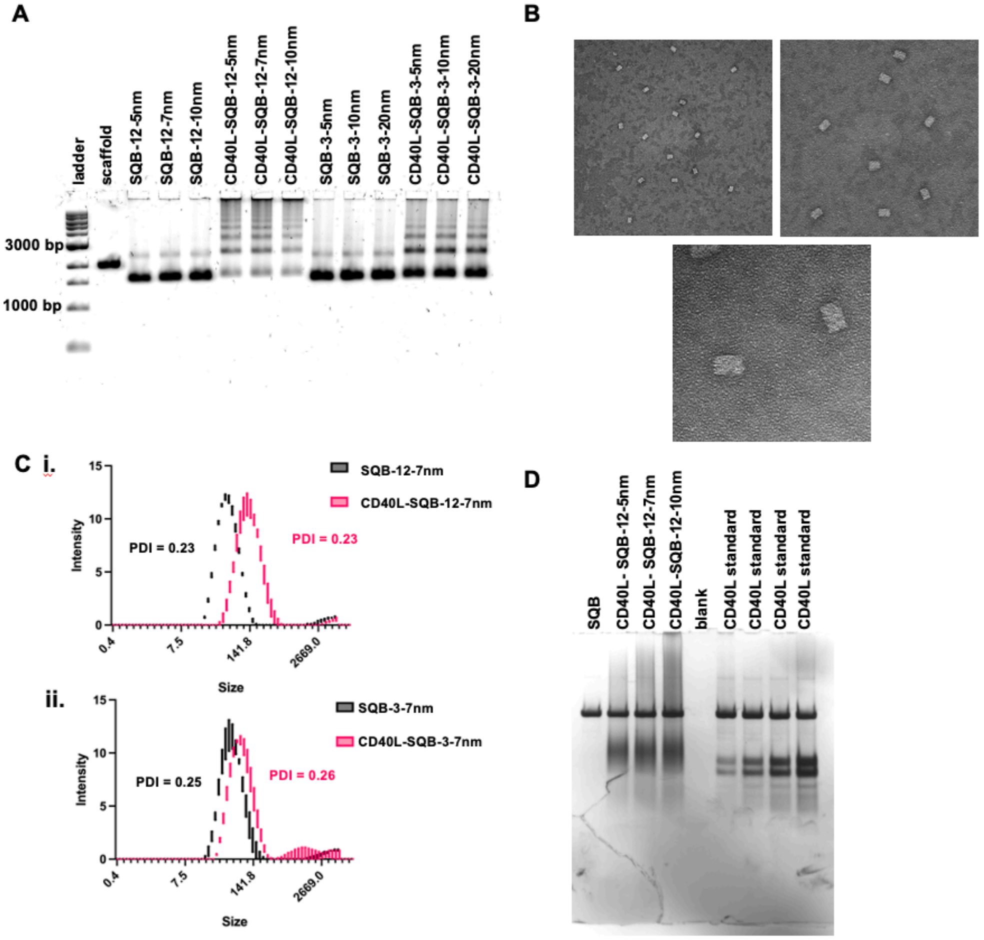

Figure 4.4: Fabrication and characterization of the CD40L-conjugated DNA origami nanoparticle. A. Agarose gel demonstrating successful conjugation of the CD40L-oligonucleotides to the SQB DNA origami nanoparticle. **B.** Representative TEM images of the CD40L-conjugated DNA origami nanoparticle. **C.** Representative dynamic light scattering graphs showing **i.** a DNA origami SQB before and after conjugation with the CD40L-oligonucleotide at 12 sites, and **ii.** a DNA origami SQB before and after conjugation with the CD40L-oligonucleotide at 3 sites. **D.** SDS-PAGE gel demonstrating the results after DNase I digestion of the CD40L-oligonucleotide alone or conjugated with the SQBs. DNase I digestion of the SQBs, accompanied by analysis of the conjugated CD40L protein using silver staining, confirms sucessful CD40L protein conjugation onto the SQB.

conjugated onto the SQB (Fig. 4.4D).

4.4.4 MOLECULAR DYNAMIC SIMULATIONS OF CD40L-CONJUGATED SQBs

Molecular dynamics simulations were used to confirm that the CD40L conjugated onto the SQB at a high density was accessible for binding to CD40, and also to validate that the spatial arrangement programmed via the molecular pegboard of the DNA origami nanoparticle maintained its precise arrangement in physiological conditions. Using a protein-DNA anisotropic network model (ANM) programmed via oxDNA, we simulated the behavior of the CD40L-conjugated DNA origami nanoparticle in physiological conditions (Fig. 4.5A). Molecular dynamics suggested that the oligonucleotide 'handles' have flexibility, leading to varied protein spacing that is typically greater than the programmed spacing on the DNA origami nanoparticle (Fig. 4.5B). The protein-protein distance is often more flexible than the DNA-DNA distance, likely due to the observed tendency of proteins to 'splay' out at the edges due to entropy (Fig. 4.5C). Additionally, proteins on the edge of the DNA origami nanoparticle have greater distance fluctuations when compared to proteins on the center of the DNA origami nanoparticle (Fig. 4.5C). With regards to the various nanoparticle spacing designs, each design has a distinct average distance between adjacent proteins (Fig. 4.5D,E), suggesting that the designs can be used in the future to understand the effects of different CD40L spacing on subsequent biological responses. The core DNA-DNA distances are similar to the programmed spacing, within 10-20% of the expected distance, but the outward-facing DNA have greater fluctuations, which leads to greater distances between the adjacent proteins compared to the programmed spacing (Fig. 4.5F). Finally, 5 nm programmed spacing appears to be a feasible spacing for packing of CD40L, and does not appear to be limited by steric hindrance. In summary, these simulations suggest that the designs are appropriate for testing differential CD40L spacing, even though the flexibility of the protein-oligonucleotides should be considered.

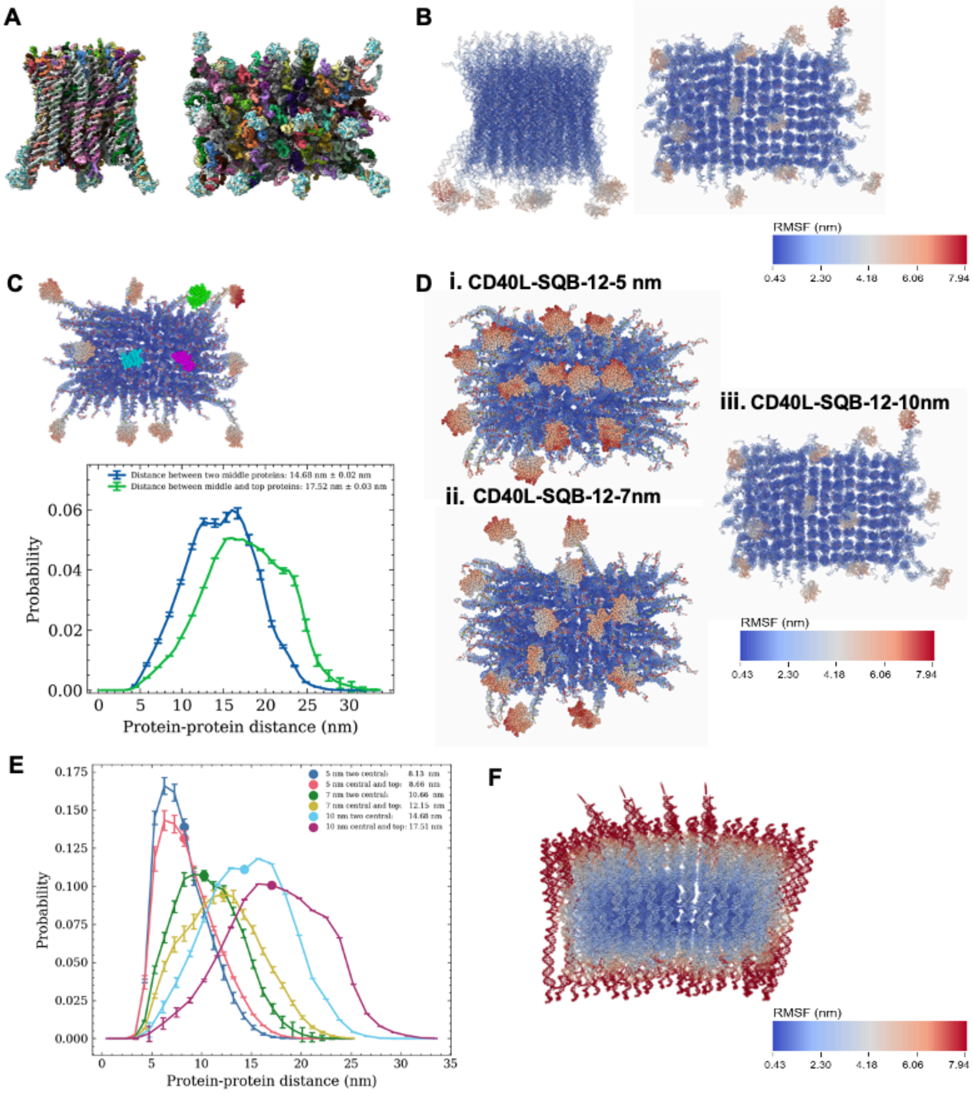

Figure 4.5: Molecular dynamics simulations of the CD40L-conjugated DNA origami nanoparticles. A. Three-dimensional representation of the CD40L-conjugated DNA origami SQB, with the scaffold strand in gray and each individual staple strand as a distinct color. **B.** Three-dimensional representation of the CD40L-SQB with 10nm programmed spacing between adjacent CD40L proteins. Schematic also demonstrates the root mean square fluctuations (RMSF) of each component throughout the molecular dynamic simulation. **C.** Graph and corresponding three-dimensional representation showing the theoretical protein-protein distance between two middle proteins compared with the protein-protein distance between the middle and the top proteins. **D.** Three-dimensional representation of the most probable conformation for **i.** the CD40L-SQB with 5 nm programmed spacing, **ii.** the CD40L-SQB with 7 nm programmed spacing, **iii.** and the CD40L-SQB with 10nm programmed spacing. Schematic also demonstrates the root mean square fluctuations (RMSF) of each component throughout the molecular dynamic simulation. **E.** Graph showiing the predicted protein-protein for each of the SQB designs represented in E, and differentiating between two middle proteins and the middle and top proteins. **F.** Schematic demonstrating the root mean square fluctuations (RMSF) in nanometers of each helix throughout the molecular dynamic simulation.

4.4.5 In vitro testing of CD40L-conjugated DNA origami nanoparticles

To test the hypothesis that the spatial arrangement of CD40L affects downstream immune signaling, we tested the various CD40L-conjugated DNA origami nanoparticle designs (Fig. 4.6A-D) in a HEK-CD40L reporter cell assay. Unfortunately, the CD40L-conjugated DNA origami nanoparticles did not demonstrate activation of CD40. Our positive controls confirmed that CD40 is activated by a commercial CD40L monomer, as well as by the CD40L-oligonucleotide construct. With these results, we have several hypotheses as to why activation was not demonstrated with the CD40L-conjugated DNA origami nanoparticle. First, we must consider that the hybridization of the CD40L onto the DNA origami nanoparticle either sterically impedes the binding of CD40L to the CD40 receptor or renders the CD40L nonfunctional. We could consider redesigning the CD40L-oligonucleotide hybridization strategy to make the CD40L protein more accessible (i.e. by increasing the linker length or changing the orientation) or modifying the hybridization protocol to minimize denaturation of the CD40L protein (i.e. by decreasing the hybridization temperature or removing the shaking step). We also considered that the PEG precipitation purification strategy or the K10PEG coating strategy could impede interaction of CD40L with CD40 or denature the CD40L protein. Additionally, we also observed some aggregation of the CD40L-SQBs, which may also occlude interaction of the CD40L with CD40. We were not able to determine the exact cause of the CD40L-SQB inactivity by the time of publication, but hope that future studies may continue to investigate how the spatial arrangement of CD40L affects immune polarization, as literature and other prior studies suggest that multimerization of CD40L is critical to CD40 pathway activation. We believe that DNA origami is uniquely suited to investigating this interaction, even though some optimization of the CD40L-conjugated DNA origami nanoparticles is required.

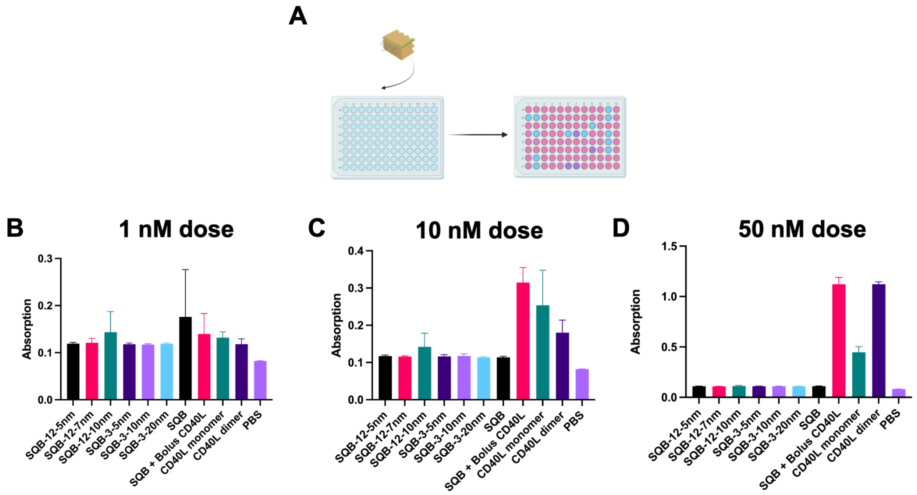

Figure 4.6: In vitro testing of CD40L-conjugated DNA origami nanoparticles. A. Schematic of in vitor testing via HEK-CD40L reporter cell assay. Upon CD40 activation, SEAP is released from the HEK-CD40L reporter cells and can be measured as a color change via spectrophotometry. **B.** 1 nM dose of CD40L via CD40L-conjugated DNA origami nanoparticles demonstrates minimal activation, as measured via SEAP absorbance, compared to relevant positive controls. **C.** 10 nM dose of CD40L via CD40L-conjugated DNA origami nanoparticles demonstrates minimal activation, as measured via SEAP absorbance, compared to relevant positive controls. **D.** 10 nM dose of CD40L via CD40L-conjugated DNA origami nanoparticles demonstrates minimal activation, as measured via SEAP absorbance, compared to relevant positive controls.

4.5 CONCLUSION

In conclusion, we have designed and constructed DNA origami nanoparticles conjugated with a high density of CD40 ligands. We hope that delivery of a high density of CD40 ligands would promote crosslinking of the CD40 receptor, enabling activation of the pathway without an prohibitively high therapeutic dose, even though this was not tested in initial studies. We also demonstrate molecular dynamics simulations which predict that the CD40 ligand is accessible to the receptor and maintains differential nanoscale arrangement in physiological conditions, despite the flexibility of the protein-protein distance.

Notably, we were not able to determine an optimal spatial arrangement of CD40L for subsequent immune activation, as CD40L did not demonstrate functionality after conjugation on the DNA origami nanoparticle. We hypothesize that the fabrication of CD40L onto the DNA origami nanoparticle may have interfered with the functionality of CD40L. We considered testing different hybridization procedures for attaching the CD40L-oligonucleotide onto the SQB, as the 37°C temperature with mechanical shaking may have been too harsh for the CD40L functionality. Additionally, we considered that the purification and coating may have also hindered the functionality of CD40L after conjugation onto the SQB, although we have not observed this with CpG conjugation. Finally, we considered redesigning the CD40L-oligonucleotide to include a longer linker, if the current linker length is too short for CD40L-CD40 binding. Moreover, various factors, such as the rigidity of the DNA origami nanoparticles, can also influence the effectiveness of CD40L-conjugated DNA origami nanparticles, especially as the rigidity of the nanoparticle differs significantly from the flexible cell membrane where CD40L is endogenously presented. Nevertheless, we do not believe that factors like rigidity would render the CD40L completely nonfunctional, but rather may be an interesting parameter to investigate in the future.

We hope that future experiments will further optimize the conjugation of CD40 ligand and perform in vitro experiments to test the efficacy of the CD40L-conjugated DNA origami nanoparticle. Ultimately, we hope that other researchers will explore whether an optimal spacing exists that could promote multimerization of the corresponding CD40 receptor, thereby licensing dendritic cells and enhancing immune responses, as prior literature highlights the importance of multimerization in CD40 activation. This information could, in turn, guide the design of a more effective immune adjuvant.

4.6 Acknowledgements

We would like to thank Maurice Perez, Michael Carr, Alex Pauer and Eric Zigon for their assistance in the lab management and facility usage, as well as the Shih Lab members for their probing questions and insightful suggestions during the course of this project. I would also like to thank Anastasia Ershova for assistance with revising this chapter.

4.7 Materials and Methods

4.7.1 Material sources

The p8634 scaffold was harvested in-house from the M13 bacteriophage, per established protocols[48]. All short oligonucleotides, including the oligonucleotides for conjugation with CD40L and all strands for DNA origami nanoparticle fabrication, were obtained from IDT (www.idtdna.com). The CD40L protein, consisting of a dimeric murine CD40L extracellular domain and a single protein stalk, was obtained from Dr. Zhirui Wang of the University of Colorado Anschutz Medical Campus Wang Protein Core, and the production process in Pichia yeast was detailed in a prior paper[79]. HEK-Blue CD40L reporter cells were obtained from InvivoGen (Catalog hkb-cd40).

4.7.2 Conjugation of CD40L protein to oligonucleotide

The CD40L dimer protein was reacted via bis-sulfone-DBCO conjugation chemistry to attach the azide-modified ‘anti-handle’ oligonucleotide (IDT) directly to the His-tag region of the protein. The protocol was adapted from prior publications which relied on bis-sulfone-DBCO conjugation for protein-oligonucleotide conjugation[39,201,149,59]. The bis-sulfone-polyethylene glycol 4-dibenzocyclooctyne (bis-sulfone-PEG4-DBCO, Click Chemistry Tools, 1144-25) was diluted to 10mM concentration in DMF, and then further diluted into 1XPBS at a pH of 7.4 to 5mM concentration and incubated for 1-3 hours at room temperature. This ‘activated’ bis-sulfone-PEG4-DBCO was then reacted with the azide-oligonucleotide at 1:1 v/v ratio with the bis-sulfone-PEG4-DBCO at a 20X excess overnight at room temperature. The excess bis-sulfone-PEG4-DBCO was removed by running the sample through a 3K Amicon filter; as a final step of purification, the buffer was exchanged to 1XPBS at pH 6.3. Conjugation was confirmed by measuring the absorbance at 309 nm to confirm DBCO incorporation. Purification was confirmed by running the purified and unpurified oligonucleotide on a Native PAGE at 200V for 60 min, staining with SYBR gold for 10 minutes, and comparing with an oligonucleotide dilution series to confirm that less than 5% of the sample is unconjugated oligonucleotide. After conjugating the oligonucleotide with the bis-sulfone-PEG4-DBCO, the bis-sulfone-oligonucleotide was conjugated with the CD40L protein. The CD40L dimer protein was buffer exchanged to 1XPBS pH 6.3 with Zeba Spin Desalting Column (7K MWCO, 0.5 ml) and then reacted overnight with the bis-sulfone-oligonucleotide at a 20:1 oligonucleotide to protein ratio.

4.7.3 Purification and validation of CD40L-oligonucleotide

The excess bis-sulfone-oligonucleotide in the CD40L protein-oligonucleotide reaction was removed, and the buffer was switched to 1XPBS pH 7.4 using 10K Amicon filtration. The Amicon, coated with 1% Tween initially, was employed for purification by centrifuging the sample at 14,000 × g for

1 min. The concentrate was resuspended in 1× PBS, pH 7.4, and the concentration process was repeated 4–7 times to ensure complete removal of the unconjugated oligonucleotide. Afterward, the column was inverted into a clean eppendorf tube and centrifuged for 2 min at 1000 × g to collect the sample. Confirmation and quantification of the protein-oligonucleotide conjugation were done via a silver stain. Samples were mixed with 4X NuPAGE LDS sample buffer (ThermoFisher; NP0008), incubated at 70°C for 10 minutes, loaded onto 4-12% NuPAGE Bis-Tris gels (ThermoFisher; NP0322), and ran at 150V for 45 minutes. Subsequently, the gel was subjected to silver staining according to the manufacturer's instructions (Pierce, 24612), and imaging was conducted using the Silver Stain setting on Image Gel 6 on Gel Doc EZ Imager (Biorad).

4.7.4 Native PAGE gel electrophoresis

Native PAGE gel electrophoresis was used to confirm that the protein-oligonucleotide product was adequately purified. An Novex Native PAGE 4-20% TBE gel was used (ThermoFisher, EC62252BOX. Samples containing approximately 5 picomoles of DNA were mixed with sucrose loading buffer (6X, made in-house) and water as needed. Subsequently, the samples were loaded onto the gel, which was run in 0.5 X TBE buffer at 200V for approximately 60 minutes at 4°C to minimize band smearing. Afterward, the gel was stained with SYBR Gold for 10 minutes to label the DNA and imaged using a Typhoon or Sapphire Gel Scanner.

4.7.5 HEK-Blue CD40L reporter cell assay

HEK-Blue CD40L reporter cells (Invivogen, #hkb-cd40) were used to confirm that conjugation of the oligonucleotide to the His-tag of the CD40L protein construct did not impede the interaction of CD40L with the CD40 receptor. The cells were cultured and samples were assayed as described by the manufacterer's protocol. 50,000 cells per well (180 μL in volume in media DMEM, 4.5 g/L glucose, 2 mM L-glutamine, 10% FBS, 1%Pen-Strep) were plated on a 96-well plate, along with 20 μL of each sample at the desired concentration. Recombinant human CD40L (Invivogen, rcyec-hcd40l) was used as a positive control, while recombinant IFNγ was used as a negative control. The plate was incubated for 20-24 hours, and 20 μL of supernatant was harvested from each well. The supernatant was added to 180 μL of Quanti-BLUE solution, incubated for 1-3 hours and SEAP levels were determined via spectrophotometer reading at 630 nm.

4.7.6 Fabrication of square block DNA origami nanoparticles

This study relied on the DNA origami square block (SQB), as published in previous lab papers[228,90]. The single-stranded p8634 scaffold DNA (harvested in-house) assembles into the square lattice nanoparticle via the complementary Watson-Crick base pairing of hundreds of short ‘staple’ oligonucleotides (IDT); sequences of all DNA strands are included in the prior publications[228,90]. The SQB folding process was conducted in a thermocycler, undergoing an 18-hour program involving strand denaturation at 80°C for 15 minutes followed by annealing at decreasing temperatures (50°C to 40°C) over specific time intervals. The folding was executed in a specified folding buffer comprising 5mM Tris, 1 mM ethylenediaminetetraacetic acid (EDTA; pH 8.0), 12 mM MgCl2, 20 – 100 nM scaffold, with staple strands in fivefold excess to the scaffold and handle-conjugated staples in tenfold excess for cargo attachment. SQBs were subjected to PEG purification before and after CD40L conjugation, as detailed below.

4.7.7 Conjugation of CD40L protein to DNA origami nanoparticles

The 126 double helices have overhang ‘handle’ strands at specific programmed sites, allowing for patterning of CD40L via ’handle/anti-handle’ Watson and Crick complementary base-pairing. To hybridize the CD40L-conjugated ‘anti-handle’ olignucleotide to the ‘handle’ oligonucleotide extruding from the SQB, the CD40L-conjugated ‘anti-handle” oligonucleotide is added in 2X excess to the SQB sample, while maintaining overall buffer conditions of 1XTE 10 mM MgCl2. The sample is hybridized at 37°C with shaking for 1-2 hours. Agarose gel electrophoresis is used to confirm hybridization. Purification is performed by PEG precipitation as detailed below.

4.7.8 PURIFICATION OF DNA ORIGAMI NANOPARTICLES

PEG purification serves the dual purpose of concentrating the sample and eliminating excess staple strands or cargo-conjugated strands for subsequent use. This purification process was conducted post-fabrication of SQBs and following cargo conjugation. A 15% w/v PEG-8000 (Fisher Scientific, BP2331) buffer, prepared in 1X TE buffer, was utilized for this process. The PEG buffer, along with MgCl2, was mixed with SQBs at a 1:1 volume ratio in a 1.5 mL Eppendorf tube and gently pipetted. The final concentration of MgCl2 in the mixture was adjusted to 10 mM. Following a 30-minute incubation, the solution was centrifuged at 16,000g for 25 minutes, yielding a pellet containing purified SQBs. The SQB pellet was resuspended in an appropriate buffer (1X TE, 10 mM MgCl2) via room temperature shaking, and the final concentration was determined using NanoDrop.

4.7.9 TEM IMAGING

The high-resolution structure and monodispersity of the DNA origami nanoparticles were visualized using negative-stain transmission electron microscopy (TEM). Carbon-coated grids, initially subjected to a 30-second plasma discharge treatment for cleanliness, were utilized for sample preparation. 4.0µL of a 5 nM solution of DNA origami nanoparticles was applied to these grids, followed by a 45-second incubation to allow nanoparticle adsorption, subsequent gentle blotting to remove excess sample, and the addition of 0.75% uranyl formate solution for contrast enhancement. After blotting away excess solution, a 2-minute incubation with a second drop of uranyl formate was performed.

TEM analysis was conducted using a JEOL JEM-1400 TEM operating at 120 kV in brightfield mode.

4.7.10 Agarose gel electrophoresis

DNA origami samples underwent analysis using 2% native agarose gel electrophoresis prepared in 0.5X TBE solution containing 11mM $MgCl_2$ and 0.005% v/v SYBR safe dye. The electrophoresis was conducted at 70V for 2 hours, and the agarose gels were imaged using a Typhoon or Sapphire Gel Scanner.

4.7.11 Dynamic light scattering

Dynamic light scattering with a Malvern Zetasizer Nano ZS was employed to measure size alterations and particle uniformity post-CD40L conjugation. Approximately 40 µL of a 5 nM SQB solution was dispensed into a clean microcuvette (Malvern Panalytical, ZEN0040) to ensure minimal air bubbles and wiped to remove fingerprints. The cuvette was analyzed in the Zetasizer, obtaining size distribution data per the manufacturer's guidelines, with three replicates for each sample. The resulting data was depicted in a size versus intensity plot.

4.7.12 Confirmation of CD40L protein conjugation on the DNA origami nanoparticle

To confirm CD40L protein conjugation onto the DNA origami nanoparticles, a DNase digestion assay was conducted, degrading the DNA component while preserving the proteins. CD40L-conjugated SQBs were incubated with DNase I (NEB) enzyme and a 10× DNase I buffer (Gibco) at 37°C for 30 minutes, targeting the degradation of DNA molecules specifically. After the DNase digestion, the sample was mixed with 4X NuPAGE LDS sample buffer (ThermoFisher; #NP0008) and incubated at 70°C for 10 minutes in the thermocycler to denature the proteins and inactivate DNase I. Subsequently, the denatured protein sample underwent electrophoresis on 4-12% NuPAGE Bis-Tris gels (ThermoFisher; #NP0322) using 1X MES SDS running buffer (ThermoFisher; #NP0002) at 150V for 45 minutes. Visualization of DNA-conjugated proteins was achieved via silver staining (Pierce, #24612), enabling detection based on silver-binding properties. Gel images were obtained using the Silver Stain setting on an Image Lab 6 system with a Gel Doc EZ Imager (Bio-Rad). Band intensities were compared to a CD40L protein control dilution series to estimate the number of CD40L complexes conjugated per DNA origami nanoparticle.

4.7.13 MOLECULAR DYNAMICS SIMULATIONS

Molecular dynamics simulations were performed by Matthew Sample and Petr Sulc at Arizona State University, relying on a protein-DNA anisotropic network model (ANM) which was implemented in oxDNA (https://oxdna.org/). We relied on the a CD40L protein dimer, adapted from the protein data bank (PDB: 3QD6). Even though this is not the exact protein used in our structures, the structure and corresponding behavior of the modeled protein should be similar to the protein used experimentally. The modeled protein is the human CD40L protein trimer, which was modified to a dimer in PyMol by deleting one of the monomers. In contrast, the protein used experimentally is a murine dimeric CD40L protein, with a single stalk. Notably, murine and human CD40L share 78% of their sequence and have a highly similar structure[184], suggesting that this was an appropriate choice for our preliminary models. The linker was also modeled as a malemide-SMCC linker which is slightly smaller than the bis-sulfone-PEG4-DBCO linker used in our experimental set-up, but is not expected to change the conclusions made from these simulations.

5

Conclusion

In the past decade, DNA nanotechnology has proven that it offers several distinct advantages for therapeutics. To our knowledge, DNA origami is one of the only nanoparticle systems that can precisely tune the nanoscale arrangement of cargo. This nanoscale arrangement is particularly relevant in biological systems, where nanoscale structural arrangements can have a dramatic effect on downstream cellular signaling pathways and ultimately cellular function. Studies, including those detailed in this thesis, show that DNA origami is highly programmable and offers precise control over the nanoscale arrangement of cargo. Furthermore, this thesis and other studies demonstrate how arrangement of cargo at the nanoscale affects subsequent physiological responses, suggesting that nanoscale arrangement is another parameter which can be tuned to create the optimal therapeutic. These investigations would be unattainable, without the nanoscale precision provided by DNA origami.

This thesis highlights how the nanoscale arrangement of specific ligands, namely CpG, changes the subsequent immune response in the context of both cancer and various infectious diseases. A later chapter details another receptor-ligand pair, CD40-CD40L, which we believe could also be differentially activated based on the nanoscale arrangement of CD40L; however, this study was ultimately hindered by challenges in the functional hybridization of the protein to the DNA origami nanoparticle. Many other therapeutic cargo could be conjugated onto the DNA origami nanoparticle for future therapeutic applications. Additionally, beyond DNA origami's application as a therapeutic, DNA origami also serves as a robust tool to study nanoscale receptor-ligand arrangements in biological systems. If future studies apply this tool to various different receptor-ligand pairs, we expect to learn the key parameters (cargo quantity, stoichiometry, nanoscale arrangement, among others) that affect biological responses. These types of receptor-ligand studies may inform the design of more precise therapeutics.

The work outlined in this thesis is one step in the development of DNA origami technology for therapeutic applications. In Chapter 2, we describe the pre-clinical validation of the CpG-conjugated DNA origami nanoparticle in various in vitro and in vivo cancer studies. In Chapter 3, we demonstrated the applicability of the DNA origami nanoparticle in other disease area, namely infectious diseases. Relying on the CpG adjuvant in the same nanoscale arrangement that was uncovered to be optimal in Chapter 2, we repurpose the nanoparticle and characterize the immune cell responses, highlighting that the DNA origami nanoparticle induces robust humoral and cellular immune responses. In Chapter 4, we detail the fabrication of CD40L-conjugated DNA origami nanoparticles as a potential adjuvant. Even though we were not able to determine an optimal spatial arrangement for CD40L as we did for CpG in Chapter 2, we were able to describe fabrication of CD40L-conjugated DNA origami nanoparticles, as well as simulate the nanoparticles behavior in physiological conditions, giving us a better understanding of the rigidity of the programmed spatial arrangement. Additionally, we still believe that CD40L is a promising molecule for future study with DNA origami technology, as the multimerization of CD40 is uniquely suited for investigation with DNA nanotechnology.

In the near term, we hope that many more studies will validate the importance of nanoscale arrangement of cargo for various receptor-ligand pairs. The DNA origami square block detailed in this thesis shows great versatility as a molecular pegboard for attachment of many different types of cargo. For instance, future studies may investigate peptide, protein, and RNA conjugation onto a DNA origami scaffold for various diseases, including cancer, infectious diseases, autoimmune diseases and more. Relying on Watson and Crick base-pairing chemisty, theoretically any type of cargo can be conjugated onto the DNA origami scaffold, as long as a complementary oligonucleotide can be stably attached to the cargo.

In the long-term, we envision a future where medicines are precisely designed and every parameter is tuned for an optimal, personalized therapeutic response. DNA origami is one tool to uncover the precise parameters for optimal therapeutics. DNA origami also serves as a viable scaffold for personalized therapeutics, including neoantigen-directed cancer vaccines, as the particle is highly modular. Finally, DNA origami also has the unique ability to react to biological stimuli, whether by changing shape in response to a pH change or by templating biomolecule assembly as a nanofactory. Even though DNA origami as a 'molecular robot' has only been demonstrated in proof-of-concept studies, we can envision a future of 'living medicine' where therapeutics can be programmed to react and perform functions inside a patient.

Even though we have not yet seen clinical translation of DNA nanotechnology, the pre-clinical studies suggest that clinical translation is a possibility for the future. We recognize that DNA origami will face some challenges in clinical translation. The square block nanoparticle design presented in these studies relies on M13 p8634 phage DNA, which would have to be validated to be safe in humans. Additionally, the current protocol for manufacturing of the DNA origami particles is achievable on the bench-scale, but may need refinement in order to scale up. Finally, DNA origami is costly; however, the cost of DNA synthesis is decreasing every year and the length of strands that can be synthesized is increasing every year, suggesting that DNA origami may be a viable therapeutic option, especially for personalized medicine delivery. Even if DNA origami does not achieve clinical translation, DNA origami studies like these uncover critical principles of therapeutic design, which are relevant to all nanoparticle platforms, regardless of the clinical translation of DNA origami itself. Furthermore, we believe that some of the principles of DNA origami could be applied to create RNA or even protein-based 'origami-type' structures in the future, as we understand more about the rules of RNA and protein folding.

In summary, this thesis demonstrates the potential of highly programmable DNA origami therapeutics in various disease areas and facilitate the clinical validation of DNA origami-based therapeutics.

A

Supplementary material for Chapter 2

Supplementary Materials for

Title: Fine tuning of CpG spatial distribution with DNA origami for improved therapeutic cancer vaccination

Authors: Yang C. Zeng[1,3,4], Olivia J. Young[1,3,4,7], Chris M. Wintersinger[1,4], Frances M. Anastassacos[3,4], James I. MacDonald[3], Giorgia Isinelli[3,8], Maxence O. Dellacherie[5], Miguel Sobral[5], Haiqing Bai[3], Amanda R. Graveline[3], Andyna Vernet[3], Melinda Sanchez[3], Kathleen Mulligan[1], Youngjin Choi[2], Thomas C. Ferrante[3], Geoffrey G. Fell[9], Donna Neuberg[9], Catherine J. Wu[6], David J. Mooney[3,5], Ick Chan Kwon[1,2,10], Ju Hee Ryu[1,2]*, William M. Shih[1,3,4]*

Affiliations:

[1] Department of Cancer Biology, Dana-Farber Cancer Institute, Harvard Medical School, Boston, Massachusetts 02115, USA

[2] Wyss Institute for Biologically Inspired Engineering at Harvard University, Boston, Massachusetts 02115, USA

[3] Department of Biological Chemistry and Molecular Pharmacology, Harvard Medical School, Boston, Massachusetts 02115, USA

[4] Harvard-Massachusetts Institute of Technology (MIT) Division of Health Sciences and Technology, Massachusetts Institute of Technology, Cambridge, Massachusetts 02139, USA

[5] Department of Drug and Health Sciences, University of Catania, Catania, Italy

[6] Harvard John A. Paulson School of Engineering and Applied Sciences, Harvard University, Cambridge, Massachusetts 02138, USA

[7] Center for Theragnosis, Biomedical Research Institute, Korea Institute of Science and Technology (KIST), Seoul 02792, Republic of Korea

[8] Department of Medical Oncology, Dana-Farber Cancer Institute, Boston, Massachusetts 02115, USA

[9] Department of Data Science, Dana-Farber Cancer Institute, Boston, Massachusetts 02115, USA

[10] KU-KIST Graduate School of Converging Science and Technology, Korea University, Seoul 02841, Republic of Korea.

Correspondence to: william_shih@dfci.harvard.edu; jhryu@kist.re.kr

This PDF file includes:

Supplementary Figures 1–34
Supplementary Tables 1–6
Supplementary Discussion
Supplementary Methods

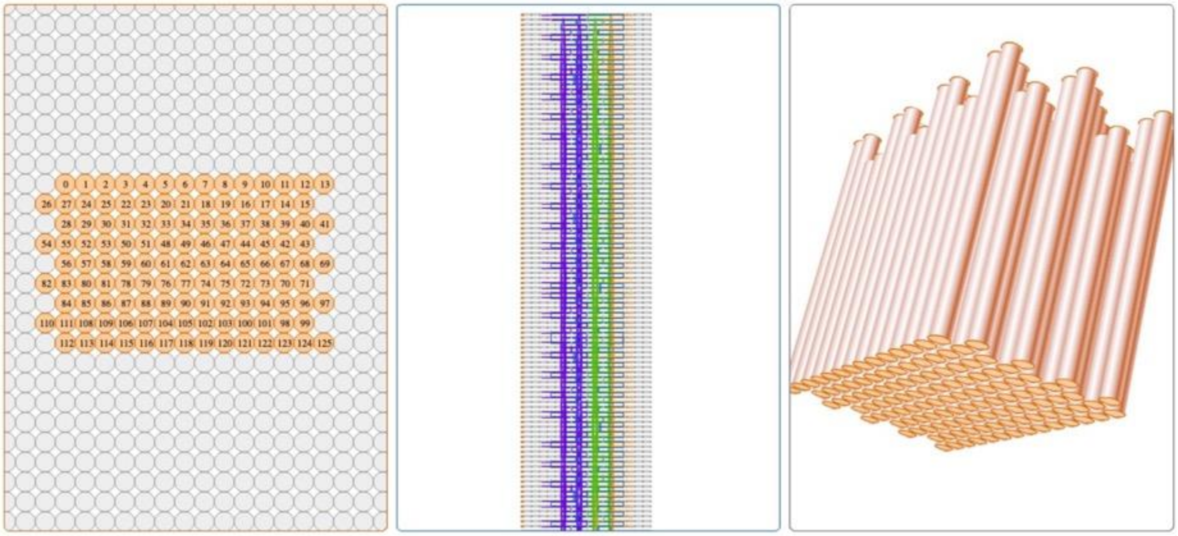

Supplementary Figure 1. CaDNAnoSQ SQB design. This is a screen shot of the basic SQB design. The structure was designed using CaDNAnoSQ and Python software. The scaffold is p8634, whose corresponding DNA sequence is presented at Supplementary Table 1.

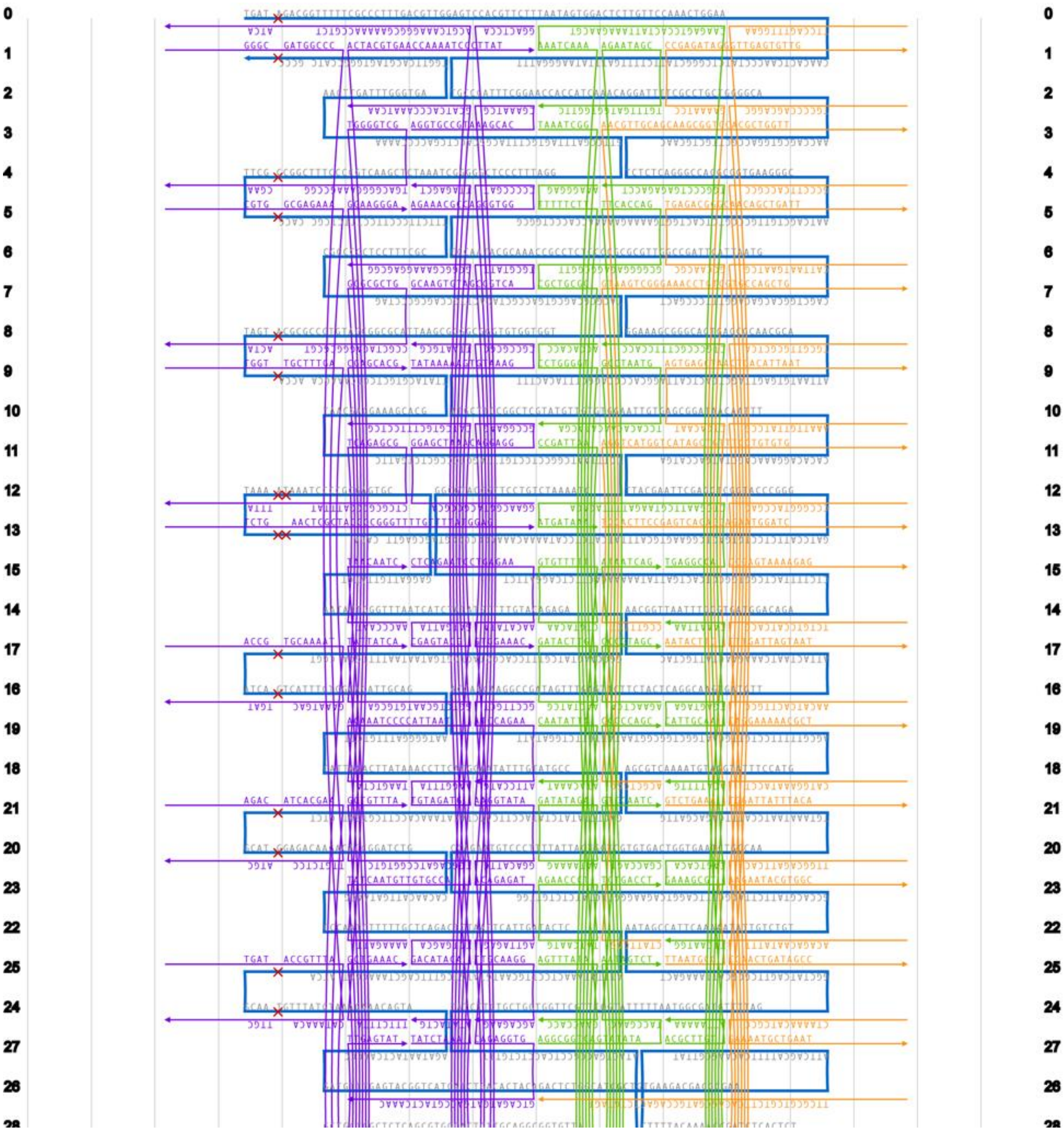
0
1
2
3
4
5
6
7
8
9
10
11
12
13
15
14
17
16
19
18
21
20
23
22
25
24
27
26
28

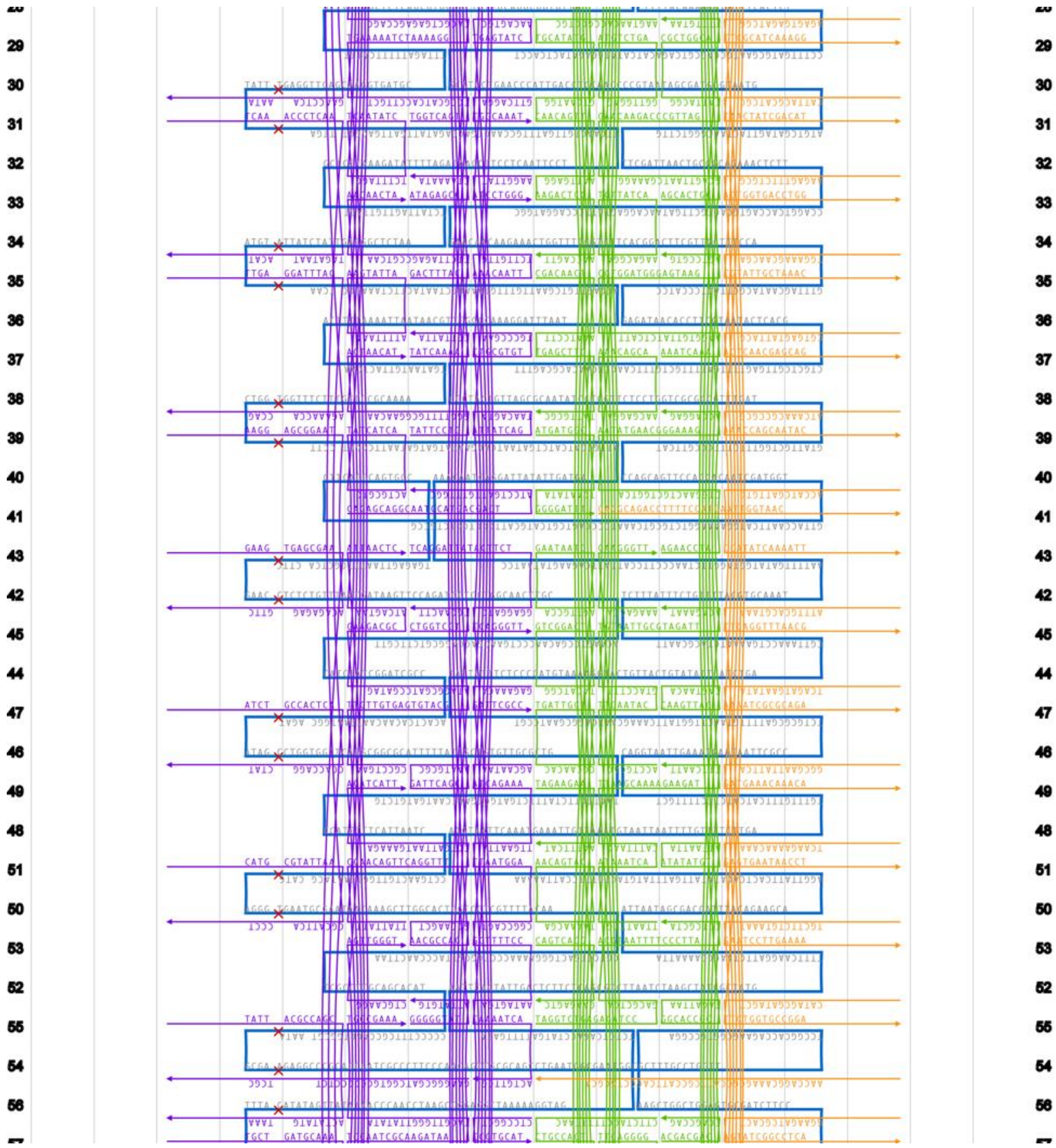
29
30
31
32
33
34
35
36
37
38
39
40
41
43
42
45
44
47
46
49
48
51
50
53
52
55
54
56

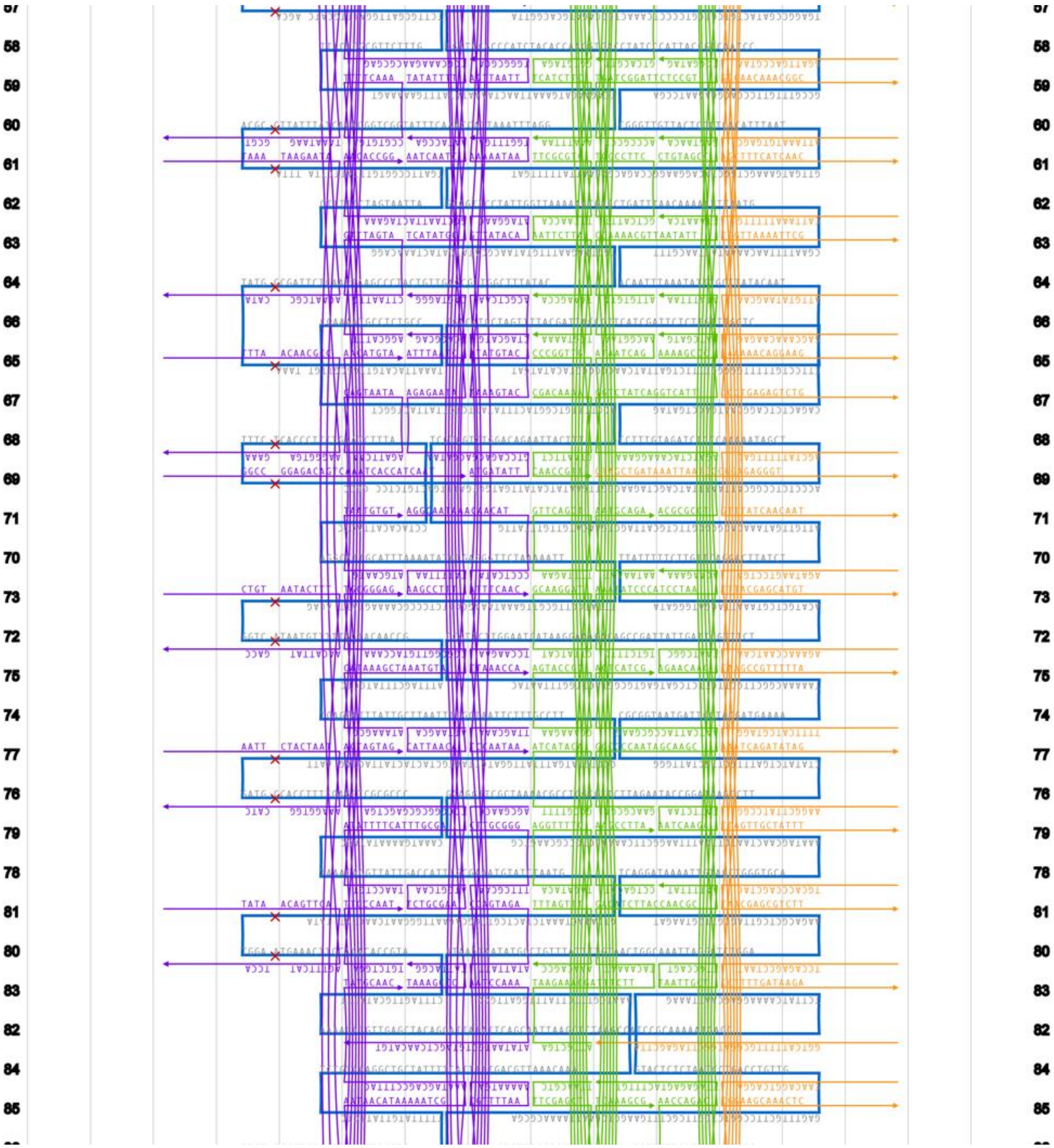
57
58
59
60
61
62
63
64
66
65
67
68
69
71
70
73
72
75
74
77
76
79
78
81
80
83
82
84
85

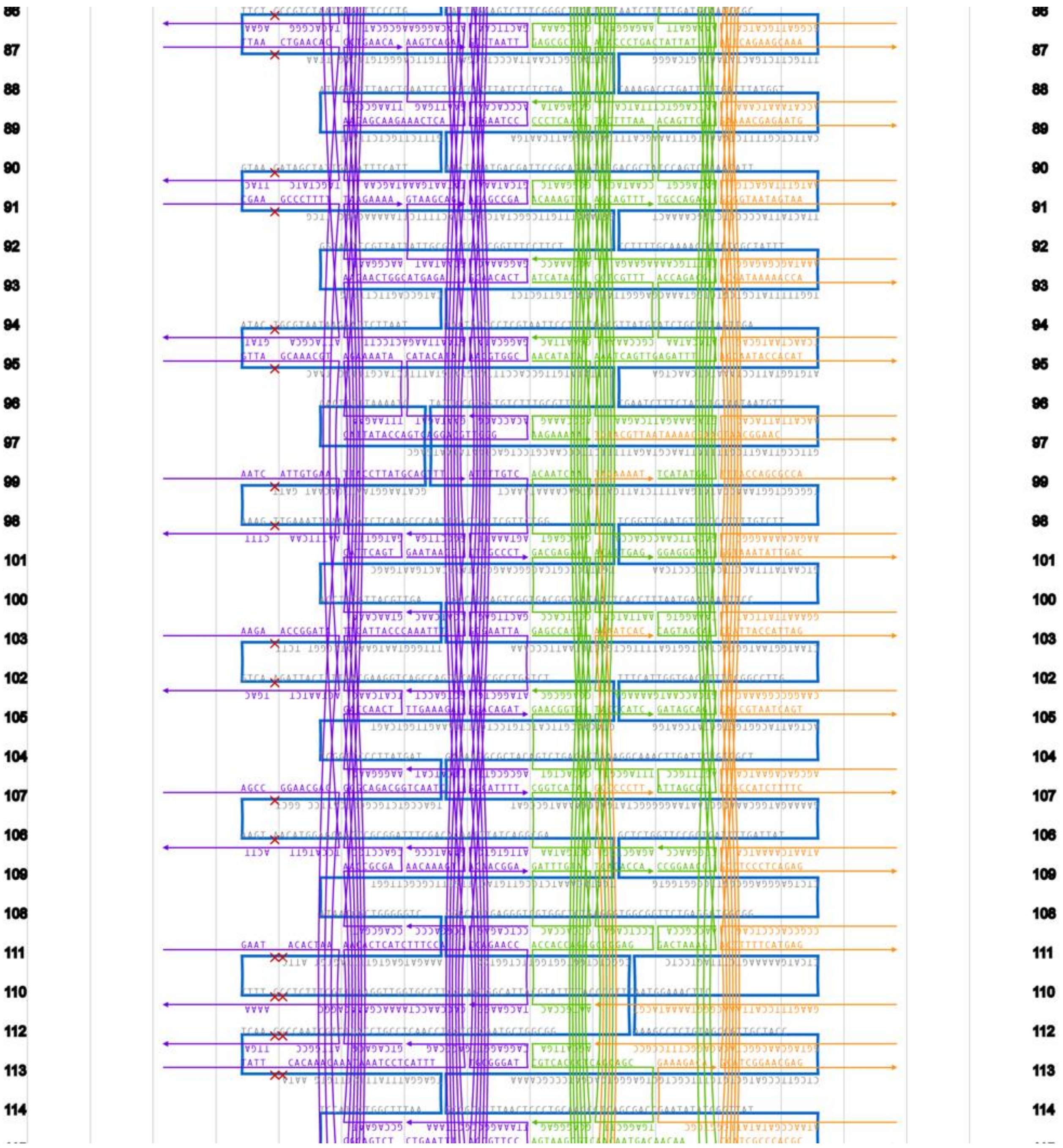
86
87
88
89
90
91
92
93
94
95
96
97
99
98
101
100
103
102
105
104
107
106
109
108
111
110
112
113
114

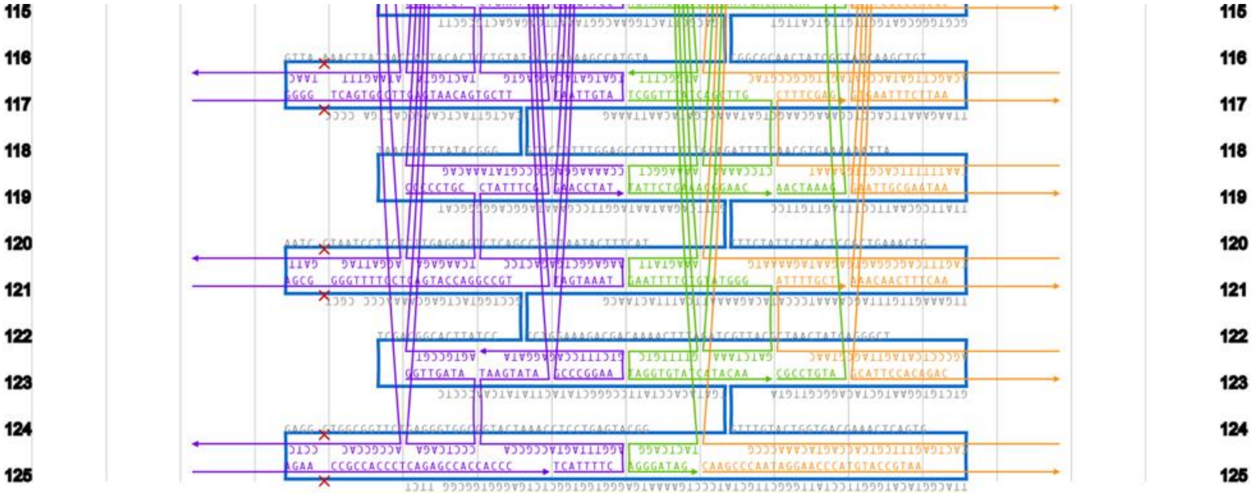

Supplementary Figure 2. Routing strategy of SQB as displayed on the CaDNAnoSQ interface.

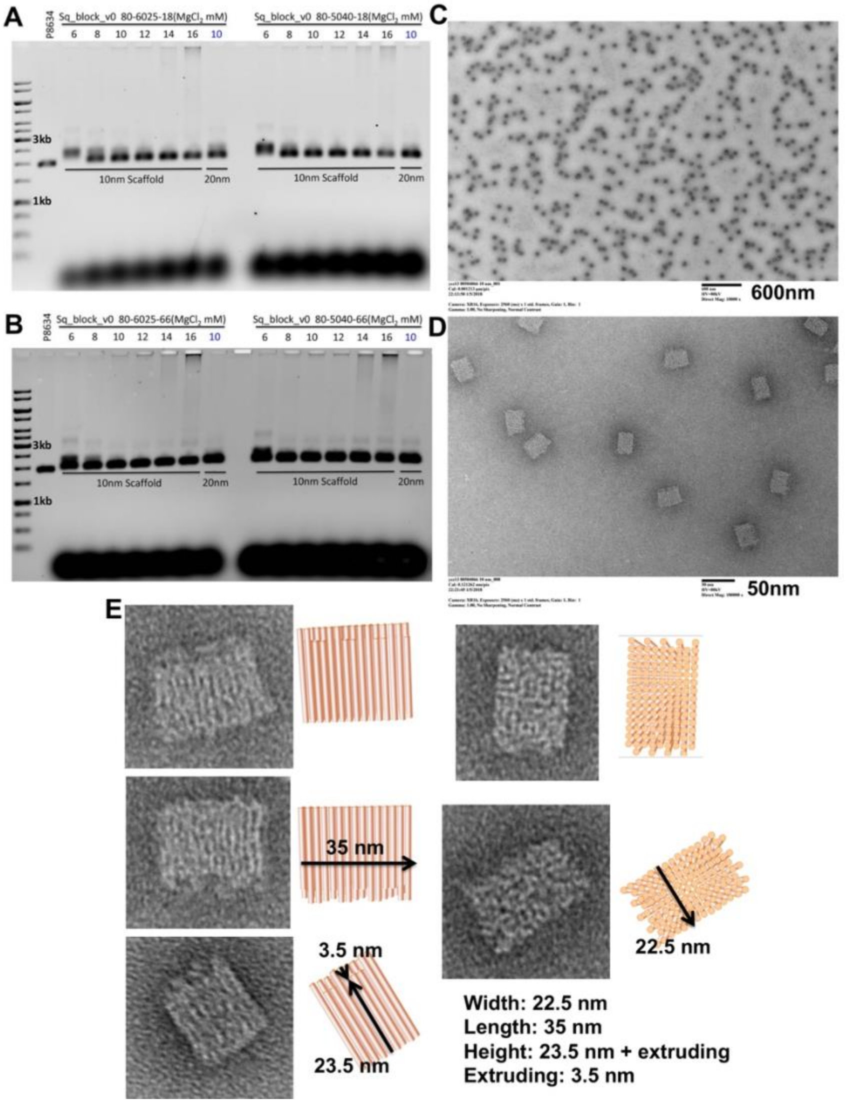

Supplementary Figure 3. SQB folding optimization. (**A, B**) The SQBs were annealed under various temperature ramps, time courses and $MgCl_2$ concentrations. Time course for **(A)** 18 hours, **(B)** 66 hours and temperature condition is left panel (temperature ramp from 60 to 25°C), right panel (50 to 40°C). $MgCl_2$ concentration are denoted at the top of agarose gel images. The optimal condition was determined as the condition which produced a high folding efficiency and minimal aggregation of the resulting SQB. The optimal temperature ramp conditions were determined to be: 80°C for 15 minutes, and then a declining temperature ramp starting at 50°C and declining to 40°C with -0.1°C every 10 minutes and 48 seconds. The optimal time course was 18 hours and the optimal $MgCl_2$ concentration was 12 mM. (**C, D**) TEM images of the optimally folded SQBs. (**C**) There is no obvious SQB aggregation. (**D**) A higher magnification image showing the SQB structure. (**E**) The high magnification images of a single SQB and the precise dimensions.

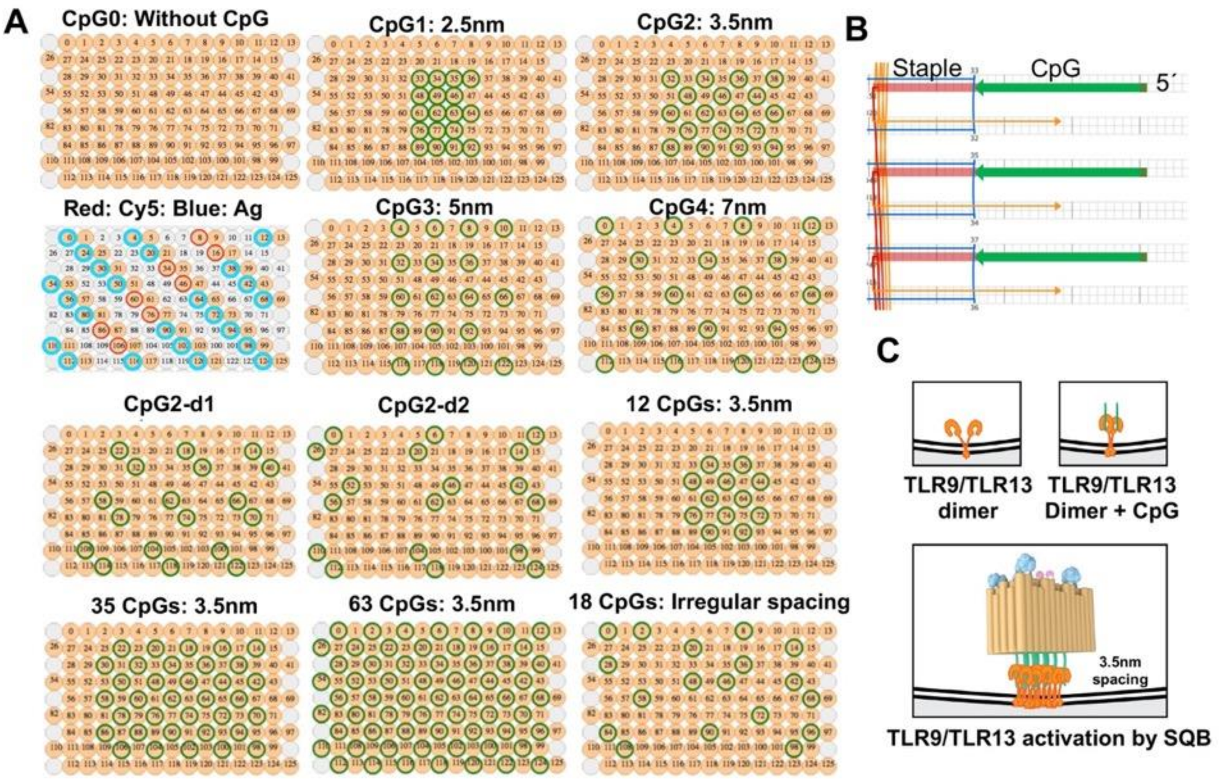

Supplementary Figure 4. CpG spatial distribution on the flat face of the SQB. (**A**) These figures show the Cy5 dye, antigen (Ag) and CpG positions on DNA origami. CpG is conjugated on the end of the double helices on the flat face of the SQB and Cy5 and antigen are conjugated on the opposite site of CpG face which has extruding helices. The CpG strands was fabricated as an extension of the staple strands at desired positions. The 126 helices are labeled between 0 and 125. The sequences of the CpG staples and positions are found in Supplementary Table 3. DNA origami without CpG conjugation is denoted as CpG0. DNA origami labeled as CpG1, 2, 3, 4 has eighteen CpG strands with various spacing distance 2.5, 3.5, 5, 7 nm, respectively. CpG2-d1 and CpG2-d2 has wider spacing for CpG dimers (dimer CpG spaced at 3.5 nm). Finally, DNA origamis with different number of CpG strands (12, 18, 35, 63) are denoted as 12 CpGs, 18 CpGs (same as CpG2), 35 CpGs and 63 CpGs, respectively. 18 CpGs with random position of CpG strands is denoted as 18 CpGs with irregular spacing (CpGi). (**B**) A schematic figure from CaDNAno file showing CpG attachment from CpG2 on the end of double helices of No. 32, 34 and 36. All the CpGs fabricated are single stranded, the CpGs are added during phosphoramidite synthesis of the staple strands by the vendor (IDT), or else added via splint-templated ligation. (**C**) Proposed model of CpG and TLR9/TLR13 interaction that induces Th1 polarization when CpG is spaced at 3.5 nm.

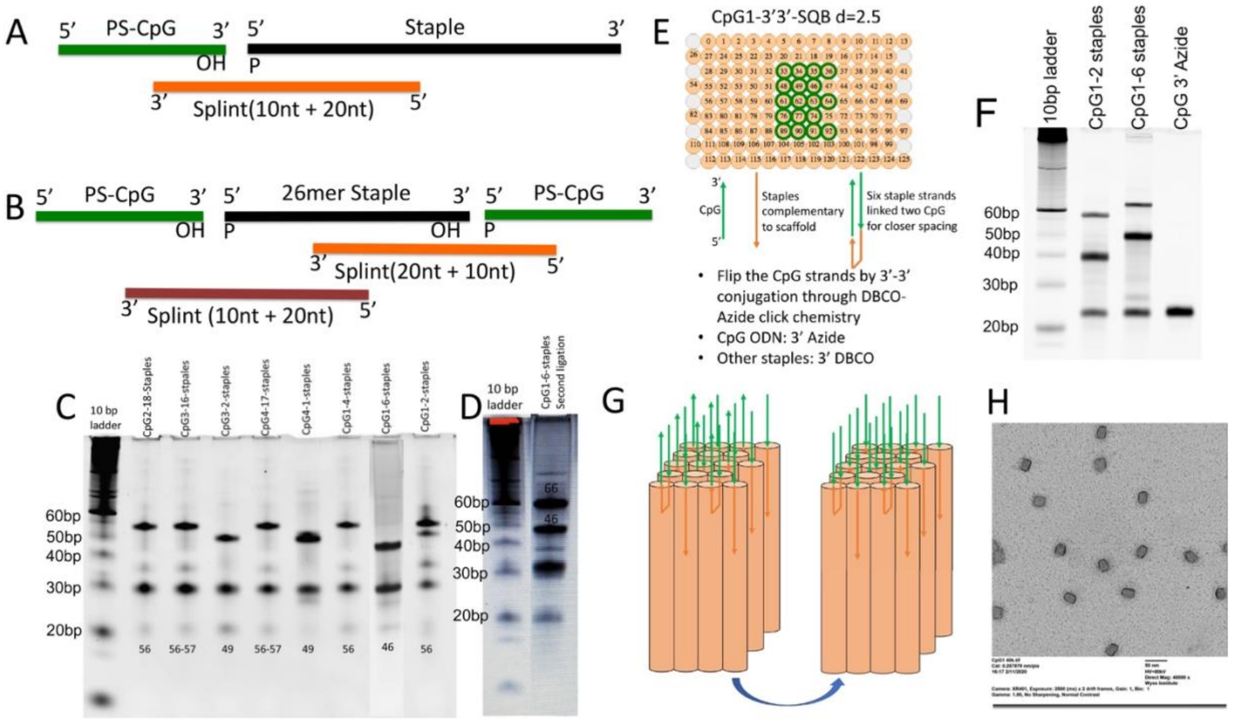

Supplementary Figure 5. CpG ligation. Most experiments in this study relied on commercially produced CpG-containing strands. We also self-assembled the CpG strands by ligating the CpG with original staples, and purifying the ligated staples via denatured PAGE gel. This technique is a viable option to minimize the costs associated with CpG-SQB fabrication. (**A**) Ligation strategy for all CpG patterns except for CpG1. The CpG has a 5´ end extruding from the origami. (**B**) Ligation strategy for CpG1 (2.5nm) where some of the staples linked CpG on both 5´ and 3´ end. (**C**) PAGE gel demonstrating the ligation results. The top band is the ligated full-length product. The second faint band is the unreacted original staples without poly Ts. The third bright band is all the splint DNA after denaturation. The faint forth band is the excess of CpG strand. (**D**) PAGE gel corresponding to the alternative ligation strategy for CpG1 with a CpG linked to both the 5´ and 3´ staple ends. (**E**) The ligation method described in (B) cannot generate uniform orientation of CpG and obtain the dense CpG patterned associated with CpG1. To this end, we applied DBCO-azide click chemistry to ligate 3´ and 3´ ends of staples and CpG strands to ensure all CpG strands have the same orientation, with the 5´ ends extruding from the SQB. The associated staples were modified with DBCO on their 3´ ends, and CpGs were modified with Azide on their 3´ ends. We also investigated a variant CpG2L (i.e. 3.5 nm spacing) with the 3´-3´ DBCO-azide linkage for all eighteen CpG extensions, and found the ability of these nanoparticles to induce Th1 polarization was diminished compared to the CpG2. Therefore we cannot conclude that the effects observed on dendritic cells between CpG1 and CpG2 are due solely to differences in spacing. (**F**) Denaturing PAGE gel result showing the successful conjugated strands (upper band). (**G**) A schematic demonstrating the alternative fabrication strategy that results in uniform CpG orientation for CpG1. Green arrows indicate CpG strands, head is the 3´ end and tail is the 5´ end. After ligation strategy with click chemistry, CpG strands have uniform orientation. (**H**) TEM imaging of CpG1-SQB, demonstrating monodispersed SQBs.

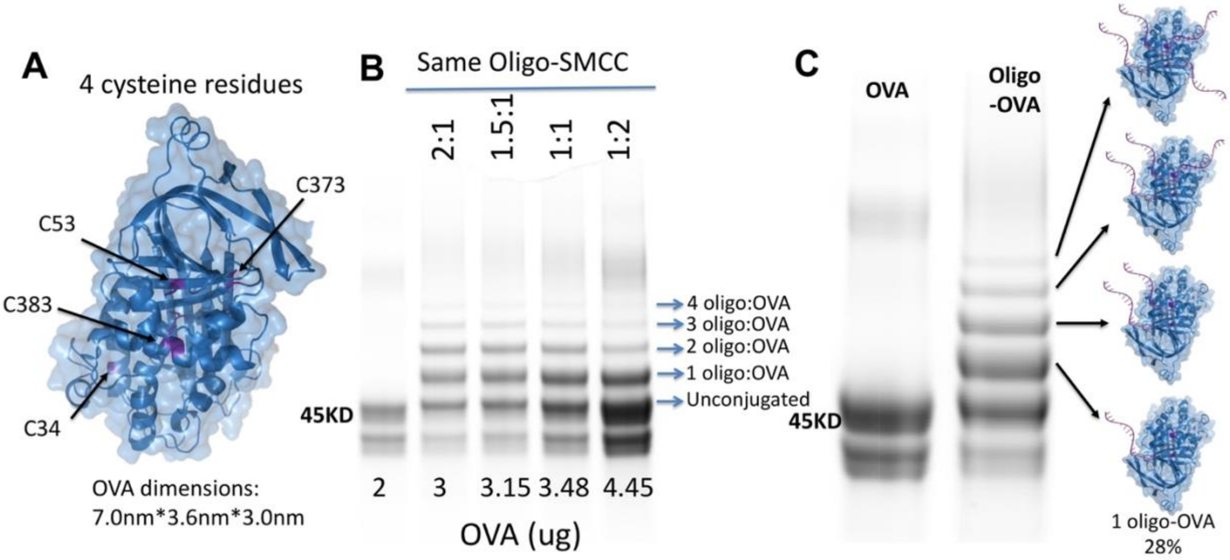

Supplementary Figure 6. Ovalbumin (OVA) conjugation optimization. There are 4 cysteine residues on the whole protein ovalbumin which could be conjugated to DNA oligonucleotides via an SMCC linkage reaction. Our aim was to generate a majority of the OVA product with a single oligonucleotide attached (1 oligo-OVA) for SQB appending. (**A**) The 3D structure of OVA protein. Cysteine residues, which can be linked with SMCC and subsequently conjugated to a DNA oligonucleotide, are labeled. (**B**) Oligo-SMCC and OVA were reacted at various ratios. The SDS PAGE gel showed the unconjugated OVA protein (first lane) or OVA conjugated with 1~4 oligos. (**C**) SDS PAGE gel of the OVA-oligo reaction products. A 1:1 molar ratio of OVA to oligo-SMCC increased the yield of the singly appended 1 oligo-OVA protein compared to more conjugated forms of the OVA and unconjugated OVA. The 1 OVA-oligo product had a yield of around 25–28% and was the dominant SMCC reaction product under the optimized conditions.

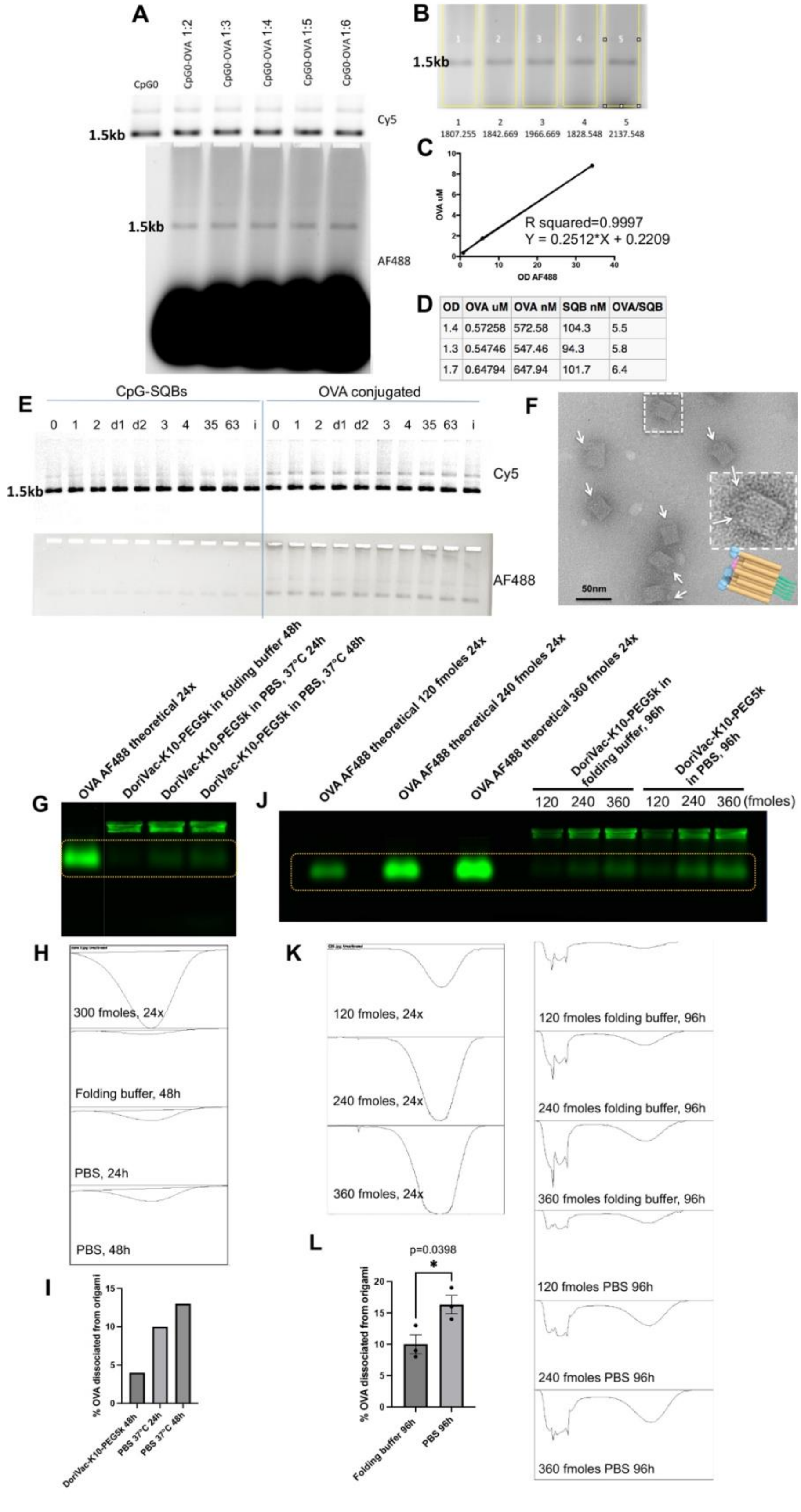

OD	OVA uM	OVA nM	SQB nM	OVA/SQB
1.4	0.57258	572.58	104.3	5.5
1.3	0.54746	547.46	94.3	5.8
1.7	0.64794	647.94	101.7	6.4

Supplementary Figure 7. OVA conjugation, purification, and concentration verification. The OVA-oligo conjugate was mixed with purified CpG-SQB directly and incubated for 2 hours at 37°C. (**A, B**) Various concentrations of OVA-oligo were mixed with the SQB to determine the appropriate amount to ensure complete hybridization. The Alexa Fluor 488 (AF488) fluorescent intensity was quantified via ImageJ and the appropriate amount of OVA-oligo for optimal conjugation was determined to be three times in excess of SQB multiplied by five times due to the yield of 1 OVA-oligo. (**C**) The AF488 intensity correlates with the number of conjugated OVA. We quantified the AF488 intensity to determine the average amount of OVA conjugated to the SQB. (**D**) We performed three different conjugation experiments of OVA to SQB and calculated independently the amount of OVA conjugated to the SQB. Due to the size constraints of the OVA protein, the average of these three trials showed that 6 OVA proteins can be appropriately conjugated to the SQB, while we were able increase this number to 12 OVA proteins in later experiment by improving the purity of the OVA-oligo. (**E**) All constructs showed AF488 signal after conjugation with OVA. CpG conjugated without OVA does not show strong AF488 signal (left panel). OVA conjugation correlates with increased AF488 signal (right panel). (d1 and d2 refer to CpG2-d1 and CpG2-d2, 35 and 63 refer to 35 and 63 CpG strands were conjugated onto SQB at spacing of 3.5 nm) (**F**) TEM images of conjugated CpG2-OVA-SQBs as the complete DoriVac vaccine. The arrows delineate the OVA protein. (**G-I**) To assess the handle/anti-handle stability, we conducted a PBS incubation experiment on OVA-conjugated DoriVac. The DoriVac was initially coated with K10-PEG5k and subsequently diluted 50 times (volume dilution) in PBS buffer. We evaluated the OVA conjugation using agarose gel analysis. Over the course of incubating the DoriVac at 37 ℃, we observed a minor release of OVA from the origami structure. To quantify the amount of OVA protein dissociated from the origami, we utilized Image J to measure the fluorescent intensity of AF488 conjugated on OVA. (**H**) This intensity measurement of OVA in the agarose gel allowed us to compare it with the theoretical intensity of 24 OVA molecules (n=1 gel image from G analyzed). (**I**) It is important to note that the K10-PEG5k coating neutralizes the charge of DNA origami, enabling them to remain in the well. As a result, the fluorescence detected in the well indicates the presence of OVA that remains conjugated to the DNA origami. (**J–L**) To further investigate, we conducted a comparison between the sample incubated in PBS for 4 days and that incubated in folding buffer. For a more precise analysis of OVA dissociation, we utilized a series of sample dilutions during gel examination. Our findings revealed that OVA dissociation occurs more rapidly in PBS than in the folding buffer through image J fluorescence intensity analysis (n=3 gel lanes analyzed from J, corresponding to three different concentrations of origami). These results underscore the importance of enhancing the preservation method for DNA origami after conjugation with cargos, especially for long-term storage, to ensure successful clinical translation. Data are presented as mean values +/- SEM. Two-tailed student's t-test was applied for statistical analysis of graph L. '*' refers to $P \leq 0.05$.

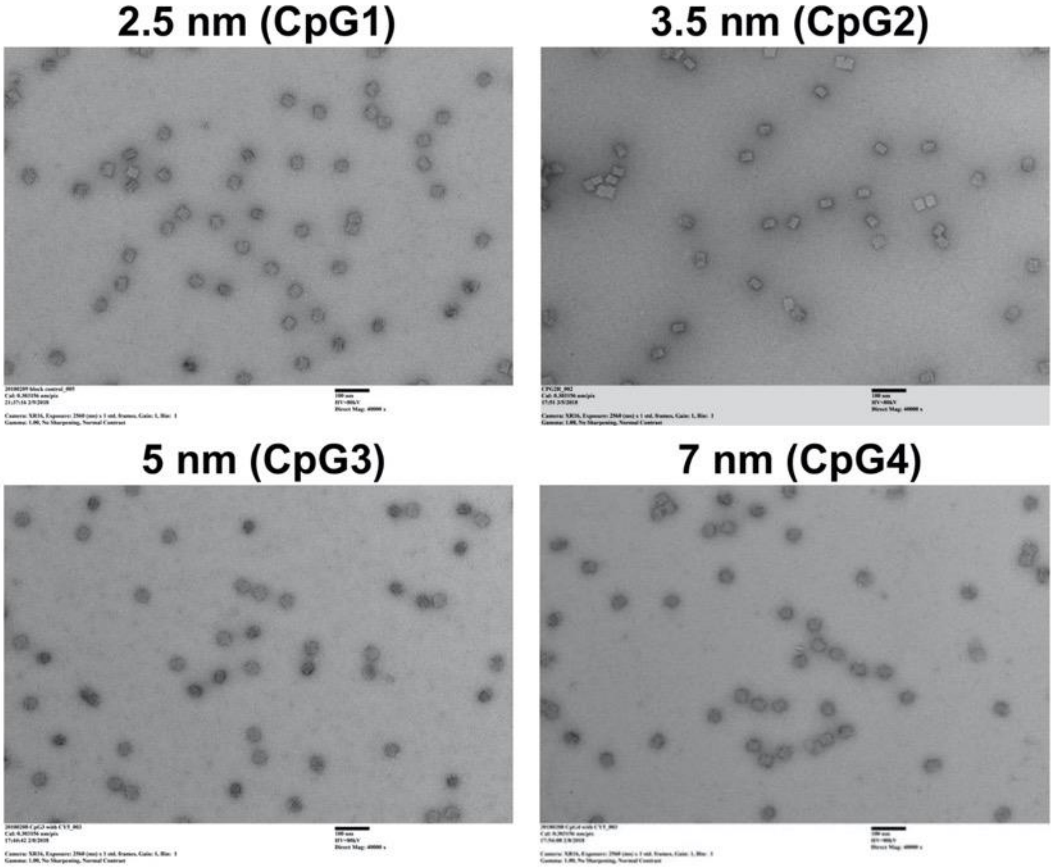

Supplementary Figure 8. Folding of CpG-SQB constructs with varied CpG spacing. TEM images of CpG1 to CpG4.

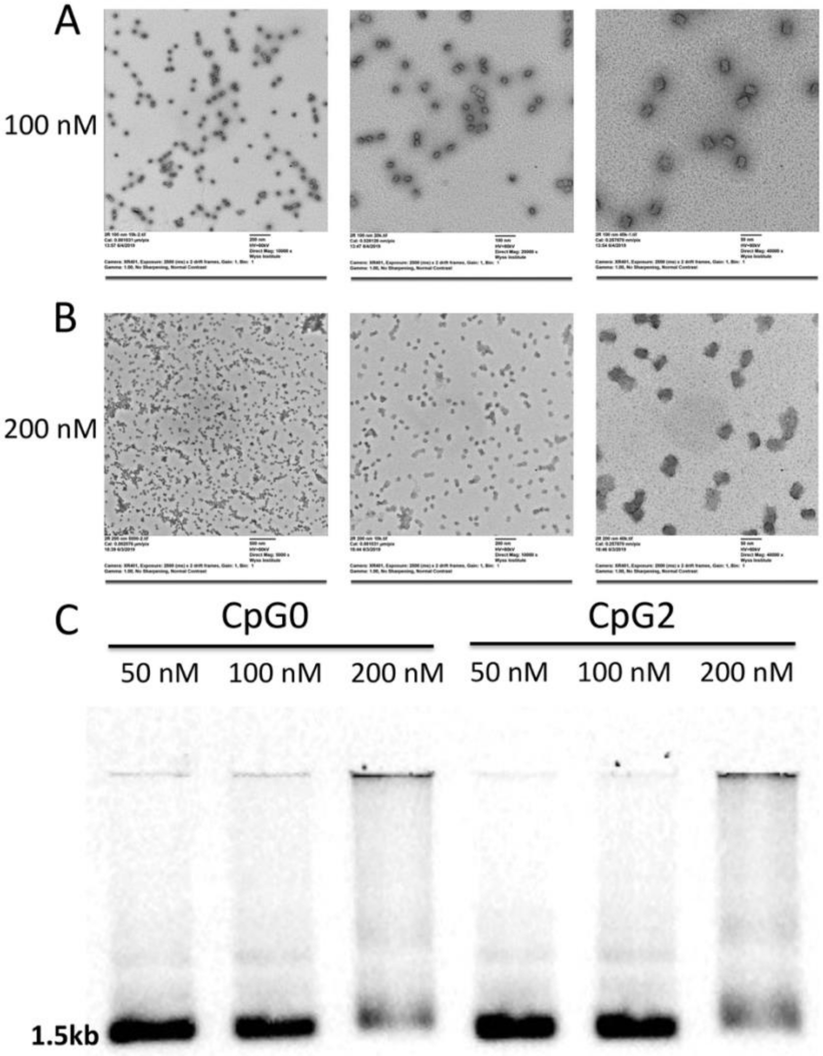

Supplementary Figure 9. Folding of CpG-SQB with higher concentration for *in vivo* application. We increased the scaffold concentration for CpG-SQB folding to as high as 100 nM scaffold concentration without jeopardizing structure integrity. For optimal folding, The scaffold was cultured with 5 times excess basic staple strands and 10-20 times excess of the functional staple strands for linking cargos. (**A, B**) TEM images of SQBs folded with 100 or 200 nM concentration of scaffold. (**C**) The agarose gel result of SQBs folded at different scaffold concentrations. 100 nM is the highest scaffold concentration that maintains structural integrity. At 200 nM scaffold concentration, the folding quality appears to be lower than for 100 nM.

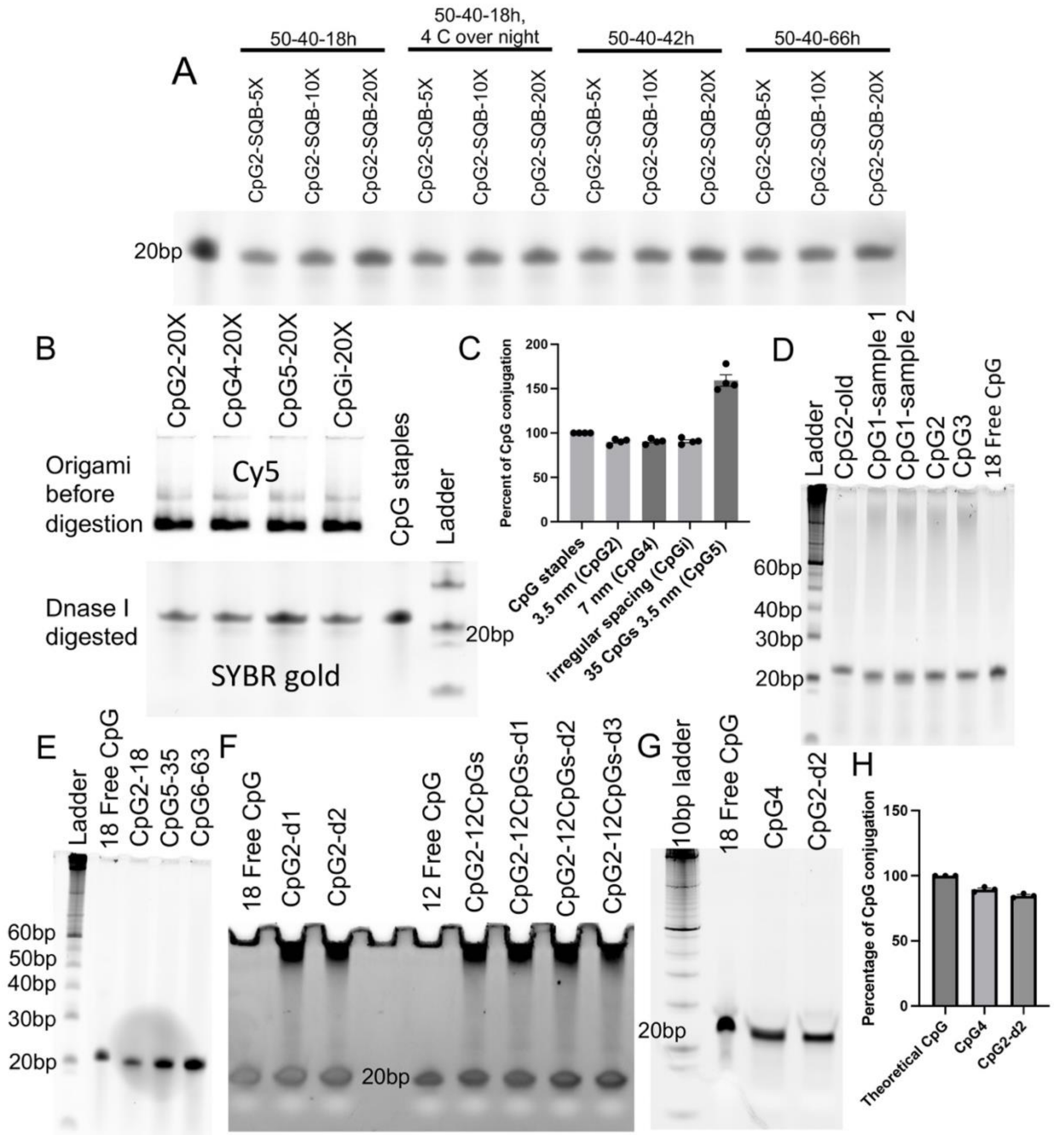

Supplementary Figure 10. CpG loading efficiency. This experiment verified the experimental number of CpG strands loaded onto the SQB DNA origami. We attempted various amounts of excess CpG-containing staple strands and verified 20 times in excess of the theoretical limit of CpG-containing staple strands could achieve ~90% loading efficiency. (**A**) The SQBs were digested by DNase I, which degrades the SQB, but not the associated CpG. CpG has a PS backbone that is not targeted by DNase. Various temperature ramps, annealing times and different amounts of excess CpG-containing staple strands were tested. After DNase I digestion, the solution was analyzed via denaturing PAGE gel at 250 V for 40 minutes. (**B**) Upper: agarose gel of various CpG-SQB constructs before DNase I digestion, denaturing PAGE gel of various CpG-SQB constrsucts after DNase I digestion. The four lanes correspond to four different constructs: CpG-SQB folded with various CpG spacings (CpG2: 3.5 nm, 18 CpGs; CpG4: 7 nm, 18 CpGs; CpGi: irregular spacing, 18 CpGs) and various amounts of CpG per SQB (CpG5: 35 CpG, 3.5 nm). The agarose gel band corresponds to the dye on SQB (upper). The corresponding denaturing gel was stained with SYBR gold (lower). (**C**) The band intensity was calculated by ImageJ and compared to the band intensity corresponding to the theoretical amount of conjugated CpG. 100% loading efficiency indicates that all 18 possible CpG sites were conjugated. "150% loading efficiency" in this case indicates that 27 CpG were successfully conjugated for a CpG-SQB design that has 35 possible CpG conjugation sites (indicating approximately 80% actual loading efficiency), n=4 ImageJ samplings from the single gel image in B. (**D–F**) Denaturing PAGE gel results of CpG loading efficiency comparing more samples corresponding to the CpG designs shown in Supplementary Figure 4 and Supplementary Figure 20. (**G, H**) Denaturing PAGE gel and quantification results showing CpG abundancy of CpG4 and CpG2-d2 after being cultured in the complete culture medium with 10% FBS for 2 hours. The CpG conjugation efficiency remained at a similar level when compared to that measured before incubation with cell media (c.f. Supplementary Figure 10 B,F,G). "18 free CpG" sample means intact 18 free CpGs without culturing, indicating theoretical CpG amount. Data are presented as mean values +/- SEM in graphs C and H.

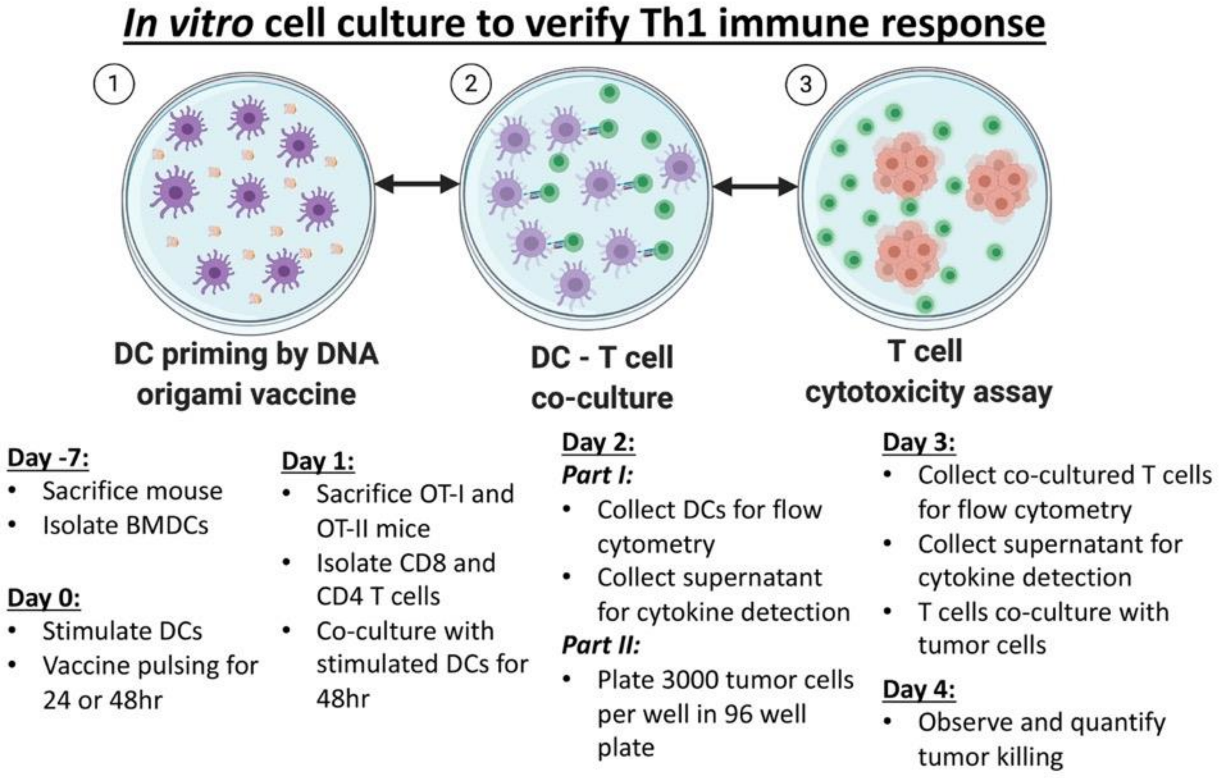

Day -7:
- Sacrifice mouse
- Isolate BMDCs

Day 0:
- Stimulate DCs
- Vaccine pulsing for 24 or 48hr

Day 1:
- Sacrifice OT-I and OT-II mice
- Isolate CD8 and CD4 T cells
- Co-culture with stimulated DCs for 48hr

Day 2:
Part I:
- Collect DCs for flow cytometry
- Collect supernatant for cytokine detection

Part II:
- Plate 3000 tumor cells per well in 96 well plate

Day 3:
- Collect co-cultured T cells for flow cytometry
- Collect supernatant for cytokine detection
- T cells co-culture with tumor cells

Day 4:
- Observe and quantify tumor killing

Supplementary Figure 11. Serial cell co-culture study design to verify Th1 immune polarization by SQB stimulation. The cell culture study took place in sequence. Dendritic cells (DCs) were isolated from mouse bone marrow to obtain immature DCs. BMDCs were stimulated by various DNA origami vaccine constructs. The DC supernatant was removed and the pulsed BMDCs were co-cultured with freshly isolated OT-I CD8 or OT-II CD4 T cells for 48 hours. SQB-stimulated DCs present the OVA antigen to T cells and provide co-stimulatory signals for T cell activation and proliferation. The DCs and T cells and associated supernatant were collected for flow cytometry and ELISA. Amplified and activated T cells were then co-cultured with B16-OVA tumor cells in a 1:10 (T cell: tumor cell) ratio. Tumor cells were labeled with calcein green fluorescent dye. Tumor killing effects were observed by fluorescence release or via live cell counting.

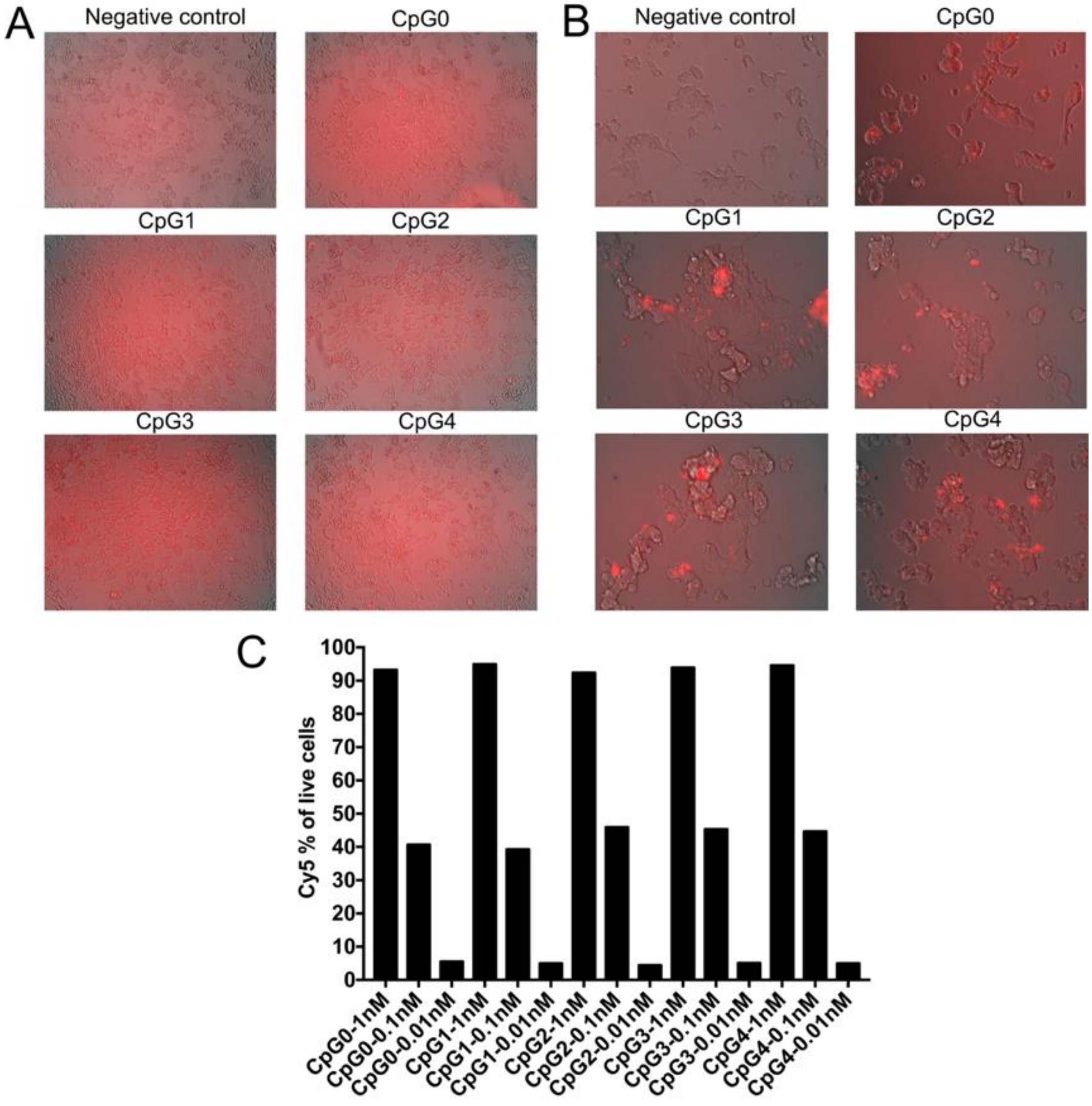

Supplementary Figure 12. CpG-SQB uptake in three cell types. Our group recently discovered that low-salt denaturation of DNA origami can be prevented, and nuclease digestion greatly slowed, by electrostatic coating of DNA nanostructures with PEGylated oligolysine (K10-PEG5k) [1]. This finding extends of the utility of DNA origami *in vivo*. 293 T cells and HeLa cells grow robustly after adding K10-PEG5k coated DNA origami structures (CpG0-SQB)**.** 293 T cells have more pseudopods for endocytosis compared to HeLa cells, leading to more efficient uptake. (**A**) Uptake of CpG-SQB in HeLa cells. Images taken by fluorescent microscope (10×). (**B**) Uptake of CpG-SQB in 293T cells. Images taken by fluorescent microscope (20×). (**C**) Percentage of Cy5-expressing BMDCs analyzed by flow cytometry, after culture with various SQB concentrations for 24 hours. 1 nM of SQB DNA origami almost saturated the BMDCs, as demonstrated by the greater than 90% uptake efficiency. Consequently, 1 nM DNA origami were applied for all subsequent cell-culture experiments.

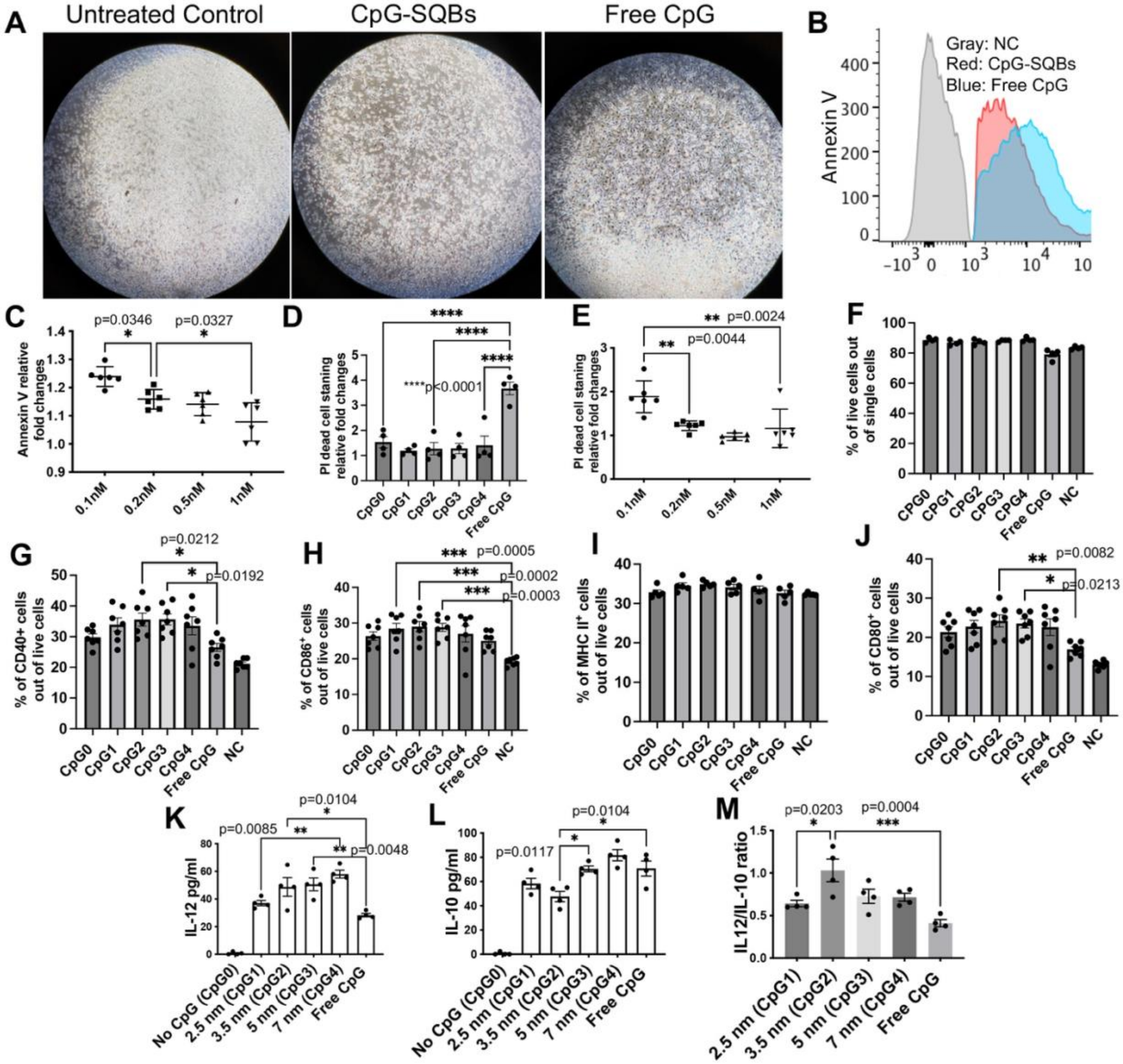

Supplementary Figure 13. BMDC maturation was stimulated by CpG-SQBs. CpG conjugated SQBs (without conjugated antigen) were applied to stimulate immature bone marrow derived dendritic cells (BMDCs). Various SQB constructs containing CpGs (based on the concentration of 1 nM SQB) or free CpG (18 nM) was treated. (**A**) Representative microscope images showing BMDCs after two-day stimulation by various constructs and relevant controls. Magnification: 10×. (**B, D**) Free CpG induced severe cell apoptosis and cell death, as detected by Annexin V and PI staining (n=4 replicates of a single prep of BMDC cells randomly distributed into separate wells). (**C, E**) Higher concentration of CpG-SQBs showed decreased cell apoptosis and cell death (n=6 replicates of a single prep of BMDC cells randomly distributed into separate wells). (**F**) BMDC viability as detected by flow cytometry after 48 hours of co-culture (n=4 replicates of a single prep of BMDC cells randomly distributed into separate wells). (**G–J**) Flow cytometry data showing frequencies of CD40, CD86, MHC II and CD80, after 2-day stimulation by CpG-SQB constructs with various spacing. 3.5 nm and 5 nm spacing of CpG on SQB showed significantly increased DC maturation compared to an equivalent amount of free CpG (n=7 or 5 replicates of a single prep of BMDC cells randomly distributed into separate wells, as shown in the dots). (**K–M**) Amount of IL-12 and IL-10 secretion in the BMDC culture supernatant after one day of stimulation, as quantified by ELISA, (n=4 replicates of a single prep of BMDC cells randomly distributed into separate wells, and culture supernatant recovered independently from each well). The IL-12/IL-10 ratio, a critical marker of Th1 polarization, revealed that 3.5 nm spacing (CpG2) was optimal. CpG0 refers to SQB without CpG and antigen in this Figure. Data are presented as mean values +/- SEM. One-way ANOVA was applied for statistical analysis of the results in the graphs with Tukey's post hoc multiple comparisons test. '*' refers to P ≤ 0.05; '**' refers to P ≤ 0.01; '***' refers to P ≤ 0.001; '****' refers to P ≤ 0.0001.

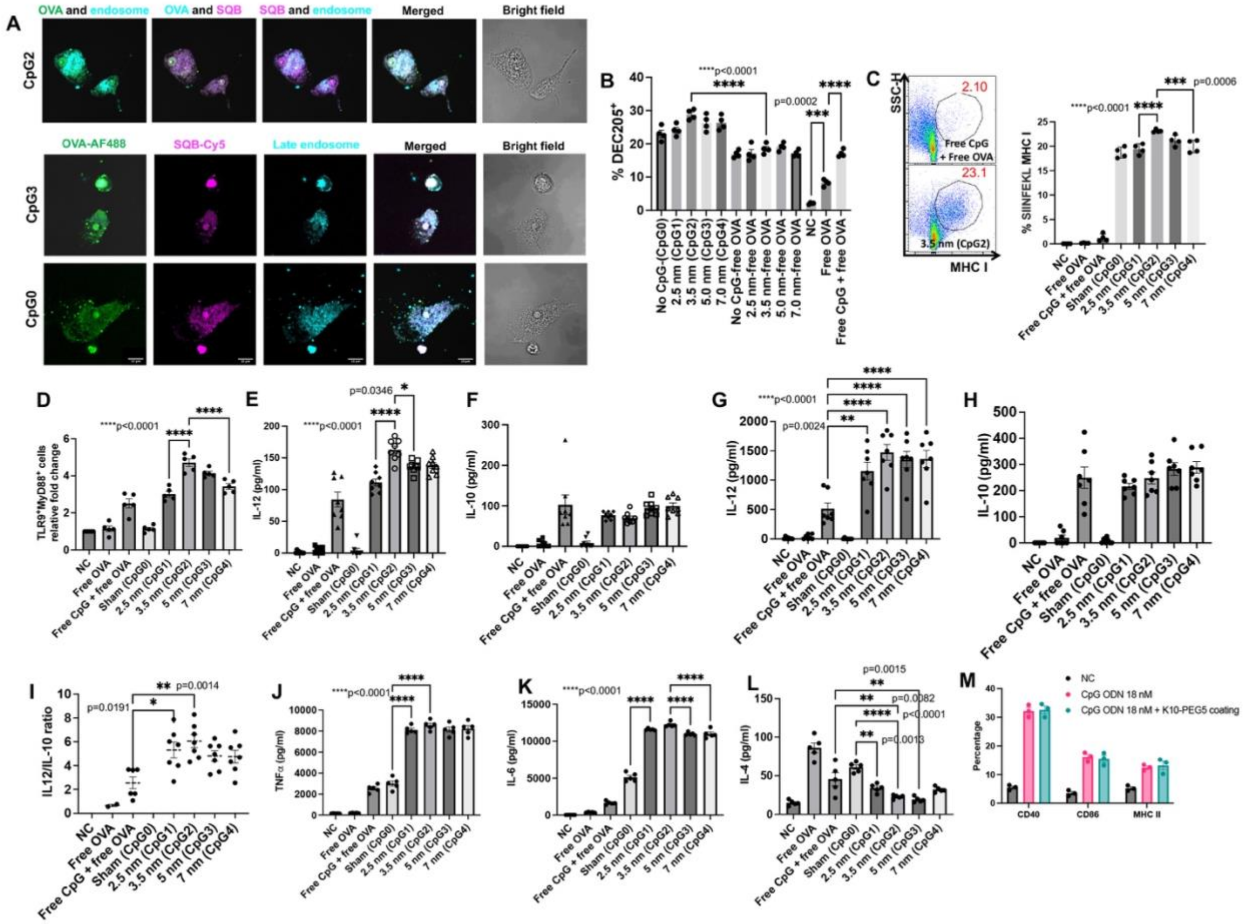

Supplementary Figure 14. BMDCs activation by various DNA origami vaccine constructs and relevant controls. (**A**) Confocal images showing the colocalization of DoriVac in the endosome and ER. All the images share the same scale bar the bottom row, scale=10 μm. (**B**) Frequency of DEC205$^+$ cells in BMDCs treated with DoriVac and various CpG-SQB controls. DEC205 was significantly increased when BMDCs were cultured with CpG-SQB with 3.5 nm CpG spacing (n=4 replicates of a single prep of BMDC cells randomly distributed into separate wells). DoriVac co-delivering of antigen and adjuvant also increased DEC205 expression**.** (**C**) Representative SIINFEKL MHC I expressing cell population scatter plots (left panel) and corresponding frequencies in the total cell population (n=4 replicates of a single prep of BMDC cells randomly distributed into separate wells). (**D**) Frequencies of double-positive TLR9 and MyD88 expressing population, detected via antibody intracellular staining (n=5 replicates of a single prep of BMDC cells randomly distributed into separate wells). CpG2 induced more TLR9 activation and downstream MyD88 expression. (**E**, **F**) ELISA detection of the Th1-polarizing IL-12 cytokine and the Th2-polarizing IL-10 cytokine after 1-day stimulation with various DNA origami vaccine constructs (based on the concentration of 1nM SQB), free OVA (4 nM) or free CpG (18 nM) (n=8 replicates of a single prep of BMDC cells randomly distributed into separate wells, and culture supernatant recovered independently from each well). (**G, H**) ELISA detection of the Th1-polarizing IL-12 cytokine and the Th2-polarizing IL-10 cytokine after 2-day stimulation (n=7 replicates of a single prep of BMDC cells randomly distributed into separate wells, and culture supernatant recovered independently from each well). (**I**) IL-12 versus IL-10 ratio on day 2 (n=7 replicates of a single prep of BMDC cells randomly distributed into separate wells, and culture supernatant recovered independently from each well; data points where cytokine levels were not detectable were omitted, thus some conditions display fewer than seven data points). (**J**, **K**) TNFα and IL-6 detection by ELISA within the BMDC supernatant. TNFα expression in all the SQB vaccine groups was significantly higher than the corresponding bolus vaccine (free CpG and free OVA) (n=5 replicates of a single prep of BMDC cells randomly distributed into separate wells, and culture supernatant recovered independently from each well). CpG2 stimulation demonstrated the most increased IL-6 expression compared to controls. (**L**) IL-4 detection by ELISA within the BMDC supernatant. CpG2 and CpG3 stimulation demonstrated the lowest IL-4 expression (n=5 replicates of a single prep of BMDC cells randomly distributed into separate wells, and culture supernatant recovered independently from each well). (**M**) Positive population (%) of BMDC maturation markers after 1-day stimulation by free CpG or CpG coated with K10-PEG5k. Sham (CpG0) refers to SQB conjugated with OVA antigen but without CpG in this Figure (n=3 replicates of a single prep of BMDC cells randomly distributed into separate wells). Data are presented as mean values +/- SEM. One-way ANOVA was applied for statistical analysis of the results in the graphs with Tukey's post hoc multiple comparisons test. '*' refers to $P \leq 0.05$; '**' refers to $P \leq 0.01$; '***' refers to $P \leq 0.001$; '****' refers to $P \leq 0.0001$.

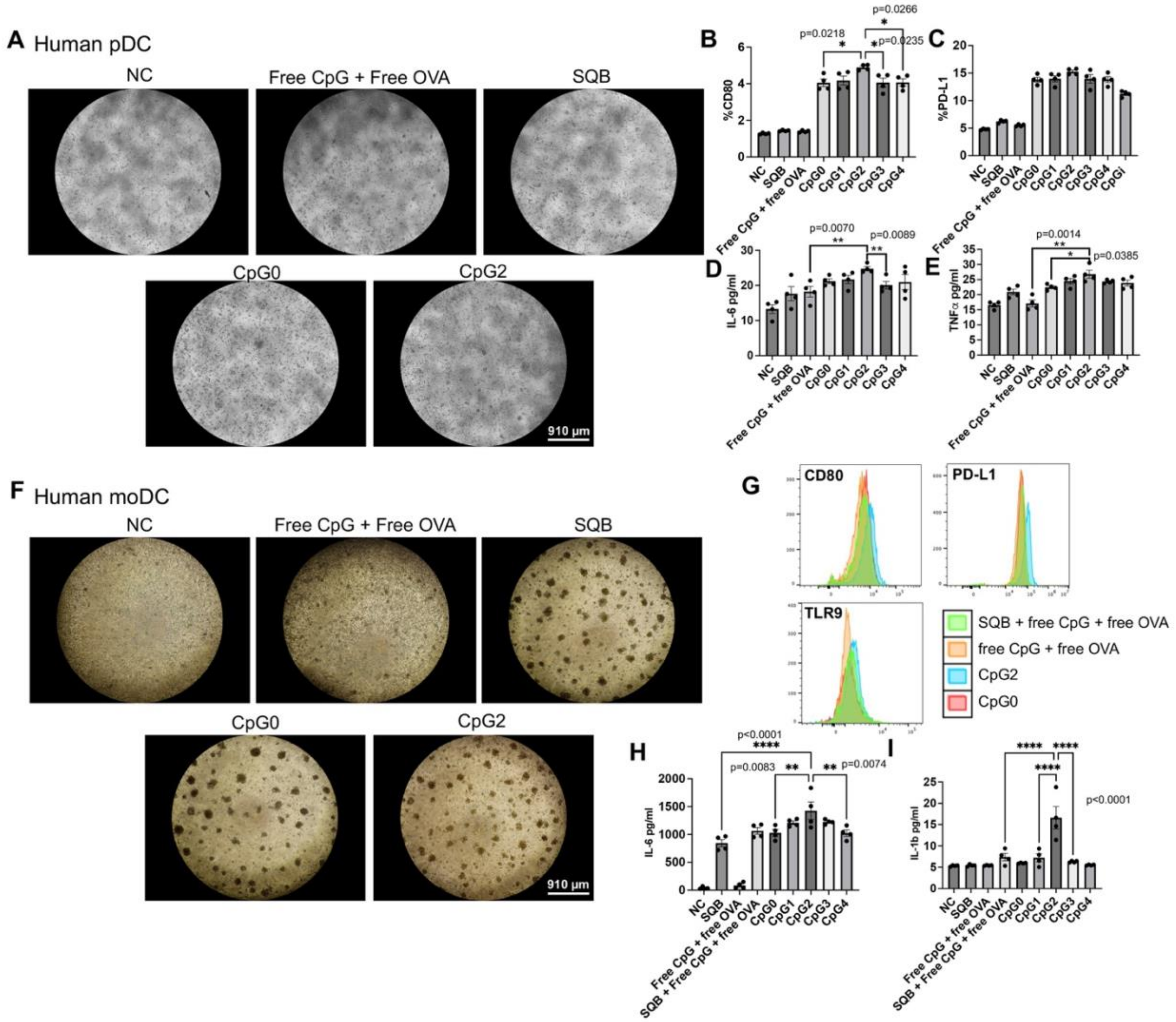

Supplementary Figure 15. **Spacing effects on human DCs.** (**A**) Representative images showing human plasmacytoid DCs (pDCs) being stimulated under different conditions. Obvious cell clots after stimulation were observed in CpG2 group. All the other spacing showed similar cell morphology compared to CpG2. (**B, C**) Flow results of CD80 and PD-L1 expression on human pDCs. (**D, E**) Luminex results showing IL-6 and TNFα. We did not observe obvious differences in IL-12 and IL-10 cytokine levels likely because the cell number is limited. (**F**) Representative images showing human monocyte derived DCs (moDCs) after various stimulationa conditions. (**G**) Flow results of CD80, PD-L1 and TLR9 showed improved cell stimulation by CpG2. All the other spacing showed similar stimulation compared to CpG2. However, the cytokine results showed that CpG2 stimulated the strongest IL-6 (**H**) and IL-1b (**I**) secretion. Various DNA origami vaccine constructs (based on the concentration of 1 nM SQB), free OVA (10 nM) or free CpG (18 nM) was treated. All the graphs in this figure have a sample number of n=4 replicates of a single prep of human pDC or moDC cells randomly distributed into separate wells. Data are presented as mean values +/- SEM. One-way ANOVA was applied for statistical analysis of the results in the graphs with Tukey's post hoc multiple comparisons test. '*' refers to $P \leq 0.05$; '**' refers to $P \leq 0.01$; '***' refers to $P \leq 0.001$; '****' refers to $P \leq 0.0001$.

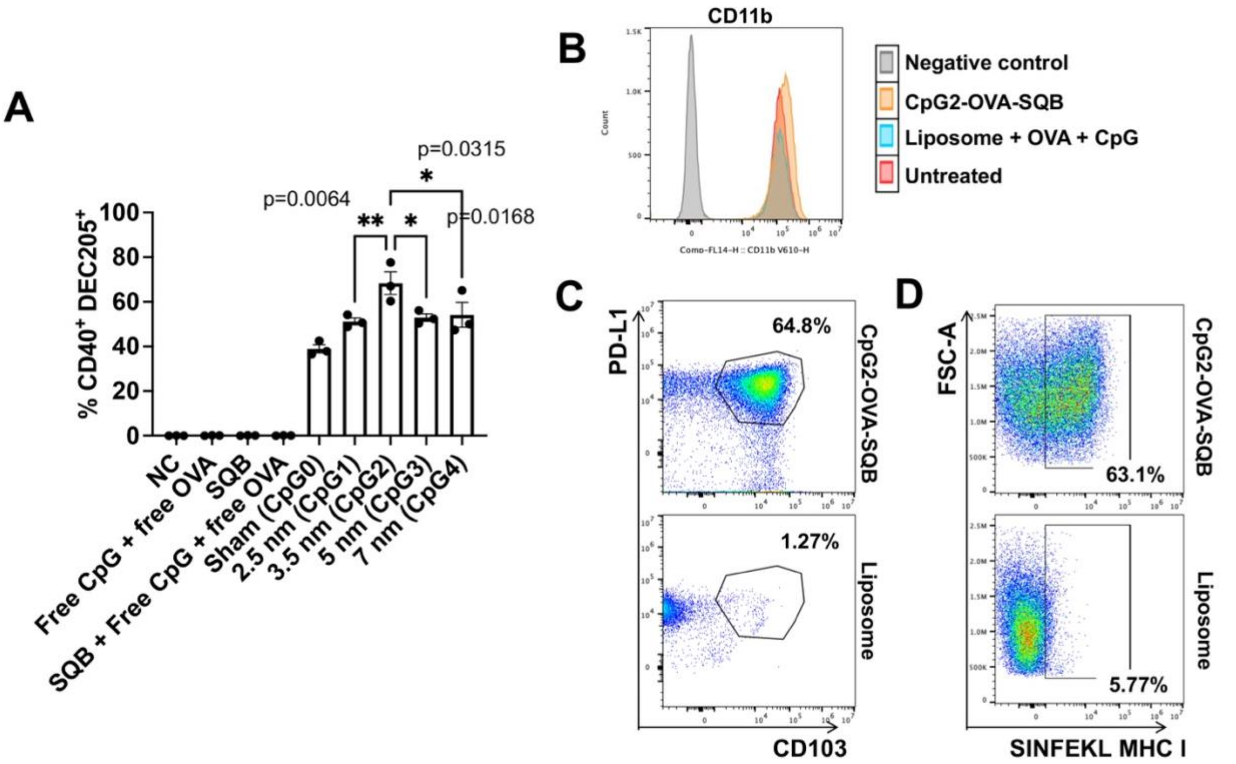

Supplementary Figure 16. **RAW264.7 cell activation and SQB versus liposome in RAW264.7.** (**A**) Double-positive CD40$^+$DEC205$^+$ population detected in BMDCs by flow cytometry, n=3 replicates of a single culture of RAW264.7 cells randomly distributed into separate wells. Comparing DoriVac with liposome carrying the equivalent amounts of CpG and OVA, DoriVac showed enhanced CD11b expression (**B**), as well as PD-L1$^+$CD103$^+$ population (**C**). (**D**) More SIINFEKL epitopes were presented through MHC I. Various DNA origami vaccine constructs (based on the concentration of 1 nM SQB), free OVA (10 nM) or free CpG (18 nM) was treated. Data are presented as mean values +/- SEM. One-way ANOVA was applied for statistical analysis of the results in graph A with Tukey's post hoc multiple comparisons test. '*' refers to $P \leq 0.05$; '**' refers to $P \leq 0.01$.

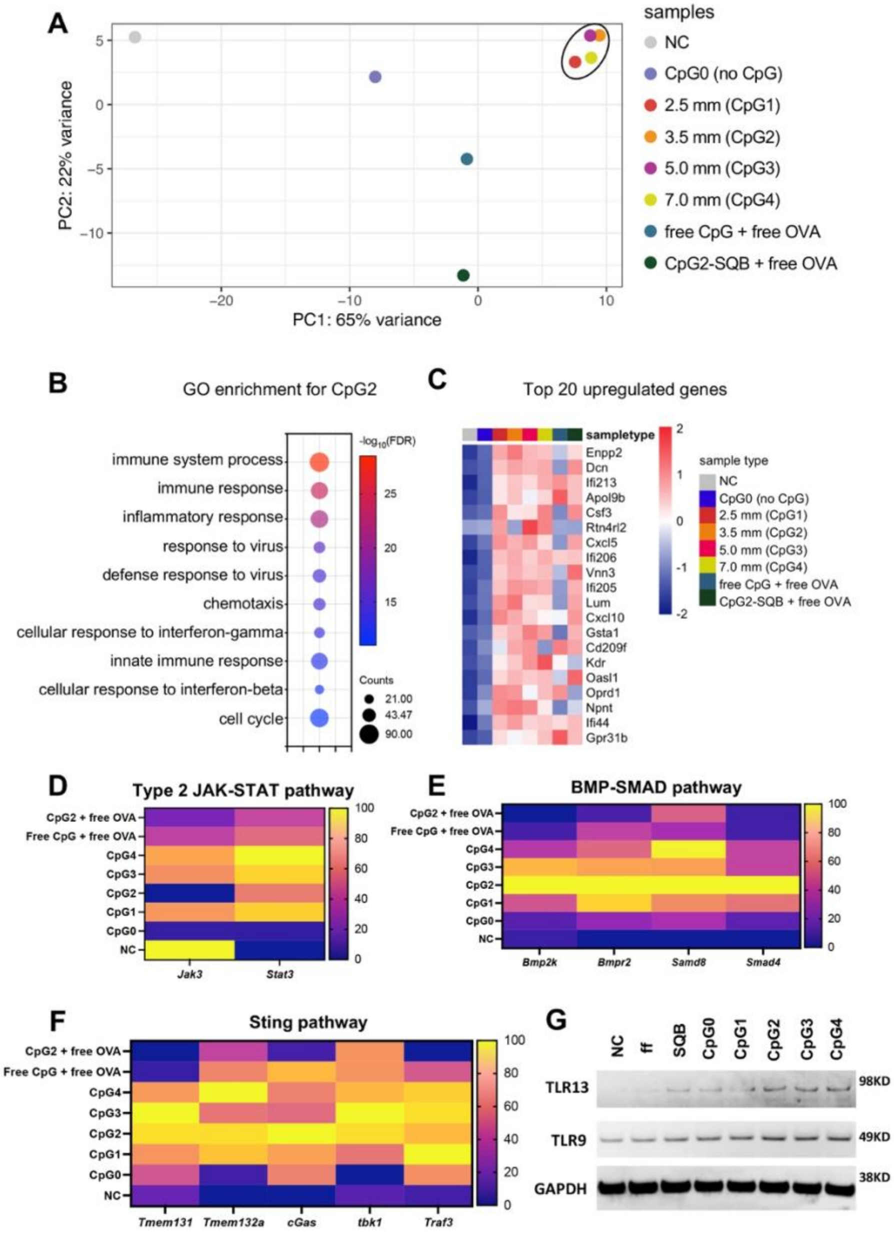

Supplementary Figure 17. RNA-sequencing analysis to characterize transcription changes induced by various origami vaccines. (**A**) Principal component analysis of the BMDC samples stimulated by various SQB constructs. (**B**) Gene Ontology (GO) enrichment of differentially expressed genes between the CpG2 stimulated group and the unstimulated negative control. (**C**) Heat map of the top 20 differentially upregulated genes in CpG2. (**D-F**) Analysis of related genes in different signaling pathways. (**G**) Western blot results showing the expression of both TLR9 and TLR13. We observe a greater quantity of TLRs were stimulated in CpG2, CpG3 and CpG4 groups (ff: free CpG + free OVA). Various DNA origami vaccine constructs (based on the concentration of 1 nM SQB), free OVA (4 nM) or free CpG (18 nM) was treated.

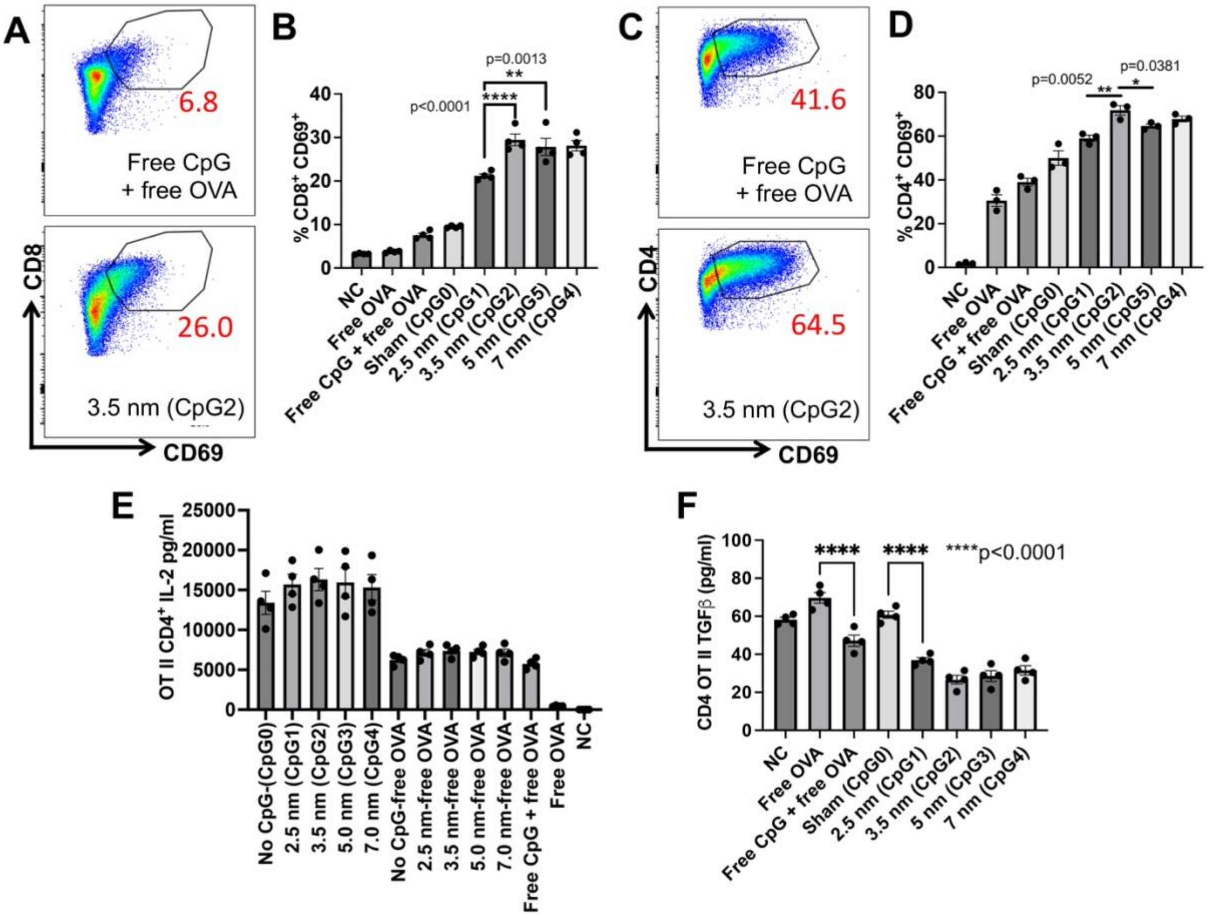

Supplementary Figure 18. T cell activation by various DoriVac and corresponding controls. (**A, B**) Representative CD69 scatter plots of CD8 and corresponding frequencies of CD69-expressing cells, n=4 replicates of a single prep of OT I CD8 T cells randomly distributed into separate wells. (**C, D**) Representative CD69 scatter plots of CD4 T cells and corresponding frequencies of CD69-expressing cells, n=3 replicates of a single prep of OT II CD4 T cells randomly distributed into separate wells. (**E**) ELISA detection of IL-2 in the supernatant of CD4 OT II cells co-cultured with pulsed BMDCs for 2 days. The IL-2 secretion showed negligible difference among different spacings. OVA conjugated CpG-SQBs (left panel) induced the highest IL-2 level, n=4 replicates of a single prep of OT II CD4 T cells randomly distributed into separate wells. (**F**) ELISA detection of TGFβ in the supernatant of CD4 OT II cells co-cultured with pulsed BMDCs for 2 days. All DoriVac demonstrated less TGFβ secretion compared to bolus vaccine and SQB without CpG (CpG0, OVA conjugated), n=4 replicates of a single prep of OT II CD4 T cells randomly distributed into separate wells. Various DNA origami vaccine constructs (based on the concentration of 1 nM SQB), free OVA (4 nM) or free CpG (18 nM) was treated. Data are presented as mean values +/- SEM. One-way ANOVA was applied for statistical analysis of the results in the graphs with Tukey's post hoc multiple comparisons test. '*' refers to P ≤ 0.05; '****' refers to P ≤ 0.0001.

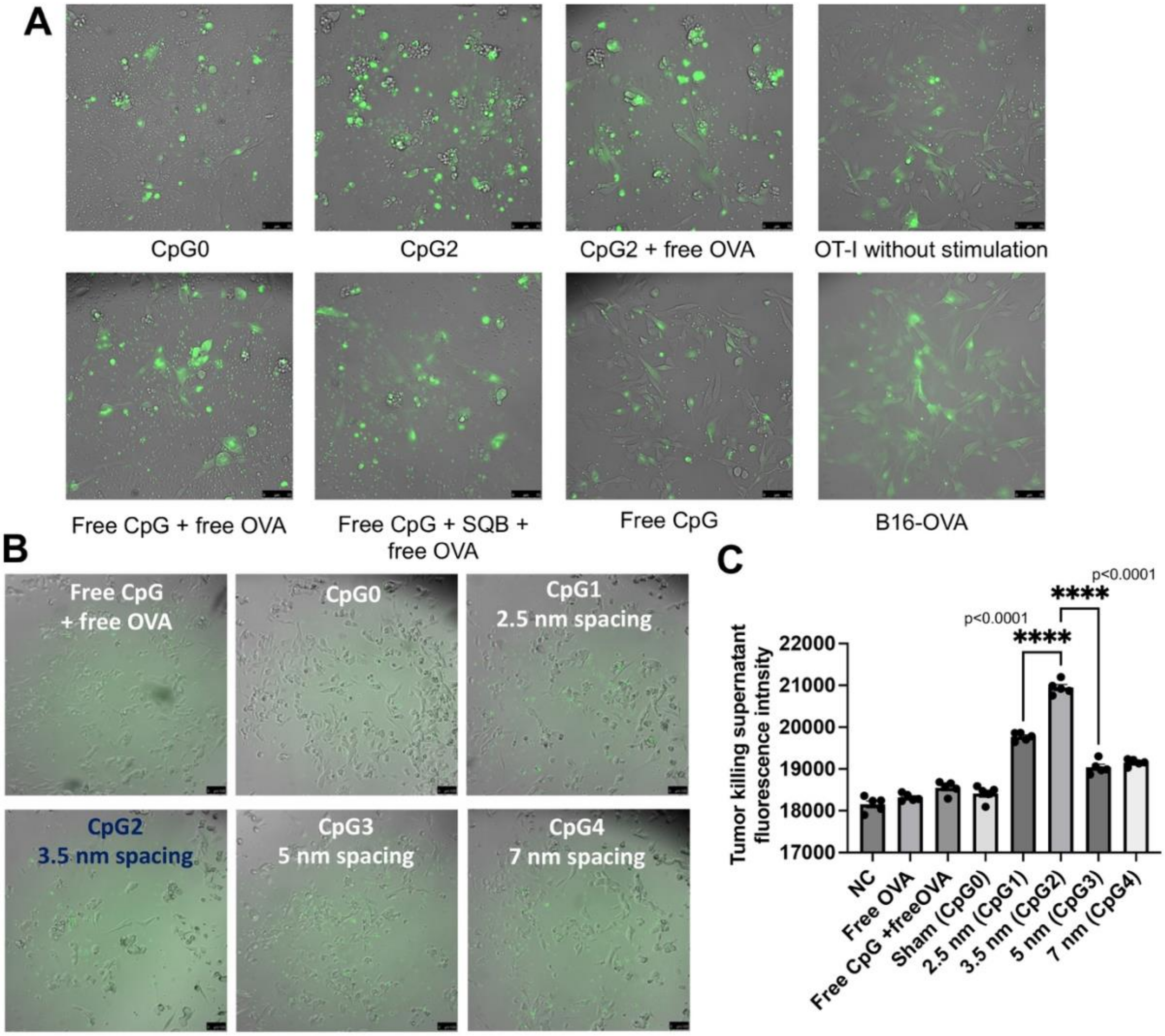

Supplementary Figure 19. ***In vitro*** **tumor killing by vaccine constructs with various CpG spacing.** (**A**) The images of activated T cell - tumor cell co-culture after 2 days. T cells were activated by co-culturing with BMDCs stimulated by DoriVac, control vaccine or unstimulated (as shown in labeling). T cells are imaged as small green dots. The B16-OVA tumor cells were stained with calcein green. Cell spreading is characteristic of healthy tumor cells. Tumor cell aggregations are characteristic of cell killing by CD8 T cells. Scale=75 µm. (**B**) The images represent a different iteration of the experiment. Tumor killing was observed on day 2. Stimulation by DoriVac with various spacings of CpG was compared. Scale=100 µm. (**C**) Calcein green intensity in the supernatant of various groups. Increased calcein is associated with greater T cell activity and increased tumor cell killing, as tumor cell killing leads to increased calcein green release. Various DNA origami vaccine constructs (based on the concentration of 1 nM SQB), free OVA (4 nM) or free CpG (18 nM) was treated, n=5 replicates of a single culture of B16-OVA tumor cells randomly distributed into separate wells. Data are presented as mean values +/- SEM. One-way ANOVA was applied for statistical analysis of the results in the graphs with Tukey's post hoc multiple comparisons test. '****' refers to $P \leq 0.0001$.

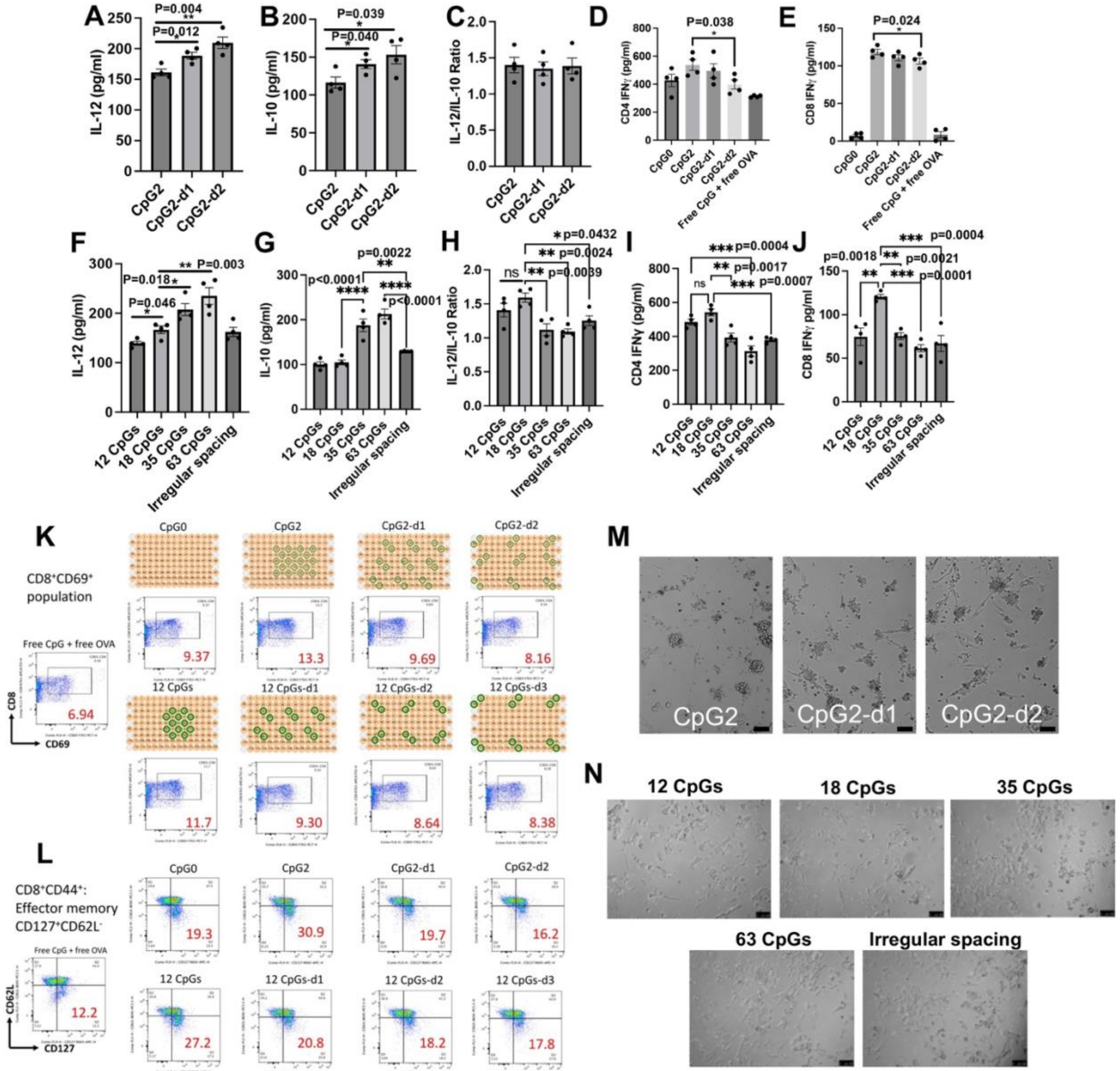

Supplementary Figure 20. DC and T cell activation and *in vitro* tumor killing by various CpG dimer patterns and densities. DNA origami SQBs are a great tool to study the dimer-trigger unit where two CpG molecules are closely associated in a dimer. Different spacing strategies (as shown in Supplementary Figure 4) are easily applied on the SQB platform with controlled CpG orientation to investigate higher-order multimerization. The OT I CD8 T cells were primed by BMDCs treated with various CpG-SQB constructs. (**A**, **B**) ELISA detection of IL-12 and IL-10 secreted from BMDCs after 1-day stimulation. IL-12 and IL-10 secretion both increased when CpG dimer spacing increased. (**C**) The IL-12/IL-10 ratio calculated from measurements in A and B. The IL-12/IL-10 ratio was constant as CpG dimer spacing increased, in contrast to the effect observed as CpG monomer spacing increased (decreased IL-12/IL-10 ratio as shown in Fig. 2G) (**D, E**) IFNγ quantification by ELISA from CD4 OT-II and CD8 OT-I T cells after 2-day coculture. (**F, G**) ELISA detection of IL-12 and IL-10 secreted from BMDCs after 1-day stimulation by different number of CpGs on DoriVac. IL-

12 and IL-10 secretion both increased in the context of additional CpGs. However, IL-10 secretion was greatly induced with 35 and 63 CpGs. (**H**) The IL-12/IL-10 ratio from measurements in F and G. The IL-12/IL-10 ratio decreased as the number of CpGs increased. When the number of CpG was increased from 12 to 18, the IL-12/IL-10 ratio remained constant. Irregular spacing also increased IL-10 secretion and decreased the IL-12/IL-10 ratio compared to CpG2. (**I, J**) Quantification of IFNγ from the supernatant of co-cultured OT-II CD4$^+$ or OT-I CD8$^+$ T cells with pulsed BMDCs for 2 days by ELISA. 12 CpGs and 18 CpGs showed no IFNγ secretion difference from CD4 OT-II T cells, but 18 CpGs induced more IFNγ secretion from CD8 OT-I T cells. 35, 63 and irregularly spaced CpGs showed less IFNγ expression in both CD4 OT-II and CD8 OT-I T cells, suggesting that 18 CpGs maximizes IFNγ secretion. (**K**) Representative flow plot of CD69 expression (a CD8 T cell activation marker) in different treatment groups. 12 CpGs and other 3 dimer patterns were also examined. (**L**) Representative flow plot of effector memory cells as indicated by the frequency of the effector memory CD8$^+$CD44$^+$CD127$^+$CD62L$^-$ population. CD8 T cell activation decreased as the dimer spacing increased, suggesting that 3.5 nm spacing of the CpG dimer is optimal. (**M**) Increased spacing of the CpG dimers decreased the amount of observed tumor-cell killing (aggregated cells) associated with activated CD8 T cells. Scale=100 μm. (**N**) 18 CpGs per SQB demonstrated the most tumor-cell killing activity compared to the relevant controls. Increased CpG density (35 or 63 CpGs per SQB) resulted in decreased tumor killing after sequential co-culture. Decreased CpG density (12 or less CpGs per SQB) also resulted in decreased tumor killing with sequential co-culture, suggesting that 18 CpGs per SQB is optimal for tumor-cell killing activity and aligning with previous results. Various DNA origami vaccine constructs (based on the concentration of 1 nM SQB), free OVA (6 nM) or free CpG (18 nM) was treated. Scale=100 μm. All the graphs in this figure have a sample number of n=4 replicates from a single prep of BMDCs randomly distributed into separate wells, and culture supernatant independently collected from each well. Data are presented as mean values +/- SEM. One-way ANOVA was applied for statistical analysis of the results in graphs A to J with Tukey's post hoc multiple comparisons test. '*' refers to $P \leq 0.05$; '**' refers to $P \leq 0.01$; '***' refers to $P \leq 0.001$; '****' refers to $P \leq 0.0001$.

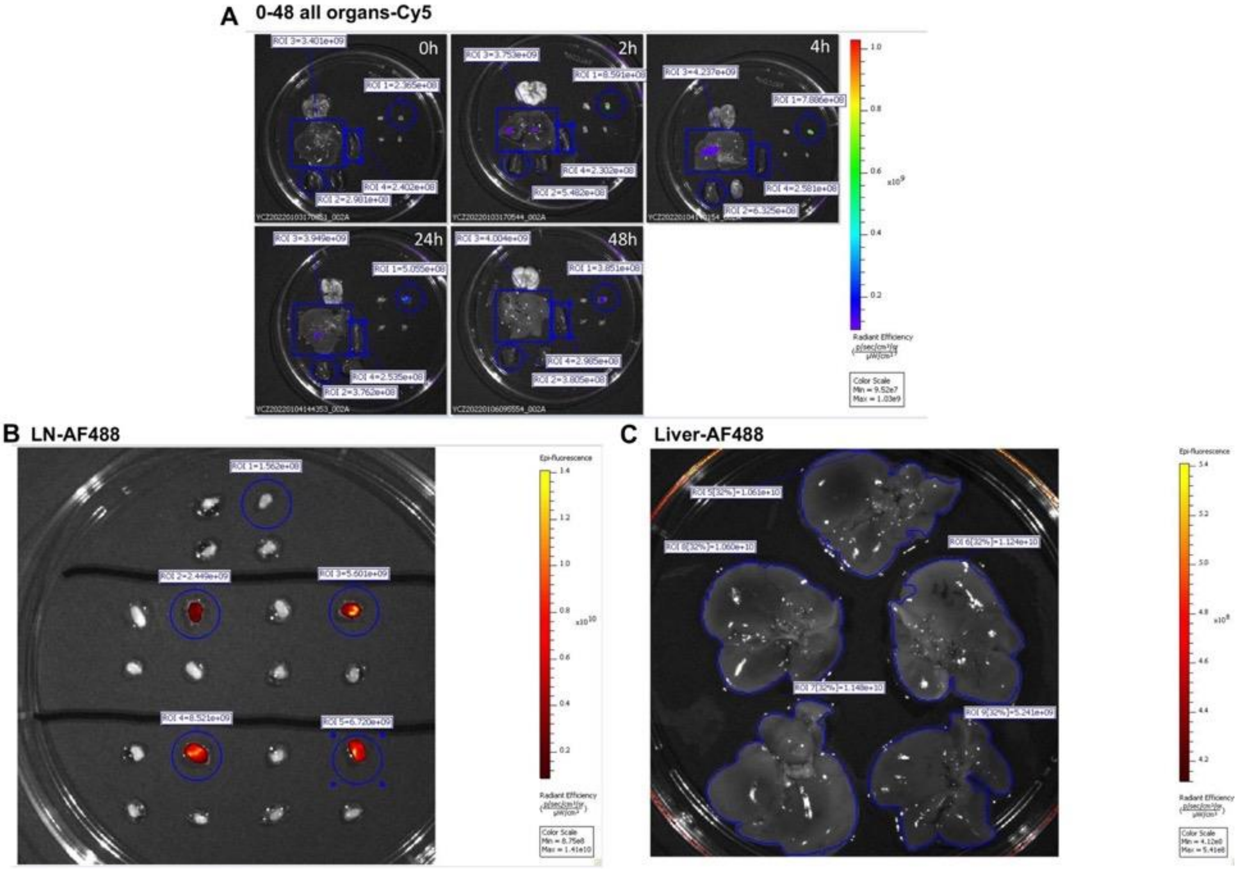

Supplementary Figure 21. DoriVac distribution. The vaccine was administrated at 0 hour with a concentration of 600 nM in 100 ul on the left shoulder of the C57BL6 mice. The AF488 and Cy5 fluorescent signal was recorded by IVIS at 2, 4, 24 and 48 hours. AF488 was labeled on OVA protein conjugated on the SQB. Cy5 was conjugated directly on the SQB. (**A**) Representative image showing the various organs' Cy5 signal at different time point. All the results were standardized to avoid individual bias. The schematic of ROI gating was also showed. The vaccine dominantly accumulated in draining lymph nodes (blue circle). (**B**) Representative image showing the LN AF488 signal gating. (**C**) Representative image showing the liver AF488 signal gating.

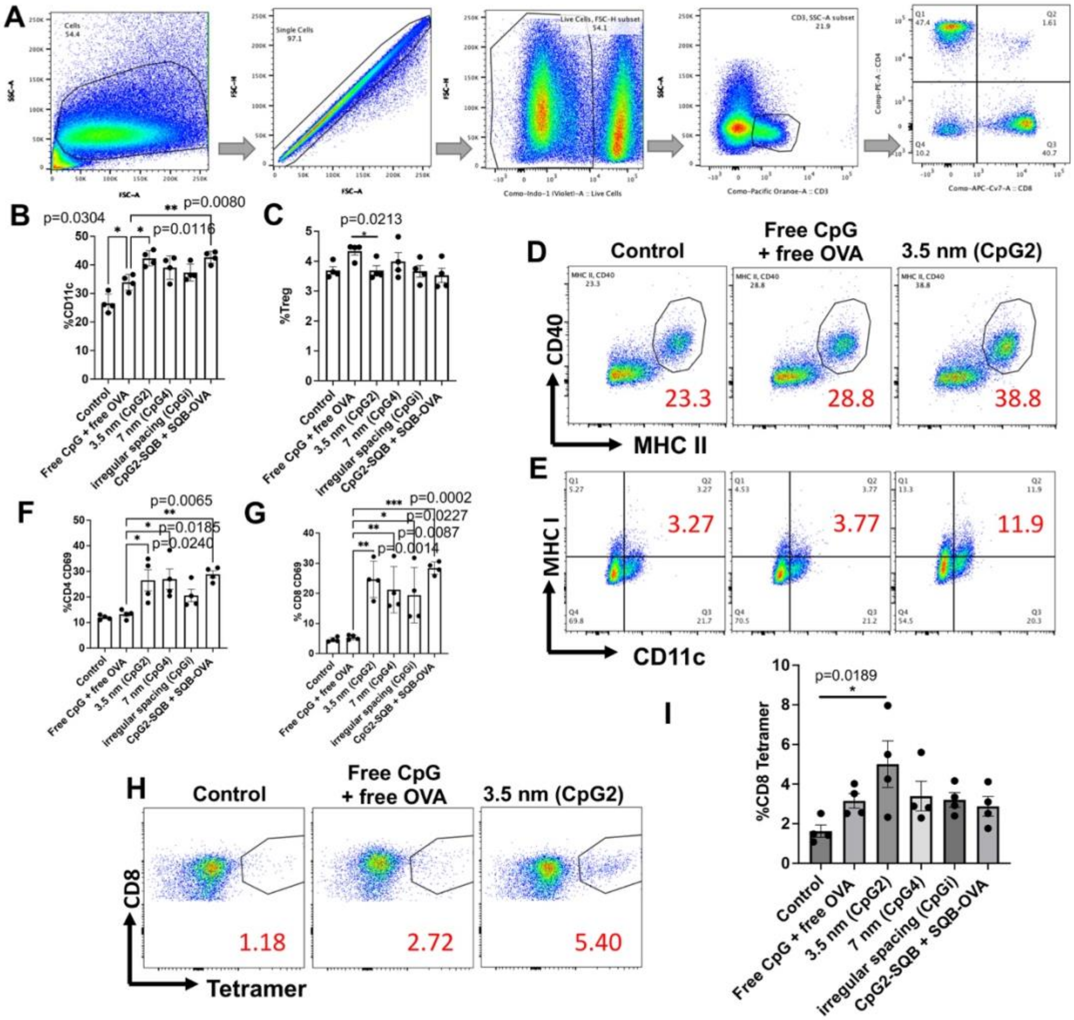

Supplementary Figure 22. Vaccination in naïve healthy mice. The mice were vaccinated by various versions of the DoriVac and bolus vaccine. The lymph nodes (LNs) were processed into single cell suspension for flow cytometry analysis on day 1 or day 8 after vaccination. Blood cells were also collected on day 8 for CD8 tetramer cell analysis. (**A**) Cell gating strategy for lymphocytes. The subset of CD3$^+$ or CD11c$^+$ cells was gated from all live cells. Based on CD3 gating, the subpopulations of CD4 and CD8 T cells were gated. (**B, C**) Frequencies of CD11c$^+$ DCs and CD4$^+$CD25$^+$FoxP3$^+$ Treg population. (**D, E**) Representative scatter plots of the CD40 and MHC II double positive population and SINFEKL MHC I population of DCs from three different treatment groups. (**F, G**) Frequencies of CD69 positive cells in CD8 and CD4 T cells in the draining LN 1 day after vaccination. (**H**) Representative scatter plots of CD8 tetramer cells found in the LN 8 days after vaccination. Note that DC and T cell activation markers showed no difference compared to untreated control on day 8 after vaccination, suggesting that vaccination boosts are necessary for durable immune responses. (**I**) Frequency of CD8 tetramer population in the blood cells, collected 8 days after vaccination. For all the graphs in this figure, n=4 lymph node samples from independent mice. Data are presented as mean values +/- SEM. One-way ANOVA was applied for statistical analysis of the flow results with Tukey's post hoc multiple comparisons test. '*' refers to $P \leq 0.05$; '**' refers to $P \leq 0.01$. '***' refers to $P \leq 0.001$.

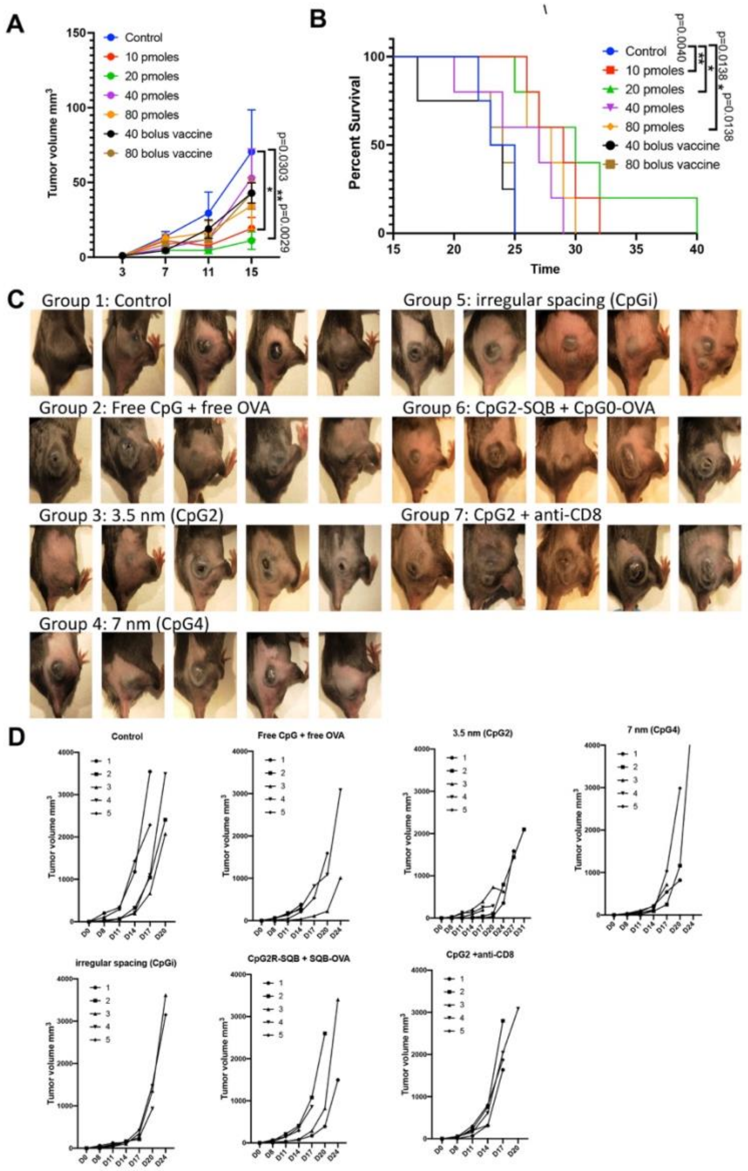

Supplementary Figure 23. Therapeutic vaccination effects of DoriVac in the B16-OVA melanoma tumor model. (**A,B**) Different vaccine concentrations were tested for a total of three doses in B16-OVA model. 40 and 80 bolus vaccine (Free CpG + Free OVA) corresponding the same amount of antigen and adjuvant in 40 pmoles and 80 pmoles DoriVac. The tumor growth and mice survival results disclose that 10 and 20 pmoles DoriVac induced the most beneficial immune response (n=4 mice in control and bolus vaccine 40 pmoles groups, n=5 mice in all the other groups). Increasingly, the increased DoriVac amount does not lead to further benefits. The bolus vaccines did not show any benefits in this study. (**C**) Full panel images showing tumor growth in various groups 15 days after tumor inoculation. (**D**) Tumor growth curves were plotted for each individual mouse in each group. Data are presented as mean values +/- SEM in Graph A. Two-way ANOVA was applied for statistical analysis of graph A with Tukey's post hoc multiple comparisons test. Survival curves were analyzed by Kaplan-Meier method and log-rank test for graph B. '*' refers to $P \leq 0.05$; '**' refers to $P \leq 0.01$.

.

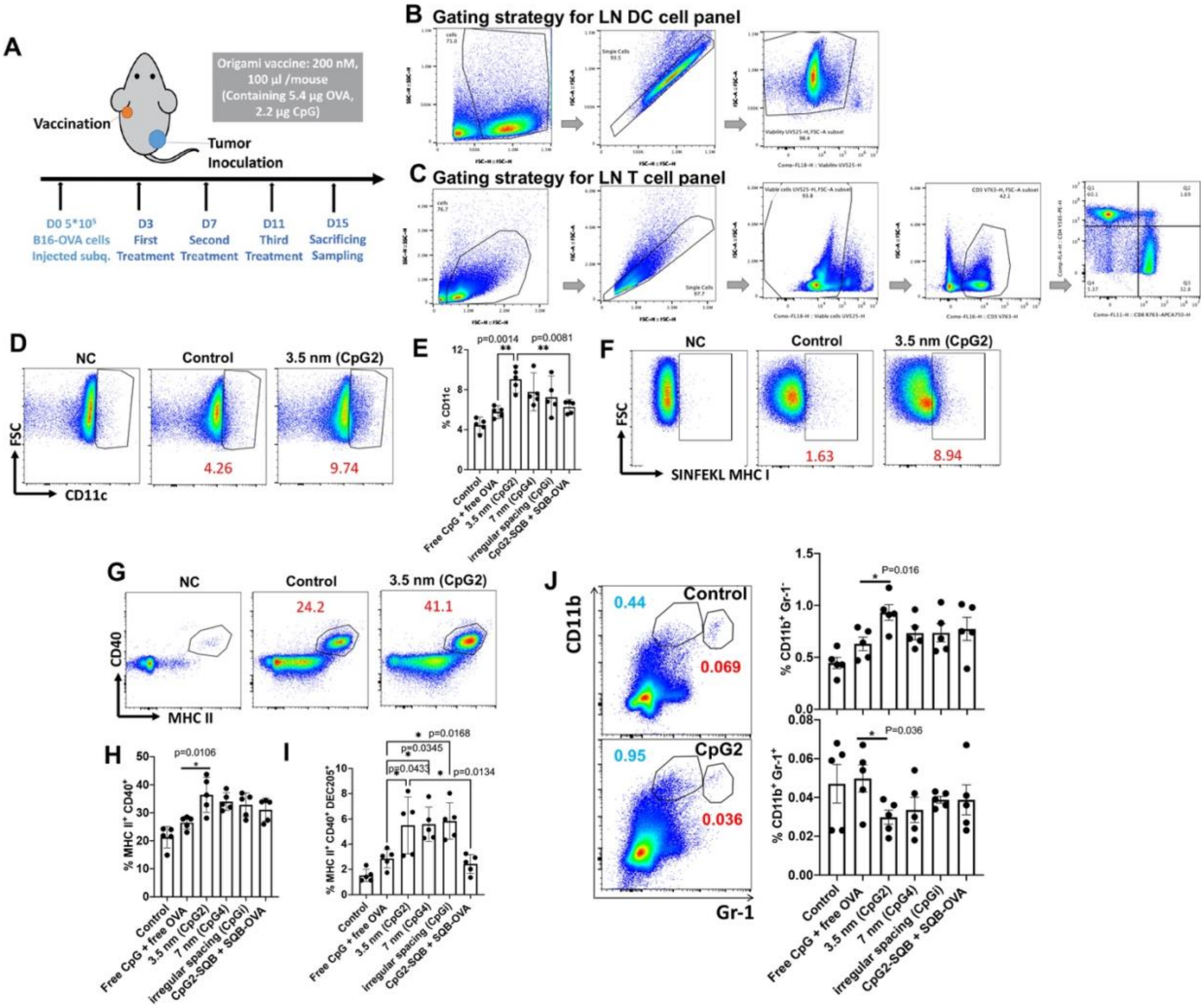

Supplementary Figure 24. Additional lymphocyte analysis from treated tumor-bearing mice. (**A**) For immune profiling experiments, mice were treated with vaccines on day 3, 7 and 11, and then sacrificed on day 15. This is a slightly different vaccination strategy than was used for the treatment experiments to ensure that all mice were alive at the time of sacrifice. (**B**) Cell gating strategy for lymphocyte DC panel. (**C**) Cell gating strategy for lymphocyte T cell panels. Live cells were gated for CD3$^+$ cells. CD4 and CD8 T cells were gated based on the CD3 gating, and then subsequently gated for T cell subpopulations. (**D, E**) Representative images from flow scatter plots and corresponding frequencies of CD11c positive population. (**F**) Representative scatter plots of SINFEKL MHC I population. (**G, H**) Representative scatter plots and corresponding frequencies of CD40 and MHC II double positive population. CpG2 showed the most significant DC maturation, as demonstrated by the frequency of CD40$^+$MHC II$^+$. (**I**) DEC205$^+$ subset was gated out of CD40$^+$ MHC II$^+$ cells. Codelivery of antigen with CpG adjuvant through SQB could greatly increase antigen uptake indicated by enhanced DEC205 expression compared to OVA delivered freely. **(J)** Representative scatter plots (left) and percentage quantifications (right) of myeloid-derived suppressor CD11b$^+$Gr-1$^+$ cells (red) and CD11b$^+$Gr-1$^-$ monocytes (blue) in the LN. For all the graphs in this figure, n=5 lymph node samples from independent tumor-model mice. Data are presented as mean values +/- SEM. One-way ANOVA was applied for statistical analysis of the flow results with Tukey's post hoc multiple comparisons test. '*' refers to $P \leq 0.05$; '**' refers to $P \leq 0.01$.

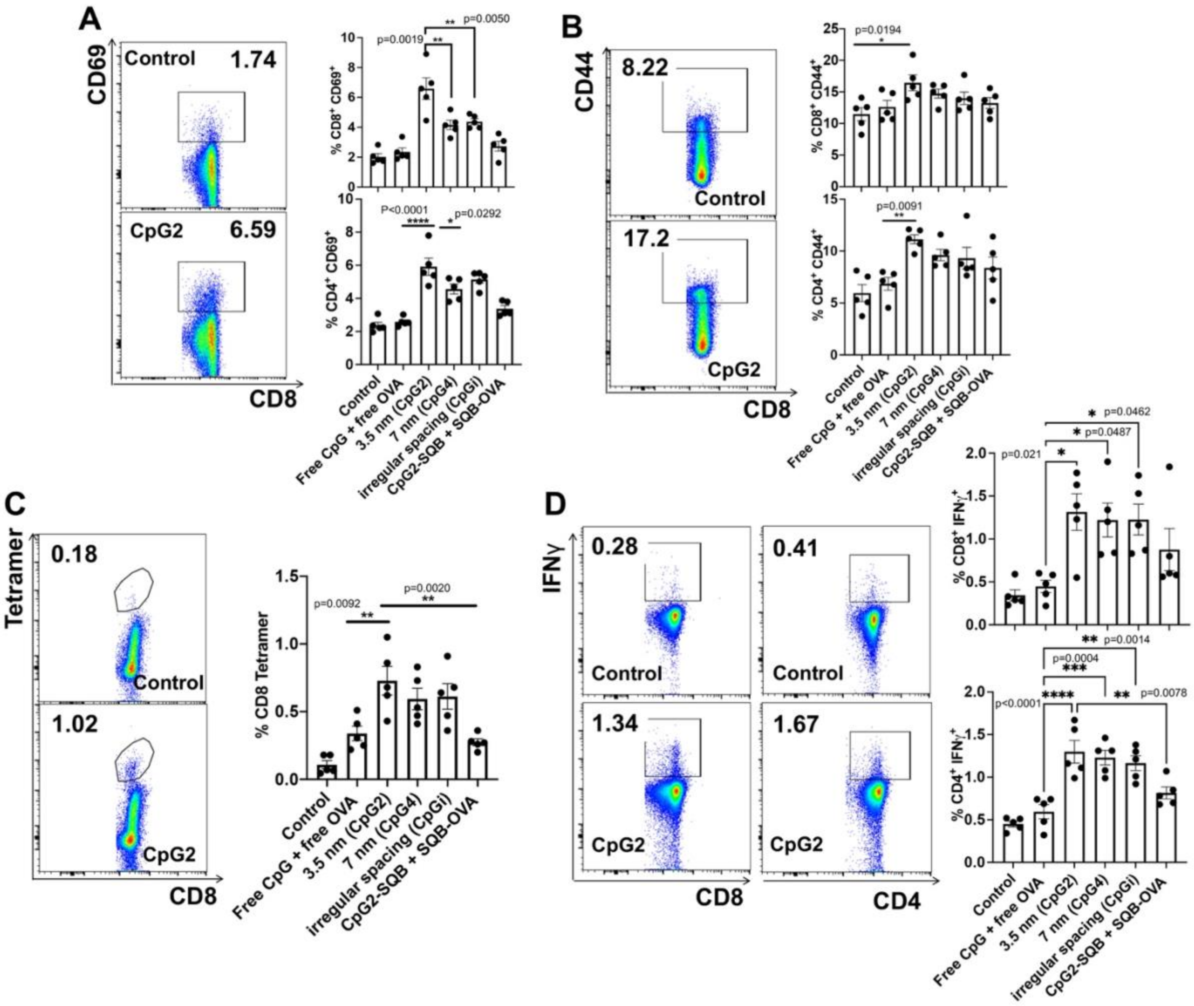

Supplementary Figure 25. Additional lymphocyte T cell analysis from treated tumor-bearing mice. (**A**) Representative CD69$^+$ scatter plots of CD8$^+$ cells (left) and percentages of CD69$^+$ cells in CD8$^+$ and CD4$^+$ T cells (right). (**B**) Representative CD44$^+$ plots of CD8$^+$ cells (left) and percentages of CD44$^+$ cells in CD8$^+$ and CD4$^+$ T cells (right). (**C**) Representative SIINFEKL tetramer plots on CD8$^+$ cells (left) and percentages of tetramer cells in CD8$^+$ T cells (right). (**D**) Representative IFNγ$^+$ scatter plots of CD8$^+$ or CD4$^+$ T cells (left) and percentages of IFNγ$^+$ cells in CD8$^+$ or CD4$^+$ T cells (right). IFNγ-expressing CD4 Th1 cells and CD8 cell were both significantly increased in all the origami vaccine groups co-delivering OVA and CpG. For all the graphs in this figure, n=5 lymph node samples from independent tumor-model mice. Data are presented as mean values +/- SEM. One-way ANOVA was applied for statistical analysis of the flow results with Tukey's post hoc multiple comparisons test. '*' refers to $P \leq 0.05$; '**' refers to $P \leq 0.01$; '***' refers to $P \leq 0.001$; '****' refers to $P \leq 0.0001$.

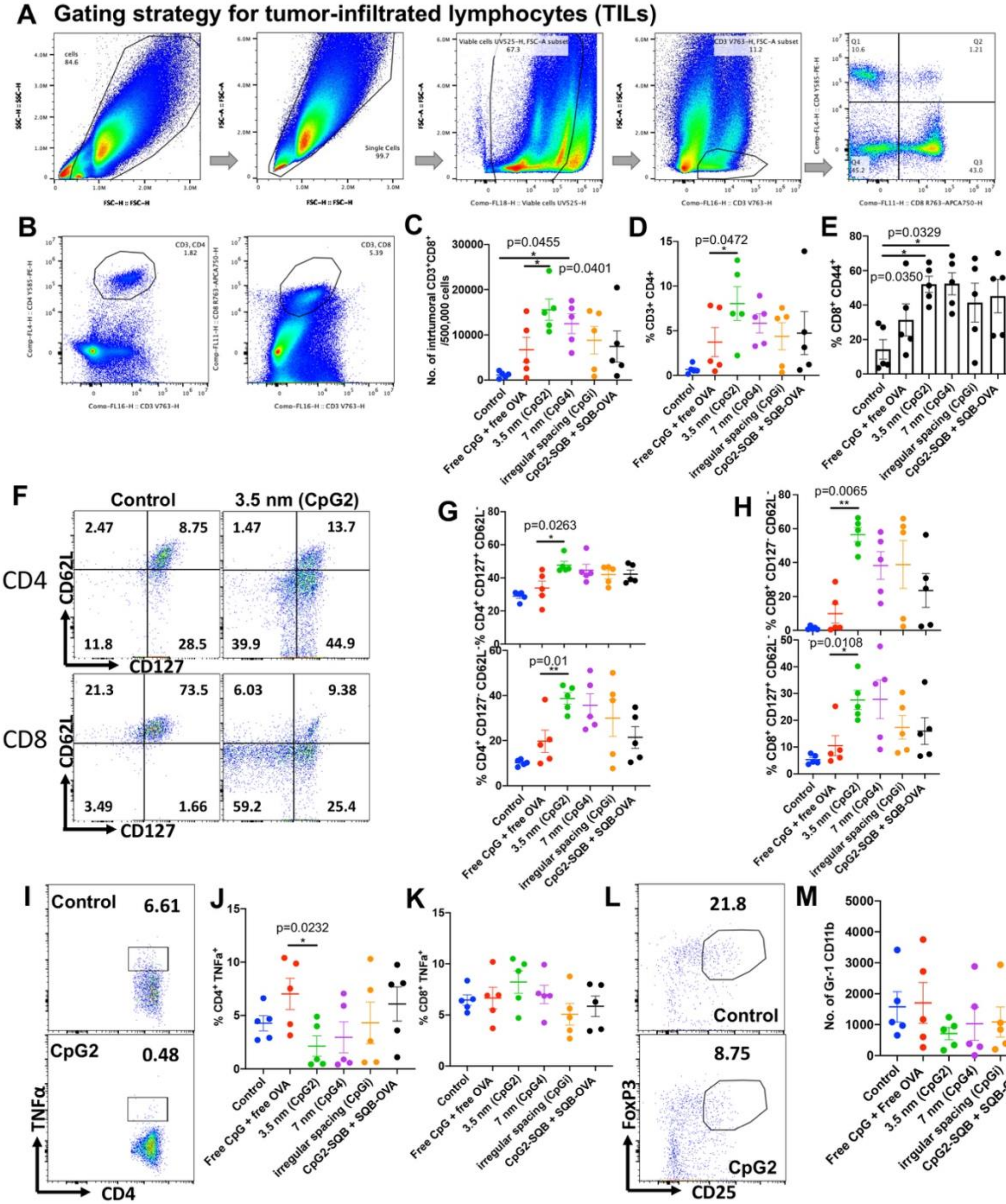

Supplementary Figure 26. Extensive tumor infiltrating lymphocytes (TILs) analysis from treated tumor-bearing mice. (**A**) The tumor tissue was collected on day 15 and processed into single cell suspension for flow cytometry. Cell gating strategy were shown. $CD3^+$ cells were gated out of live cells directly. Based on CD3 gating, CD4 and CD8 T cells were gated for T cell subpopulations. (**B**) In some cases, $CD3^+CD4^+$ or $CD3^+CD8^+$ cells were gated separately. (**C, D**) Number or frequency of infiltrated CD4 and CD8 T cell populations. (**E**) CpG2 and CpG4 groups showed increased frequency of the $CD8^+CD44^+$ memory cell population. (**F**) Gating for T memory cell sub-populations by CD62L and CD127. (**G**) CpG2 showed significantly increased T effector memory

$CD4^+CD127^+CD62L^-$ T cell and effector $CD4^+CD127^-CD62L^-$ T cell population compared to relevant controls. (**H**) CpG2 showed significantly increased $CD8^+CD127^-CD62L^-$ effector and effector memory $CD8^+CD127^+CD62L^-$ T cell population compared to relevant controls. (**I**) Representative scatter plots of $CD4^+$ $TNF\alpha^+$ population. (**J**) The $CD4^+$ $TNF\alpha^+$ population was significantly downregulated in CpG2 group. (**K**) The $CD8^+$ $TNF\alpha^+$ subpopulation frequency did not show an obvious difference among various groups. (**L**) Representative scatter plots of the $CD4^+$ Treg subpopulation in the tumor environment of treated mice. (**M**) Quantification of $Gr\text{-}1^+CD11b^+$ myeloid-derived suppressor cells in tumor tissue. For all the graphs in this figure, n=5 tumor samples from independent mice. Data are presented as mean values +/- SEM. One-way ANOVA was applied for statistical analysis of the flow results with Tukey's post hoc multiple comparisons test. '*' refers to $P \leq 0.05$; '**' refers to $P \leq 0.01$.

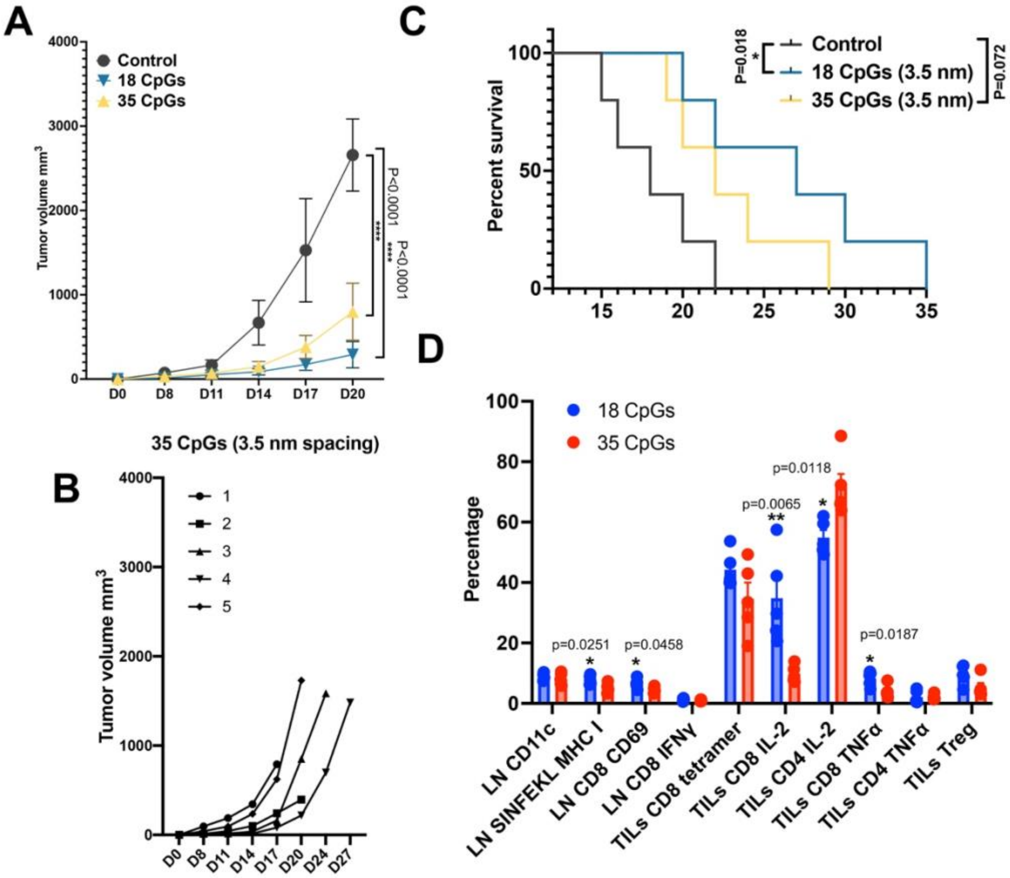

Supplementary Figure 27. 35 CpGs at 3.5 nm spacing showed reduced therapeutic effects compared to 18 CpGs at the same spacing when administered on the DNA origami SQB platform. (**A**) Tumor growth was not significantly different between 18 CpGs and 35 CpGs treated groups (n=5 mice). (**B**) Tumor growth curves of all 5 mice treated with the 35 CpGs per SQB vaccine showed similar profiles (Tumor growth curve of mice treated with 18 CpGs per SQB vaccine is shown in Supplementary Figure 23E: CpG2). (**C**) Survival curves of the DoriVac treated groups with 35 CpGs compared to 18 CpGs. The DoriVac with 35 CpGs per SQB group had median survival of 22 days versus 26 days in 18 CpGs group. (**D**) Immune cell profiling showed significant differences between the different treatment groups, n=5 samples from independent mice either from LN or TILs (tumor infiltrated lymphocytes). The differences were mainly associated with cross-presentation and CD8 T cell response. 35 CpGs induced less CD8 activation but increased the CD4$^+$ IL-2$^+$ population. Data are presented as mean values +/- SEM. Two-way ANOVA was applied for statistical analysis of graph A with Tukey's post hoc multiple comparisons test. Two-tailed student t-test was applied for statistical analysis of graph D. '*' refers to $P \leq 0.05$; '**' refers to $P \leq 0.01$; '***' refers to $P \leq 0.001$; '****' refers to $P \leq 0.0001$.

.

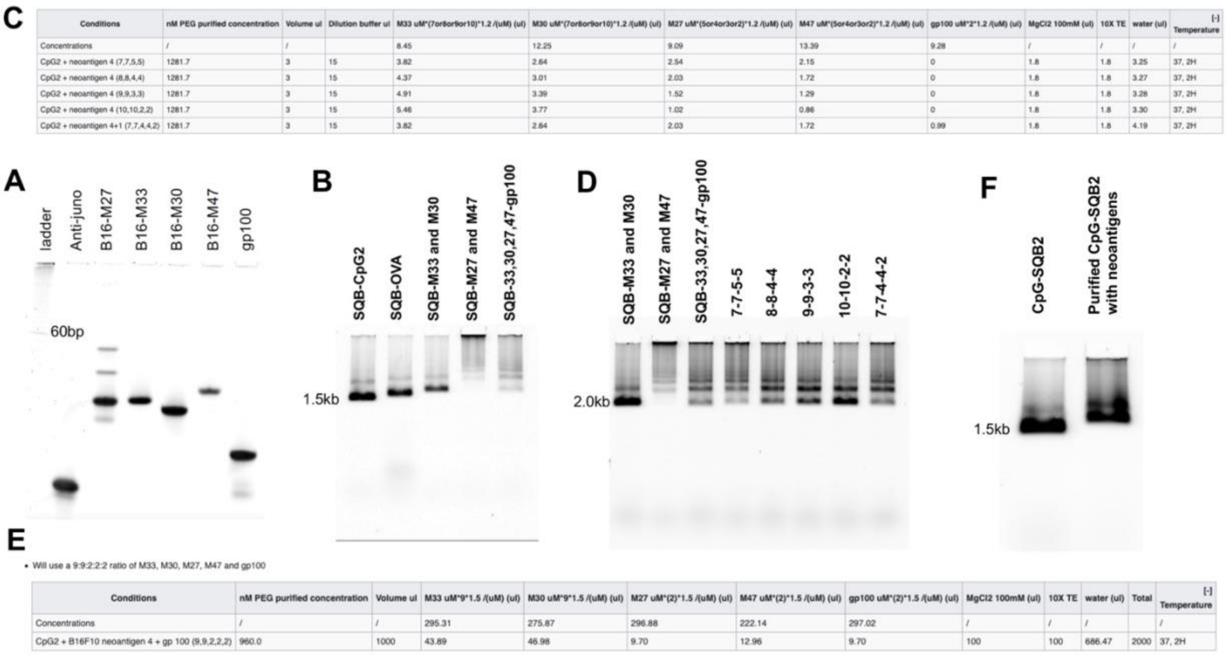

Conditions	nM PEG purified concentration	Volume ul	Dilution buffer ul	M33 uM*(7or8or9or10)*1.2 /(uM) (ul)	M30 uM*(7or8or9or10)*1.2 /(uM) (ul)	M27 uM*(5or4or3or2)*1.2 /(uM) (ul)	M47 uM*(5or4or3or2)*1.2 /(uM) (ul)	gp100 uM*2*1.2 /(uM) (ul)	MgCl2 100mM (ul)	10X TE	water (ul)	[-] Temperature
Concentrations	/	/		8.45	12.25	9.09	13.39	9.28	/	/	/	/
CpG2 + neoantigen 4 (7,7,5,5)	1281.7	3	15	3.82	2.64	2.54	2.15	0	1.8	1.8	3.25	37, 2H
CpG2 + neoantigen 4 (8,8,4,4)	1281.7	3	15	4.37	3.01	2.03	1.72	0	1.8	1.8	3.27	37, 2H
CpG2 + neoantigen 4 (9,9,3,3)	1281.7	3	15	4.91	3.39	1.52	1.29	0	1.8	1.8	3.28	37, 2H
CpG2 + neoantigen 4 (10,10,2,2)	1281.7	3	15	5.46	3.77	1.02	0.86	0	1.8	1.8	3.30	37, 2H
CpG2 + neoantigen 4+1 (7,7,4,4,2)	1281.7	3	15	3.82	2.64	2.03	1.72	0.99	1.8	1.8	4.19	37, 2H

- Will use a 9:9:2:2:2 ratio of M33, M30, M27, M47 and gp100

Conditions	nM PEG purified concentration	Volume ul	M33 uM*9*1.5 /(uM) (ul)	M30 uM*9*1.5 /(uM) (ul)	M27 uM*(2)*1.5 /(uM) (ul)	M47 uM*(2)*1.5 /(uM) (ul)	gp100 uM*(2)*1.5 /(uM) (ul)	MgCl2 100mM (ul)	10X TE	water (ul)	Total	[-] Temperature
Concentrations	/	/	295.31	275.87	296.88	222.14	297.02	/	/	/		/
CpG2 + B16F10 neoantigen 4 + gp 100 (9,9,2,2,2)	960.0	1000	43.89	46.98	9.70	12.96	9.70	100	100	686.47	2000	37, 2H

Supplementary Figure 28. Fabrication of neoantigen vaccines. (**A**) Denaturing page gel showing conjugated neoantigen peptides or tumor associated peptide (gp100) with single stranded oligo DNA using DBCO-Azide click chemistry. These products were purified through band cutting and ethanol precipitation. (**B**) Agarose gel result showing conjugation of neoantigens with CpG2-SQB. Conjugation with M33 and M30 did not lead to aggregation while, conjugation with M27 and M47 did. (**C**) A protocol showing how different proportions of the peptides were tested, while maintaining a constant total number of MHC I and MHC II peptides identical. (**D**) Agarose gel result showing the testing of different proportions of peptides. (**E**) A protocol demonstrating how we fabricated the vaccine eventually for the animal study. (**F**) Agarose gel result showing purified neoantigen DoriVac compared to the CpG2-SQB.

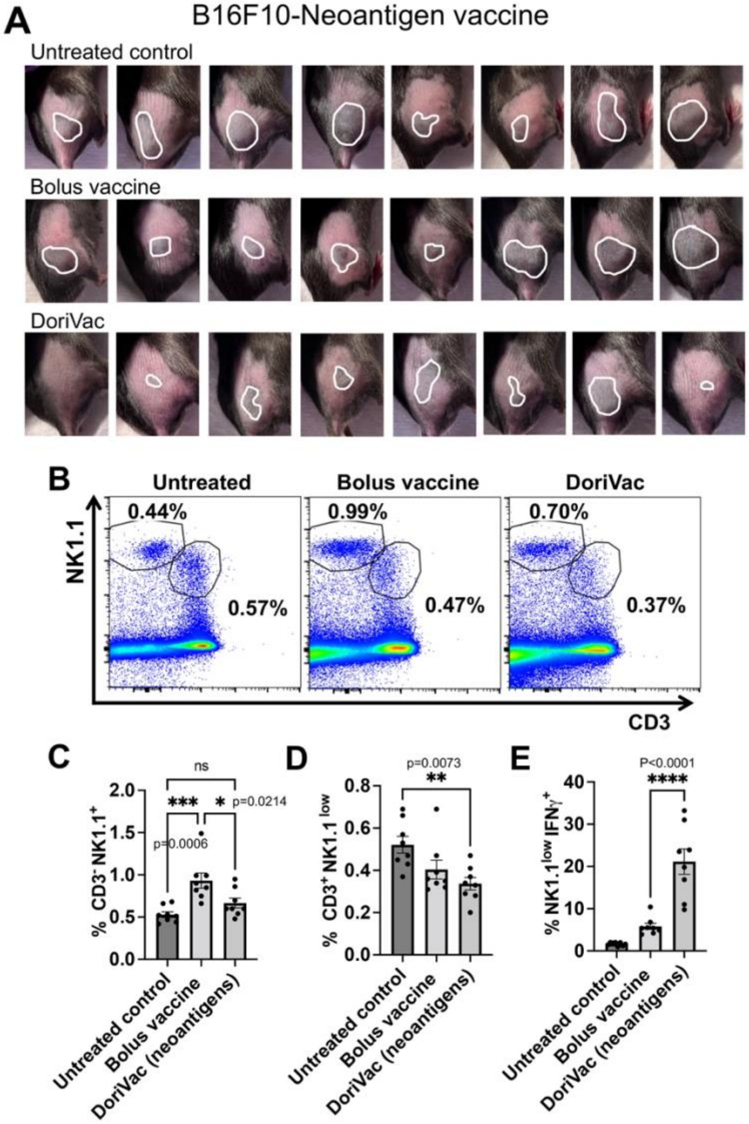

Supplementary Figure 29. Neoantigen modified DoriVac treatment in B16F10 melanoma model.(**A**) Tumor images were taken on day 12 post tumor inoculation. (**B-D**) Representative scatter plots and percentages of NK cells in the draining LN. NK1.1 and CD3 were plotted together to evaluate the NK1.1^{+}CD3^{-} and NK1.1^{low}CD3^{+} populations. (**E**) Percentages of IFNγ expression NK cells in the NK1.1^{low}CD3^{+} population. For C-E, n=8 lymph node samples from independent mice. Data are presented as mean values +/- SEM. One-way ANOVA was applied for statistical analysis of graph C-E with Tukey's post hoc multiple comparisons test. '*' refers to $P \leq 0.05$; '**' refers to $P \leq 0.01$; '***' refers to $P \leq 0.001$; '****' refers to $P \leq 0.0001$.

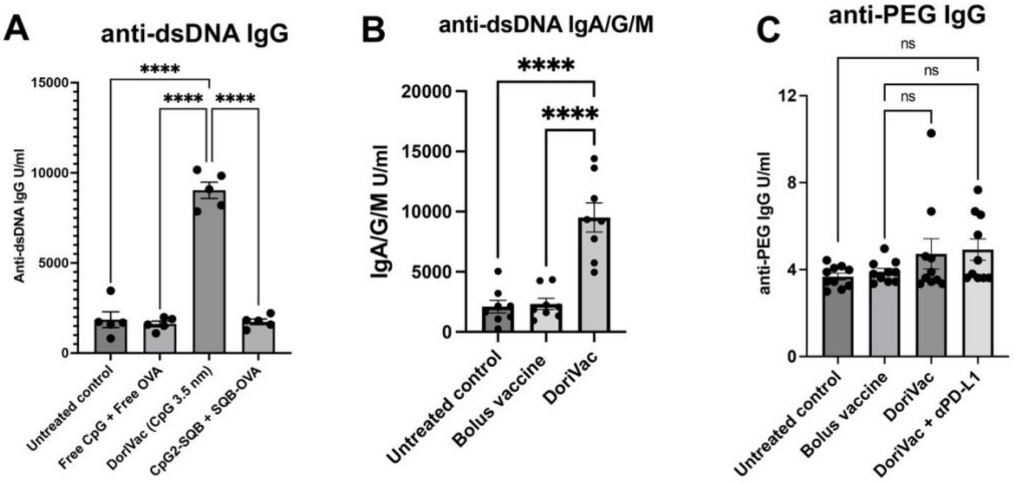

Supplementary Figure 30. Immunogenicity of DNA origami. (**A**) The anti-dsDNA IgG antibody titer was measured by ELISA after administering 3 doses of 20 pmol DoriVac in the B16OVA tumor model. Note that the group of CpG2-SQB + SQB-OVA was treated with 40 pmole of SQB nanoparticles to include same amount of OVA and CpG with DoriVac. However, this group didn't show increased anti-dsDNA IgG, indicating that the anti-dsDNA IgG might not be correlated with DNA origami nanoparticle used for treatment (n=5 plasma samples from independent mice). By analyzing anti-tumor effect occurred by DoriVac, the increase in anti-dsDNA IgG may be attributed to their anti-tumor effects. (**B**) The anti-dsDNA IgA/G/M antibody titer in the blood was measured after administering 3 doses of 20 pmol DoriVac in the B16F10 tumor model. The titer showed a four-fold increase compared to the control and bolus vaccine groups (n=8 plasma samples from independent mice). (**C**) The anti-PEG IgG antibody titer was measured by ELISA after administering 3 doses of 20 pmol DoriVac in the B16OVA tumor model. No significant elevation of anti-PEG IgG was observed in mouse serum (n=10 plasma samples from independent mice). Data are presented as mean values +/- SEM. One-way ANOVA was applied for statistical analysis with Tukey's post hoc multiple comparisons test. '****' refers to $P \leq 0.0001$.

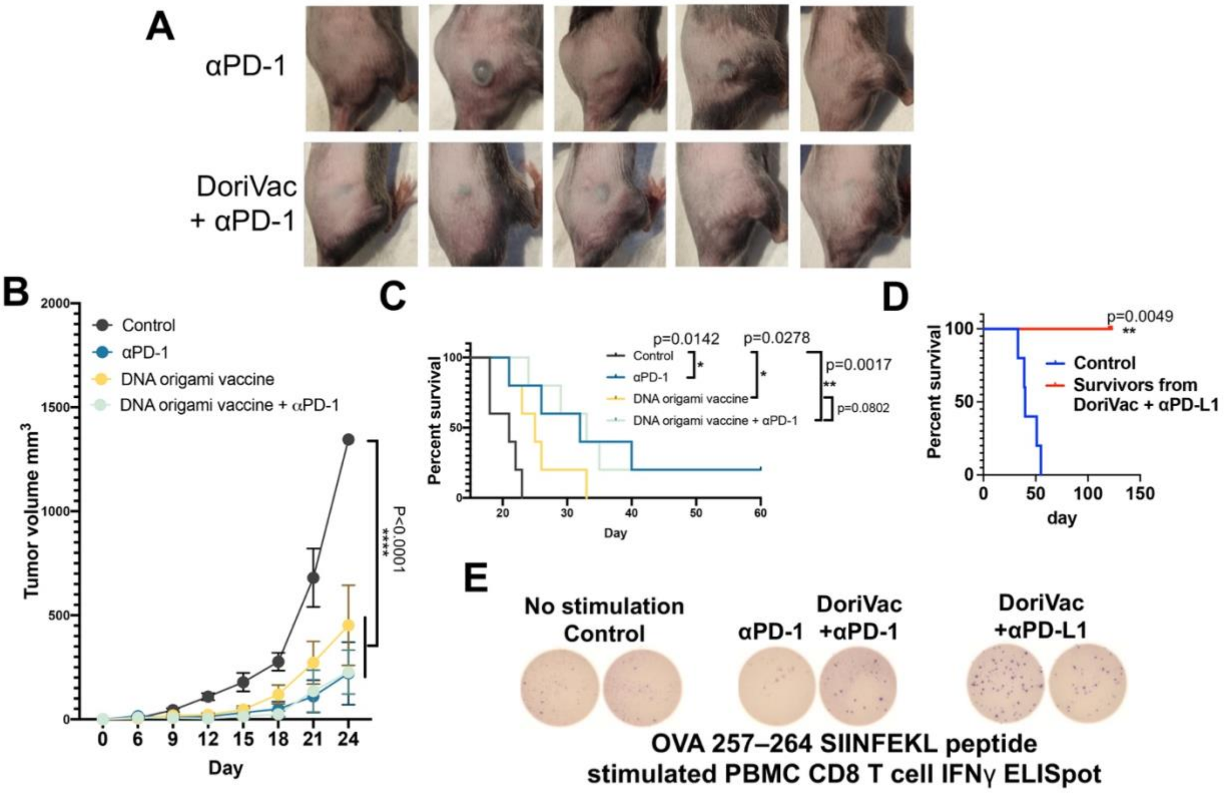

Supplementary Figure 31. DoriVac treatment combined with αPD-L1 or αPD-1 for melanoma. (**A**) Tumor images were taken on day 12 post tumor inoculation. (**B**) Tumor growth curve. DoriVac combination with αPD-1 did not exhibit synergy effects. αPD-1 was applied at the same time points and doses as αPD-L1 (n=5 mice).(**C**) Percent survival of B16-OVA tumor-bearing mice in various treatment groups. The median survival of untreated control, DoriVac treated, αPD-1treated and combination treated groups are 21, 25, 32, and 33 days, respectively. One mouse from the αPD-1 monotherapy group and one mouse from the combination group showed durable tumor regression and survived. n=5 mice. (**D**) The survival curve of mice from DoriVac and αPD-L1 combination group compared to controls. The survived mice were rechallenged with 2×10^5 B16-OVA tumor cells after 4 months. All the survived mice from the treatment groups (αPD-1(n=1), DoriVac + αPD-1(n=1) and DoriVac + αPD-L1 (n=4)) showed complete tumor remission after rechallenging. (**E**) One year after tumor rechallenging, before we sacrificed the mice, we took blood samples and performed an IFNγ ELISpot experiment on the survived mice PBMCs, stimulating with SIINFEKL peptides to look at the quantity of antigen-specific T cell responses. All the DoriVac applied groups showed obvious CD8 T cell responses as evidenced by the IFNγ spots. Two mice from DoriVac + αPD-L1 group were sacrificed in advance for student practice purposes and were not able to be tested for ELISpot. Data are presented as mean values +/- SEM in graph B. One-way ANOVA was applied for statistical analysis with Tukey's post hoc multiple comparisons test. '****' refers to $P \leq 0.0001$ compared all other groups with the untreated control. Survival curves were analyzed by Kaplan-Meier method and log-rank test for graphs C and D. '*' refers to $P \leq 0.05$; '**' refers to $P \leq 0.01$. In graph C, '**' refers to $P \leq 0.01$ comparing the two groups.

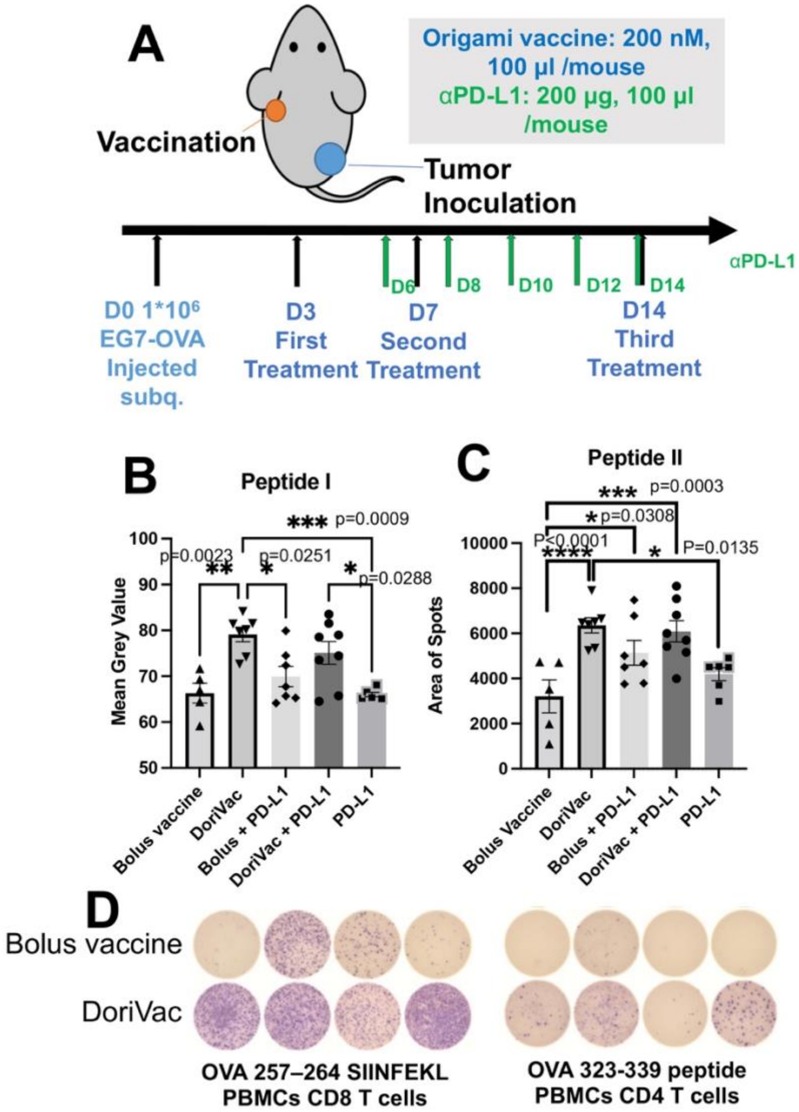

Supplementary Figure 32. DoriVac treatment in EG7-OVA lymphoma model.(**A**) Schematic delineating mouse EG7-OVA lymphoma model setup and therapeutic vaccination treatment plan in C57BL/6 mice. (**B, C**) Statistical summary of the splenocyte ELISpot results of Fig. 6G, H (n=5-8 splenocytes from independent mice, based on how many mice survived in different group). (**D**) ELISpot results showing the memory CD8 T cells in PBMCs 6 months after the tumor rechallenge in EG7-OVA model, comparing the bolus vaccine and DoriVac group. Data are presented as mean values +/- SEM in graph B and C. One-way ANOVA was applied for statistical analysis with Tukey's post hoc multiple comparisons test. '*' refers to $P \leq 0.05$; '**' refers to $P \leq 0.01$; '***' refers to $P \leq 0.001$; '****' refers to $P \leq 0.0001$.

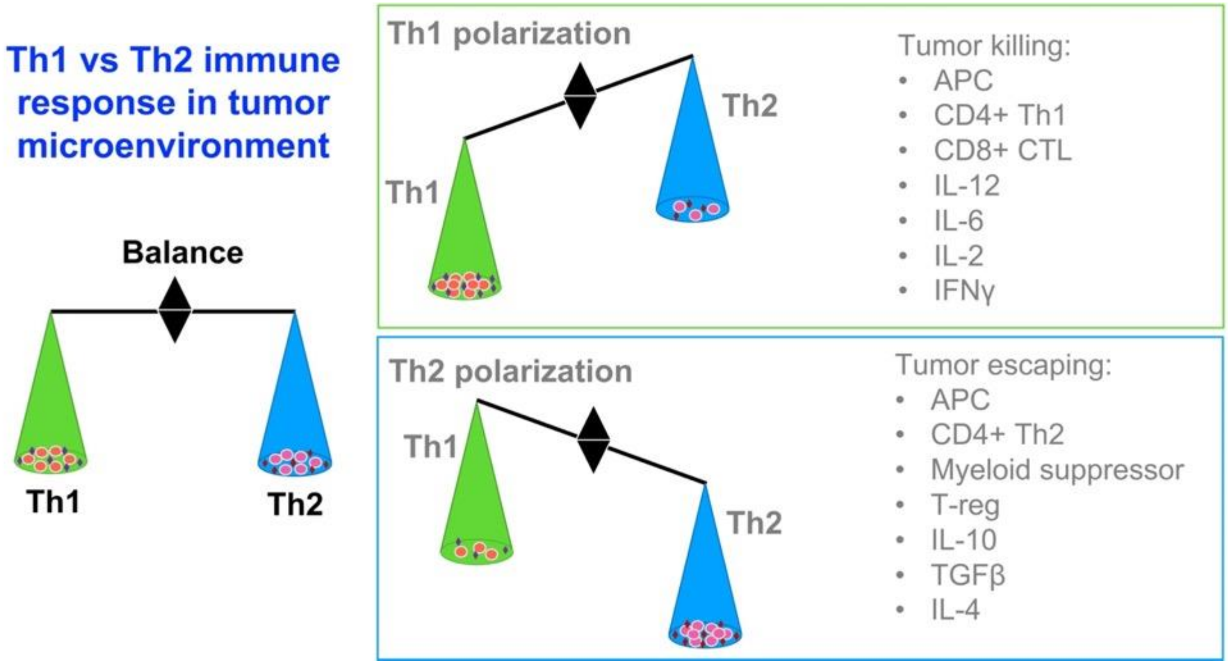

Supplementary Figure 33. Summary of Th1 versus Th2 immune polarization. (A) Conventionally, type I (Th1) and type II (Th2) refer to two categories of CD4 positive T helper cells. However, in the context of the tumor immune microenvironment, Th1 and Th2 refer to two types of immune polarization characterized by specific infiltrating cells and cytokines. Th1 polarized immune responses are associated with increased DC maturation, Th1 polarization of CD4 cells, CD8-mediated killing of tumor cells and increased cancer regression. IL-12, IL-6, IFNγ and IL-2 are identified as critical Th1-polarizing cytokines. In the context of Th2 immune polarization, the tumor can escape immune surveillance. The Th2-polarized microenvironment is characterized by Th2-polarized CD4 cells, T regulatory cells, myeloid suppressor cells and cytokines IL-10, TGFβ and IL-4, which serve to dampen the anti-tumor response. One factor that may affect Th1 or Th2 immune polarization is the choice of immune adjuvant, such as CpG and dsRNA. In this experiment, SQBs co-delivering antigen and adjuvant CpG at optimal spacing induces improved Th1-polarized immune response which is beneficial for anti-tumor immunity.

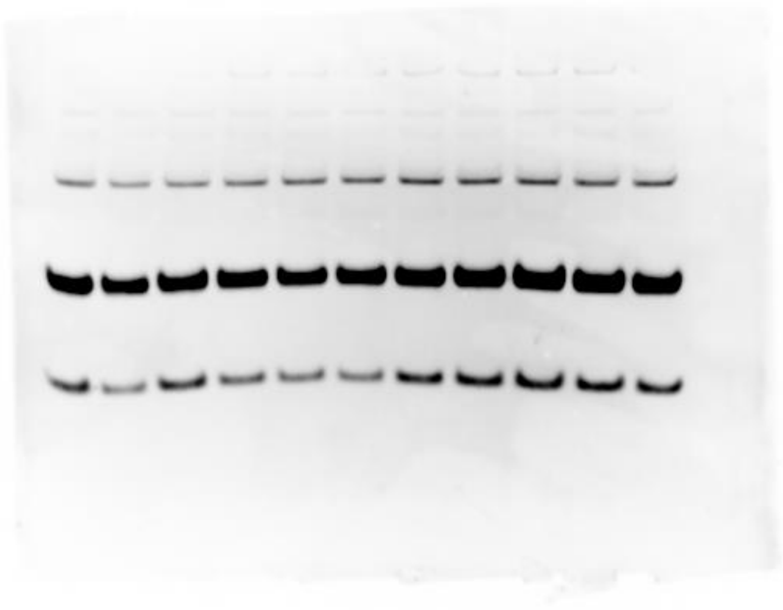

Supplementary Figure 34. Full scan for Supplementary Figure 17G, starting from the second lane to the ninth lane.

DNA scaffold for SQB | p8634 sequence

```
AATGCTACTACTATTAGTAGAATTGATGCCACCTTTTCAGCTCGCGCCCCAAATGAAAATATAGCTAAACAGGTTATT
GACCATTTGCGAAATGTATCTAATGGTCAAACTAAATCTACTCGTTCGCAGAATTGGGAATCAACTGTTATATGGAA
TGAAACTTCCAGACACCGTACTTTAGTTGCATATTTAAAACATGTTGAGCTACAGCATTATATTCAGCAATTAAGCTC
TAAGCCATCCGCAAAAATGACCTCTTATCAAAAGGAGCAATTAAAGGTACTCTCTAATCCTGACCTGTTGGAGTTTG
CTTCCGGTCTGGTTCGCTTTGAAGCTCGAATTAAAACGCGATATTTGAAGTCTTTCGGGCTTCCTCTTAATCTTTTTG
ATGCAATCCGCTTTGCTTCTGACTATAATAGTCAGGGTAAAGACCTGATTTTTGATTTATGGTCATTCTCGTTTTCTG
AACTGTTTAAAGCATTTGAGGGGGATTCAATGAATATTTATGACGATTCCGCAGTATTGGACGCTATCCAGTCTAAA
CATTTTACTATTACCCCCTCTGGCAAAACTTCTTTTGCAAAAGCCTCTCGCTATTTTGGTTTTTATCGTCGTCTGGTAA
ACGAGGGTTATGATAGTGTTGCTCTTACTATGCCTCGTAATTCCTTTTGGCGTTATGTATCTGCATTAGTTGAATGT
GGTATTCCTAAATCTCAACTGATGAATCTTTCTACCTGTAATAATGTTGTTCCGTTAGTTCGTTTTATTAACGTAGATT
TTTCTTCCCAACGTCCTGACTGGTATAATGAGCCAGTTCTTAAAATCGCATAAGGTAATTCACAATGATTAAAGTTGA
AATTAAACCATCTCAAGCCCAATTTACTACTCGTTCTGGTGTTTCTCGTCAGGGCAAGCCTTATTCACTGAATGAGCA
GCTTTGTTACGTTGATTTGGGTAATGAATATCCGGTTCTTGTCAAGATTACTCTTGATGAAGGTCAGCCAGCCTATG
CGCCTGGTCTGTACACCGTTCATCTGTCCTCTTTCAAAGTTGGTCAGTTCGGTTCCCTTATGATTGACCGTCTGCGCC
TCGTTCCGGCTAAGTAACATGGAGCAGGTCGCGGATTTCGACACAATTTATCAGGCGATGATACAAATCTCCGTTGT
ACTTTGTTTCGCGCTTGGTATAATCGCTGGGGGTCAAAGATGAGTGTTTTAGTGTATTCTTTTGCCTCTTTCGTTTTA
GGTTGGTGCCTTCGTAGTGGCATTACGTATTTTACCCGTTTAATGGAAACTTCCTCATGAAAAAGTCTTTAGTCCTCA
AAGCCTCTGTAGCCGTTGCTACCCTCGTTCCGATGCTGTCTTTCGCTGCTGAGGGTGACGATCCCGCAAAAGCGGCC
TTTAACTCCCTGCAAGCCTCAGCGACCGAATATATCGGTTATGCGTGGGCGATGGTTGTTGTCATTGTCGGCGCAAC
TATCGGTATCAAGCTGTTTAAGAAATTCACCTCGAAAGCAAGCTGATAAACCGATACAATTAAAGGCTCCTTTTGGA
GCCTTTTTTTTGGAGATTTTCAACGTGAAAAAATTATTATTCGCAATTCCTTTAGTTGTTCCTTTCTATTCTCACTCCG
CTGAAACTGTTGAAAGTTGTTTAGCAAAATCCCATACAGAAAATTCATTTACTAACGTCTGGAAAGACGACAAAACT
TTAGATCGTTACGCTAACTATGAGGGCTGTCTGTGGAATGCTACAGGCGTTGTAGTTTGTACTGGTGACGAAACTC
AGTGTTACGGTACATGGGTTCCTATTGGGCTTGCTATCCCTGAAAATGAGGGTGGTGGCTCTGAGGGTGGCGGTT
CTGAGGGTGGCGGTTCTGAGGGTGGCGGTACTAAACCTCCTGAGTACGGTGATACACCTATTCCGGGCTATACTTA
TATCAACCCTCTCGACGGCACTTATCCGCCTGGTACTGAGCAAAACCCCGCTAATCCTAATCCTTCTCTTGAGGAGTC
TCAGCCTCTTAATACTTTCATGTTTCAGAATAATAGGTTCCGAAATAGGCAGGGGGCATTAACTGTTTATACGGGCA
CTGTTACTCAAGGCACTGACCCCGTTAAAACTTATTACCAGTACACTCCTGTATCATCAAAAGCCATGTATGACGCTT
ACTGGAACGGTAAATTCAGAGACTGCGCTTTCCATTCTGGCTTTAATGAGGATTTATTTGTTTGTGAATATCAAGGC
CAATCGTCTGACCTGCCTCAACCTCCTGTCAATGCTGGCGGCGGCTCTGGTGGTGGTTCTGGTGGCGGCTCTGAGG
GTGGTGGCTCTGAGGGTGGCGGTTCTGAGGGTGGCGGCTCTGAGGGAGGCGGTTCCGGTGGTGGCTCTGGTTCC
GGTGATTTTGATTATGAAAAGATGGCAAACGCTAATAAGGGGGCTATGACCGAAAATGCCGATGAAAACGCGCTAC
AGTCTGACGCTAAAGGCAAACTTGATTCTGTCGCTACTGATTACGGTGCTGCTATCGATGGTTTCATTGGTGACGTT
TCCGGCCTTGCTAATGGTAATGGTGCTACTGGTGATTTTGCTGGCTCTAATTCCCAAATGGCTCAAGTCGGTGACGG
TGATAATTCACCTTTAATGAATAATTTCCGTCAATATTTACCTTCCCTCCCTCAATCGGTTGAATGTCGCCCTTTTGTC
TTTGGCGCTGGTAAACCATATGAATTTTCTATTGATTGTGACAAAATAAACTTATTCCGTGGTGTCTTTGCGTTTCTT
TTATATGTTGCCACCTTTATGTATGTATTTTCTACGTTTGCTAACATACTGCGTAATAAGGAGTCTTAATCATGCCAG
TTCTTTTGGGTATTCCGTTATTATTGCGTTTCCTCGGTTTCCTTCTGGTAACTTTGTTCGGCTATCTGCTTACTTTTCT
TAAAAAGGGCTTCGGTAAGATAGCTATTGCTATTTCATTGTTTCTTGCTCTTATTATTGGGCTTAACTCAATTCTTGT
GGGTTATCTCTCTGATATTAGCGCTCAATTACCCTCTGACTTTGTTCAGGGTGTTCAGTTAATTCTCCCGTCTAATGC
GCTTCCCTGTTTTTATGTTATTCTCTCTGTAAAGGCTGCTATTTTCATTTTTGACGTTAAACAAAAAATCGTTTCTTAT
TTGGATTGGGATAAATAATATGGCTGTTTATTTTGTAACTGGCAAATTAGGCTCTGGAAAGACGCTCGTTAGCGTT
GGTAAGATTCAGGATAAAATTGTAGCTGGGTGCAAAATAGCAACTAATCTTGATTTAAGGCTTCAAAACCTCCCGCA
AGTCGGGAGGTTCGCTAAAACGCCTCGCGTTCTTAGAATACCGGATAAGCCTTCTATATCTGATTTGCTTGCTATTG
GGCGCGGTAATGATTCCTACGATGAAAATAAAAACGGCTTGCTTGTTCTCGATGAGTGCGGTACTTGGTTTAATACC
CGTTCTTGGAATGATAAGGAAAGACAGCCGATTATTGATTGGTTTCTACATGCTCGTAAATTAGGATGGGATATTAT
TTTTCTTGTTCAGGACTTATCTATTGTTGATAAACAGGCGCGTTCTGCATTAGCTGAACATGTTGTTTATTGTCGTCG
TCTGGACAGAATTACTTTACCTTTTGTCGGTACTTTATATTCTCTTATTACTGGCTCGAAAATGCCTCTGCCTAAATTA
CATGTTGGCGTTGTTAAATATGGCGATTCTCAATTAAGCCCTACTGTTGAGCGTTGGCTTTATACTGGTAAGAATTT
GTATAACGCATATGATACTAAACAGGCTTTTTCTAGTAATTATGATTCCGGTGTTTATTCTTATTTAACGCCTTATTTA
TCACACGGTCGGTATTTCAAACCATTAAATTTAGGTCAGAAGATGAAATTAACTAAAATATATTTGAAAAAGTTTTCT
CGCGTTCTTTGTCTTGCGATTGGATTTGCATCAGCATTTACATATAGTTATATAACCCAACCTAAGCCGGAGGTTAAA
AAGGTAGTCTCTCAGACCTATGATTTTGATAAATTCACTATTGACTCTTCTCAGCGTCTTAATCTAAGCTATCGCTAT
GTTTTCAAGGATTCTAAGGGAAAATTAATTAATAGCGACGATTTACAGAAGCAAGGTTATTCACTCACATATATTGA
TTTATGTACTGTTTCCATTAAAAAAGGTAATTCAAATGAAATTGTTAAATGTAATTAATTTTGTTTTCTTGATGTTTGT
TTCATCATCTTCTTTTGCTCAGGTAATTGAAATGAATAATTCGCCTCTGCGCGATTTTGTAACTTGGTATTCAAAGCA
ATCAGGCGAATCCGTTATTGTTTCTCCCGATGTAAAAGGTACTGTTACTGTATATTCATCTGACGTTAAACCTGAAAA
TCTACGCAATTTCTTTATTTCTGTTTTACGTGCAAATAATTTTGATATGGTAGGTTCTAACCCTTCCATTATTCAGAAG
TATAATCCAAACAATCAGGATTATATTGATGAATTGCCATCATCTGATAATCAGGAATATGATGATAATTCCGCTCCT
TCTGGTGGTTTCTTTGTTCCGCAAAATGATAATGTTACTCAAACTTTTAAAATTAATAACGTTCGGGCAAAGGATTTA
ATACGAGTTGTCGAATTGTTTGTAAAGTCTAATACTTCTAAATCCTCAAATGTATTATCTATTGACGGCTCTAATCTA
TTAGTTGTTAGTGCTCCTAAAGATATTTTAGATAACCTTCCTCAATTCCTTTCAACTGTTGATTTGCCAACTGACCAGA
```

TATTGATTGAGGGTTTGATATTTGAGGTTCAGCAAGGTGATGCTTTAGATTTTTCATTTGCTGCTGGCTCTCAGCGT
GGCACTGTTGCAGGCGGTGTTAATACTGACCGCCTCACCTCTGTTTTATCTTCTGCTGGTGGTTCGTTCGGTATTTT
TAATGGCGATGTTTTAGGGCTATCAGTTCGCGCATTAAAGACTAATAGCCATTCAAAAATATTGTCTGTGCCACGTA
TTCTTACGCTTTCAGGTCAGAAGGGTTCTATCTCTGTTGGCCAGAATGTCCCTTTTATTACTGGTCGTGTGACTGGT
GAATCTGCCAATGTAAATAATCCATTTCAGACGATTGAGCGTCAAAATGTAGGTATTTCCATGAGCGTTTTTCCTGTT
GCAATGGCTGGCGGTAATATTGTTCTGGATATTACCAGCAAGGCCGATAGTTTGAGTTCTTCTACTCAGGCAAGTG
ATGTTATTACTAATCAAAGAAGTATTGCTACAACGGTTAATTTGCGTGATGGACAGACTCTTTTACTCGGTGGCCTC
ACTGATTATAAAAACACTTCTCAGGATTCTGGCGTACCGTTCCTGTCTAAAATCCCTTTAATCGGCCTCCTGTTTAGC
TCCCGCTCTGATTCTAACGAGGAAAGCACGTTATACGTGCTCGTCAAAGCAACCATAGTACGCGCCCTGTAGCGGCG
CATTAAGCGCGGCGGGTGTGGTGGTTACGCGCAGCGTGACCGCTACACTTGCCAGCGCCCTAGCGCCCGCTCCTTT
CGCTTTCTTCCCTTCCTTTCTCGCCACGTTCGCCGGCTTTCCCCGTCAAGCTCTAAATCGGGGGCTCCCTTTAGGGTT
CCGATTTAGTGCTTTACGGCACCTCGACCCCAAAAAACTTGATTTGGGTGATGGTTCACGTAGTGGGCCATCGCCCT
GATAGACGGTTTTTCGCCCTTTGACGTTGGAGTCCACGTTCTTTAATAGTGGACTCTTGTTCCAAACTGGAACAACA
CTCAACCCTATCTCGGGCTATTCTTTTGATTTATAAGGGATTTTGCCGATTTCGGAACCACCATCAAACAGGATTTTC
GCCTGCTGGGGCAAACCAGCGTGGACCGCTTGCTGCAACTCTCTCAGGGCCAGGCGGTGAAGGGCAATCAGCTGT
TGCCCGTCTCACTGGTGAAAAGAAAAACCACCCTGGCGCCCAATACGCAAACCGCCTCTCCCCGCGCGTTGGCCGAT
TCATTAATGCAGCTGGCACGACAGGTTTCCCGACTGGAAAGCGGGCAGTGAGCGCAACGCAATTAATGTGAGTTAG
CTCACTCATTAGGCACCCCAGGCTTTACACTTTATGCTTCCGGCTCGTATGTTGTGTGGAATTGTGAGCGGATAACA
ATTTCACACAGGAAACAGCTATGACCATGATTACGAATTCGAGCTCGGTACCCGGGGATCCATTCTCCTGTGACTCG
GAAGTGCATTTATCATCTCCATAAAACAAAACCCGCCGTAGCGAGTTCAGATAAAATAAATCCCCGCGAGTGCGAGG
ATTGTTATGTAATATTGGGTTTAATCATCTATATGTTTTGTACAGAGAGGGCAAGTATCGTTTCCACCGTACTCGTG
ATAATAATTTTGCACGGTATCAGTCATTTCTCGCACATTGCAGAATGGGGATTTGTCTTCATTAGACTTATAAACCTT
CATGGAATATTTGTATGCCGACTCTATATCTATACCTTCATCTACATAAACACCTTCGTGATGTCTGCATGGAGACAA
GACACCGGATCTGCACAACATTGATAACGCCCAATCTTTTTGCTCAGACTCTAACTCATTGATACTCATTTATAAACTC
CTTGCAATGTATGTCGTTTCAGCTAAACGGTATCAGCAATGTTTATGTAAAGAAACAGTAAGATAATACTCAACCCG
ATGTTTGAGTACGGTCATCATCTGACACTACAGACTCTGGCATCGCTGTGAAGACGACGCGAAATTCAGCATTTTCA
CAAGCGTTATCTTTTACAAAACCGATCTCACTCTCCTTTGATGCGAATGCCAGCGTCAGACATCATATGCAGATACTC
ACCTGCATCCTGAACCCATTGACCTCCAACCCCGTAATAGCGATGCGTAATGATGTCGATAGTTACTAACGGGTCTT
GTTCGATTAACTGCCGCAGAAACTCTTCCAGGTCACCAGTGCAGTGCTTGATAACAGGAGTCTTCCCAGGATGGCG
AACAACAAGAAACTGGTTTCCGTCTTCACGGACTTCGTTGCTTTCCAGTTTAGCAATACGCTTACTCCCATCCGAGAT
AACACCTTCGTAATACTCACGCTGCTCGTTGAGTTTTGATTTTGCTGTTTCAAGCTCAACACGCAGTTTCCCTACTGT
TAGCGCAATATCCTCGTTCTCCTGGTCGCGGCGTTTGATGTATTGCTGGTTTCTTTCCCGTTCATCCAGCAGTTCCAG
CACAATCGATGGTGTTACCAATTCATGGAAAAGGTCTGCGTCAAATCCCCAGTCGTCATGCATTGCCTGCTCTGCCG
CTTCACGCAGTGCCTGAGAGTTAATTTCGCTCACTTCGAACCTCTCTGTTTACTGATAAGTTCCAGATCCTCCTGGCA
ACTTGCACAAGTCCGACAACCCTGAACGACCAGGCGTCTTCGTTCATCTATCGGATCGCCACACTCACAACAATGAG
TGGCAGATATAGCCTGGTGGTTCAGGCGGCGCATTTTTATTGCTGTGTTGCGCTGTAATTCTTCTATTTCTGATGCT
GAATCAATGATGTCTGCCATCTTTCATTAATCCCTGAACTGTTGGTTAATACGCATGAGGGTGAATGCGAATAATAA
AGCTTGGCACTGGCCGTCGTTTTACAACGTCGTGACTGGGAAAACCCTGGCGTTACCCAACTTAATCGCCTTGCAGC
ACATCCCCCTTTCGCCAGCTGGCGTAATAGCGAAGAGGCCCGCACCGATCGCCCTTCCCAACAGTTGCGCAGCCTGA
ATGGCGAATGGCGCTTTGCCTGGTTTCCGGCACCAGAAGCGGTGCCGGAAAGCTGGCTGGAGTGCGATCTTCCTG
AGGCCGATACTGTCGTCGTCCCCTCAAACTGGCAGATGCACGGTTACGATGCGCCCATCTACACCAACGTGACCTAT
CCCATTACGGTCAATCCGCCGTTTGTTCCCACGGAGAATCCGACGGGTTGTTACTCGCTCACATTTAATGTTGATGA
AAGCTGGCTACAGGAAGGCCAGACGCGAATTATTTTTGATGGCGTTCCTATTGGTTAAAAAATGAGCTGATTTAAC
AAAAATTTAATGCGAATTTTAACAAAATATTAACGTTTACAATTTAAATATTTGCTTATACAATCTTCCTGTTTTTGGG
GCTTTTCTGATTATCAACCGGGGTACATATGATTGACATGCTAGTTTTACGATTACCGTTCATCGATTCTCTTGTTTG
CTCCAGACTCTCAGGCAATGACCTGATAGCCTTTGTAGATCTCTCAAAAATAGCTACCCTCTCCGGCATTAATTTATC
AGCTAGAACGGTTGAATATCATATTGATGGTGATTTGACTGTCTCCGGCCTTTCTCACCCTTTTGAATCTTTACCTAC
ACATTACTCAGGCATTGCATTTAAAATATATGAGGGTTCTAAAAATTTTTATCCTTGCGTTGAAATAAAGGCTTCTCC
CGCAAAAGTATTACAGGGTCATAATGTTTTTGGTACAACCGATTTAGCTTTATGCTCTGAGGCTTTATTGCTTAATTT
TGCTAATTCTTTGCCTTGCCTGTATGATTTATTGGATGTT

Supplementary Table 1. Sequence of P8634.

Basic staple strands	Length and positions
GGACTCCACAGAGGTGGTCAGATGATGACCGTACTCAAAC	40mer, [0, 63] start, [26, 40] end
TTTTTTTTTTGGGCGATGGCCCCATAAACATTGCTTTTTTTTTT	44mer, [1, 17] start, [24, 17] end
AGGTGCCGTAAAGCACCGAAATCGTTGCAAGGAGCAGAAG	40mer, [3, 48] start, [24, 56] end
TTTTTTTTTTCGTGGCGAGAAATTGTCTCCATGCTTTTTTTTTT	44mer, [5, 17] start, [20, 17] end
AGAAACGCCAGGGTGGCCCCCGATACAGAGATAGTTAGAGTGGCAAAT	48mer, [5, 48] start, [31, 63] end
GCAAGTGTAGCGGTCATGCGTATTAAGGTATAGGACATTCATCCTGGG	48mer, [7, 48] start, [33, 63] end
TTTTTTTTTTTGGTTGCTTTGAGAAATGACTGATTTTTTTTTTT	44mer, [9, 17] start, [16, 17] end
TATAAAAAGTGTAAAGCGCCGCGCATCCAGAAATTCCATG	40mer, [9, 48] start, [18, 56] end
GGAACGGTACGCCGCAGGAGCTAAACAGGAGGGCCGGAAGGTGGAAAC	48mer, [12, 63] start, [17, 63] end
TTTTTTTTTTTCTGAACTCGCTACGGCGGGTTTTGTTTTATGGAG	45mer, [13, 17] start, [13, 63] end
CTCAGAATCCTGAGAAAACATATAATTATCAGTAACAGTATCAGGGTT	48mer, [15, 48] start, [45, 63] end
AACCCAATTCAGAGCGCTCGCGGGGATTTATTTTATTTTTTTTTT	45mer, [14, 47] start, [12, 17] end
TTTTTTTTTTACCGTGCAAAATAGAAACCACCAGTTTTTTTTTT	44mer, [17, 17] start, [38, 17] end
GCCTTGCTCTGCGTGTTGCCCGAAGATTCGCC	32mer, [16, 63] start, [47, 63] end
TAAGTCTAGGGCGCTGCCGCTACAGGGCGCGTACTATTTTTTTTTT	46mer, [18, 47] start, [8, 17] end
TTTTTTTTTTAGACATCACGAATAGATAATACATTTTTTTTTTT	44mer, [21, 17] start, [34, 17] end
AAAAGATTTGGGGTCGTGACGGGGAAAGCCGGCGAATTTTTTTTTT	46mer, [22, 47] start, [4, 17] end
TTTTTTTTTTTGATACCGTTTAGAACCTCAAATATTTTTTTTTT	44mer, [25, 17] start, [30, 17] end
TTTCTTTAACTACGTGAACCAAAATCCCTTAT	32mer, [24, 47] start, [1, 63] end
TATCTAAAACGTCAAAGGGCGAAAAACCGTCTATCATTTTTTTTTT	46mer, [27, 48] start, [0, 17] end
TGAGTATCAACAGTGCCAAAATCAACTGTTGG	32mer, [29, 56] start, [54, 56] end
GTTCAGGAGGTTTTCCAATAGTGACCGTGCAT	32mer, [30, 63] start, [57, 63] end
TTTTTTTTTTTCAAACCCTCAACGCATTCACCCTTTTTTTTTTT	44mer, [31, 17] start, [50, 17] end
TGGTCAGTTCTGAGCAGACATACAGCATCACCCAAATCAA	40mer, [31, 48] start, [2, 40] end
AAGGTTATTTAATGGACGGCCAGTAGTTAATTTGGGCGCA	40mer, [32, 63] start, [58, 56] end
ATAGAGCCTGGCAGATCCGGTGTCGGAAGGGA	32mer, [33, 48] start, [5, 47] end
TTTTTTTTTTTTGAGGATTTAGCCACCAGGCTATTTTTTTTTTT	44mer, [35, 17] start, [46, 17] end
GACTTTACAAGGTTTATGTAGATGGGGGCGAAAGGAGCGG	40mer, [35, 48] start, [6, 40] end
AAACAATTTCTTGTTGATCAGAAATTGAATTAAAAAATAATGGTTTGA	48mer, [35, 56] start, [60, 56] end
TATCAAAAGGTCTGCAATGTGCGACGAGCACG	32mer, [37, 48] start, [9, 47] end
TTTTTTTTTTAAGGAGCGGAATACAGAGAGGTTCTTTTTTTTTT	44mer, [39, 17] start, [42, 17] end
TATTCCTGGATGATTACGAGTACGCATCGTGCTTTCCTCG	40mer, [39, 48] start, [10, 40] end
CAGAGCAGGCAATGCATGACGACTATCCTGATTGTTTGGC	40mer, [41, 40] start, [40, 48] end
TTTTTTTTTTGAAGTGAGCGAAAAGGGTGAGAAATTTTTTTTTT	44mer, [43, 17] start, [68, 17] end
TCAGGATTATACTTCTGGAGGATCTAAAGTACCTAGCATGATTTCAAC	48mer, [43, 48] start, [73, 63] end
CTGGTCGTGGGTTTTGCGGAACAATATTATCA	32mer, [45, 48] start, [17, 47] end
GAGAAACAATATGTACACGCTCAATTAAACCA	32mer, [44, 63] start, [75, 63] end
TTTTTTTTTTATCTGCCACTCAAGAATCGCCATATTTTTTTTTT	44mer, [47, 17] start, [64, 17] end
CGCCTGAAAAGTATTAATTTTAAAACAAATCCCCATTAATTTAATGCG	48mer, [46, 47] start, [8, 48] end
AGCAATAAGTTATACAATAGGAACTCCAATAA	32mer, [46, 63] start, [77, 63] end
TTTTTTTTTTCATGCGTATTAATAAATAAGGCGTTTTTTTTTTT	44mer, [51, 17] start, [60, 17] end
TTATTATTTCAATATCTCTTTAGGTATCAATGTTGTGCCATTAGAGCT	48mer, [50, 47] start, [4, 48] end
CTGCAAGGTGAAAAATCTAAAAGGATATACTG	32mer, [52, 47] start, [24, 48] end
TTTTTTTTTTTATTACGCCAGCACTATATGTAAATTTTTTTTTT	44mer, [55, 17] start, [56, 17] end
GGGGGTATCACGCTGAGAGCCAGCTTGAGTAT	32mer, [55, 48] start, [27, 47] end
GAAGGGCGATCGGTGCGGGCCTCTTCGCTTTTTTTTTT	38mer, [54, 55] start, [54, 17] end
CTCCGGCTAATCCAAAATATAATGCTGTAGCTCAACATGT	40mer, [56, 63] start, [82, 40] end
TTTTTTTTTTTGCTGATGCAAAAGTTTCATTCCATTTTTTTTTT	44mer, [57, 17] start, [80, 17] end
TATATTTTGCCAAGCTAACGCCAGTGCGCATCACCTTGCTGCTGAAAC	48mer, [59, 48] start, [25, 47] end
TTTTTTTTTTTAAATAAGAATAAAAGGTGGCATCTTTTTTTTTT	44mer, [61, 17] start, [76, 17] end
AATCAATCCCTGATTAATGAAAGAAACAACTA	32mer, [61, 48] start, [33, 47] end
TCATATGCAAATGCGCGATTCAGCTTCTTAGAGCCGTCAAGGTGTTTA	48mer, [63, 48] start, [21, 47] end
AGGCATTTGAAGACGCATCAGTAATATCATCAACTGCGTGTAACAATC	48mer, [66, 47] start, [15, 47] end
TTTTTTTTTTTTTAACAACGCCAACATTATGACCTTTTTTTTTT	44mer, [65, 17] start, [72, 17] end
ATTTAATCATAGGCGATCCGATAGAGTAACAT	32mer, [65, 48] start, [37, 47] end
TTTTTTTTTTGGCCGGAGACAGTCAAATCACCATCAAT	38mer, [69, 17] start, [69, 55] end
ATGATATTGTCCAGACGACGATAAAGAGAATATGGAACTT	40mer, [69, 56] start, [42, 48] end
AGGCAATAAACAACATCCCTCATAAAGGTGGCGAGGCATACTTGCCCT	48mer, [71, 48] start, [101, 63] end
ATGCAATGCAGTAATAAGATTCAAATTAACTC	32mer, [70, 47] start, [43, 47] end
TTTTTTTTTTCTGTAATACTTTATTACGCAGTATTTTTTTTTTT	44mer, [73, 17] start, [94, 17] end
TCCAAGAAGCAACACTGAGGAAACGGGAATTAATAGGCTGGAACCTAT	48mer, [72, 63] start, [119, 63] end
ATAAAGCCGTTTAGTACTTAATTGTTGTTGTGAGTGTACGCGTTATTA	48mer, [74, 47] start, [36, 48] end
ATTAAGCACATTAACAGCCTAATTACTAGAAAACATCATT	40mer, [74, 55] start, [49, 47] end
TTAGCAAAATAGCCGAGTCATAAAGGACAGAT	32mer, [74, 63] start, [105, 63] end
TTTTTTTTTTAATTCTACTAATTAGCTATCTTACTTTTTTTTTT	44mer, [77, 17] start, [90, 17] end
AGCGAACCTTGAATCCACCCACAAGGCATTTT	32mer, [76, 63] start, [107, 63] end
CTTGCGGGTTTCGCAAGGGTAATTGACTTCAAACAACGGA	40mer, [79, 56] start, [109, 63] end
TAACCTGTTTTTCAAACCGTGTGACCAACAGTTCAGGTTTCTAAAATA	48mer, [78, 47] start, [32, 48] end
ATGGTCAATCTGCGAATCGCAAAGAACGCGAGAGTTGGGT	40mer, [78, 55] start, [53, 47] end
TTTTTTTTTTTATAACAGTTGATAGACGGGAGAATTTTTTTTTT	44mer, [81, 17] start, [86, 17] end

CGAGTAGAATATTATTCGTTTTAAAAAAATGACCAGAACCTACGAAGG	48mer, [81, 56] start, [110, 56] end
TGTCTGGATCCAATCGCAAGATAAATTATGTG	32mer, [80, 47] start, [52, 48] end
TAAAGCCCTAGGTTGGGTTATATATGGCGAAA	32mer, [83, 48] start, [55, 47] end
TTTTTTTTTTTTAACTGAACACTCCATGTTACTTTTTTTTTTTT	44mer, [87, 17] start, [106, 17] end
TTAAGCCCATATTTCATTTGCGAAATACCGA	32mer, [88, 47] start, [60, 48] end
TTTTTTTTTTCGAAGCCCTTTTAGTAATCTTGACTTTTTTTTTT	44mer, [91, 17] start, [102, 17] end
AACGGAATCATAAAGCTAAATGTACAGTAGGG	32mer, [92, 47] start, [64, 48] end
TTTTTTTTTTGTTAGCAAACGTAATTTCAACTTTTTTTTTTTTT	44mer, [95, 17] start, [98, 17] end
GAATAGATCATACATATATTTTAAAAGCCTTTTCAGGCAG	40mer, [96, 55] start, [66, 48] end
CATTATACCAGTCAGGACGTTGGGACACCACG	32mer, [97, 40] start, [96, 56] end
TTTTTTTTTTAATCATTGTGAAACCGCCACCCTCTTTTTTTTTT	44mer, [99, 17] start, [124, 17] end
ATTTTGTCAGTAAATTGCCCGGAAGTCTTTCCAGAGGATA	40mer, [99, 56] start, [122, 48] end
GAATAAGGGTAATTAAGACTCCTTTGCGGGAG	32mer, [101, 48] start, [73, 47] end
GTAACAAAAAGAACTGGCATGAGACGGCGGTTGTACCAAAAACATGTA	48mer, [100, 47] start, [65, 47] end
GACTTGAGTAGTAAATAAGAGGCTGAGACTCCCTATTTCGGCTGACCT	48mer, [100, 63] start, [102, 48] end
TTTTTTTTTTAAGAACCGGATAAGGATTAGGATTTTTTTTTTTT	44mer, [103, 17] start, [120, 17] end
TTGAAAGATATAATGAAATAGCAAAGTAGTAG	32mer, [105, 48] start, [77, 47] end
AAGGGAACAAGAGCAAGAAACTCATCCGGGCGCGAGCTGAAACACCGG	48mer, [104, 47] start, [61, 47] end
AGCGCGTTTAATTGTATGATGATACAGGAGTGCTGAATTTGAAATCCG	48mer, [104, 63] start, [106, 48] end
TTTTTTTTTTAGCCGGAACGAGATAAGTTTAACTTTTTTTTTTT	44mer, [107, 17] start, [116, 17] end
ATTGTGTCACCGTTCCTTAAAGGCCGCTTAAA	32mer, [106, 63] start, [114, 48] end
AACAAAGTATACAGGGAAGCGCATTTCCCAAT	32mer, [109, 48] start, [81, 47] end
CCAGCGATAATAACATAAAAATCGTATTACGG	32mer, [108, 47] start, [80, 48] end
CCTCAGAGTGCGGGATCAGGAGGTTGAGGCAG	32mer, [108, 63] start, [112, 48] end
TTTTTTTTTTGAATACACTAAATTGGCCTTGATTTTTTTTTT	42mer, [111, 17] start, [112, 17] end
CACCAACCTAAAACGAAAGAGGCAAAATTTTTTTTTT	37mer, [110, 55] start, [110, 17] end
GTCAGACGAACACTCATCTTTCCAAAATAGCAGCCTTTACTATGCAAC	48mer, [112, 47] start, [83, 47] end
TTTTTTTTTTTATTCACAAACAAATAAATCCTCATTTCCGGACCC	45mer, [113, 17] start, [108, 48] end
GCCAGAATAAGCGCGACGACCTGCCCTGAACA	32mer, [114, 47] start, [87, 47] end
CGCAGTCTTACTGGTAGCGCAGACGGTCAATCGAATTGAGAAGTCAGA	48mer, [115, 40] start, [87, 55] end
TTTTTTTTTTGGGGTCAGTGCCTTGAGTAACAGTGCTTTTCATCAT	46mer, [117, 17] start, [104, 48] end
CCAAAAGGAGCCCCGTATAAACAGGACCAACTTCATCAAGTAAGAAAA	48mer, [118, 63] start, [91, 47] end
CCCCCTGCTCAAGAGATTCATTACCCAAATTTGCAATAATGTAAGCAG	48mer, [119, 40] start, [91, 55] end
TTTTTTTTTTAGCGGGGTTTGCTCAGTACCAGGCCGTCCATCAAC	46mer, [121, 17] start, [100, 48] end
AGTGCCGTCATTCAGTGATGGTTTAGAAAATATTTAAGAATAATGTGT	48mer, [122, 47] start, [71, 47] end
GGTTGATACCCTCAGATTACCTTATGCAGTTT	32mer, [123, 40] start, [99, 55] end
TTTTTTTTTTAGAACCGCCACCCTCAGAGCCACCACCC	38mer, [125, 17] start, [125, 55] end
TCATTTTCAGGTTTAGTACCGCCATAAGTATAGGGCTTGA	40mer, [125, 56] start, [98, 48] end
TAAATCGGTATCAATGAGAACCCTAATTGAGGAAGACTCCAATTTCAT	48mer, [3, 64] start, [48, 64] end
AAAGGGAGTTTTTCTTAATAAAAGGATATAGAAACCAGTT	40mer, [4, 71] start, [34, 64] end
ACCACACCCCTGGGGTAACTATCGGATACTTGTATTGCGC	40mer, [8, 71] start, [38, 64] end
CCGATTAACTGTACAAGTGTTTTTTCAATATAGGGGATTT	40mer, [11, 64] start, [41, 71] end
TGAGGCCACTCGAATTCGTAAGATTTTAGACAATGATAAA	40mer, [15, 80] start, [13, 71] end
AGAACTCAGCCTAATGTCCACACAACATACGA	32mer, [16, 79] start, [10, 64] end
CAATATTAAAATCCTTTGAGCTTGTACATCGGGTCGGACTTCGTAAAA	48mer, [19, 64] start, [66, 64] end
CGACCAGTTTCACCAGGCGGGGAGAGGCGGTTCGCTGCGCATACAAAT	48mer, [20, 79] start, [18, 64] end
AGTTTATAGTCAATGGCAACAGTTTAAAACGAAACAGTACAAATTTAA	48mer, [25, 64] start, [60, 64] end
AGGCGGTCAGTATATATACCGAACAGAATAGCTGTTTGATGGTGGTTC	48mer, [27, 64] start, [2, 64] end
ACGCTTGTCAAGAGTCCACTATTAAAGAACGTAAATCAAAGAACCACC	48mer, [27, 80] start, [24, 64] end
AAGTAACACCGCCTGCTGCATATGGAAGAGTC	32mer, [28, 79] start, [52, 64] end
AGCACTGCCAGTCACAGAAAGCGTTGGCCCTGAGAGACCT	40mer, [33, 80] start, [4, 72] end
CGACAACTCGCAACACTGATTGCTTAAAGCCA	32mer, [35, 64] start, [64, 64] end
AAATCAAATGAGTAGACATTGCAACTGCCCGCTTTCCACC	40mer, [37, 80] start, [8, 72] end
ATGATGGCAGTTGCCAGAATAATGGTAATTCTCAACCGTT	40mer, [39, 64] start, [69, 71] end
AGAACCTACTGGAACTGCTGGTCAATAATCAG	32mer, [43, 80] start, [15, 79] end
AAAGAGCAAATATGAACGGGAAAGCAAATTAA	32mer, [42, 79] start, [14, 80] end
ACCTGCAGCGTGGATGGGAGTAAGACATTTTG	32mer, [46, 79] start, [18, 80] end
TAGAAGAATTTAACCAAATTCTTAGCAAAGAAAGTACCGCAGGAAACC	48mer, [49, 64] start, [92, 64] end
TTAATTTGGAACAAGACCCGTTAGTTGAATGG	32mer, [50, 79] start, [22, 80] end
CAGTCACGGGTGTAGATCATCTTCTAGATACAAGGTTTTGGAGAGATA	48mer, [53, 64] start, [88, 64] end
ACGTAATTTTCCCTTATATTACGGCGCTGGCAATTAAAAA	40mer, [53, 72] start, [24, 80] end
TAGGTCTGAGAGATCCGACGCTGAATGTCTGAGGTTGGAGAATAGTCT	48mer, [55, 64] start, [25, 79] end
CTTCTACCTTTTTAACCTGCCAGTAAACAGCC	32mer, [56, 79] start, [80, 64] end
ACGACGACTAGATTAAGGCACCGCTTTTGTAA	32mer, [57, 80] start, [28, 80] end
ACCCGCCTATAAATCACATTTAACTGTTATCAAAGACGGAGTCCAATC	48mer, [60, 79] start, [21, 79] end
TTCGCGTCGGCGTTTTATCATACAGCGGAATCACAAAGTTCCAGGCGC	48mer, [61, 64] start, [102, 64] end
CTGTAGCCATTAATTAATATATGTGCAGTTAATCGAAAGGTCTGACCT	48mer, [61, 80] start, [23, 79] end
ATTGTGTATTGAATACGTACCTTTAAACAGCAAACGAGGACCCGTAGC	48mer, [64, 79] start, [17, 79] end
CCCGGTTGCTTATCATGCAAGGATGGAATTAC	32mer, [65, 64] start, [94, 64] end
AAAAGCCCCAGTAACACAAGTTACAAGGTGTTATCTCATTCCGCCAGC	48mer, [65, 80] start, [19, 79] end
CGACAAAATTTTAGAAGTTCAGCTACGCAAAGAAGAAAAA	40mer, [67, 64] start, [97, 71] end
ACGCGCCTAGATCTACAAAGGAAAGAAGGGTT	32mer, [71, 80] start, [43, 79] end

AATAAAATGGTCTATCAGGTCATTACAGAAAT	32mer, [70, 79] start, [42, 80] end
TGTCTTTCATAATCAGAACGGTAATGTAATTGCGTAGATTACCAGGAG	48mer, [72, 79] start, [38, 80] end
GAACGCGATGGCCTTCGCTCATTTTTAAGCAAAAGAAGATAGTCCGTG	48mer, [76, 79] start, [34, 80] end
CCTGACATTGATCGGATTCTCCGTCGTCGCTA	32mer, [78, 79] start, [50, 80] end
TTTAGTTTGCCCGAAAGAGCGCTACCTGATAACGGTCATAATGGCTTT	48mer, [81, 64] start, [116, 64] end
ATTGCTGATAAGAAACGATTTCTTTACAAAATTTGAGGGGGTCACGTT	48mer, [82, 71] start, [58, 72] end
TTAACGTCTTCGAGCTGCCACCACGATTTGTAGCAGGGAG	40mer, [84, 71] start, [114, 64] end
AAGAGGAAGACATCTTACCAACGCTGGGATAG	32mer, [86, 79] start, [58, 80] end
CCCTCAAACAGACTGTGAACGGTGAAAAGGCTTATTCTGAAACGGAAC	48mer, [89, 64] start, [119, 79] end
TGCCAGAGAATCATTACCGCGAAGCCAAAACGTTAATATTTTTCAATT	48mer, [91, 80] start, [46, 80] end
ATCATAACCCGTCACCGACGAGAAGTTTTGTCTAGGTGTATCATACAA	48mer, [93, 64] start, [123, 79] end
AACATATAGAACGAGTACAATCAATACTCAGGAGGGATAG	40mer, [95, 64] start, [125, 71] end
TCATATGGGTAGAAAGATTCAGAAAATGCAGA	32mer, [99, 80] start, [71, 79] end
GGAGGGAAATACATAAACCAGACGTAATCGGCAGAACAAGATATTTAA	48mer, [101, 80] start, [64, 80] end
AATTATCACCTCGTTTCGCCAAAAAAATATCCCATCCTAAAATCGATG	48mer, [100, 79] start, [66, 80] end
TAAAGGTGCAGTAGCACTTTTGCAAAAGAAGAACTCATCG	40mer, [100, 87] start, [75, 79] end
GAGCCAGCAAAGTATTGAATTTTCTGTATGGGGATCTAAAACATTGAG	48mer, [103, 64] start, [101, 79] end
GATAGCAGGATAGCGTACAGTTCATATTCTAAAATCAAGAGAGTAACA	48mer, [105, 80] start, [60, 80] end
TTTAGCGTTGCTTTAACCAATACTGGCCCCAATAGCAAGCTTAAATCA	48mer, [104, 79] start, [62, 80] end
AGTTTGCCATTAGCGTAATCAGGTCTTTATCAAAGCCTTA	40mer, [104, 87] start, [79, 79] end
AGAGCTCGATACCCTGACTATTATAATTTTAT	32mer, [106, 79] start, [78, 80] end
CCGGAACCAAAAGATTAACCAGACTTGCCAGTTAATTGCTCCAGCCAG	48mer, [109, 80] start, [56, 80] end
AACCGCCAGACTAAAGTTAGAGAGTACTTTGT	32mer, [108, 87] start, [84, 72] end
AATGCCACACCACCAGAGCCGGAGCCCTCAGATCAAAGCG	40mer, [110, 71] start, [85, 79] end
AGCATTGACGTCACCCTCAGCAGCTGAGGCTTTCACACCA	40mer, [112, 71] start, [109, 79] end
AGTAAGCGTCAACAATGACAACAACCGGAACC	32mer, [115, 64] start, [106, 80] end
TCGGTTTATCAGCTTGCTCCAAAATACCCATC	32mer, [117, 64] start, [105, 79] end
AACTAAAGGTCACCAATGAAAAGAACCAGTTT	32mer, [119, 80] start, [91, 79] end
CGCCTGTAGACATTCAACCGACCAAAATCAGTTGAGATTTACAAGAAA	48mer, [123, 80] start, [70, 80] end
TTTTTTTTTTTTCCAGTTTGGAAGAAAATGCTGAATTTTTTTTTTT	46mer, [0, 110] start, [27, 110] end
TTTTTTTTTTTGCCCCAGCAGGCCGAACTGATAGCCTTTTTTTTTT	46mer, [2, 110] start, [25, 110] end
TTTTTTTTTTGCCCTTCACCGCCAAGAATACGTGGCTTTTTTTTTT	46mer, [4, 110] start, [23, 110] end
TTTTTTTTTTCATTAATGAATCGTGGATTATTTACATTTTTTTTTT	46mer, [6, 110] start, [21, 110] end
TTTTTTTTTTTGCGTTGCGCTCACAGGAAAAACGCTTTTTTTTTTT	46mer, [8, 110] start, [19, 110] end
TTTTTTTTTTAAATTGTTATCCGTTTGATTAGTAATTTTTTTTTTT	46mer, [10, 110] start, [17, 110] end
TTTTTTTTTTCCCGGGTACCGAGCCGAGTAAAAGAGTTTTTTTTTT	46mer, [12, 110] start, [15, 110] end
TGCACTTCCGAGTCACAGGAGAATGGATCTTTTTTTTTT	39mer, [13, 72] start, [13, 110] end
CCGTTTCTAGGTCATGGTCATAGCTGTTTCCTGTGTGTTTTTTTTTT	47mer, [14, 79] start, [11, 110] end
TTTTTTTTTTTCTGTCCATCACGAAACCAGCAATACTTTTTTTTTT	46mer, [14, 110] start, [39, 110] end
AATACTTCCTCACAATAGTGAGCTAACTCACATTAATTTTTTTTTTT	47mer, [17, 80] start, [9, 110] end
TTTTTTTTTTAACATCACTTGCCACTCAACGAGCAGTTTTTTTTTT	46mer, [16, 110] start, [37, 110] end
ACGCTGGCGTAAGTCGGGAAACCTGTCGTGCCAGCTGTTTTTTTTTT	47mer, [18, 79] start, [7, 110] end
TTTTTTTTTTCATGGAAATACCTCGTATTGCTAAACTTTTTTTTTT	46mer, [18, 110] start, [35, 110] end
GTCTGAAAGCCAACGCTGAGACGGGCAACAGCTGATTTTTTTTTTTT	47mer, [21, 80] start, [5, 110] end
TTTTTTTTTTTTGGCAGATTCACACTGGTGACCTGGTTTTTTTTTT	46mer, [20, 110] start, [33, 110] end
CTATTGAGAACGTTGCAGCAAGCGGTCCACGCTGGTTTTTTTTTTTT	47mer, [22, 79] start, [3, 110] end
TTTTTTTTTTACAGACAATATTTTAACTATCGACATTTTTTTTTTT	46mer, [22, 110] start, [31, 110] end
TTAATGCGGAAAATCCCCGAGATAGGGTTGAGTGTTGTTTTTTTTTT	47mer, [25, 80] start, [1, 110] end
TTTTTTTTTTCTAAAACATCGCCTTCGCATCAAAGGTTTTTTTTTT	46mer, [24, 110] start, [29, 110] end
TTTTTTTTTTTTCGCGTCGTCTTCACAGCGATGCCAGAGTCTGTAGT	47mer, [26, 110] start, [26, 64] end
TTTTTTTTTTAGAGTGAGATCGGTTCTGGTGCCGGATTTTTTTTTT	46mer, [28, 110] start, [55, 110] end
TTTTTTTTTTCATTACGCATCGCGAATCCTTGAAAATTTTTTTTTT	46mer, [30, 110] start, [53, 110] end
TTTTTTTTTTAAGAGTTTCTGCGGAGTGAATAACCTTTTTTTTTTT	46mer, [32, 110] start, [51, 110] end
TTTTTTTTTTTGGAAAGCAACGAGATGAAACAAACATTTTTTTTTT	46mer, [34, 110] start, [49, 110] end
TTTTTTTTTTCGTGAGTATTACGAAAATCGCGCAGATTTTTTTTTT	46mer, [36, 110] start, [47, 110] end
TTTTTTTTTTATCAAACGCCGCGTTCAGGTTTAACGTTTTTTTTTT	46mer, [38, 110] start, [45, 110] end
TTTTTTTTTTACCATCGATTGTGCCATATCAAAATTTTTTTTTTTT	46mer, [40, 110] start, [43, 110] end
GACGCAGACCTTTTCCATGAATTGGTAACTTTTTTTTTT	39mer, [41, 72] start, [41, 110] end
TTTTTTTTTTATTTGCACGTAAAGCCTGAGAGTCTGTTTTTTTTTT	46mer, [42, 110] start, [67, 110] end
TTTTTTTTTTTCAGATGAATATACAAAAACAGGAAGTTTTTTTTTT	46mer, [44, 110] start, [65, 110] end
TTTTTTTTTTGGCGAATTATTCATTGTTAAAATTCGTTTTTTTTTT	46mer, [46, 110] start, [63, 110] end
TTTTTTTTTTTCAAGAAAACAAAAGCTTTCATCAACTTTTTTTTTT	46mer, [48, 110] start, [61, 110] end
TTTTTTTTTTTGCTTCTGTAAATGGGAACAAACGGCTTTTTTTTTT	46mer, [50, 110] start, [59, 110] end
TTTTTTTTTTCATAGCGATAGCTAGTATCGGCCTCATTTTTTTTTT	46mer, [52, 110] start, [57, 110] end
TTTTTTTTTTAACCAGGCAAAGCGCCATTCGCCATTCAGGCTGCGCA	47mer, [54, 110] start, [54, 64] end
TTTTTTTTTTGGAAGATCGCACTCCTTTTGATAAGATTTTTTTTTT	46mer, [56, 110] start, [83, 110] end
TTTTTTTTTTGGATTGACCGTAATAACGAGCGTCTTTTTTTTTTTT	46mer, [58, 110] start, [81, 110] end
TTTTTTTTTTATTAAATGTGAGCTTAGTTGCTATTTTTTTTTTTTT	46mer, [60, 110] start, [79, 110] end
TTTTTTTTTTCATTAAATTTTGAAATCAGATATAGTTTTTTTTTTT	46mer, [62, 110] start, [77, 110] end
TTTTTTTTTTATTGTATAAGCAACAAGCCGTTTTATTTTTTTTTTT	46mer, [64, 110] start, [75, 110] end
TTTTTTTTTTGAGCAAACAAGAGTTTACGAGCATGTTTTTTTTTTT	46mer, [66, 110] start, [73, 110] end
TTTTTTTTTTAGCTATTTTTGAGGTTTATCAACAATTTTTTTTTTT	46mer, [68, 110] start, [71, 110] end

CTAGCTGATAAATTAATGCCGGAGAGGGTTTTTTTTTTT	39mer, [69, 72] start, [69, 110] end
TTTTTTTTTTAGATAAGTCCTGAAGGAATACCACATTTTTTTTTTT	46mer, [70, 110] start, [95, 110] end
TTTTTTTTTTAGAAACCAATCAAACGATAAAAACCATTTTTTTTTT	46mer, [72, 110] start, [93, 110] end
TTTTTTTTTTTTTTCATCGTAGGGGGGTAATAGTAATTTTTTTTTT	46mer, [74, 110] start, [91, 110] end
TTTTTTTTTTAAGGCTTATCCGGGAAAACGAGAATGTTTTTTTTTT	46mer, [76, 110] start, [89, 110] end
TTTTTTTTTTGCACCCAGCTACAGTCAGAAGCAAATTTTTTTTTTT	46mer, [78, 110] start, [87, 110] end
TTTTTTTTTTCCAGAGCCTAATCGGAAGCAAACTCTTTTTTTTTTT	46mer, [80, 110] start, [85, 110] end
TTTTTTTTTTGGTCATTTTTGCGGATGGCTTAGAGCTTA	39mer, [82, 110] start, [82, 72] end
TTTTTTTTTTCAACAGGTCAGGAACTTTTTCATGAGTTTTTTTTTT	46mer, [84, 110] start, [111, 110] end
TTTTTTTTTTGCGGATTGCATCAGCCTCCCTCAGAGTTTTTTTTTT	46mer, [86, 110] start, [109, 110] end
TTTTTTTTTTACCATAAATCAAATTGCCATCTTTTCTTTTTTTTTT	46mer, [88, 110] start, [107, 110] end
TTTTTTTTTTAATGTTTAGACTGCACCGTAATCAGTTTTTTTTTTT	46mer, [90, 110] start, [105, 110] end
TTTTTTTTTTAAATAGCGAGAGGCCATTACCATTAGTTTTTTTTTT	46mer, [92, 110] start, [103, 110] end
TTTTTTTTTTCAACTAATGCAGGGTAAATATTGACTTTTTTTTTTT	46mer, [94, 110] start, [101, 110] end
TTTTTTTTTTAACATTATTACAGTTTACCAGCGCCATTTTTTTTTT	46mer, [96, 110] start, [99, 110] end
TCTACGTTAATAAAACGAACTAACGGAACTTTTTTTTTT	39mer, [97, 72] start, [97, 110] end
TTTTTTTTTTAAGACAAAAGGGCGCATTCCACAGACTTTTTTTTTT	46mer, [98, 110] start, [123, 110] end
TTTTTTTTTTGGAAATTATTCATAAACAACTTTCAATTTTTTTTTT	46mer, [100, 110] start, [121, 110] end
TTTTTTTTTTCAAGGCCGGAAACGAATTGCGAATAATTTTTTTTTT	46mer, [102, 110] start, [119, 110] end
TTTTTTTTTTAGCGACAGAATCAGTGAATTTCTTAATTTTTTTTTT	46mer, [104, 110] start, [117, 110] end
TTTTTTTTTTATAATCAAAATCACCATCGCCCACGCTTTTTTTTTT	46mer, [106, 110] start, [115, 110] end
TTTTTTTTTTCCGCCACCCTCAGGCATCGGAACGAGTTTTTTTTTT	46mer, [108, 110] start, [113, 110] end
TTTTTTTTTTGAAGTTTCCATTAAACGGGTAAAATACGT	39mer, [110, 110] start, [110, 72] end
TTTTTTTTTTGGTAGCAACGGCTACAGAGGCTTTCCGCC	39mer, [112, 110] start, [112, 72] end
TTTTTTTTTTATAACCGATATATTCGGTCGCGAAAGACA	39mer, [114, 110] start, [113, 87] end
TTTTTTTTTTACAGCTTGATACCGATAGTTGCGCCGTACGCCCCCTT	47mer, [116, 110] start, [107, 79] end
TTTTTTTTTTTAATTTTTTCACGTTGAAAATCTTTCGAG	39mer, [118, 110] start, [117, 87] end
TTTTTTTTTTCAGTTTCAGCGGAGTGAGAATAGAAAATGAAAATCAC	47mer, [120, 110] start, [103, 79] end
TTTTTTTTTTAGCCCTCATAGTTAGCGTAACATTTTGCT	39mer, [122, 110] start, [121, 87] end
TTTTTTTTTTCACTGAGTTTCGTCACCAGTACAAACCCGTAGAAAAT	47mer, [124, 110] start, [99, 79] end
CAAGCCCAATAGGAACCCATGTACCGTAATTTTTTTTTT	39mer, [125, 72] start, [125, 110] end

Supplementary Table 2. DNA oligonucleotide staple sequences for SQB design corresponding to figure S2. (Left: purple strands, middle: green strands, right: orange strands)

CpG-containing staples for various CpG spacing patterns	Start	End
2.5nm spacing-CpG1-18 strands		
TTTTTTTTTTCATGGAAATACCTCGTATTGCTAAACt*c*c*a*t*g*a*c*g*t*t*c*c*t*g*a*c*g*t*t*	18[110]	35[120]
TTTTTTTTTTTTGGCAGATTCACACTGGTGACCTGGt*c*c*a*t*g*a*c*g*t*t*c*c*t*g*a*c*g*t*t*	20[110]	33[120]
t*c*c*a*t*g*a*c*g*t*t*c*c*t*g*a*c*g*t*t*TGGAAAGCAACGAGATGAAACAAACAt*c*c*a*t*g*a*c*g*t*t*c*c*t*g*a*c*g*t*t*	34[120]	49[120]
t*c*c*a*t*g*a*c*g*t*t*c*c*t*g*a*c*g*t*t*CGTGAGTATTACGAAAATCGCGCAGATTTTTTTTTT	36[120]	47[110]
t*c*c*a*t*g*a*c*g*t*t*c*c*t*g*a*c*g*t*t*GGCGAATTATTCATTGTTAAAATTCGt*c*c*a*t*g*a*c*g*t*t*c*c*t*g*a*c*g*t*t*	46[120]	63[120]
t*c*c*a*t*g*a*c*g*t*t*c*c*t*g*a*c*g*t*t*TCAAGAAAACAAAAGCTTTCATCAACt*c*c*a*t*g*a*c*g*t*t*c*c*t*g*a*c*g*t*t*	48[120]	61[120]
t*c*c*a*t*g*a*c*g*t*t*c*c*t*g*a*c*g*t*t*CATTAAATTTTTGAAATCAGATATAGt*c*c*a*t*g*a*c*g*t*t*c*c*t*g*a*c*g*t*t*	62[120]	77[120]
t*c*c*a*t*g*a*c*g*t*t*c*c*t*g*a*c*g*t*t*ATTGTATAAGCAACAAGCCGTTTTTATTTTTTTTTT	64[120]	75[110]
t*c*c*a*t*g*a*c*g*t*t*c*c*t*g*a*c*g*t*t*TTTTCATCGTAGGGGGGTAATAGTAAt*c*c*a*t*g*a*c*g*t*t*c*c*t*g*a*c*g*t*t*	74[120]	91[120]
t*c*c*a*t*g*a*c*g*t*t*c*c*t*g*a*c*g*t*t*AAGGCTTATCCGGGAAAACGAGAATGt*c*c*a*t*g*a*c*g*t*t*c*c*t*g*a*c*g*t*t*	76[120]	89[120]
t*c*c*a*t*g*a*c*g*t*t*c*c*t*g*a*c*g*t*t*AATGTTTAGACTGCACCGTAATCAGTTTTTTTTTT	90[120]	105[110]
t*c*c*a*t*g*a*c*g*t*t*c*c*t*g*a*c*g*t*t*AAATAGCGAGAGGCCATTACCATTAGTTTTTTTTTT	92[120]	103[110]
2.5nm spacing-CpG1-18 strands 3´-3´ linkage		
TTTTTTTTTTCATGGAAATACCTCGTATTGCTAAAC *ʇ*ʇ*ƃ*ɔ*ɐ*ƃ*ʇ*ɔ*ɔ*ʇ*ʇ*ƃ*ɔ*ɐ*ƃ*ʇ*ɐ*ɔ*ɔ*ʇ	18[110]	35[120]
TTTTTTTTTTTTGGCAGATTCACACTGGTGACCTGG *ʇ*ʇ*ƃ*ɔ*ɐ*ƃ*ʇ*ɔ*ɔ*ʇ*ʇ*ƃ*ɔ*ɐ*ƃ*ʇ*ɐ*ɔ*ɔ*ʇ	20[110]	33[120]
t*c*c*a*t*g*a*c*g*t*t*c*c*t*g*a*c*g*t*t*TGGAAAGCAACGAGATGAAACAAACA *ʇ*ʇ*ƃ*ɔ*ɐ*ƃ*ʇ*ɔ*ɔ*ʇ*ʇ*ƃ*ɔ*ɐ*ƃ*ʇ*ɐ*ɔ*ɔ*ʇ	34[120]	49[120]
t*c*c*a*t*g*a*c*g*t*t*c*c*t*g*a*c*g*t*t*CGTGAGTATTACGAAAATCGCGCAGATTTTTTTTTT	36[120]	47[110]
t*c*c*a*t*g*a*c*g*t*t*c*c*t*g*a*c*g*t*t*GGCGAATTATTCATTGTTAAAATTCG *ʇ*ʇ*ƃ*ɔ*ɐ*ƃ*ʇ*ɔ*ɔ*ʇ*ʇ*ƃ*ɔ*ɐ*ƃ*ʇ*ɐ*ɔ*ɔ*ʇ	46[120]	63[120]
t*c*c*a*t*g*a*c*g*t*t*c*c*t*g*a*c*g*t*t*TCAAGAAAACAAAAGCTTTCATCAAC *ʇ*ʇ*ƃ*ɔ*ɐ*ƃ*ʇ*ɔ*ɔ*ʇ*ʇ*ƃ*ɔ*ɐ*ƃ*ʇ*ɐ*ɔ*ɔ*ʇ	48[120]	61[120]
t*c*c*a*t*g*a*c*g*t*t*c*c*t*g*a*c*g*t*t*CATTAAATTTTTGAAATCAGATATAG *ʇ*ʇ*ƃ*ɔ*ɐ*ƃ*ʇ*ɔ*ɔ*ʇ*ʇ*ƃ*ɔ*ɐ*ƃ*ʇ*ɐ*ɔ*ɔ*ʇ	62[120]	77[120]
t*c*c*a*t*g*a*c*g*t*t*c*c*t*g*a*c*g*t*t*ATTGTATAAGCAACAAGCCGTTTTTATTTTTTTTTT	64[120]	75[110]
t*c*c*a*t*g*a*c*g*t*t*c*c*t*g*a*c*g*t*t*TTTTCATCGTAGGGGGGTAATAGTAA *ʇ*ʇ*ƃ*ɔ*ɐ*ƃ*ʇ*ɔ*ɔ*ʇ*ʇ*ƃ*ɔ*ɐ*ƃ*ʇ*ɐ*ɔ*ɔ*ʇ	74[120]	91[120]
t*c*c*a*t*g*a*c*g*t*t*c*c*t*g*a*c*g*t*t*AAGGCTTATCCGGGAAAACGAGAATG *ʇ*ʇ*ƃ*ɔ*ɐ*ƃ*ʇ*ɔ*ɔ*ʇ*ʇ*ƃ*ɔ*ɐ*ƃ*ʇ*ɐ*ɔ*ɔ*ʇ	76[120]	89[120]
t*c*c*a*t*g*a*c*g*t*t*c*c*t*g*a*c*g*t*t*AATGTTTAGACTGCACCGTAATCAGTTTTTTTTTT	90[120]	105[110]
t*c*c*a*t*g*a*c*g*t*t*c*c*t*g*a*c*g*t*t*AAATAGCGAGAGGCCATTACCATTAGTTTTTTTTTT	92[120]	103[110]
3.5nm spacing-CpG2-18 strands		
t*c*c*a*t*g*a*c*g*t*t*c*c*t*g*a*c*g*t*t*AAGAGTTTCTGCGGAGTGAATAACCTTTTTTTTTT	32[120]	51[110]
t*c*c*a*t*g*a*c*g*t*t*c*c*t*g*a*c*g*t*t*TGGAAAGCAACGAGATGAAACAAACATTTTTTTTTT	34[120]	49[110]
t*c*c*a*t*g*a*c*g*t*t*c*c*t*g*a*c*g*t*t*CGTGAGTATTACGAAAATCGCGCAGATTTTTTTTTT	36[120]	47[110]
t*c*c*a*t*g*a*c*g*t*t*c*c*t*g*a*c*g*t*t*ATCAAACGCCGCGTTCAGGTTTAACGTTTTTTTTTT	38[120]	45[110]
t*c*c*a*t*g*a*c*g*t*t*c*c*t*g*a*c*g*t*t*TCAGATGAATATACAAAAACAGGAAGTTTTTTTTTT	44[120]	65[110]
t*c*c*a*t*g*a*c*g*t*t*c*c*t*g*a*c*g*t*t*GGCGAATTATTCATTGTTAAAATTCGTTTTTTTTTT	46[120]	63[110]
t*c*c*a*t*g*a*c*g*t*t*c*c*t*g*a*c*g*t*t*TCAAGAAAACAAAAGCTTTCATCAACTTTTTTTTTT	48[120]	61[110]
t*c*c*a*t*g*a*c*g*t*t*c*c*t*g*a*c*g*t*t*ATTAAATGTGAGCTTAGTTGCTATTTTTTTTTTTTT	60[120]	79[110]
t*c*c*a*t*g*a*c*g*t*t*c*c*t*g*a*c*g*t*t*CATTAAATTTTTGAAATCAGATATAGTTTTTTTTTT	62[120]	77[110]
t*c*c*a*t*g*a*c*g*t*t*c*c*t*g*a*c*g*t*t*ATTGTATAAGCAACAAGCCGTTTTTATTTTTTTTTT	64[120]	75[110]
t*c*c*a*t*g*a*c*g*t*t*c*c*t*g*a*c*g*t*t*GAGCAAACAAGAGTTTACGAGCATGTTTTTTTTTTT	66[120]	73[110]
t*c*c*a*t*g*a*c*g*t*t*c*c*t*g*a*c*g*t*t*AGAAACCAATCAAACGATAAAAACCATTTTTTTTTT	72[120]	93[110]
t*c*c*a*t*g*a*c*g*t*t*c*c*t*g*a*c*g*t*t*TTTTCATCGTAGGGGGGTAATAGTAATTTTTTTTTT	74[120]	91[110]
t*c*c*a*t*g*a*c*g*t*t*c*c*t*g*a*c*g*t*t*AAGGCTTATCCGGGAAAACGAGAATGTTTTTTTTTT	76[120]	89[110]
t*c*c*a*t*g*a*c*g*t*t*c*c*t*g*a*c*g*t*t*ACCATAAATCAAATTGCCATCTTTTCTTTTTTTTTT	88[120]	107[110]
t*c*c*a*t*g*a*c*g*t*t*c*c*t*g*a*c*g*t*t*AATGTTTAGACTGCACCGTAATCAGTTTTTTTTTT	90[120]	105[110]
t*c*c*a*t*g*a*c*g*t*t*c*c*t*g*a*c*g*t*t*AAATAGCGAGAGGCCATTACCATTAGTTTTTTTTTT	92[120]	103[110]
t*c*c*a*t*g*a*c*g*t*t*c*c*t*g*a*c*g*t*t*TCAACTAATGCAGGGTAAATATTGACTTTTTTTTTT	94[120]	101[110]
5nm spacing-CpG3-18 staples		
t*c*c*a*t*g*a*c*g*t*t*c*c*t*g*a*c*g*t*t*GCCCTTCACCGCCAAGAATACGTGGCTTTTTTTTTT	4[120]	23[110]
t*c*c*a*t*g*a*c*g*t*t*c*c*t*g*a*c*g*t*t*CATTAATGAATCGTGGATTATTTACATTTTTTTTTT	6[120]	21[110]
t*c*c*a*t*g*a*c*g*t*t*c*c*t*g*a*c*g*t*t*TGCGTTGCGCTCACAGGAAAAACGCTTTTTTTTTTT	8[120]	19[110]
t*c*c*a*t*g*a*c*g*t*t*c*c*t*g*a*c*g*t*t*AAATTGTTATCCGTTTGATTAGTAATTTTTTTTTTT	10[120]	17[110]
t*c*c*a*t*g*a*c*g*t*t*c*c*t*g*a*c*g*t*t*AAGAGTTTCTGCGGAGTGAATAACCTTTTTTTTTT	32[120]	51[110]
t*c*c*a*t*g*a*c*g*t*t*c*c*t*g*a*c*g*t*t*TGGAAAGCAACGAGATGAAACAAACATTTTTTTTTT	34[120]	49[110]
t*c*c*a*t*g*a*c*g*t*t*c*c*t*g*a*c*g*t*t*CGTGAGTATTACGAAAATCGCGCAGATTTTTTTTTT	36[120]	47[110]
t*c*c*a*t*g*a*c*g*t*t*c*c*t*g*a*c*g*t*t*ATTAAATGTGAGCTTAGTTGCTATTTTTTTTTTTTT	60[120]	79[110]
t*c*c*a*t*g*a*c*g*t*t*c*c*t*g*a*c*g*t*t*CATTAAATTTTTGAAATCAGATATAGTTTTTTTTTT	62[120]	77[110]
t*c*c*a*t*g*a*c*g*t*t*c*c*t*g*a*c*g*t*t*ATTGTATAAGCAACAAGCCGTTTTTATTTTTTTTTT	64[120]	75[110]
t*c*c*a*t*g*a*c*g*t*t*c*c*t*g*a*c*g*t*t*GAGCAAACAAGAGTTTACGAGCATGTTTTTTTTTTT	66[120]	73[110]
t*c*c*a*t*g*a*c*g*t*t*c*c*t*g*a*c*g*t*t*ACCATAAATCAAATTGCCATCTTTTCTTTTTTTTTT	88[120]	107[110]
t*c*c*a*t*g*a*c*g*t*t*c*c*t*g*a*c*g*t*t*AATGTTTAGACTGCACCGTAATCAGTTTTTTTTTT	90[120]	105[110]
t*c*c*a*t*g*a*c*g*t*t*c*c*t*g*a*c*g*t*t*AAATAGCGAGAGGCCATTACCATTAGTTTTTTTTTT	92[120]	103[110]

t*c*c*a*t*g*a*c*g*t*t*c*c*t*g*a*c*g*t*t*ACAGCTTGATACCGATAGTTGCGCCGTACGCCCCCTT	116[120]	107[79]
t*c*c*a*t*g*a*c*g*t*t*c*c*t*g*a*c*g*t*t*TAATTTTTTCACGTTGAAAATCTTTCGAG	118[120]	117[87]
t*c*c*a*t*g*a*c*g*t*t*c*c*t*g*a*c*g*t*t*CAGTTTCAGCGGAGTGAGAATAGAAAATGAAAATCAC	120[120]	103[79]
t*c*c*a*t*g*a*c*g*t*t*c*c*t*g*a*c*g*t*t*AGCCCTCATAGTTAGCGTAACATTTTGCT	122[120]	121[87]
7.5nm spacing-CpG4-18 staples		
t*c*c*a*t*g*a*c*g*t*t*c*c*t*g*a*c*g*t*t*TTCCAGTTTGGAAGAAAATGCTGAATTTTTTTTTTT	0[110]	27[110]
t*c*c*a*t*g*a*c*g*t*t*c*c*t*g*a*c*g*t*t*GCCCTTCACCGCCAAGAATACGTGGCTTTTTTTTTT	4[110]	23[110]
t*c*c*a*t*g*a*c*g*t*t*c*c*t*g*a*c*g*t*t*TGCGTTGCGCTCACAGGAAAAACGCTTTTTTTTTTT	8[110]	19[110]
t*c*c*a*t*g*a*c*g*t*t*c*c*t*g*a*c*g*t*t*CCCGGGTACCGAGCCGAGTAAAAGAGTTTTTTTTTT	12[110]	15[110]
t*c*c*a*t*g*a*c*g*t*t*c*c*t*g*a*c*g*t*t*CATTACGCATCGCGAATCCTTGAAAATTTTTTTTTT	30[110]	53[110]
t*c*c*a*t*g*a*c*g*t*t*c*c*t*g*a*c*g*t*t*TGGAAAGCAACGAGATGAAACAAACATTTTTTTTTT	34[110]	49[110]
t*c*c*a*t*g*a*c*g*t*t*c*c*t*g*a*c*g*t*t*ATCAAACGCCGCGTTCAGGTTTAACGTTTTTTTTTT	38[110]	45[110]
t*c*c*a*t*g*a*c*g*t*t*c*c*t*g*a*c*g*t*t*GGAAGATCGCACTCCTTTTGATAAGATTTTTTTTTT	56[110]	83[110]
t*c*c*a*t*g*a*c*g*t*t*c*c*t*g*a*c*g*t*t*ATTAAATGTGAGCTTAGTTGCTATTTTTTTTTTTTT	60[110]	79[110]
t*c*c*a*t*g*a*c*g*t*t*c*c*t*g*a*c*g*t*t*ATTGTATAAGCAACAAGCCGTTTTTATTTTTTTTTT	64[110]	75[110]
t*c*c*a*t*g*a*c*g*t*t*c*c*t*g*a*c*g*t*t*AGCTATTTTTGAGGTTTATCAACAATTTTTTTTTTT	68[110]	71[110]
t*c*c*a*t*g*a*c*g*t*t*c*c*t*g*a*c*g*t*t*GCGGATTGCATCAGCCTCCCTCAGAGTTTTTTTTTT	86[110]	109[110]
t*c*c*a*t*g*a*c*g*t*t*c*c*t*g*a*c*g*t*t*AATGTTTAGACTGCACCGTAATCAGTTTTTTTTTTT	90[110]	105[110]
t*c*c*a*t*g*a*c*g*t*t*c*c*t*g*a*c*g*t*t*TCAACTAATGCAGGGTAAATATTGACTTTTTTTTTT	94[110]	101[110]
t*c*c*a*t*g*a*c*g*t*t*c*c*t*g*a*c*g*t*t*GGTAGCAACGGCTACAGAGGCTTTCCGCC	112[110]	112[72]
t*c*c*a*t*g*a*c*g*t*t*c*c*t*g*a*c*g*t*t*ACAGCTTGATACCGATAGTTGCGCCGTACGCCCCCTT	116[110]	107[79]
t*c*c*a*t*g*a*c*g*t*t*c*c*t*g*a*c*g*t*t*CAGTTTCAGCGGAGTGAGAATAGAAAATGAAAATCAC	120[110]	103[79]
t*c*c*a*t*g*a*c*g*t*t*c*c*t*g*a*c*g*t*t*CACTGAGTTTCGTCACCAGTACAAACCCGTAGAAAAT	124[110]	99[79]
CpG2-dimer 1		
*t*c*c*a*t*g*a*c*g*t*t*c*c*t*g*a*c*g*t*tTCTGTCCATCACGAAACCAGCAATACTTTTTTTTTT	14[110]	39[110]
*t*c*c*a*t*g*a*c*g*t*t*c*c*t*g*a*c*g*t*tCATGGAAATACCTCGTATTGCTAAACTTTTTTTTTT	18[110]	35[110]
*t*c*c*a*t*g*a*c*g*t*t*c*c*t*g*a*c*g*t*tACAGACAATATTTTAACTATCGACATTTTTTTTTTT	22[110]	31[110]
*t*c*c*a*t*g*a*c*g*t*t*c*c*t*g*a*c*g*t*tAAGAGTTTCTGCGGAGTGAATAACCTTTTTTTTTTT	32[110]	51[110]
*t*c*c*a*t*g*a*c*g*t*t*c*c*t*g*a*c*g*t*tCGTGAGTATTACGAAAATCGCGCAGATTTTTTTTTT	36[110]	47[110]
*t*c*c*a*t*g*a*c*g*t*t*c*c*t*g*a*c*g*t*tACCATCGATTGTGCCATATCAAAATTTTTTTTTTTT	40[110]	43[110]
*t*c*c*a*t*g*a*c*g*t*t*c*c*t*g*a*c*g*t*tGGATTGACCGTAATAACGAGCGTCTTTTTTTTTTTT	58[110]	81[110]
*t*c*c*a*t*g*a*c*g*t*t*c*c*t*g*a*c*g*t*tCATTAAATTTTTGAAATCAGATATAGTTTTTTTTTT	62[110]	77[110]
*t*c*c*a*t*g*a*c*g*t*t*c*c*t*g*a*c*g*t*tGAGCAAACAAGAGTTTACGAGCATGTTTTTTTTTTT	66[110]	73[110]
*t*c*c*a*t*g*a*c*g*t*t*c*c*t*g*a*c*g*t*tAGATAAGTCCTGAAGGAATACCACATTTTTTTTTTT	70[110]	95[110]
*t*c*c*a*t*g*a*c*g*t*t*c*c*t*g*a*c*g*t*tTTTTCATCGTAGGGGGGTAATAGTAATTTTTTTTTTT	74[110]	91[110]
*t*c*c*a*t*g*a*c*g*t*t*c*c*t*g*a*c*g*t*tTGCACCCAGCTACAGTCAGAAGCAAATTTTTTTTTT	78[110]	87[110]
*t*c*c*a*t*g*a*c*g*t*t*c*c*t*g*a*c*g*t*tGGAAATTATTCATAAACAACTTTCAATTTTTTTTTT	100[110]	121[110]
*t*c*c*a*t*g*a*c*g*t*t*c*c*t*g*a*c*g*t*tAGCGACAGAATCAGTGAATTTCTTAATTTTTTTTTTT	104[110]	117[110]
*t*c*c*a*t*g*a*c*g*t*t*c*c*t*g*a*c*g*t*tCCGCCACCCTCAGGCATCGGAACGAGTTTTTTTTTT	108[110]	113[110]
*t*c*c*a*t*g*a*c*g*t*t*c*c*t*g*a*c*g*t*tATAACCGATATATTCGGTCGCGAAAGACA	114[110]	113[87]
*t*c*c*a*t*g*a*c*g*t*t*c*c*t*g*a*c*g*t*tTAATTTTTTCACGTTGAAAATCTTTCGAG	118[110]	117[87]
*t*c*c*a*t*g*a*c*g*t*t*c*c*t*g*a*c*g*t*tAGCCCTCATAGTTAGCGTAACATTTTGCT	122[110]	121[87]
*t*c*c*a*t*g*a*c*g*t*t*c*c*t*g*a*c*g*t*tTCTGTCCATCACGAAACCAGCAATACTTTTTTTTTT	14[110]	39[110]
CpG2-dimer 2		
*t*c*c*a*t*g*a*c*g*t*t*c*c*t*g*a*c*g*t*tTTCCAGTTTGGAAGAAAATGCTGAATTTTTTTTTTT	0[110]	27[110]
*t*c*c*a*t*g*a*c*g*t*t*c*c*t*g*a*c*g*t*tCATTAATGAATCGTGGATTATTTACATTTTTTTTTTT	6[110]	21[110]
*t*c*c*a*t*g*a*c*g*t*t*c*c*t*g*a*c*g*t*tCCCGGGTACCGAGCCGAGTAAAAGAGTTTTTTTTTT	12[110]	15[110]
*t*c*c*a*t*g*a*c*g*t*t*c*c*t*g*a*c*g*t*tTCTGTCCATCACGAAACCAGCAATACTTTTTTTTTT	14[110]	39[110]
*t*c*c*a*t*g*a*c*g*t*t*c*c*t*g*a*c*g*t*tTTGGCAGATTCACACTGGTGACCTGGTTTTTTTTTT	20[110]	33[110]
*t*c*c*a*t*g*a*c*g*t*t*c*c*t*g*a*c*g*t*tTTCGCGTCGTCTTCACAGCGATGCCAGAGTCTGTAGT	26[110]	26[64]
*t*c*c*a*t*g*a*c*g*t*t*c*c*t*g*a*c*g*t*tATTTGCACGTAAAGCCTGAGAGTCTGTTTTTTTTTT	42[110]	67[110]
*t*c*c*a*t*g*a*c*g*t*t*c*c*t*g*a*c*g*t*tGGCGAATTATTCATTGTTAAAATTCGTTTTTTTTTT	46[110]	63[110]
*t*c*c*a*t*g*a*c*g*t*t*c*c*t*g*a*c*g*t*tCATAGCGATAGCTAGTATCGGCCTCATTTTTTTTTT	52[110]	57[110]
*t*c*c*a*t*g*a*c*g*t*t*c*c*t*g*a*c*g*t*tGGAAGATCGCACTCCTTTTGATAAGATTTTTTTTTT	56[110]	83[110]
*t*c*c*a*t*g*a*c*g*t*t*c*c*t*g*a*c*g*t*tCATTAAATTTTTGAAATCAGATATAGTTTTTTTTTT	62[110]	77[110]
*t*c*c*a*t*g*a*c*g*t*t*c*c*t*g*a*c*g*t*tAGCTATTTTTGAGGTTTATCAACAATTTTTTTTTTT	68[110]	71[110]
*t*c*c*a*t*g*a*c*g*t*t*c*c*t*g*a*c*g*t*tAAGACAAAAGGGCGCATTCCACAGACTTTTTTTTTT	98[110]	123[110]
*t*c*c*a*t*g*a*c*g*t*t*c*c*t*g*a*c*g*t*tAGCGACAGAATCAGTGAATTTCTTAATTTTTTTTTTT	104[110]	117[110]
*t*c*c*a*t*g*a*c*g*t*t*c*c*t*g*a*c*g*t*tGAAGTTTCCATTAAACGGGTAAAATACGT	110[110]	110[72]
*t*c*c*a*t*g*a*c*g*t*t*c*c*t*g*a*c*g*t*tGGTAGCAACGGCTACAGAGGCTTTCCGCC	112[110]	112[72]
*t*c*c*a*t*g*a*c*g*t*t*c*c*t*g*a*c*g*t*tTAATTTTTTCACGTTGAAAATCTTTCGAG	118[110]	117[87]
*t*c*c*a*t*g*a*c*g*t*t*c*c*t*g*a*c*g*t*tCACTGAGTTTCGTCACCAGTACAAACCCGTAGAAAAT	124[110]	99[79]
3.5nm spacing-12 CpG strands		

*t*c*c*a*t*g*a*c*g*t*t*c*c*t*g*a*c*g*t*tTGGAAAGCAACGAGATGAAACAAACATTTTTTTTTT	34[110]	49[110]
*t*c*c*a*t*g*a*c*g*t*t*c*c*t*g*a*c*g*t*tCGTGAGTATTACGAAAATCGCGCAGATTTTTTTTTT	36[110]	47[110]
*t*c*c*a*t*g*a*c*g*t*t*c*c*t*g*a*c*g*t*tTCAGATGAATATACAAAAACAGGAAGTTTTTTTTTT	44[110]	65[110]
*t*c*c*a*t*g*a*c*g*t*t*c*c*t*g*a*c*g*t*tGGCGAATTATTCATTGTTAAAATTCGTTTTTTTTTT	46[110]	63[110]
*t*c*c*a*t*g*a*c*g*t*t*c*c*t*g*a*c*g*t*tTCAAGAAAACAAAAGCTTTCATCAACTTTTTTTTTT	48[110]	61[110]
*t*c*c*a*t*g*a*c*g*t*t*c*c*t*g*a*c*g*t*tCATTAAATTTTTGAAATCAGATATAGTTTTTTTTTT	62[110]	77[110]
*t*c*c*a*t*g*a*c*g*t*t*c*c*t*g*a*c*g*t*tATTGTATAAGCAACAAGCCGTTTTTATTTTTTTTTT	64[110]	75[110]
*t*c*c*a*t*g*a*c*g*t*t*c*c*t*g*a*c*g*t*tAGAAACCAATCAAACGATAAAAACCATTTTTTTTTT	72[110]	93[110]
*t*c*c*a*t*g*a*c*g*t*t*c*c*t*g*a*c*g*t*tTTTTCATCGTAGGGGGGTAATAGTAATTTTTTTTTT	74[110]	91[110]
*t*c*c*a*t*g*a*c*g*t*t*c*c*t*g*a*c*g*t*tAAGGCTTATCCGGGAAAACGAGAATGTTTTTTTTTT	76[110]	89[110]
*t*c*c*a*t*g*a*c*g*t*t*c*c*t*g*a*c*g*t*tAATGTTTAGACTGCACCGTAATCAGTTTTTTTTTT	90[110]	105[110]
*t*c*c*a*t*g*a*c*g*t*t*c*c*t*g*a*c*g*t*tAAATAGCGAGAGGCCATTACCATTAGTTTTTTTTTT	92[110]	103[110]
3.5nm spacing-35 CpG strands		
t*c*c*a*t*g*a*c*g*t*t*c*c*t*g*a*c*g*t*t*TCTGTCCATCACGAAACCAGCAATACTTTTTTTTTT	14[110]	39[110]
t*c*c*a*t*g*a*c*g*t*t*c*c*t*g*a*c*g*t*t*AACATCACTTGCCACTCAACGAGCAGTTTTTTTTTT	16[110]	37[110]
t*c*c*a*t*g*a*c*g*t*t*c*c*t*g*a*c*g*t*t*CATGGAAATACCTCGTATTGCTAAACTTTTTTTTTT	18[110]	35[110]
t*c*c*a*t*g*a*c*g*t*t*c*c*t*g*a*c*g*t*t*TTGGCAGATTCACACTGGTGACCTGGTTTTTTTTTT	20[110]	33[110]
t*c*c*a*t*g*a*c*g*t*t*c*c*t*g*a*c*g*t*t*ACAGACAATATTTTAACTATCGACATTTTTTTTTT	22[110]	31[110]
t*c*c*a*t*g*a*c*g*t*t*c*c*t*g*a*c*g*t*t*CATTACGCATCGCGAATCCTTGAAAATTTTTTTTTT	30[110]	53[110]
t*c*c*a*t*g*a*c*g*t*t*c*c*t*g*a*c*g*t*t*AAGAGTTTCTGCGGAGTGAATAACCTTTTTTTTTT	32[110]	51[110]
t*c*c*a*t*g*a*c*g*t*t*c*c*t*g*a*c*g*t*t*TGGAAAGCAACGAGATGAAACAAACATTTTTTTTTT	34[110]	49[110]
t*c*c*a*t*g*a*c*g*t*t*c*c*t*g*a*c*g*t*t*CGTGAGTATTACGAAAATCGCGCAGATTTTTTTTTT	36[110]	47[110]
t*c*c*a*t*g*a*c*g*t*t*c*c*t*g*a*c*g*t*t*ATCAAACGCCGCGTTCAGGTTTAACGTTTTTTTTTT	38[110]	45[110]
t*c*c*a*t*g*a*c*g*t*t*c*c*t*g*a*c*g*t*t*ATTTGCACGTAAAGCCTGAGAGTCTGTTTTTTTTTT	42[110]	67[110]
t*c*c*a*t*g*a*c*g*t*t*c*c*t*g*a*c*g*t*t*TCAGATGAATATACAAAAACAGGAAGTTTTTTTTTT	44[110]	65[110]
t*c*c*a*t*g*a*c*g*t*t*c*c*t*g*a*c*g*t*t*GGCGAATTATTCATTGTTAAAATTCGTTTTTTTTTT	46[110]	63[110]
t*c*c*a*t*g*a*c*g*t*t*c*c*t*g*a*c*g*t*t*TCAAGAAAACAAAAGCTTTCATCAACTTTTTTTTTT	48[110]	61[110]
t*c*c*a*t*g*a*c*g*t*t*c*c*t*g*a*c*g*t*t*TGCTTCTGTAAATGGGAACAAACGGCTTTTTTTTTT	50[110]	59[110]
t*c*c*a*t*g*a*c*g*t*t*c*c*t*g*a*c*g*t*t*GGATTGACCGTAATAACGAGCGTCTTTTTTTTTTTT	58[110]	81[110]
t*c*c*a*t*g*a*c*g*t*t*c*c*t*g*a*c*g*t*t*ATTAAATGTGAGCTTAGTTGCTATTTTTTTTTTTTT	60[110]	79[110]
t*c*c*a*t*g*a*c*g*t*t*c*c*t*g*a*c*g*t*t*CATTAAATTTTTGAAATCAGATATAGTTTTTTTTTT	62[110]	77[110]
t*c*c*a*t*g*a*c*g*t*t*c*c*t*g*a*c*g*t*t*ATTGTATAAGCAACAAGCCGTTTTTATTTTTTTTTT	64[110]	75[110]
t*c*c*a*t*g*a*c*g*t*t*c*c*t*g*a*c*g*t*t*GAGCAAACAAGAGTTTACGAGCATGTTTTTTTTTTT	66[110]	73[110]
t*c*c*a*t*g*a*c*g*t*t*c*c*t*g*a*c*g*t*t*AGATAAGTCCTGAAGGAATACCACATTTTTTTTTTT	70[110]	95[110]
t*c*c*a*t*g*a*c*g*t*t*c*c*t*g*a*c*g*t*t*AGAAACCAATCAAACGATAAAAACCATTTTTTTTTT	72[110]	93[110]
t*c*c*a*t*g*a*c*g*t*t*c*c*t*g*a*c*g*t*t*TTTTCATCGTAGGGGGGTAATAGTAATTTTTTTTTT	74[110]	91[110]
t*c*c*a*t*g*a*c*g*t*t*c*c*t*g*a*c*g*t*t*AAGGCTTATCCGGGAAAACGAGAATGTTTTTTTTTT	76[110]	89[110]
t*c*c*a*t*g*a*c*g*t*t*c*c*t*g*a*c*g*t*t*TGCACCCAGCTACAGTCAGAAGCAAATTTTTTTTTT	78[110]	87[110]
t*c*c*a*t*g*a*c*g*t*t*c*c*t*g*a*c*g*t*t*GCGGATTGCATCAGCCTCCCTCAGAGTTTTTTTTTT	86[110]	109[110]
t*c*c*a*t*g*a*c*g*t*t*c*c*t*g*a*c*g*t*t*ACCATAAATCAAATTGCCATCTTTCTTTTTTTTTT	88[110]	107[110]
t*c*c*a*t*g*a*c*g*t*t*c*c*t*g*a*c*g*t*t*AATGTTTAGACTGCACCGTAATCAGTTTTTTTTTT	90[110]	105[110]
t*c*c*a*t*g*a*c*g*t*t*c*c*t*g*a*c*g*t*t*AAATAGCGAGAGGCCATTACCATTAGTTTTTTTTTT	92[110]	103[110]
t*c*c*a*t*g*a*c*g*t*t*c*c*t*g*a*c*g*t*t*TCAACTAATGCAGGGTAAATATTGACTTTTTTTTTT	94[110]	101[110]
t*c*c*a*t*g*a*c*g*t*t*c*c*t*g*a*c*g*t*t*AAGACAAAAGGGCGCATTCCACAGACTTTTTTTTTT	98[110]	123[110]
t*c*c*a*t*g*a*c*g*t*t*c*c*t*g*a*c*g*t*t*GGAAATTATTCATAAACAACTTTCAATTTTTTTTTT	100[110]	121[110]
t*c*c*a*t*g*a*c*g*t*t*c*c*t*g*a*c*g*t*t*CAAGGCCGGAAACGAATTGCGAATAATTTTTTTTTT	102[110]	119[110]
t*c*c*a*t*g*a*c*g*t*t*c*c*t*g*a*c*g*t*t*AGCGACAGAATCAGTGAATTTCTTAATTTTTTTTTT	104[110]	117[110]
t*c*c*a*t*g*a*c*g*t*t*c*c*t*g*a*c*g*t*t*ATAATCAAAATCACCATCGCCCACGCTTTTTTTTTT	106[110]	115[110]
3.5nm spacing-63 CpG strands		
*t*c*c*a*t*g*a*c*g*t*t*c*c*t*g*a*c*g*t*tTTCCAGTTTGGAAGAAAATGCTGAATTTTTTTTTTT	0[110]	27[110]
*t*c*c*a*t*g*a*c*g*t*t*c*c*t*g*a*c*g*t*tTGCCCCAGCAGGCCGAACTGATAGCCTTTTTTTTTT	2[110]	25[110]
*t*c*c*a*t*g*a*c*g*t*t*c*c*t*g*a*c*g*t*tGCCCTTCACCGCCAAGAATACGTGGCTTTTTTTTTT	4[110]	23[110]
*t*c*c*a*t*g*a*c*g*t*t*c*c*t*g*a*c*g*t*tCATTAATGAATCGTGGATTATTTACATTTTTTTTTT	6[110]	21[110]
*t*c*c*a*t*g*a*c*g*t*t*c*c*t*g*a*c*g*t*tTGCGTTGCGCTCACAGGAAAAACGCTTTTTTTTTT	8[110]	19[110]
*t*c*c*a*t*g*a*c*g*t*t*c*c*t*g*a*c*g*t*tAAATTGTTATCCGTTTGATTAGTAATTTTTTTTTTT	10[110]	17[110]
*t*c*c*a*t*g*a*c*g*t*t*c*c*t*g*a*c*g*t*tCCCGGGTACCGAGCCGAGTAAAAGAGTTTTTTTTTT	12[110]	15[110]
*t*c*c*a*t*g*a*c*g*t*t*c*c*t*g*a*c*g*t*tTCTGTCCATCACGAAACCAGCAATACTTTTTTTTTT	14[110]	39[110]
*t*c*c*a*t*g*a*c*g*t*t*c*c*t*g*a*c*g*t*tAACATCACTTGCCACTCAACGAGCAGTTTTTTTTTT	16[110]	37[110]
*t*c*c*a*t*g*a*c*g*t*t*c*c*t*g*a*c*g*t*tCATGGAAATACCTCGTATTGCTAAACTTTTTTTTTT	18[110]	35[110]
*t*c*c*a*t*g*a*c*g*t*t*c*c*t*g*a*c*g*t*tTTGGCAGATTCACACTGGTGACCTGGTTTTTTTTTT	20[110]	33[110]
*t*c*c*a*t*g*a*c*g*t*t*c*c*t*g*a*c*g*t*tACAGACAATATTTTAACTATCGACATTTTTTTTTT	22[110]	31[110]
*t*c*c*a*t*g*a*c*g*t*t*c*c*t*g*a*c*g*t*tCTAAAACATCGCCTTCGCATCAAAGGTTTTTTTTTT	24[110]	29[110]
*t*c*c*a*t*g*a*c*g*t*t*c*c*t*g*a*c*g*t*tTTCGCGTCGTCTTCACAGCGATGCCAGAGTCTGTAGT	26[110]	26[64]
*t*c*c*a*t*g*a*c*g*t*t*c*c*t*g*a*c*g*t*tAGAGTGAGATCGGTTCTGGTGCCGGATTTTTTTTTT	28[110]	55[110]
*t*c*c*a*t*g*a*c*g*t*t*c*c*t*g*a*c*g*t*tCATTACGCATCGCGAATCCTTGAAAATTTTTTTTTT	30[110]	53[110]

*t*c*c*a*t*g*a*c*g*t*t*c*c*t*g*a*c*g*t*tAAGAGTTTCTGCGGAGTGAATAACCTTTTTTTTTT	32[110]	51[110]
*t*c*c*a*t*g*a*c*g*t*t*c*c*t*g*a*c*g*t*tTGGAAAGCAACGAGATGAAACAAACATTTTTTTTTT	34[110]	49[110]
*t*c*c*a*t*g*a*c*g*t*t*c*c*t*g*a*c*g*t*tCGTGAGTATTACGAAAATCGCGCAGATTTTTTTTTT	36[110]	47[110]
*t*c*c*a*t*g*a*c*g*t*t*c*c*t*g*a*c*g*t*tATCAAACGCCGCGTTCAGGTTTAACGTTTTTTTTTT	38[110]	45[110]
*t*c*c*a*t*g*a*c*g*t*t*c*c*t*g*a*c*g*t*tACCATCGATTGTGCCATATCAAAATTTTTTTTTTT	40[110]	43[110]
*t*c*c*a*t*g*a*c*g*t*t*c*c*t*g*a*c*g*t*tATTTGCACGTAAAGCCTGAGAGTCTGTTTTTTTTTT	42[110]	67[110]
*t*c*c*a*t*g*a*c*g*t*t*c*c*t*g*a*c*g*t*tTCAGATGAATATACAAAAACAGGAAGTTTTTTTTTT	44[110]	65[110]
*t*c*c*a*t*g*a*c*g*t*t*c*c*t*g*a*c*g*t*tGGCGAATTATTCATTGTTAAAATTCGTTTTTTTTTT	46[110]	63[110]
*t*c*c*a*t*g*a*c*g*t*t*c*c*t*g*a*c*g*t*tTCAAGAAAACAAAAGCTTTCATCAACTTTTTTTTTT	48[110]	61[110]
*t*c*c*a*t*g*a*c*g*t*t*c*c*t*g*a*c*g*t*tTGCTTCTGTAAATGGGAACAAACGGCTTTTTTTTTT	50[110]	59[110]
*t*c*c*a*t*g*a*c*g*t*t*c*c*t*g*a*c*g*t*tCATAGCGATAGCTAGTATCGGCCTCATTTTTTTTTT	52[110]	57[110]
*t*c*c*a*t*g*a*c*g*t*t*c*c*t*g*a*c*g*t*tAACCAGGCAAAGCGCCATTCGCCATTCAGGCTGCGCA	54[110]	54[64]
*t*c*c*a*t*g*a*c*g*t*t*c*c*t*g*a*c*g*t*tGGAAGATCGCACTCCTTTTGATAAGATTTTTTTTTT	56[110]	83[110]
*t*c*c*a*t*g*a*c*g*t*t*c*c*t*g*a*c*g*t*tGGATTGACCGTAATAACGAGCGTCTTTTTTTTTTT	58[110]	81[110]
*t*c*c*a*t*g*a*c*g*t*t*c*c*t*g*a*c*g*t*tATTAAATGTGAGCTTAGTTGCTATTTTTTTTTTTT	60[110]	79[110]
*t*c*c*a*t*g*a*c*g*t*t*c*c*t*g*a*c*g*t*tCATTAAATTTTTGAAATCAGATATAGTTTTTTTTTT	62[110]	77[110]
*t*c*c*a*t*g*a*c*g*t*t*c*c*t*g*a*c*g*t*tATTGTATAAGCAACAAGCCGTTTTTATTTTTTTTTT	64[110]	75[110]
*t*c*c*a*t*g*a*c*g*t*t*c*c*t*g*a*c*g*t*tGAGCAAACAAGAGTTTACGAGCATGTTTTTTTTTTT	66[110]	73[110]
*t*c*c*a*t*g*a*c*g*t*t*c*c*t*g*a*c*g*t*tAGCTATTTTTGAGGTTTATCAACAATTTTTTTTTTT	68[110]	71[110]
*t*c*c*a*t*g*a*c*g*t*t*c*c*t*g*a*c*g*t*tAGATAAGTCCTGAAGGAATACCACATTTTTTTTTT	70[110]	95[110]
*t*c*c*a*t*g*a*c*g*t*t*c*c*t*g*a*c*g*t*tAGAAACCAATCAAACGATAAAAACCATTTTTTTTTT	72[110]	93[110]
*t*c*c*a*t*g*a*c*g*t*t*c*c*t*g*a*c*g*t*tTTTTCATCGTAGGGGGGTAATAGTAATTTTTTTTTT	74[110]	91[110]
*t*c*c*a*t*g*a*c*g*t*t*c*c*t*g*a*c*g*t*tAAGGCTTATCCGGGAAAACGAGAATGTTTTTTTTTT	76[110]	89[110]
*t*c*c*a*t*g*a*c*g*t*t*c*c*t*g*a*c*g*t*tTGCACCCAGCTACAGTCAGAAGCAAATTTTTTTTTT	78[110]	87[110]
*t*c*c*a*t*g*a*c*g*t*t*c*c*t*g*a*c*g*t*tTCCAGAGCCTAATCGGAAGCAAACTCTTTTTTTTTT	80[110]	85[110]
*t*c*c*a*t*g*a*c*g*t*t*c*c*t*g*a*c*g*t*tGGTCATTTTTGCGGATGGCTTAGAGCTTA	82[110]	82[72]
*t*c*c*a*t*g*a*c*g*t*t*c*c*t*g*a*c*g*t*tCAACAGGTCAGGAACTTTTTCATGAGTTTTTTTTTT	84[110]	111[110]
*t*c*c*a*t*g*a*c*g*t*t*c*c*t*g*a*c*g*t*tGCGGATTGCATCAGCCTCCCTCAGAGTTTTTTTTTT	86[110]	109[110]
*t*c*c*a*t*g*a*c*g*t*t*c*c*t*g*a*c*g*t*tACCATAAATCAAATTGCCATCTTTTCTTTTTTTTTT	88[110]	107[110]
*t*c*c*a*t*g*a*c*g*t*t*c*c*t*g*a*c*g*t*tAATGTTTAGACTGCACCGTAATCAGTTTTTTTTTT	90[110]	105[110]
*t*c*c*a*t*g*a*c*g*t*t*c*c*t*g*a*c*g*t*tAAATAGCGAGAGGCCATTACCATTAGTTTTTTTTTT	92[110]	103[110]
*t*c*c*a*t*g*a*c*g*t*t*c*c*t*g*a*c*g*t*tTCAACTAATGCAGGGTAAATATTGACTTTTTTTTTT	94[110]	101[110]
*t*c*c*a*t*g*a*c*g*t*t*c*c*t*g*a*c*g*t*tAACATTATTACAGTTTACCAGCGCCATTTTTTTTTT	96[110]	99[110]
*t*c*c*a*t*g*a*c*g*t*t*c*c*t*g*a*c*g*t*tAAGACAAAAGGGCGCATTCCACAGACTTTTTTTTTT	98[110]	123[110]
*t*c*c*a*t*g*a*c*g*t*t*c*c*t*g*a*c*g*t*tGGAAATTATTCATAAACAACTTTCAATTTTTTTTTT	100[110]	121[110]
*t*c*c*a*t*g*a*c*g*t*t*c*c*t*g*a*c*g*t*tCAAGGCCGGAAACGAATTGCGAATAATTTTTTTTTT	102[110]	119[110]
*t*c*c*a*t*g*a*c*g*t*t*c*c*t*g*a*c*g*t*tAGCGACAGAATCAGTGAATTTCTTAATTTTTTTTTT	104[110]	117[110]
*t*c*c*a*t*g*a*c*g*t*t*c*c*t*g*a*c*g*t*tATAATCAAAATCACCATCGCCCACGCTTTTTTTTTT	106[110]	115[110]
*t*c*c*a*t*g*a*c*g*t*t*c*c*t*g*a*c*g*t*tCCGCCACCCTCAGGCATCGGAACGAGTTTTTTTTTT	108[110]	113[110]
*t*c*c*a*t*g*a*c*g*t*t*c*c*t*g*a*c*g*t*tGAAGTTTCCATTAAACGGGTAAAATACGT	110[110]	110[72]
*t*c*c*a*t*g*a*c*g*t*t*c*c*t*g*a*c*g*t*tGGTAGCAACGGCTACAGAGGCTTTCCGCC	112[110]	112[72]
*t*c*c*a*t*g*a*c*g*t*t*c*c*t*g*a*c*g*t*tATAACCGATATATTCGGTCGCGAAAGACA	114[110]	113[87]
*t*c*c*a*t*g*a*c*g*t*t*c*c*t*g*a*c*g*t*tACAGCTTGATACCGATAGTTGCGCCGTACGCCCCCTT	116[110]	107[79]
*t*c*c*a*t*g*a*c*g*t*t*c*c*t*g*a*c*g*t*tTAATTTTTTCACGTTGAAAATCTTTCGAG	118[110]	117[87]
*t*c*c*a*t*g*a*c*g*t*t*c*c*t*g*a*c*g*t*tCAGTTTCAGCGGAGTGAGAATAGAAAATGAAAATCAC	120[110]	103[79]
*t*c*c*a*t*g*a*c*g*t*t*c*c*t*g*a*c*g*t*tAGCCCTCATAGTTAGCGTAACATTTTGCT	122[110]	121[87]
*t*c*c*a*t*g*a*c*g*t*t*c*c*t*g*a*c*g*t*tCACTGAGTTTCGTCACCAGTACAAACCCGTAGAAAAT	124[110]	99[79]
irregular spacing-CpGi-18 staples		
t*c*c*a*t*g*a*c*g*t*t*c*c*t*g*a*c*g*t*t*TTCCAGTTTGGAAGAAAATGCTGAATTTTTTTTTTT	0[110]	27[110]
t*c*c*a*t*g*a*c*g*t*t*c*c*t*g*a*c*g*t*t*TGCCCCAGCAGGCCGAACTGATAGCCTTTTTTTTTT	2[110]	25[110]
t*c*c*a*t*g*a*c*g*t*t*c*c*t*g*a*c*g*t*t*TGCGTTGCGCTCACAGGAAAAACGCTTTTTTTTTT	8[110]	19[110]
t*c*c*a*t*g*a*c*g*t*t*c*c*t*g*a*c*g*t*t*TCTGTCCATCACGAAACCAGCAATACTTTTTTTTTT	14[110]	39[110]
t*c*c*a*t*g*a*c*g*t*t*c*c*t*g*a*c*g*t*t*TTGGCAGATTCACACTGGTGACCTGGTTTTTTTTTT	20[110]	33[110]
t*c*c*a*t*g*a*c*g*t*t*c*c*t*g*a*c*g*t*t*AGAGTGAGATCGGTTCTGGTGCCGGATTTTTTTTTT	28[110]	55[110]
t*c*c*a*t*g*a*c*g*t*t*c*c*t*g*a*c*g*t*t*CGTGAGTATTACGAAAATCGCGCAGATTTTTTTTTT	36[110]	47[110]
t*c*c*a*t*g*a*c*g*t*t*c*c*t*g*a*c*g*t*t*ATTTGCACGTAAAGCCTGAGAGTCTGTTTTTTTTTT	42[110]	67[110]
t*c*c*a*t*g*a*c*g*t*t*c*c*t*g*a*c*g*t*t*GGCGAATTATTCATTGTTAAAATTCGTTTTTTTTTT	46[110]	63[110]
t*c*c*a*t*g*a*c*g*t*t*c*c*t*g*a*c*g*t*t*TCAAGAAAACAAAAGCTTTCATCAACTTTTTTTTTT	48[110]	61[110]
t*c*c*a*t*g*a*c*g*t*t*c*c*t*g*a*c*g*t*t*GGATTGACCGTAATAACGAGCGTCTTTTTTTTTTT	58[110]	81[110]
t*c*c*a*t*g*a*c*g*t*t*c*c*t*g*a*c*g*t*t*AGCTATTTTTGAGGTTTATCAACAATTTTTTTTTTT	68[110]	71[110]
t*c*c*a*t*g*a*c*g*t*t*c*c*t*g*a*c*g*t*t*AGAAACCAATCAAACGATAAAAACCATTTTTTTTTT	72[110]	93[110]
t*c*c*a*t*g*a*c*g*t*t*c*c*t*g*a*c*g*t*t*CAACAGGTCAGGAACTTTTTCATGAGTTTTTTTTTT	84[110]	111[110]
t*c*c*a*t*g*a*c*g*t*t*c*c*t*g*a*c*g*t*t*AATGTTTAGACTGCACCGTAATCAGTTTTTTTTTT	90[110]	105[110]
t*c*c*a*t*g*a*c*g*t*t*c*c*t*g*a*c*g*t*t*AACATTATTACAGTTTACCAGCGCCATTTTTTTTTT	96[110]	99[110]
t*c*c*a*t*g*a*c*g*t*t*c*c*t*g*a*c*g*t*t*AAGACAAAAGGGCGCATTCCACAGACTTTTTTTTTT	98[110]	123[110]
t*c*c*a*t*g*a*c*g*t*t*c*c*t*g*a*c*g*t*t*CCGCCACCCTCAGGCATCGGAACGAGTTTTTTTTTT	108[110]	113[110]

Supplementary Table 3. CpG-containing staple sequences for various CpG spacing patterns. The CpG strands were self-ligated or fabricated by IDT company. The CpG strands replace original poly-T strands (orange) at desired helix positions as shown in the second column. For all the CpG-containing staple strands, a sequence of poly T oligonucleotide at the 5´ end or 3´ end (or both) was substituted by the CpG sequence. The majority of the staple stands have the CpG sequence on the 5´end to maintain equivalent orientation of CpG across all designs. CpG1 has 3´-3´ linkage to achieve same CpG orientation. The positions in the second column correspond to the labeled helices in Supplementary Figure 4 (helices are numbered between 0 and 125). * refers to the PS modification of CpG oligonucleotides. In the second and third columns, the number before the square brackets refers to the helix position; the number inside the square brackets refers to the nucleotide base position corresponding to the CaDNAno file.

Antibodies	Fluorophores	Catalog No. (Mostly from Biolegend)		Antibodies	Fluorophores	Catalog No. (Mostly from Biolegend)
CD11c	BV570	117331		CD3	BV570	100225
CD40	PE	124610		CD4	PE	100408
CD80	APC/fire750	561134		CD8	APC/CY7	100714
CD86	PE/CY7	105014		CD69	PE-CY7	104512
MHC-II	BV421	107632		CD25	BV711	102024
PD-L1	BV711	124319		CD62L	PerCP	104430
DEC205	PerCP/Cy5.5	138208		CD127	APC	135012
Viability	Zombie UV	423108		CD44	AF700	103026
CD11b	BV605	101257		FoxP3	BV421	126419
Gr-1	FITC	108406		IL-2	PE-cy5	503824
F4/80	PE594	123146		IFNγ	BV510	505841
CD206	BV650	141723		IL-4	PE594	504132
NK1.1	PE	156504		TNFα	PE594	506346
TLR9	FITC	ab58864		CD8 Tetramer	BV421	MBL-TB-5001-4
MyD88	/	ab135693		Goat Anti-Rabbit IgG H&L	AF594	ab150080

Supplementary Table 4. Antibodies used for flow cytometry for mouse cells. These antibodies were grouped into different panels depending on the experimental goals.

Antibodies	Fluorophores	Catalog No. BD Bioscience
CD40	BV510	563456
CD80	APC/CY7	561134
CD86	PE/CY7	561128
MHC-II	BV421	562804
PD-L1	AF700	565188
CD205	BV605	744058
TLR9	PE	560425
IL-4	BV711	564112
IFNγ	PerCP-Cy™5.5	560704

Supplementary Table 5. Antibodies used for flow cytometry for human cells.

.

Supplementary Discussion

Recent advances have illustrated the potential benefits of DNA origami in the context of cancer immunotherapy [2-4]. Several studies have demonstrated that the spatial arrangements of ligands on DNA origami resulted in significant differences in activation of their cognate receptors and downstream signaling in cells [5-7]. In this study, DoriVac improved both CD4 and CD8 T cell proliferation, activation, and cytokine secretion, most noticeably with a CpG spacing of 3.5 nm and 18 CpGs per SQB. Previous studies also investigated other CpG engineering strategies, such as 3´-3´ linked CpG immunomer [8], CpG side chains of DNA duplex [9], DNA dendrimer with looped CpG [10], and G-quadruplex-based CpG [11,12]. All these studies indicated that higher-order CpG display may be needed for enhanced immune activation. In this work, we report a finely tuned nanospacing of CpG that is narrower than that explored in previous DNA origami studies. We speculate that the mechanistic basis for the preferred 3.5 nm spacing may relate to the required distance between binding sites on a TLR dimer, based on the CpG-TLR9 crystal structure, and also to geometrical constraints of higher-order TLR9 multimerization [13]. More generally, co-presenting antigen and adjuvant with precisely defined configurations and stoichiometries on DNA origami provides a tool to characterize critical spatial parameters of danger signals and antigens for future vaccine development. Our comprehensive pre-clinical results confirm that the improved activation, cross-presentation, and cytokine secretion induced on DCs by DoriVac with optimal CpG configurations translate into superior T cell priming and polarization (compared to bolus vaccine, liposomal controls, and suboptimal CpG configurations on SQB). We also observed NK cell activation, which offers additional anti-tumor benefits. The effect was more pronounced when the antigen was co-delivered on the same particle as the CpG adjuvant, demonstrating that co-delivery is a critical aspect of this modular platform.

Some previous studies reported that CpG could assist with elimination of large tumors. These cases were either achieved by aggressive application of CpG both peritumorally and contralaterally [14] or preceded by surgical excision of the primary tumor [15]. CpG-functionalized nanoparticle vaccines have also been broadly investigated recent years [16]. For example, CpG and HPV E7 peptide co-delivered by mannose-modified liposomes decreased tumor growth of established large TC-1 grafted tumors in a mouse model [17]. As of 2022, several CpG based drugs for cancer are in clinical trials, with none yet having been approved by the FDA [18-20]. Display of CpG on DNA origami has been studied by several research groups. Schuller et al attached up to 62 CpG sequences on hollow 30-helix DNA origami to stimulate cellular immunity [21]. CpG displayed on origami, compared to free CpG, induced greater secretion of IL-6 and IL-12 in DC cells. Comberlato et al. designed spatial patterns of CpG motifs on DNA origami, with 7 nm spacing that significantly activated TLR9 in RAW264.7 macrophages [22]. This work represents the earliest published report of how varying CpG nanospacing on DNA origami can affect immune cell activation. Following this study, Du et al reported that DNA origami wireframe modified with different CpG copy numbers and spatial organization lead to different levels of Type I and Type III interferon (IFN) production through TLR9 signaling[23]. Two other recent publications explored CpG display on DNA origami without variation in nanospacing, and both reported therapeutic efficacy in mouse models. One study applied CpG on a pH-responsive DNA origami nanodevice together with antigens, leading to a potent anti-tumoral T-cell response [4]. The other study applied DNA origami to co-deliver the receptor binding domain of SARS-CoV-2 along with CpGs, leading to robust protective immunity against SARS-CoV-2 [24].

We achieved notable therapeutic effects in various tumor models by applying a modest dose of antigen and adjuvant (only 5.4 μg of antigen and 2.2 μg of CpG adjuvant) delivered by a DNA origami nanoparticle, which is a much smaller dose than that used in prior murine studies (100 μg antigen and 100 μg of CpG) [25]. A similar finding was reported in a previous study, where 4 μg of CpG was fabricated on ultrasmall (~25–50 nm) polymeric nanoparticles and co-delivered with antigen, resulting in substantial protection of mice from syngeneic tumor challenge [26]. Another recent study used spherical nucleic acid (SNA) nanoparticles that contained 9 nmol (~60 μg) of CpG in their animal efficacy study [27]. In contrast, we were able to achieve a protective immune response against tumors using as little as 0.36 nmol (2.2 μg) of CpG in DoriVac. This highlights an advantage of DNA origami-based vaccines in achieving effective immune responses with minimal amounts of adjuvant. The significant therapeutic effects observed in the context of a low dose of adjuvant suggest that the DNA origami vaccine could potentially reduce adjuvant-related toxicity [28,29,30].

Supplemental methods

Fluorescent labeling of SQBs

SQBs were labeled with Cy5 fluorophores. DNA oligonucleotides /5AmMC6/GGGATAAGTTGATTGCAGAGC-3´(anti-handle) were modified with a 5´ amine and covalently coupled to Cy5 fluorophores via N-hydroxysuccinimide (NHS) ester coupling (Lumiprobe). DNA oligonucleotide (1 mM in ddH_2O) was mixed with 10 times excess of Cy5-NHS (10 mM in DMSO) and supplemented with 10% of $NaHCO_3$ (1M, buffer at pH 8.0). The reaction was carried out in the dark overnight at room temperature shaking at 400 rpm. Zeba size-exclusion and desalting columns (7K MWCO; Thermo Scientific, Waltham, MA) were used to remove unreacted dye through centrifugation at 1000 *g* for 2 minutes. The columns were washed with 400 μL of ddH2O three times before use, according to manufacturer's protocol. The Cy5 conjugated oligonucleotides were added to the SQB folding pool with 5 times excess to ensure complete conjugation. Eight staples linked with complementary handle strands (5´-GCTCTGCAATCAACTTATCCC-3´) were used to capture the Cy5-linked strands.

Agarose gel electrophoresis

Folded SQB samples or purified SQB samples (CpG and/or OVA conjugated) were subjected to 2% native agarose gel electrophoresis at 70 V for 2.5 hours (gel prepared in 0.5 × TBE buffer supplemented with 11 mM $MgCl_2$ and/or 0.005% (v/v) EtBr or SYBR safe). The gel was imaged using a Typhoon imager.

TEM analysis

The structural integrity of the SQB was verified using negative stain transmission electron microscopy (TEM). Prior to adding the samples, grids were cleaned using plasma discharge for 30 seconds. 3.0 μL of 4-10 nM SQB solution was then deposited on a carbon coated Formvar grid (Electron Microscopy Sciences). After 3 minutes, the sample was wicked from the grid by gently blotting the grid with the edge of the filter paper. A drop of uranyl formate solution (2% w/v in H_2O) was then deposited onto the grid for 30 seconds, and the excess solution was wicked using filter paper. Studies were conducted using a JEOL JEM-1400 transmission electron microscope in brightfield mode at 80 kV.

DNase I degradation assay

SQBs (1 μg) were incubated with 1.0 U/μL DNase I (NEB) with 10 × DNase I buffer diluted in water (Gibco). Samples were incubated at 37°C for 30 minutes and then analyzed using 15% denaturing polyacrylamide (PAGE) gel to observe the CpG loading efficiency comparing to the calculated theoretical CpG oligos. Denaturing PAGE gel (15%) was homemade using 9 mL urea concentrate, 4.5 mL urea diluent, 1.5 mL urea buffer (all three from Fisher Scientific), 10 μL tetramethylethylenediamine (TEMED) and 150 μL 10 wt% ammonium persulfate (APS) casting into mini-cassette (ThermoFisher Novex). Loading wells were generated by inserting the comb into the cassette.

Cell uptake assay

Cell uptake were performed using HeLa tumor cell line and Human Embryonic Kidney cells (HEK293) maintained in high-glucose Dulbecco's modified Eagle medium (DMEM) (Gibco, Gaithersburg) and 10% fetal bovine serum (FBS) (Lonza, Wakersville) with penicillin–streptomycin. For flow cytometry, HEK293 cells were seeded at a density of 250,000 cells/mL into tissue culture treated 48 well plates (BD Life Sciences) and allowed to grow for 24 hours in 200 μL of media. CpG-SQBs with various spacings were added to a final concentration of 0.1–1 nM and incubated with cells. All samples were performed in triplicate. Raw264.7 cells were purchased from ATCC and applied for some of the stimulation studies. CpG-SQBs with various spacings were added to a final concentration of 1 nM and incubated with cells Raw264.7.

Western Blot

Cells were plated and stimulated with different versions of vaccines. Following stimulation, cells were lysed using Pierce RIPA buffer (Thermo Scientific). Protein levels were detected using Pierce BCA protein assay (Thermo Fisher Scientific, 23227). Samples were then prepared combined with 4x LDS sample buffer and DTT before being sonicated for 15 minutes followed by a 10-minute incubation at 70°C. Proteins were separated using an SDS Page gel before transfer. Thermo Fisher iBlot 2 Dry Blotting System was used to transfer proteins to the membrane. After transfer, the membrane was blocked for 30 minutes in 2% Dry Milk Powder (RPI, M17200) in PBS-T (1% Tween 20 in Dulbecco's Phosphate Buffered Saline) and incubated with a primary antibody then a second antibody. Primary antibodies used included anti-mouse TLR9 (Abcam, ab58864), anti-mouse TLR13 (Novus, NBP2-24539SS), and anti-GAPDH (Biovision, A1814). Secondary antibodies used included Anti-Rabbit IgG (H+L), Mouse/Human ads-HRP (Southern Biotech, 4050-05) and Mouse IgG HRP-conjugated Antibody (R&D Systems, HAF007).

Preparation of pDC and moDC

Human PBMCs were obtained from Catherine Wu's lab. Plasmacytoid DCs (pDCs) were isolated using the kit purchased from Miltenyi Biotec (130-097-415). Human monocyte derived DCs (moDCs) were kindly given by our neibougher lab. Both the pDCs and moDCs were cultured in 10% low-endotoxin FBS containing DMEM culture medium. The cells were stimulated by 1nM of various SQB-CpGs in 96-well plate. The cell number is 100,000 or 200,000 cells per well.

Liposome Preparation

First, 6.2mg of POPC (Anatrace, P516) was measured into a glass tube and dissolved in sufficient amount of chloroform (VWR, BDH83627.400). The tube was then covered with parafilm, and a constant stream of Nitrogen gas was blown into the tube until all chloroform evaporated. Then, the tube was dried in a vacuum overnight. Lipids were then dissolved in 1 × TE (5 mM Tris and 1 mM EDTA) with 1% sodium cholate (VWR, 101183-986) to a final concentration of 6.25mM by sonicating for 1 hour. Dissolved lipids were incubated at 4°C for 1 hour with appropriate amounts of CpG and OVA-AF488 (Ovalbumin, Alexa Fluor™ 488 Conjugate, ThermoFisher, O34781). Incorporation frequencies were determined previously using a standard curve made by measuring fluorescent signals of liposomes after incorporation of various concentrations of OVA-AF488 or Cy5-tagged oligonucleotide. This protocol was optimized to ensure that the CpG and OVA were incorporated at an equivalent dose to that delivered by the SQB. Bio-Beads SM-2 Adsorbents (Bio-Rad, 1523920) were prepared via 3 washes with 0.5mL 1 × TE followed by spinning at 3 minutes at 16000 rcf and removing the floating, inactivated beads after each step. Activated Bio-beads were then added to each sample are a ratio of 300mg of Bio-beads to 250 μL of sample and gently rotated at 4°C overnight. Liposomes were concentrated using a 30 kDa Amicon Ultra-0.5 Centrifugal Filter Unit (Millipore Sigma, UFC5030) and then diluted with 1 × TE to the desired final concentration.

Neoantigen peptide antigen conjugation with 'handle' oligonucleotide

A 'anti-juno handle' oligonucleotide, which corresponds to 24 sites on the extruding face of the SQB, were ordered from IDT with an amine modification on the 5' terminal (NH2-TTCTAGGGTTAAAAGGGGACG). These handle strands will replace some of the poly-T oligonucleotides on the extruding face of the SQB. The neoantigen peptides were ordered from GenScript with an azide-modified lysine on the N terminal. The 'handle' oligonucleotide was diluted to a final concentration of 1000 μM with phosphate buffer (pH 8.0). The neoantigen peptides were dissolved in DMSO, according to the manufacturer's instructions. The oligonucleotide was conjugated with dibenzocyclooctyne-N-hydroxysuccinimidyl ester (DBCO-NHS ester; Millipore, #761524). The DBCO-NHS ester (diluted in DMSO to 2000 μM concentration) was incubated with the oligonucleotide (diluted in phosphate buffer pH 8.0 to 200 μM concentration) in 1:1 volume ratio and incubated overnight at ambient temperature. The final concentration of DBCO-NHS ester exceeded the concentration of the oligonucleotide 10:1, to ensure that all oligonucleotides were successfully conjugated with DBCO-NHS ester. After incubation, the product was purified via Illustra NAP column (GE Healthcare Life Sciences, #17-0852-02) and eluted with sterile water. The flow-through was concentrated via 3K Amicron Ultra Centrifugal Filter Unit (Millipore; #UFC500324) at 14,000 rcf for 15 minutes at 4°C. DBCO incorporation was confirmed by observation of an OD310 peak and final concentration was determined via measurement of A280 using the NanoDrop.

The N-terminal azide modified neoantigen peptides (M27: REGVELCPGNKYEMRRHGTTHSLVIHD; M33: DSGSPFPAAVILRDALHMARGLKYLHQ, M30: PSKPSFQEFVDWENVSPELNSTDQPFL, M47: GRGHLLGRLAAIVGKQVLLGRKVVVVR) were conjugated with the DBCO-conjugated oligonucleotide via a copper-free click chemistry reaction. The peptide was combined with the DBCO-conjugated oligonucleotide at a ratio of 1.5: 1. 10X PBS was added to the reaction mixture so that the final reaction included 1XPBS. The reaction was incubated overnight at room temperature. 15% denaturing PAGE (dPAGE) was used to confirm successful conjugation of the peptide to the DBCO-modified oligonucleotide. 8% dPAGE was used to purify the samples. The reaction mixture was combined with formamide loading buffer (FLB) at a volume ratio of 1:1. The resulting mixture was loaded into a dPAGE gel, and the gel run at 250V for 50 minutes. The peptide-conjugated oligonucleotide band was observed via UV shadowing on a thin layer chromatography (TLC) plate and cut out with a razor blade. The gel was crushed with a pestle in a 15 mL Falcon tube. 1 × TE buffer was added in a 1:1 volume ratio and the solution was incubated overnight at 25°C, shaking at high speed. The gel solution was filtered through Freeze 'N Squeeze DNA Gel Extraction Spin Columns (Bio-Rad; #7326165) according to the manufacturer's protocol and then purified via ethanol precipitation. The peptide-oligonucleotide pellet was resuspended in 1 × PBS, and the concentration was determined via NanoDrop. Successful purification was confirmed via dPAGE analysis.

Denaturing PAGE (dPAGE) verification of peptide-conjugated oligonucleotide

Denaturing PAGE gels were cast using SequaGel-UreaGel System Kit (Fisher Scientific; #EC-833). 5 picomoles of the samples were mixed with formamide loading buffer (FLB) in 1:1 volume ratio. The mixture was denatured at 95°C for 2 minutes and then loaded into the wells. The gel was run in 0.5 × TBE buffer for 45 minutes at 250V. The gel was stained with SYBR Gold for 10 minutes and then imaged with the Typhoon Gel Scanner.

Ethanol precipitation

The peptide-oligonucleotide conjugates were purified via ethanol precipitation. After filtering, 100% ethanol and 3M NaOAc were added to the sample in a 50mL Falcon tube, so that a final concentration of 80% ethanol and 0.3M NaOAc was achieved. The solution was placed in the -80°C freezer for a minimum of one hour. The sample was then spun down at high speed in a pre-cooled RC6+ Superspeed Centrifuge (Thermo Scientific). The sample was spun for 16,000g for 1 hour at -20°C. A white pellet was observed after spinning. The pellet was washed twice with 5 mL of 75% ethanol. The pellet was dried at ambient temperature and resuspended in 1 × PBS.

Neoantigen peptide-conjugated oligonucleotide hybridization with SQB

The purified peptide-conjugated oligonucleotides were hybridized to the PEG purified SQB. The peptide-conjugated oligonucleotides were added in 2 × excess to the SQB, maintaining a final concentration of 10mM $MgCl_2$ and 1 × TE via addition of stock solutions of 10 × TE and 100mM $MgCl_2$. The SQBs were added last to ensure that they are not subjected to variable concentrations of TE and $MgCl_2$, which can disrupt the structural integrity of the DNA origami. The peptide-SQB solution was incubated for 1-2 hours at 37°C while shaking. The purity and integrity of the sample was confirmed via agarose gel electrophoresis and TEM. The peptide-SQBs were purified via PEG purification and their concentration was determined via NanoDrop. The number of peptides conjugated to each SQB was determined via a DNA I degradation assay (below).

DNAse I degradation and silver stain analysis

The peptide loaded SQBs were subjected to DNase I degradation. 1 picomole of SQBs was incubated with 1.0 U/µl DNase I (NEB) with 10 × DNase I buffer diluted in water (Gibco). Samples were incubated in the thermocycler for 30 minutes at 37°C. The sample was combined with 4 × NuPAGE LDS sample buffer (ThermoFisher; #NP0008), incubated at 70°C for 10 minutes in the thermocycler, and loaded in 4-12% NuPAGE Bis-Tris gels (ThermoFisher; #NP0322). The gel was run in 1 × MES SDS running buffer (ThermoFisher; #NP0002) at 200V for 32 minutes. The gel was analyzed via silver stain (Pierce, #24612), following the manufacturer's protocol. The gel was imaged under Silver Stain setting on Image Lab 6 on a Gel Doc EZ Imager (Bio-Rad). ImageJ was used to quantify the band intensity and determine the conjugation efficiency of the peptides to the SQBs.

Processing LNs

The axillary and superficial cervical LNs on the left side of the mouse (the same side as the vaccine injection) were collected for flow. The LNs were meshed through a 70 µm cell strainer using a syringe plunger to obtain a single cell suspension. The suspension was separated and stained with various panels of multiple antibodies. The cells were then washed and analyzed using flow cytometry (LSRFortessa, BD).

Processing blood cells

Blood cells were collected in heparin-coated tubes to prevent clotting. Plasma was collected by spinning at 500 x g for 5 minutes to separate the plasma cells from other blood cells. Plasma was saved at -80 °C before analyzing. The blood cells were treated with red blood cell lysis buffer 3 times. The remaining peripheral blood mononuclear cells (PBMCs) were analyzed using flow cytometry or via ELIspot (LSRFortessa, BD).

Tumor cell processing into single cell suspension

Mice were sacrificed on day 15 after tumor inoculation. The melanoma tumors ranged from 2–15 mm in diameter at the time of sacrifice for tumor-cell processing. The tumors were dissociated from the skin and muscle. The tumor tissues were then sliced into 1–2 mm pieces and dissociated in DMEM supplemented with 80 U/mL collagenase type IV (Gibco # 17104019), 20 U/mL DNase I in HBSS (Sigma #11284932001), and 2 mg/mL bovine serum albumin (Sigma, #05470) for 1.5 hours at 37°C, shaking at a slow speed to ensure proper mixing. The resultant cell suspension was filtered through a 70 μm cell strainer to obtain a single cell suspension. The cells were then stained with antibodies in various panels for flow cytometry analysis.

Anti-dsDNA antibody and anti-PEG antibody test

The plasma samples collected from various animal tumor model studies were applied to evaluate the anti-dsDNA antibody and anti-PEG antibody in the mouse serum after being treated by different conditions. The anti-mouse dsDNA IgG (#5120), anti-mouse PEG IgG (#PEG-030), and anti-mouse dsDNA IgA/G/M (#5110) ELISA kits were purchased from Alpha Diagnostic. For anti-dsDNA antibody tests, the plasma samples were diluted 100 times. For anti-PEG antibody tests, the plasma samples were diluted 10 times. The experiments were performed following the detailed instruction provided by the manufacturer.

Extended statistical analyses

The linear mixed effect model for tumor volume trajectory in figure 5B was estimated using a random intercept for each mouse, and fixed effect estimates for time, treatment modalities and their interaction. The intercept is defined as the control group starting at day 0. Day is treated as continuous and is highly significant. It modifies the effect of the control across time. All other arm variables represent the intercept for the growth rates of various modalities of treatment. The intercepts are not significantly different from the controls. The interaction variables, between Day and Arm measure the trajectories of that modalities rate. Here the trajectory growth rate for 3.5nm (CpG2) is significantly lower than the control, and show the greatest reduction in tumor volume across time when compared to the control. Irregular Spacing (CpGi) & Free CpG2+Free OVA are both statistically different from the control, and show a greater reduction in tumor volume across time than the control. The statistical difference between CpG2-SQB+SQB-OVA & 7nm (CPG4) and the control is marginally significant, with both arms responding better than the control. If we change the reference arm from control to CpG2, the growth of every other treatment is larger than the CpG2 whose growth rate is now dictated by day and its intercept (Supplementary Table 6). The trajectory growth rate for CpG2 is significantly slower than CpG4 and CpGi. For other tumor growth results with less groups involved, two-way ANOVA was applied with Tukey's multiple comparisons test.

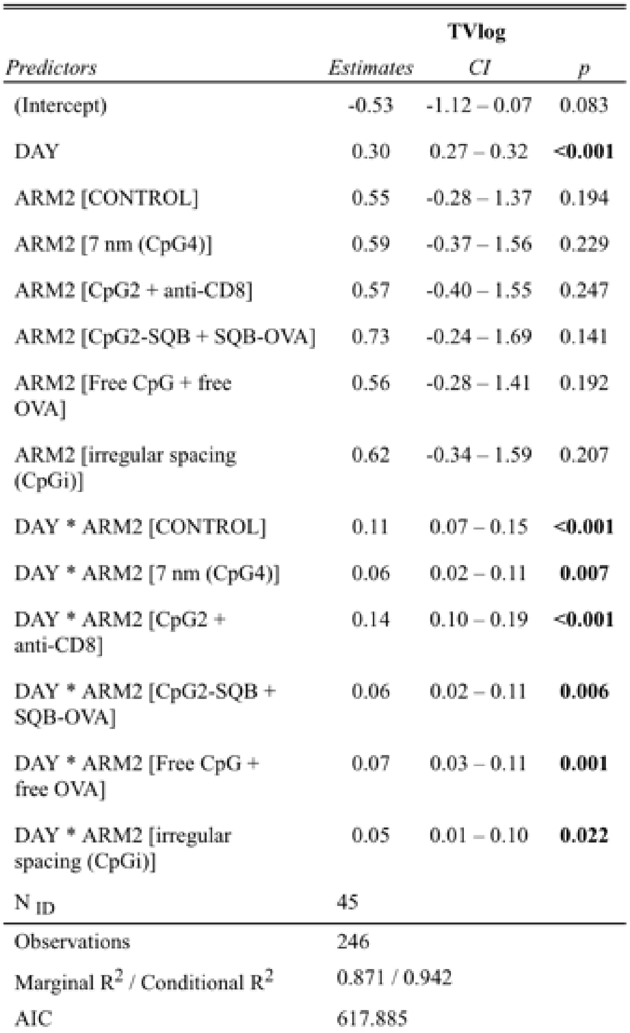

	TVlog		
Predictors	*Estimates*	*CI*	*p*
(Intercept)	-0.53	-1.12 – 0.07	0.083
DAY	0.30	0.27 – 0.32	**<0.001**
ARM2 [CONTROL]	0.55	-0.28 – 1.37	0.194
ARM2 [7 nm (CpG4)]	0.59	-0.37 – 1.56	0.229
ARM2 [CpG2 + anti-CD8]	0.57	-0.40 – 1.55	0.247
ARM2 [CpG2-SQB + SQB-OVA]	0.73	-0.24 – 1.69	0.141
ARM2 [Free CpG + free OVA]	0.56	-0.28 – 1.41	0.192
ARM2 [irregular spacing (CpGi)]	0.62	-0.34 – 1.59	0.207
DAY * ARM2 [CONTROL]	0.11	0.07 – 0.15	**<0.001**
DAY * ARM2 [7 nm (CpG4)]	0.06	0.02 – 0.11	**0.007**
DAY * ARM2 [CpG2 + anti-CD8]	0.14	0.10 – 0.19	**<0.001**
DAY * ARM2 [CpG2-SQB + SQB-OVA]	0.06	0.02 – 0.11	**0.006**
DAY * ARM2 [Free CpG + free OVA]	0.07	0.03 – 0.11	**0.001**
DAY * ARM2 [irregular spacing (CpGi)]	0.05	0.01 – 0.10	**0.022**
N_{ID}	45		
Observations	246		
Marginal R^2 / Conditional R^2	0.871 / 0.942		
AIC	617.885		

Supplementary Table 6. Statistics results for Fig. 5B tumor trajectory growth when using CpG2 as the reference arm.

Statistics and Reproducibility

We have collected TEM images such as those shown in Figures 1D and G for independently fabricated nanostructures more than ten times, all with similar results. For Figures 1H and 1I, we have generated similar agarose gels twice, both times with similar results. For Figure 1K, we performed similar experiments three times, all with similar results. For Supplementary Figure 3 A and B, we performed this experiment a single time . For Supplementary Figure 3 C–E, we have repeated these experiments more than ten times, all with similar results. For Supplementary Figure 5 C and D, we have performed these experiments multiple times as a validation process. Figure Supplementary Figure 5 F and H, we have done twice. For Supplementary Figure 6 B and C, we have repeated more than 10 times. For Supplementary Figure 7 A and B, we have done twice. For Supplementary Figure 7 E and F, we have repeated at least 3 times. For Supplementary Figure 7 G and J, we have done twice. For Supplementary Figure 8, we have repeated at least 4 times as our validation process. For Supplementary Figure 9A–C, we have done once. For Supplementary Figure 10A, D-F, we have done once. For Supplementary

Figure 12A and B, we have done once. For Supplementary Figure 13A, we have repeated at least 6 times. For Supplementary Figure 14A, we have done once. For Supplementary Figure 17G, we have done twice. For Supplementary Figure 19A, we have repeated three time. For Supplementary Figure 20 M and N, we have done twice. For Supplementary Figure 28 A, B, D and F, we have done three times. All the independently repeated experiments showed similar results.

Supplementary References

1. Ponnuswamy, N., *et al.* Oligolysine-based coating protects DNA nanostructures from low-salt denaturation and nuclease degradation. *Nat Commun* **8**, 15654 (2017).
2. Li, S., *et al.* A DNA nanorobot functions as a cancer therapeutic in response to a molecular trigger in vivo. *Nat Biotechnol* **36**, 258-264 (2018).
3. Tseng, C.Y., Wang, W.X., Douglas, T.R. & Chou, L.Y.T. Engineering DNA Nanostructures to Manipulate Immune Receptor Signaling and Immune Cell Fates. *Adv Healthc Mater* **11**, e2101844 (2022).
4. Liu, S., *et al.* A DNA nanodevice-based vaccine for cancer immunotherapy. *Nat Mater* **20**, 421-430 (2021).
5. Veneziano, R., *et al.* Role of nanoscale antigen organization on B-cell activation probed using DNA origami. *Nat Nanotechnol* **15**, 716-723 (2020).
6. Shaw, A., *et al.* Binding to nanopatterned antigens is dominated by the spatial tolerance of antibodies. *Nat Nanotechnol* **14**, 184-190 (2019).
7. Verheyen, T., *et al.* Spatial organization-dependent EphA2 transcriptional responses revealed by ligand nanocalipers. *Nucleic Acids Res* **48**, 5777-5787 (2020).
8. Yu, D., *et al.* 'Immunomers'--novel 3'-3'-linked CpG oligodeoxyribonucleotides as potent immunomodulatory agents. *Nucleic Acids Res* **30**, 4460-4469 (2002).
9. Minari, J., Mochizuki, S. & Sakurai, K. Enhanced cytokine secretion owing to multiple CpG side chains of DNA duplex. *Oligonucleotides* **18**, 337-344 (2008).
10. Qu, Y., *et al.* Self-Assembled DNA Dendrimer Nanoparticle for Efficient Delivery of Immunostimulatory CpG Motifs. *ACS Appl Mater Interfaces* **9**, 20324-20329 (2017).
11. Hoshi, K., *et al.* G-Quadruplex Structure Improves the Immunostimulatory Effects of CpG Oligonucleotides. *Nucleic Acid Ther* **29**, 224-229 (2019).
12. Tu, A.T.T., Hoshi, K., Ikebukuro, K., Hanagata, N. & Yamazaki, T. Monomeric G-Quadruplex-Based CpG Oligodeoxynucleotides as Potent Toll-Like Receptor 9 Agonists. *Biomacromolecules* **21**, 3644-3657 (2020).
13. Ohto, U., *et al.* Structural basis of CpG and inhibitory DNA recognition by Toll-like receptor 9. *Nature* **520**, 702-705 (2015).
14. Heckelsmiller, K., *et al.* Combined dendritic cell- and CpG oligonucleotide-based immune therapy cures large murine tumors that resist chemotherapy. *Eur J Immunol* **32**, 3235-3245 (2002).
15. Ohashi, K., *et al.* Surgical excision combined with autologous whole tumor cell vaccination is an effective therapy for murine neuroblastoma. *J Pediatr Surg* **41**, 1361-1368 (2006).
16. Chen, W., *et al.* CpG-Based Nanovaccines for Cancer Immunotherapy. *Int J Nanomedicine* **16**, 5281-5299 (2021).
17. Zhao, Y., *et al.* Mannose-Modified Liposome Co-Delivery of Human Papillomavirus Type 16 E7 Peptide and CpG Oligodeoxynucleotide Adjuvant Enhances Antitumor Activity Against Established Large TC-1 Grafted Tumors in Mice. *Int J Nanomedicine* **15**, 9571-9586 (2020).

18. Zhang, Z.*, et al.* CpG Oligodeoxynucleotides for Anticancer Monotherapy from Preclinical Stages to Clinical Trials. *Pharmaceutics* **14**(2021).
19. Shirota, H., Tross, D. & Klinman, D.M. CpG Oligonucleotides as Cancer Vaccine Adjuvants. *Vaccines (Basel)* **3**, 390-407 (2015).
20. Saxena, M., van der Burg, S.H., Melief, C.J.M. & Bhardwaj, N. Therapeutic cancer vaccines. *Nat Rev Cancer* **21**, 360-378 (2021).
21. Schuller, V.J.*, et al.* Cellular immunostimulation by CpG-sequence-coated DNA origami structures. *ACS Nano* **5**, 9696-9702 (2011).
22. Comberlato, A., Koga, M.M., Nussing, S., Parish, I.A. & Bastings, M.M.C. Spatially Controlled Activation of Toll-like Receptor 9 with DNA-Based Nanomaterials. *Nano Lett* **22**, 2506-2513 (2022).
23. Du, R.R.*, et al.* Innate Immune Stimulation Using 3D Wireframe DNA Origami. *ACS Nano* **16**, 20340-20352 (2022).
24. Oktay, E.*, et al.* DNA origami presenting the receptor binding domain of SARS-CoV-2 elicit robust protective immune response. *Commun Biol* **6**, 308 (2023).
25. Li, A.W.*, et al.* A facile approach to enhance antigen response for personalized cancer vaccination. *Nat Mater* **17**, 528-534 (2018).
26. de Titta, A.*, et al.* Nanoparticle conjugation of CpG enhances adjuvancy for cellular immunity and memory recall at low dose. *Proc Natl Acad Sci U S A* **110**, 19902-19907 (2013).
27. Teplensky, M.H.*, et al.* Multi-antigen spherical nucleic acid cancer vaccines. *Nat Biomed Eng* (2023).
28. Yew, N.S.*, et al.* CpG-depleted plasmid DNA vectors with enhanced safety and long-term gene expression in vivo. *Mol Ther* **5**, 731-738 (2002).
29. Lucas, C.R.*, et al.* DNA Origami Nanostructures Elicit Dose-Dependent Immunogenicity and Are Nontoxic up to High Doses In Vivo. *Small*, e2108063 (2022).
30. Wamhoff, E.C.*, et al.* Evaluation of Nonmodified Wireframe DNA Origami for Acute Toxicity and Biodistribution in Mice. *ACS Appl Bio Mater* (2023).

B

Supplementary material for Chapter 3

Supplementary Information for:

DNA origami vaccine (DoriVac) nanoparticles improve both humoral and cellular immune responses to infectious diseases

Yang C. Zeng[1,2,3*], Olivia J. Young[2,3,4*], Longlong Si[2*], Min Wen Ku[2*], Giorgia Isinelli[2], Anjali Rajwar[2], Amanda Jiang[2], Chris M. Wintersinger[1,3], Amanda R. Graveline[2], Andyna Vernet[2], Melinda Sanchez[2], Ju Hee Ryu[1,5], Ick Chan Kwon[1,5,6], Girija Goyal[2#], Donald E. Ingber[2,7,8#], William M. Shih[1,2,3#].

* These authors contributed equally to this work
\# Correspondence to: william.shih@wyss.harvard.edu; don.ingber@wyss.harvard.edu; girija.goyal@wyss.harvard.edu

[1]Department of Cancer Biology, Dana-Farber Cancer Institute, Harvard Medical School, Boston, Massachusetts 02115, USA
[2]Wyss Institute for Biologically Inspired Engineering at Harvard University, Boston, Massachusetts 02115, USA
[3]Department of Biological Chemistry and Molecular Pharmacology, Harvard Medical School, Boston, Massachusetts 02115, USA
[4]Harvard-Massachusetts Institute of Technology (MIT) Division of Health Sciences and Technology, Massachusetts Institute of Technology, Cambridge, Massachusetts, 02139, USA
[5]Center for Theragnosis, Biomedical Research Institute, Korea Institute of Science and Technology (KIST), Seoul 02792, Republic of Korea
[6]KU-KIST Graduate School of Converging Science and Technology, Korea University, Seoul 02841, Republic of Korea
[7]Vascular Biology Program, Department of Surgery, Boston Children's Hospital and Harvard Medical School, Boston, MA, 02115 USA
[8]Harvard John A. Paulson School of Engineering and Applied Sciences, Boston, MA, 02134 USA

Variant	**Sequence**
SARS-CoV-2 (Alpha)	GDISGINASVVNIQKEIDRLNEVAKNLNESLIDL QELGKYEQYIK
SARS-CoV-2 (Omicron)	GDISGINASVVNIQKEIDRLNEVAKNLNESLIDL QELGKYEQGSG

Supplementary Table 1 | Differences between HR2 sequences in variants of SARS-CoV-2. The amino acids that differ between the two variant sequences are colored in red. HR2 peptide is highly conserved, compared to many epitopes within the spike region, which renders the effectiveness of HR2-based SARS-CoV-2 vaccines less susceptible to antigenic drift.

Peptide Name	**Sequence**	**Molecular Weight**	**Number of Residues**	**Net Charge at pH 7**	**Hydrophobicity (GRAVY)**
SARS-CoV-2 HR2	{Lys(N3)}GDI SGINASVVNI QKEIDRLNE VAKNLNESLI DLQELGKYE QYIK	5203.81 g/mol	46	-2.0	-0.52
HIV HR2	{Lys(N3)}WN NMTWMEWD REINNYTSLI HSLIEESQNQ QEKNEQELL ELDKWASLW NWF	6600.19 g/mol	52	-5.9	-1.14
Ebola HR2	{Lys(N3)}IEP HDWTKNITD KIDQIIHDFV DK	3049.38 g/mol	25	-1.8	-0.98

Supplementary Table 2 | Peptide sequences and relevant properties. Peptides were purchased with N-terminal azide modifications from IDT. The azide modifications enable a click-chemistry reaction between the azide-modified peptide and a DBCO-modified oligonucleotide. A negative value in the Grand AVerage of hydropathY (GRAVY) score indicates peptides that are net hydrophilic at pH 7.

Sample	**Intensity of DoriVac Band**	**Intensity of Peptide Band (Control)**	**Percent Conjugation Efficiency**
SARS-CoV-2 DoriVac	5885.468	5770.296	102.0%
Ebola DoriVac	2660.154	2573.125	103.4%
HIV DoriVac	3330.874	3436.288	96.9%

Supplementary Table 3 | Peptide conjugation efficiency. Peptide conjugation efficiency was determined by using the band intensity of a DNase I-digested infectious disease SQB, as calculated by ImageJ, and comparing it with the band intensity of the theoretical amount of peptide.

Antibody	Fluorophore	BioLegend Catalog Number
CD11c	BV510	117338
CD40	PE	124610
CD80	APC/fire 750	104740
CD86	PE/Cy7	105014
MHC-II	BV421	107632
PD-L1	BV785	124331
DEC205	PerCp/Cy 5.5	138207
CD11b	BV605	101257
CD103	AF700	121442
Gr-1	FITC	108406
Viability	Zombie UV	423108

Supplementary Table 4 | Antibodies used for dendritic-cell (DC) flow cytometry. These antibodies were grouped into different panels depending on the experimental goals.

Antibody	Fluorophore	BioLegend Catalog Number
B220	BV510	103247
CD19	AF700	115528
CD138	BV650	142518
Ter119 (Ly-76)	BV785	116245
CD38	PE/Fire 700	102747
IgG1	PerCP/Cyanine5.5	406612
IgG2a	BV421	407117
CD40	PE/CY7	124622
CD27	APC/fire750	124237
PD-L2	PE594	107216
Fas (CD95)	FITC	152606
Viability	Zombie UV	423108

Supplementary Table 5 | Antibodies used for B cells flow cytometry. These antibodies were grouped into different panels depending on the experimental goals.

Antibody	Fluorophore	BioLegend Catalog Number
CD3	BV785	100232
CD8	APC/Cy7	100713
CD4	PE	100408
CD69	PE-Cy7	104512
CD62L	PerCp	104430
CD44	AF-700	103026
CD127	APC	135012
CD25	BV650	102037
PD-1	BV605	135220
CD107a	FITC-AF488	121608
Viability	Zombie UV	423108
FoxP3 (Intra)	BV421	126419
TNFα (Intra)	PE594	506346
IL-2 (Intra)	PE - Cy5	503824
IFN-γ (Intra)	BV510	505841

Supplementary Table 6 | Antibodies used for T cells flow cytometry. These antibodies were grouped into different panels depending on the experimental goals.

MHC-I or MHC-II	Allele	Start	End	Length	Peptide	Core peptide region	Rank
MHC-I	H-2-Db	8	17	10	ASVVNIQKEI	ASVVNIQEI	0.04
MHC-I	H-2-Db	3	11	9	ISGINASVV	ISGINASVV	0.09
MHC-I	H-2-Kb	6	13	8	INASVVNI	INAS-VVNI	0.37
MHC-I	H-2-Kb	30	37	8	SLIDLQEL	SLID-LQEL	0.37
MHC-I	H-2-Db	8	20	13	ASVVNIQKEIDRL	ASVVNIDRL	0.39
MHC-I	H-2-Db	29	37	9	ESLIDLQEL	ESLIDLQEL	0.44
MHC-I	H-2-Kb	13	20	8	IQKEIDRL	IQKE-IDRL	0.99
MHC-I	H-2-Db	4	11	8	SGINASVV	SGI-NASVV	0.68
MHC-II	H2-IAb	2	16	15	DISGINASVVNIQKE	INASVVNIQ	2
MHC-II	H2-IAb	3	17	15	ISGINASVVNIQKEI	INASVVNIQ	2.4
MHC-II	H2-IAb	1	15	15	GDISGINASVVNIQK	INASVVNIQ	3.4
MHC-II	H2-IAb	4	18	15	SGINASVVNIQKEID	INASVVNIQ	4.4
MHC-II	H2-IAb	5	19	15	GINASVVNIQKEIDR	INASVVNIQ	18
MHC-II	H2-IAb	15	29	15	KEIDRLNEVAKNLNE	DRLNEVAKN	29
MHC-II	H2-IAb	14	28	15	QKEIDRLNEVAKNLN	DRLNEVAKN	36
MHC-II	H2-IAb	16	30	15	EIDRLNEVAKNLNES	DRLNEVAKN	40

Supplementary Table 7 | Predicted murine MHC epitopes of the SARS-CoV-2 HR2 peptide and associated MHC binding. NetMHCpan-4.1 was used to predict the top eight murine MHC-I and MHC-II epitopes of each HR2 peptide. The default cutoff for MHC binders was used as described by NetMHCpan[59]. A lower rank score for the peptide is associated with stronger binding to MHC. 0.5% was defined as the cutoff for 'strong' MHC-I binders while 2% was defined as the cutoff for 'weak' MHC-I binders. Any peptides that had a rank score >2% were assumed to not bind to MHC-I. 2% was defined as the cutoff for 'strong' MHC-II binders while 10% was defined as the cutoff for 'weak' MHC-II binders. Any peptides that had a rank score >10% were assumed to not bind to MHC-II.

MHC-I or MHC-II	Allele	Start	End	Length	Peptide	Core peptide region	Rank
MHC-I	H-2-Db	11	19	9	REINNYTSL	REINNYTSL	0.09
MHC-I	H-2-Kb	17	24	8	TSLIHSLI	TSL-IHSLI	0.42
MHC-I	H-2-Kb	16	23	8	YTSLIHSL	YTS-LIHSL	0.5
MHC-I	H-2-Db	30	38	9	QQEKNEQEL	QQEKNEQEL	0.39
MHC-I	H-2-Db	27	38	12	SQNQQEKNEQEL	SQNQNEQEL	0.43
MHC-I	H-2-Kb	12	19	8	EINNYTSL	EINN-YTSL	0.79
MHC-I	H-2-Db	11	20	10	REINNYTSLI	REINNYTSI	0.7
MHC-I	H-2-Db	29	38	10	NQQEKNEQEL	NQQENEQEL	0.85
MHC-II	H2-IAb	16	30	15	YTSLIHSLIEESQNQ	LIHSLIEES	11
MHC-II	H2-IAb	15	29	15	NYTSLIHSLIEESQN	LIHSLIEES	14
MHC-II	H2-IAb	14	28	15	NNYTSLIHSLIEESQ	LIHSLIEES	20
MHC-II	H2-IAb	17	31	15	TSLIHSLIEESQNQQ	LIHSLIEES	20
MHC-II	H2-IAb	12	26	15	EINNYTSLIHSLIEE	NYTSLIHSL	21
MHC-II	H2-IAb	13	27	15	INNYTSLIHSLIEES	YTSLIHSLI	23
MHC-II	H2-IAb	11	25	15	REINNYTSLIHSLIE	NYTSLIHSL	26
MHC-II	H2-IAb	21	35	15	HSLIEESQNQQEKNE	IEESQNQQE	30

Supplementary Table 8 | Predicted murine MHC epitopes of the HIV HR2 peptide and associated MHC binding. NetMHCpan-4.1 was used to predict the top eight murine MHC-I and MHC-II epitopes of each HR2 peptide. The default cut-off for MHC binders was used as described by NetMHCpan[59]. A lower rank score for the peptide is associated with stronger binding to MHC. 0.5% was defined as the cut-off for 'strong' MHC-I binders while 2% was defined as the cut-off for 'weak' MHC-I binders. Any peptides that had a rank score >2% were assumed to not bind to MHC-I. 2% was defined as the cut-off for 'strong' MHC-II binders while 10% was defined as the cut-off for 'weak' MHC-II binders. Any peptides that had a rank score >10% were assumed to not bind to MHC-II.

MHC-I or MHC-II	Allele	Start	End	Length	Peptide	Core peptide region	Rank
MHC-I	H-2-Db	8	17	10	KNITDKIDQI	KNITDIDQI	1.8
MHC-I	H-2-Kb	13	21	9	KIDQIIHDF	KIDQIIHDF	4
MHC-I	H-2-Kb	10	17	8	ITDKIDQI	IT-DKIDQI	4.9
MHC-I	H-2-Db	10	18	9	ITDKIDQII	ITDKIDQII	4
MHC-I	H-2-Db	8	18	11	KNITDKIDQII	KNITIDQII	5.3
MHC-I	H-2-Db	6	14	9	WTKNITDKI	WTKNITDKI	5.6
MHC-I	H-2-Db	13	21	9	KIDQIIHDF	KIDQIIHDF	6.1
MHC-I	H-2-Kb	9	17	9	NITDKIDQI	NITDKIDQI	7.4
MHC-II	H2-IAb	3	17	15	PHDWTKNITDKIDQI	WTKNITDKI	19
MHC-II	H2-IAb	2	16	15	EPHDWTKNITDKIDQ	WTKNITDKI	19
MHC-II	H2-IAb	1	15	15	IEPHDWTKNITDKID	WTKNITDKI	23
MHC-II	H2-IAb	4	18	15	HDWTKNITDKIDQII	WTKNITDKI	31
MHC-II	H2-IAb	5	19	15	DWTKNITDKIDQIIH	WTKNITDKI	57
MHC-II	H2-IAb	6	20	15	WTKNITDKIDQIIHD	NITDKIDQI	60
MHC-II	H2-IAb	7	21	15	TKNITDKIDQIIHDF	ITDKIDQII	62
MHC-II	H2-IAb	10	24	15	ITDKIDQIIHDFVDK	IDQIIHDFV	67

Supplementary Table 9 | Predicted murine MHC epitopes of the Ebola HR2 peptide and associated MHC binding. NetMHCpan-4.1 was used to predict the top eight murine MHC-I and MHC-II epitopes of each HR2 peptide. The default cut-off for MHC binders was used as described by NetMHCpan[59]. A lower rank score for the peptide is associated with stronger binding to MHC. 0.5% was defined as the cut-off for 'strong' MHC-I binders while 2% was defined as the cut-off for 'weak' MHC-I binders. Any peptides that had a rank score >2% were assumed to not bind to MHC-I. 2% was defined as the cut-off for 'strong' MHC-II binders while 10% was defined as the cut-off for 'weak' MHC-II binders. Any peptides that had a rank score >10% were assumed to not bind to MHC-II.

Infectious disease	**MHC-I strong binders**	**MHC-I weak binders**	**MHC-II strong binders**	**MHC-II weak binders**
SARS-CoV-2	6	>8	0	4
HIV	2	>8	0	0
Ebola	0	1	0	0

Supplementary Table 10 | Summary Table of 'strong' and 'weak' MHC binding epitopes for various HR2 peptides. NetMHCpan-4.1 was used to predict the top eight murine MHC-I and MHC-II epitopes of each HR2 peptide. The default cutoff for MHC binders was used as described by NetMHCpan[59]. A lower rank score for the peptide is associated with stronger binding to MHC. 0.5% was defined as the cutoff for 'strong' MHC-I binders while 2% was defined as the cutoff for 'weak' MHC-I binders. Any peptides that had a rank score >2% were assumed to not bind to MHC-I. 2% was defined as the cutoff for 'strong' MHC-II binders while 10% was defined as the cutoff for 'weak' MHC-II binders. Any peptides that had a rank score >10% were assumed to not bind to MHC-II.

Antibody	Fluorophore	Catalog Number	Supplier
CD1c	BV421	331526	Biolegend
CD14	BUV395	563561	BD
CD86	BV605	305430	Biolegend
CD40	APC/Fire™ 750	334345	Biolegend
HLA-DR	PE-Cy7	307616	Biolegend
CD83	FITC	305306	Biolegend
ViaKrome 808 Fixable Viability Dye	ViaKrome 808	C36628	Beckman Coulter

Supplementary Table 11 | Antibodies used for human monocyte-derived dendritic cells (DCs) flow cytometry. These antibodies were grouped into different panels depending on the experimental goals.

Antibody	Fluorophore	Catalog Number	Supplier
CD3	PerCP Cy5.5	317336	Biolegend
CD4	BV650	317436	Biolegend
CD8	AF700	344724	Biolegend
IFNγ	BV421	506538	Biolegend
TNFα	FITC	502906	Biolegend
IL2	PE-Cy7	500326	Biolegend
Mouse IgG1, ϰ Isotype Ctrl Antibody	BV421	400158	Biolegend
Mouse IgG1, ϰ Isotype Ctrl Antibody	FITC	400108	Biolegend
Rat IgG2a, ϰ Isotype Ctrl Antibody	PE-Cy7	400522	Biolegend
ViaKrome 808 Fixable Viability Dye	ViaKrome 808	C36628	Beckman Coulter

Supplementary Table 12 | Antibodies used for human intracellular cytokine staining flow cytometry. These antibodies were grouped into different panels depending on the experimental goals.

Protein Name	**Supplier**	**Catalog Number**	**Number of Lysines**	**Molecular Weight**
HBsAg	Advanced Immunochemical Inc.	7-HbADW	4	25,394.7 g/mol
E8L	Sino Biological	40890-V08B	21	35,750 g/mol
H3L	Sino Biological	40893-V08H1	22	33,690 g/mol
M1R	Sino Biological	40904-V07H	10	21,590 g/mol

Supplementary Table 13 | Protein sources and relevant properties. The number of lysines for each protein is relevant to the protein-oligonucleotide conjugation reaction, as the oligonucleotide is conjugated to lysine residues via an NHS ester reaction with the amino group on the lysines, followed by a DBCO-azide click chemistry reaction.

HLA-A or HLA-DRB	Start	End	Length	Peptide	Core peptide region	Rank
HLA-A*02:01	19	27	9	RLNEVAKNL	RLNEVAKNL	0.16
HLA-A*02:01	26	34	9	NLNESLIDL	NLNESLIDL	0.18
HLA-A*02:01	30	37	8	SLIDLQEL	SLID-LQEL	0.37
HLA-A*02:01	25	34	10	KNLNESLIDL	KLNESLIDL	0.66
HLA-A*02:01	24	34	11	AKNLNESLIDL	ALNESLIDL	1.1
HLA-A*02:01	5	13	9	GINASVVNI	GINASVVNI	1.1
HLA-A*02:01	15	23	9	KEIDRLNEV	KEIDRLNEV	1.5
HLA-A*02:01	13	23	11	IQKEIDRLNEV	IQIDRLNEV	1.5
HLA-DRB1*01:11	1	15	15	GDISGINASVVNIQK	ISGINASVV	12
HLA-DRB1*01:11	14	28	15	QKEIDRLNEVAKNLN	IDRLNEVAK	26
HLA-DRB1*01:11	2	16	15	DISGINASVVNIQKE	INASVVNIQ	28
HLA-DRB1*01:11	3	17	15	ISGINASVVNIQKEI	INASVVNIQ	29
HLA-DRB1*01:11	13	27	15	IQKEIDRLNEVAKNL	IDRLNEVAK	32
HLA-DRB1*01:11	10	24	15	VVNIQKEIDRLNEVA	IQKEIDRLN	34
HLA-DRB1*01:11	12	26	15	NIQKEIDRLNEVAKN	IDRLNEVAK	35
HLA-DRB1*01:11	8	22	15	ASVVNIQKEIDRLNE	VNIQKEIDR	38

Supplementary Table 14 | Predicted human HLA epitopes of the SARS-CoV-2 HR2 peptide and associated HLA binding. NetMHCpan-4.1 was used to predict the top eight human HLA-A*02:01 and HLA-DRB1*01:11 epitopes of each HR2 peptide. The default cutoff for HLA binders was used as described by NetMHCpan[59]. A lower rank score for the peptide is associated with stronger HLA binding. 0.5% was defined as the cutoff for 'strong' HLA-A*02:01 binders while 2% was defined as the cutoff for 'weak' HLA-A*02:01 binders. Any peptides that had a rank score >2% were assumed to not bind to HLA-A*02:01. 2% was defined as the cutoff for 'strong' HLA-DRB1*01:11 binders while 10% was defined as the cutoff for 'weak' HLA-DRB1*01:11 binders. Any peptides that had a rank score >10% were assumed to not bind to HLA-DRB1*01:11. HLA-A*02:01 and HLA-DRB1*01:11 were chosen as representative human HLAs, as they are the most well-studied HLAs of each class.

HLA-A or HLA-DRB	Start	End	Length	Peptide	Core peptide region	Rank
HLA-A*02:01	38	47	10	LLELDKWASL	LLLDKWASL	1.2
HLA-A*02:01	16	23	8	YTSLIHSL	YTS-LIHSL	2.7
HLA-A*02:01	37	47	11	ELLELDKWASL	ELLELDASL	3.2
HLA-A*02:01	16	24	9	YTSLIHSLI	YTSLIHSLI	3.9
HLA-A*02:01	18	26	9	SLIHSLIEE	SLIHSLIEE	4.1
HLA-A*02:01	18	27	10	SLIHSLIEES	SLIHSLIES	4.3
HLA-A*02:01	22	30	9	SLIEESQNQ	SLIEESQNQ	4.7
HLA-A*02:01	15	23	9	NYTSLIHSL	NYTSLIHSL	4.9
HLA-DRB1*01:11	13	27	15	INNYTSLIHSLIEES	YTSLIHSLI	4.2
HLA-DRB1*01:11	12	26	15	EINNYTSLIHSLIEE	YTSLIHSLI	5.7
HLA-DRB1*01:11	14	28	15	NNYTSLIHSLIEESQ	YTSLIHSLI	9
HLA-DRB1*01:11	11	25	15	REINNYTSLIHSLIE	YTSLIHSLI	12
HLA-DRB1*01:11	17	31	15	TSLIHSLIEESQNQQ	IHSLIEESQ	29
HLA-DRB1*01:11	16	30	15	YTSLIHSLIEESQNQ	IHSLIEESQ	33
HLA-DRB1*01:11	15	29	15	NYTSLIHSLIEESQN	YTSLIHSLI	33
HLA-DRB1*01:11	10	24	15	DREINNYTSLIHSLI	YTSLIHSLI	34

Supplementary Table 15 | Predicted human HLA epitopes of the HIV HR2 peptide and associated HLA binding. NetMHCpan-4.1 was used to predict the top eight human HLA-A*02:01 and HLA-DRB1*01:11 epitopes of each HR2 peptide. The default cutoff for HLA binders was used as described by NetMHCpan[59]. A lower rank score for the peptide is associated with stronger HLA binding. 0.5% was defined as the cutoff for 'strong' HLA-A*02:01 binders while 2% was defined as the cutoff for 'weak' HLA-A*02:01 binders. Any peptides that had a rank score >2% were assumed to not bind to HLA-A*02:01. 2% was defined as the cutoff for 'strong' HLA-DRB1*01:11 binders while 10% was defined as the cutoff for 'weak' HLA-DRB1*01:11 binders. Any peptides that had a rank score >10% were assumed to not bind to HLA-DRB1*01:11. HLA-A*02:01 and HLA-DRB1*01:11 were chosen as representative human HLAs, as they are the most well-studied HLAs of each class.

HLA-A or HLA-DRB	Start	End	Length	Peptide	Core peptide region	Rank
HLA-A*02:01	13	22	10	KIDQIIHDFV	KIDQIIHFV	0.71
HLA-A*02:01	13	21	9	KIDQIIHDF	KIDQIIHDF	1.4
HLA-A*02:01	9	17	9	NITDKIDQI	NITDKIDQI	1.6
HLA-A*02:01	10	18	9	ITDKIDQII	ITDKIDQII	3.2
HLA-A*02:01	8	17	10	KNITDKIDQI	KITDKIDQI	4.5
HLA-A*02:01	10	17	8	ITDKIDQI	ITD-KIDQI	9.2
HLA-A*02:01	12	22	11	DKIDQIIHDFV	KIDQIIHFV	9.5
HLA-A*02:01	13	23	11	KIDQIIHDFVD	KIDQIIHFV	11
HLA-DRB1*01:11	3	17	15	PHDWTKNITDKIDQI	WTKNITDKI	8.6
HLA-DRB1*01:11	2	16	15	EPHDWTKNITDKIDQ	WTKNITDKI	9.7
HLA-DRB1*01:11	1	15	15	IEPHDWTKNITDKID	WTKNITDKI	17
HLA-DRB1*01:11	4	18	15	HDWTKNITDKIDQII	WTKNITDKI	20
HLA-DRB1*01:11	7	21	15	TKNITDKIDQIIHDF	ITDKIDQII	35
HLA-DRB1*01:11	10	24	15	ITDKIDQIIHDFVDK	IDQIIHDFV	36
HLA-DRB1*01:11	6	20	15	WTKNITDKIDQIIHD	ITDKIDQII	38
HLA-DRB1*01:11	5	19	15	DWTKNITDKIDQIIH	WTKNITDKI	43

Supplementary Table 16 | Predicted human HLA epitopes of the Ebola HR2 peptide and associated HLA binding. NetMHCpan-4.1 was used to predict the top eight human HLA-A*02:01 and HLA-DRB1*01:11 epitopes of each HR2 peptide. The default cutoff for HLA binders was used as described by NetMHCpan[59]. A lower rank score for the peptide is associated with stronger HLA binding. 0.5% was defined as the cutoff for 'strong' HLA-A*02:01 binders while 2% was defined as the cutoff for 'weak' HLA-A*02:01 binders. Any peptides that had a rank score >2% were assumed to not bind to HLA-A*02:01. 2% was defined as the cutoff for 'strong' HLA-DRB1*01:11 binders while 10% was defined as the cutoff for 'weak' HLA-DRB1*01:11 binders. Any peptides that had a rank score >10% were assumed to not bind to HLA-DRB1*01:11. HLA-A*02:01 and HLA-DRB1*01:11 were chosen as representative human HLAs, as they are the most well-studied HLAs of each class.

Infectious disease	**HLA-A strong binders**	**HLA-A weak binders**	**HLA-DRB strong binders**	**HLA-DRB weak binders**
SARS-CoV-2	3	>8	0	0
HIV	0	1	0	3
Ebola	0	3	0	2

Supplementary Table 17 | Summary Table of 'strong' and 'weak' HLA binding epitopes for various HR2 peptides. NetMHCpan-4.1 was used to predict the top eight human HLA-A*02:01 and HLA-DRB1*01:11 epitopes of each HR2 peptide. The default cutoff for HLA binders was used as described by NetMHCpan[59]. A lower rank score for the peptide is associated with stronger HLA binding. 0.5% was defined as the cutoff for 'strong' HLA-A*02:01 binders while 2% was defined as the cutoff for 'weak' HLA-A*02:01 binders. Any peptides that had a rank score >2% were assumed to not bind to HLA-A*02:01. 2% was defined as the cutoff for 'strong' HLA-DRB1*01:11 binders while 10% was defined as the cutoff for 'weak' HLA-DRB1*01:11 binders. Any peptides that had a rank score >10% were assumed to not bind to HLA-DRB1*01:11. HLA-A*02:01 and HLA-DRB1*01:11 were chosen as representative human HLAs, as they are the most well-studied HLAs of each class.

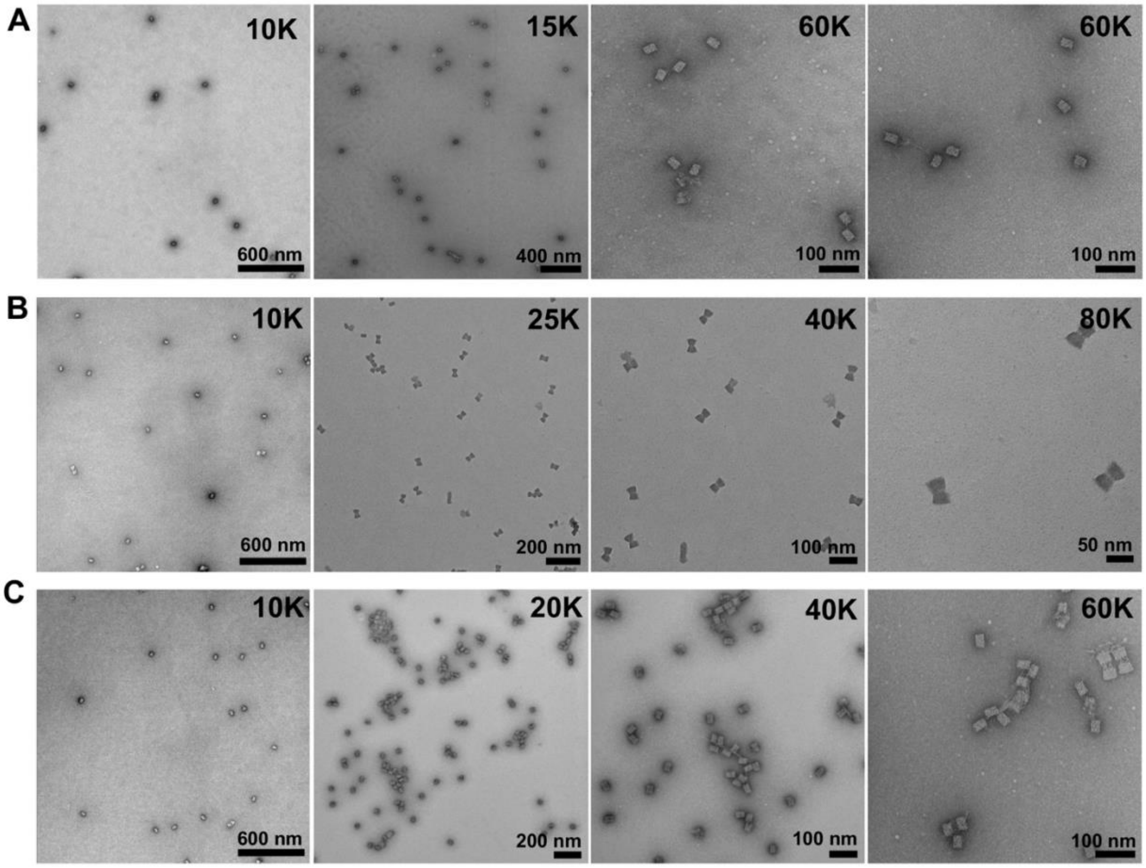

Supplementary Fig. 1 | HR2-functionalized DoriVac large scale TEM image. a, Negative stain TEM image of DoriVac nanoparticles demonstrated that the nanoparticles were monodispersed, further supporting the agarose gel results. **b,** Negative stain TEM image of HIV nanoparticles demonstrated that the nanoparticles were majority monodispersed, with some dimers observed, further supporting the agarose gel results. **c,** Negative stain TEM image of Ebola nanoparticles demonstrated that the nanoparticles were majority monodispersed, with some dimers observed, further supporting the agarose gel results.

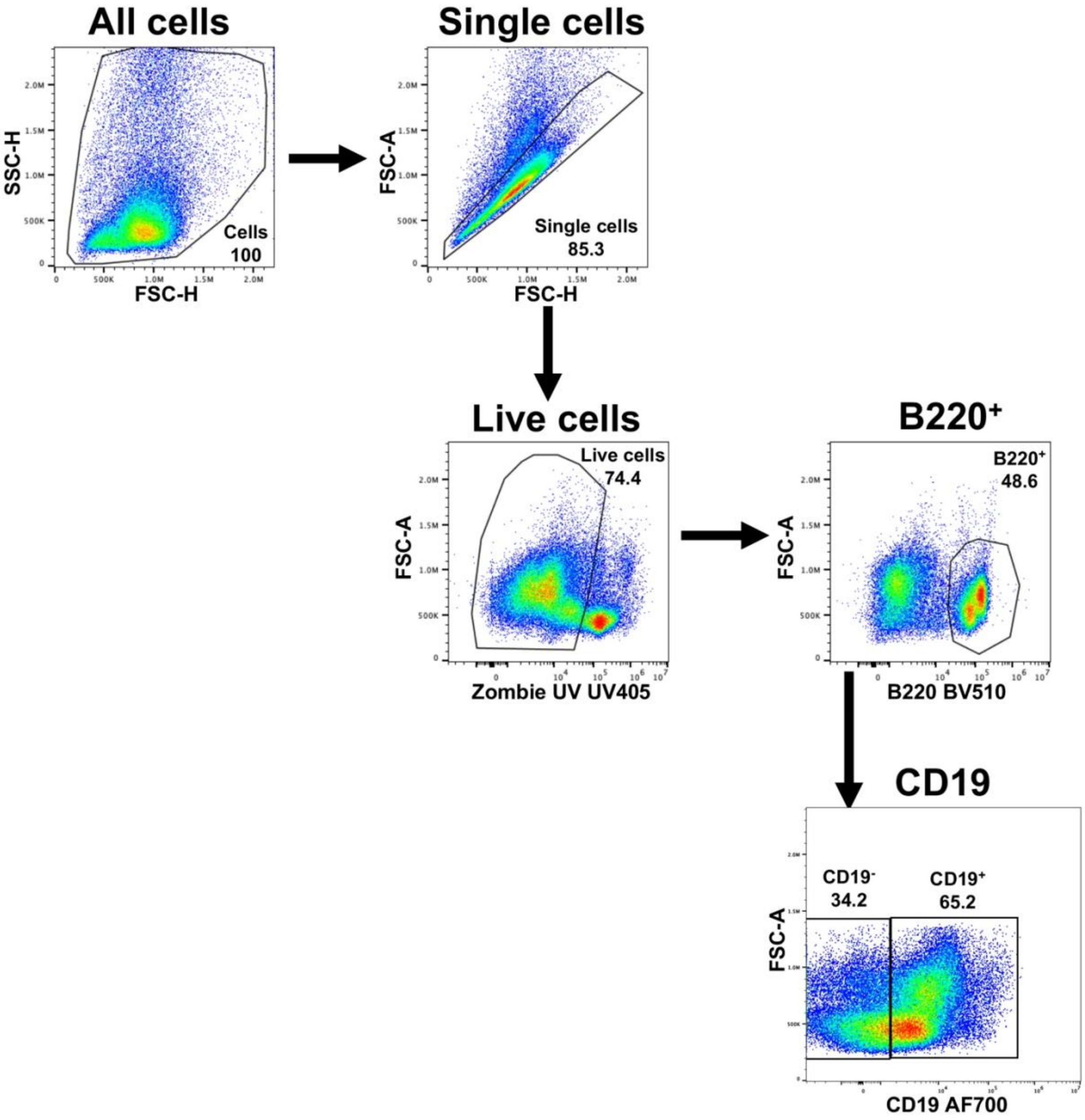

Supplementary Fig. 2 | B cell gating strategies. B cells were analysed using flow cytometry. This figure demonstrates the gating strategy to analyse B cells from frozen PBMC samples.

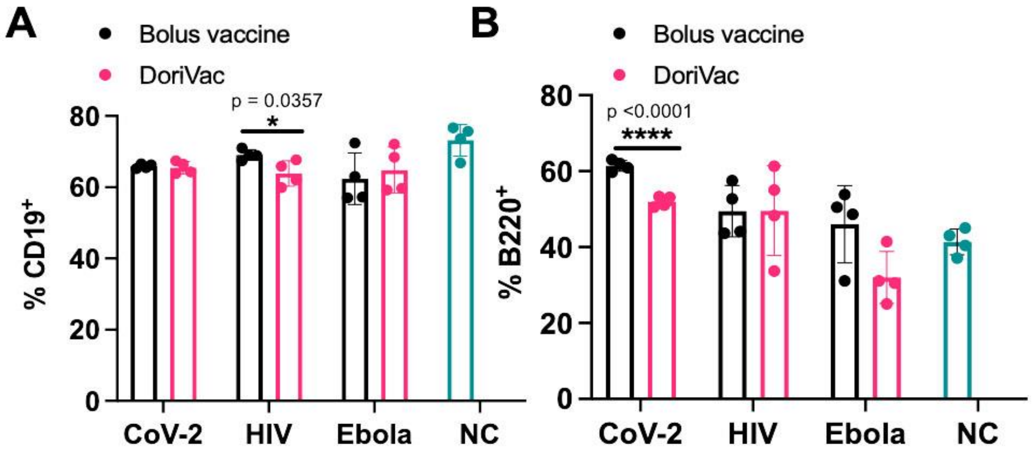

Supplementary Fig. 3 | Additional data demonstrating robust humoral responses for B cells. a, The CD19$^+$ B cell population in the blood on Day 21, as determined by flow cytometry, showed no significant difference after bolus vaccine treatment compared with DoriVac treatment. **b,** The B220$^+$ B cell population in the blood on Day 21, as determined by flow cytometry, showed minimal difference after bolus vaccine treatment compared with DoriVac treatment. Data are represented as mean ± SD. The flow data were analyzed by multiple unpaired t-tests and significance was defined as a two-tailed p value less than 0.05. '*' refers to $p \leq 0.05$; '****' refers to $p \leq 0.0001$.

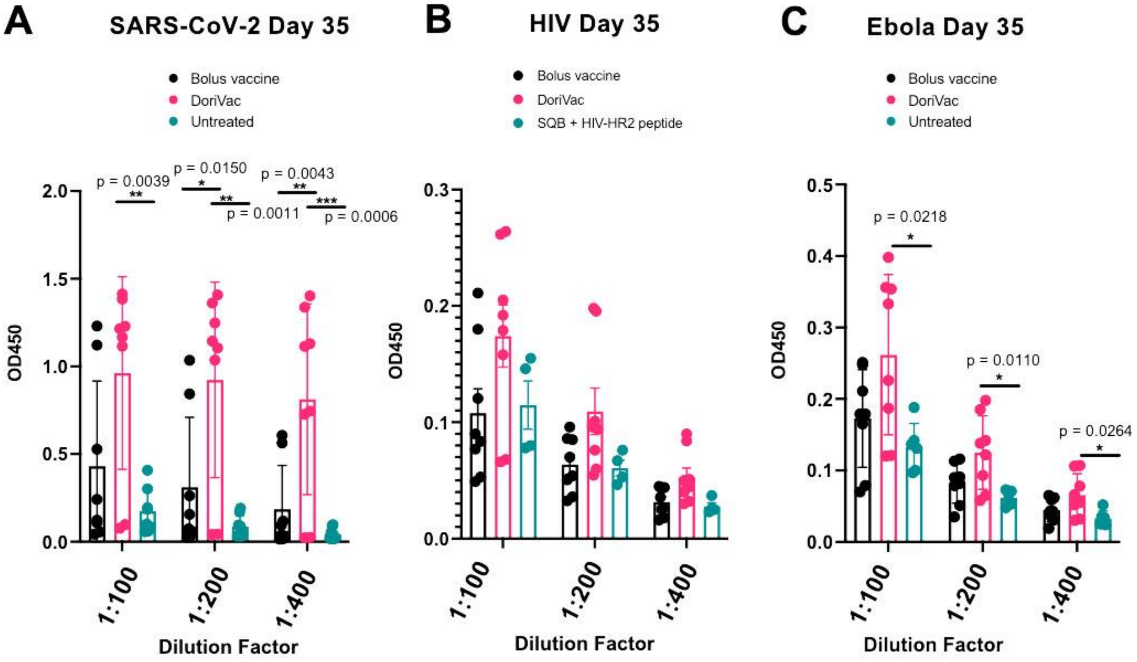

Supplementary Fig. 4 | Additional data demonstrating robust IgG antibody production. a, DoriVac treatment enhanced SARS-CoV-2 peptide-specific IgG antibody production in the plasma, as determined by ELISA assay, after two doses of the vaccine (on Day 35) compared to a bolus vaccine of free peptide and free CpG. **b,** DoriVac treatment enhanced HIV-peptide-specific IgG antibody production in the plasma, as determined by ELISA assay, after two doses of the vaccine (on Day 35) compared to a bolus vaccine. **c,** DoriVac treatment enhanced Ebola-peptide-specific IgG antibody production in the plasma, as determined by ELISA assay, after two doses of the vaccine (on Day 35) compared to a bolus vaccine. Data has been normalized. Data are represented as mean ± SD. The ELISA data was analyzed by one-way ANOVA (with correction for multiple comparisons using a Tukey's test) and significance was defined as a multiplicity-adjusted p value less than 0.05 (n=8). '*' refers to $P \leq 0.05$; '**' refers to $P \leq 0.01$. '***' refers to $P \leq 0.001$.

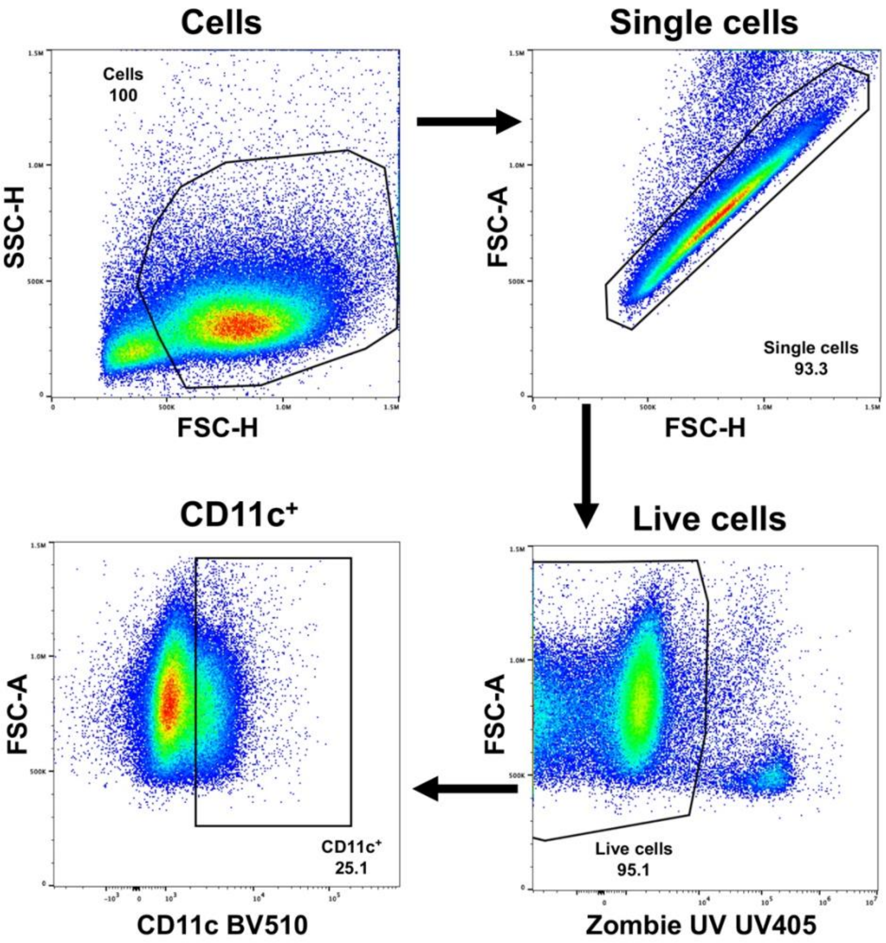

Supplementary Fig. 5 | DC gating strategies for lymph node samples. Dendritic cells were analyzed using flow cytometry. This figure demonstrates the gating strategy to analyze dendritic cells collected from the lymph nodes.

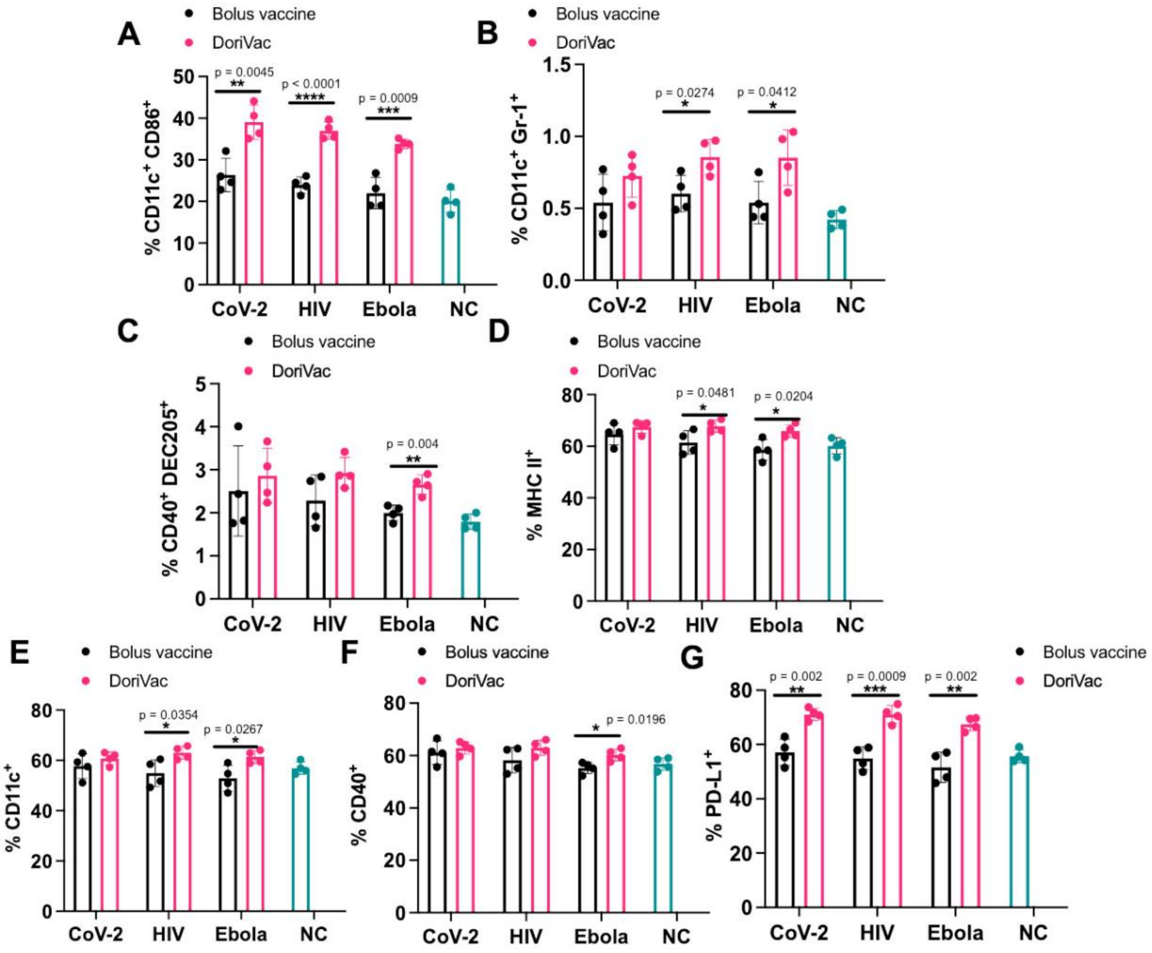

Supplementary Fig. 6 | Additional data demonstrating DC responses in the splenocytes on Day 21. Spleens were collected on Day 21 after two doses of treatment and processed into single-cell suspensions for flow cytometry. **a,** Percentages of CD11c$^+$ CD86$^+$, as determined by flow cytometry, in the splenocyte population (n=4). DoriVac demonstrated a significant increase in this activated DC population compared to bolus-vaccine treatment. **b,** Percentages of CD11c$^+$ Gr-1$^+$ DCs, as determined by flow cytometry, in the splenocyte population (n=4). DoriVac treatment demonstrated an increase in this plasmacytoid DC (pDC) – like subpopulation compared to bolus-vaccine treatment. **c,** Percentages of CD40$^+$ DEC205$^+$ DCs, as determined by flow cytometry, in the splenocytes (n=4). DoriVac treatment demonstrated an increase in this activated, endocytic subpopulation compared to bolus-vaccine treatment. **d,** Percentages of MHC-II$^+$ DCs, as determined by flow cytometry, in the draining lymph node (n=4). DoriVac treatment demonstrated a significant increase in this activated DC population compared to bolus-vaccine treatment. **e,** DoriVac treatment led to a notable increase in the CD11c$^+$ dendritic-cell population, as determined by flow cytometry. **f,** The lymphocytes were more activated (as indicated by upregulation of CD40$^+$) after DoriVac treatment compared to bolus vaccine treatment, as determined by flow cytometry. **g,** An increase in the PD-L1$^+$ subpopulation was observed after DoriVac treatment, compared to bolus-vaccine treatment, as determined by flow cytometry. Data are represented as mean ± SD. The flow data were analyzed by multiple unpaired t-tests and significance was defined as a two-tailed p value less than 0.05. '*' refers to $p \leq 0.05$; '**' refers to $p \leq 0.01$; '***' refers to $p \leq 0.001$; '****' refers to $p \leq 0.0001$.

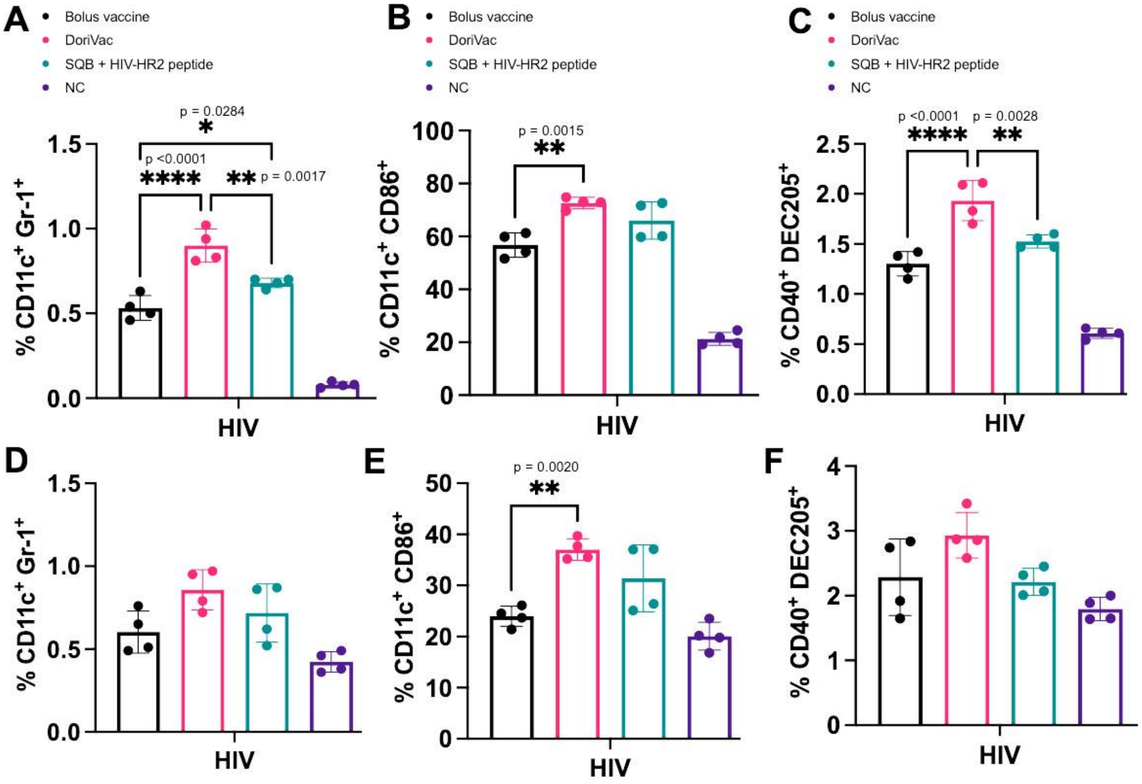

Supplementary Fig. 7 | Co-delivery of CpG and peptide on SQB is critical to robust DC responses. Half of the mice were sacrificed on Day 21 and draining lymph nodes were collected. **a,** Percentages of human pDC-like (CD11c$^+$ Gr-1$^+$) DCs in the draining lymph node (n=4), as determined by flow cytometry. DoriVac treatment demonstrated a significant increase in this plasmacytoid DC (pDC) – like subpopulation compared to treatment with the CpG SQB and HIV peptide, administered as a solution. **b,** Percentages of activated cDCs (CD11c$^+$ CD86$^+$) in the draining lymph node, as determined by flow cytometry. DoriVac treatment showed significant activation compared to the bolus vaccine and slightly more than the DNA origami SQB and HIV peptide administered as separate components. **c,** Percentages of CD40$^+$ DEC205$^+$ DCs in the draining lymph node (n=4), as determined by flow cytometry. The DoriVac treatment demonstrated a significant increase in this activated, endocytic subpopulation compared to bolus vaccine treatment and more than the DNA origami SQB and HIV peptide administered as separate components. **d,** Percentages of human pDC-like DCs in the splenocytes on Day 21 (n=4), as determined by flow cytometry. DoriVac treatment shows a significant increase compared to the bolus control. **e,** Percentages of activated cDCs in the splenocyte population, as determined by flow cytometry. DoriVac induced a significant increase in this population compared to the bolus control. **f,** Percentages of activated, endocytic DCs in the splenocytes population, as determined by flow cytometry. DoriVac showed significant increase in this population compared to the DNA origami SQB and HIV peptide delivered separately. Data are represented as mean ± SD. The flow data was analyzed by one-way ANOVA (with correction for multiple comparisons using a Tukey's test) and significance was defined as a multiplicity-adjusted p value less than 0.05 (n=4). '*' refers to $P \leq 0.05$; '**' refers to $P \leq 0.01$; '***' refers to $P \leq 0.001$; '****' refers to $P \leq 0.0001$.

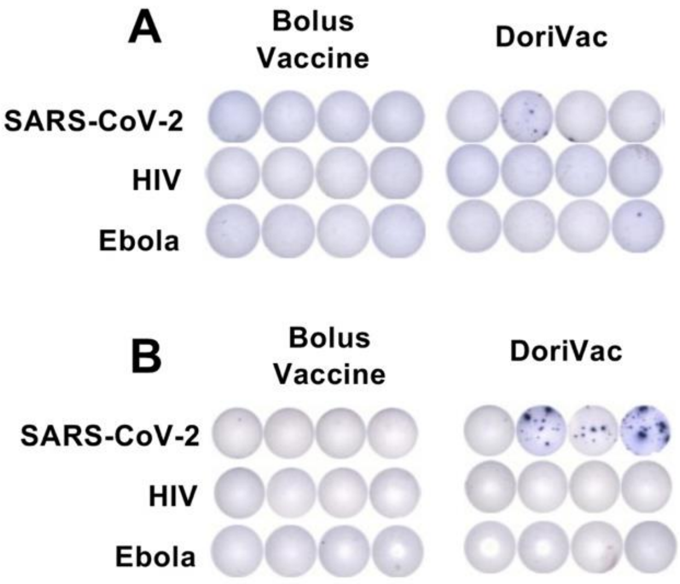

Supplementary Fig. 8 | Additional data on antigen-specific T cell responses on Day 21 and 28. a, Interferon-gamma (IFNγ) ELISpot demonstrating frequency of antigen-specific splenocytes on Day 21. Minimal difference is observed between the bolus-vaccine treated group and the DoriVac-treated group. **b,** IFNγ ELISpot demonstrating frequency of antigen-specific PBMCs on Day 28. There is a notable increase in the frequency of SARS-CoV-2 antigen-specific T cells.

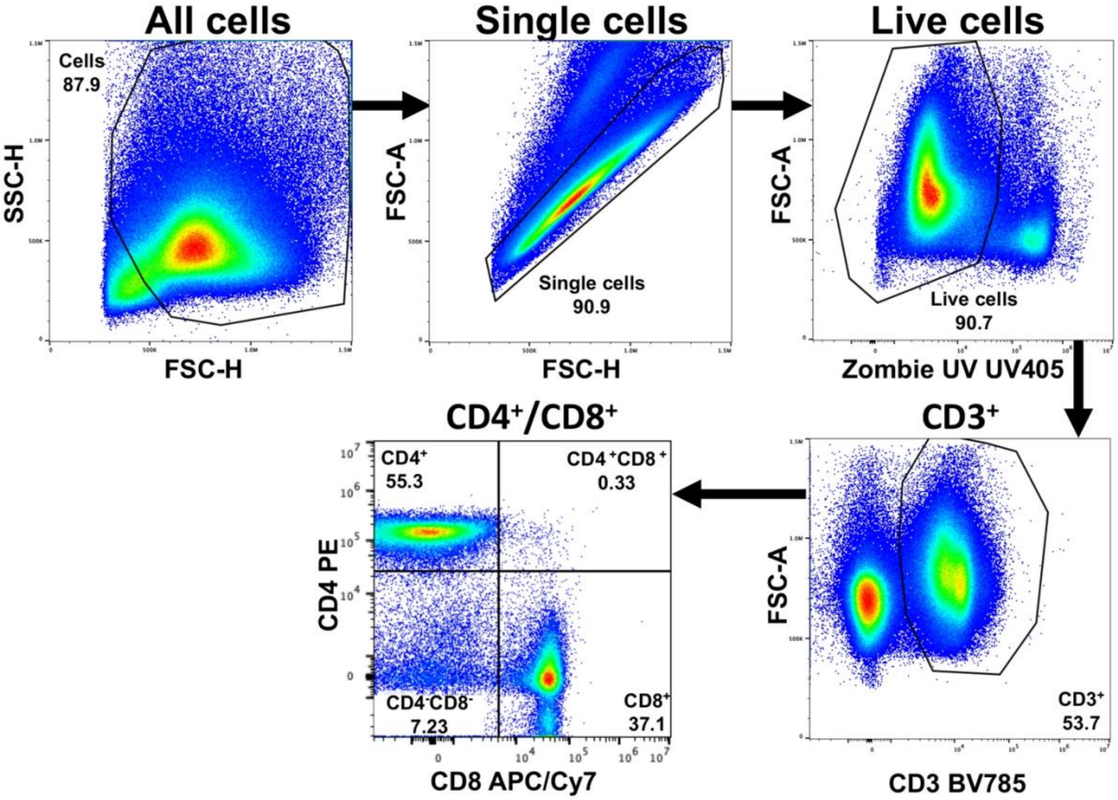

Supplementary Fig. 9 | T cell gating strategies. T cells were analyzed using flow cytometry. This figure demonstrates the gating strategy to analyze T cells in lymph nodes and spleen. Images shown are from the lymph nodes.

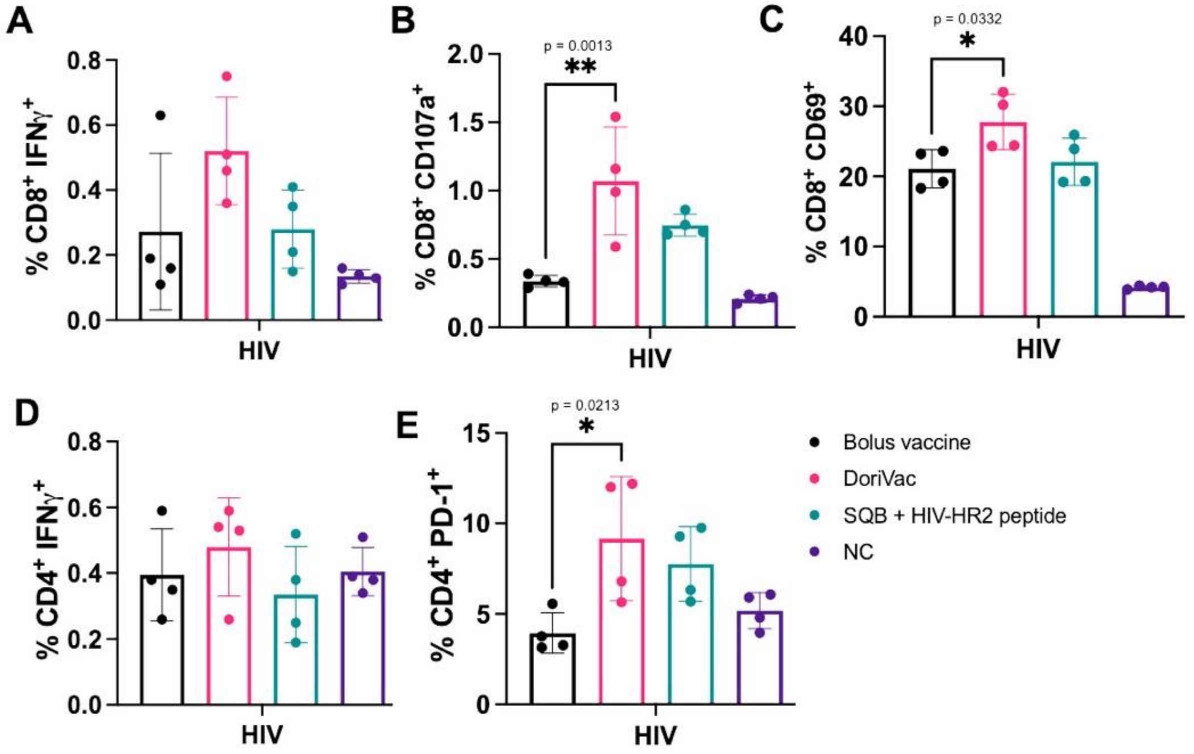

Supplementary Fig. 10 | Co-delivery of CpG and antigen peptide is essential to robust T cell responses. **a,** IFN-γ$^+$ CD8$^+$ T cells in the lymph node (LN) were upregulated on Day 21 in the DoriVac treatment group, compared to the bolus vaccine or the DNA origami SQB with HIV peptide groups, as determined by flow cytometry. **b,** CD107a$^+$ CD8$^+$ cytotoxic T cells in the LN were upregulated on Day 21 in the DoriVac treatment group, compared to the bolus vaccine or the DNA origami SQB with HIV peptide groups, as determined by flow cytometry. **c,** CD69$^+$ CD8$^+$ activated T cells in the LN showed upregulation on Day 21 after treatment with DoriVac, as determined by flow cytometry. **d,** IFN-γ$^+$ CD4$^+$ T cells in the LN were upregulated in the context of DoriVac treatment group on Day 21, compared to the DNA origami SQB with HIV peptide group, as determined by flow cytometry. **e,** PD-1$^+$ CD4$^+$ T cells in the LN were upregulated in the context of the DoriVac treated group on Day 21, compared to the bolus vaccine and DNA origami SQB with HIV peptide group, as determined by flow cytometry. Data are represented as mean ± SD. The flow data was analyzed by one-way ANOVA (with correction for multiple comparisons using a Tukey's test) and significance was defined as a multiplicity-adjusted p value less than 0.05 (n=4). '*' refers to $P \leq 0.05$; '**' refers to $P \leq 0.01$.

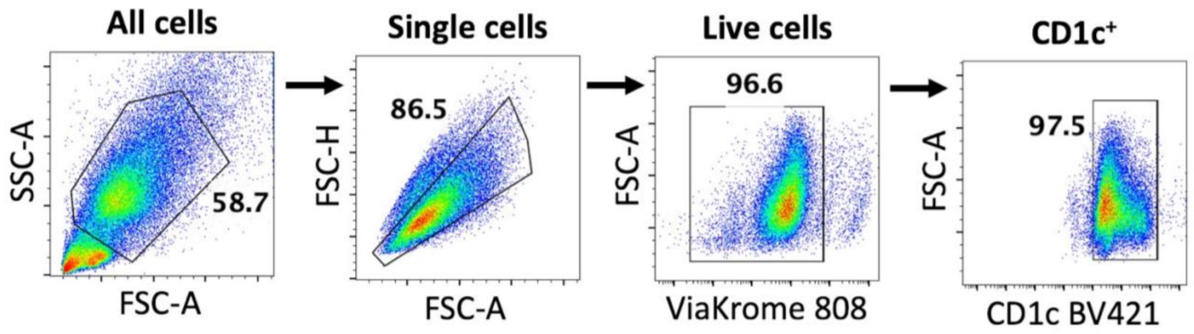

Supplementary Fig. 11 | Activation of human monocyte-derived dendritic cells (moDCs) analysis using flow cytometry. This figure demonstrates the gating strategy to analyse cells collected from moDCs after treatment with DNA origami vaccines.

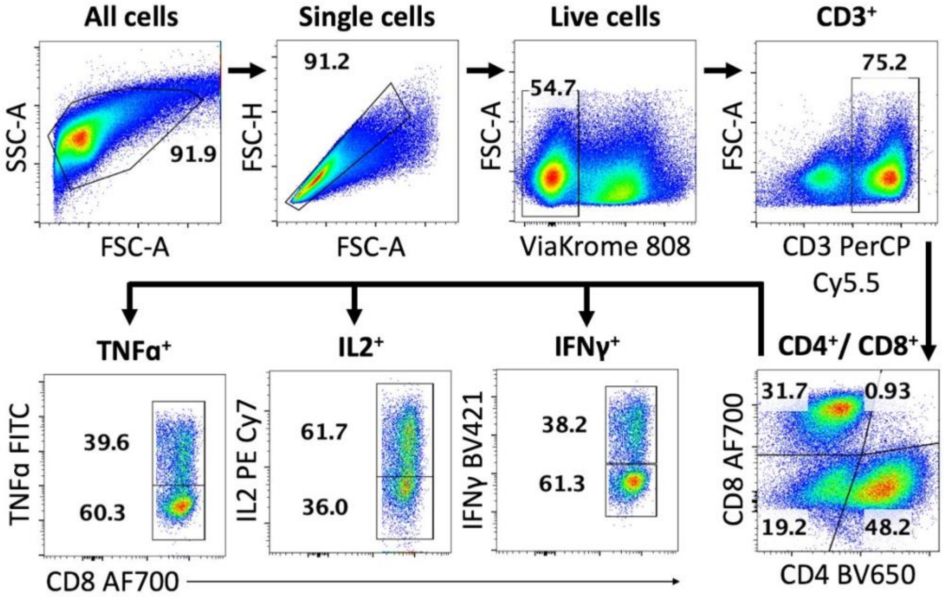

Supplementary Fig. 12 | Intracellular cytokine staining analysis using flow cytometry for cells from LN organ-on-a-chips. This figure demonstrates the gating strategy to analyse cells collected from LN organ-on-a-chips.

C

Supplementary material for Chapter 4

Supplementary Information for:

Constructing DNA origami nanoparticles with immunostimulatory CD40 ligands as a novel adjuvant

Olivia J. Young[2,3,4], Yang C. Zeng[1,2,3], William M. Shih[1,2,3].

[1]Department of Cancer Biology, Dana-Farber Cancer Institute, Harvard Medical School, Boston, Massachusetts 02115, USA
[2]Wyss Institute for Biologically Inspired Engineering at Harvard University, Boston, Massachusetts 02115, USA
[3]Department of Biological Chemistry and Molecular Pharmacology, Harvard Medical School, Boston, Massachusetts 02115, USA
[4]Harvard-Massachusetts Institute of Technology (MIT) Division of Health Sciences and Technology, Massachusetts Institute of Technology, Cambridge, Massachusetts, 02139, USA

Protein	**Sequence**
CD40L dimer	GDEDPQIAAHVVSEANSNAASVLQWAKKGYYTMKSNLVMLENGKQLTVKREGLYYVYTQVTFCSNREPSSQRPFIVGLWLKPSSGSERILLKAANTHSSSQLCEQQSVHLGGVFELQAGASVFVNVTEASQVIHRVGFSSFGLLKLGGGGSGGGGSGGGGSGDEDPQIAAHVVSEANSNAASVLQWAKKGYYTMKSNLVMLENGKQLTVKREGLYYVYTQVTFCSNREPSSQRPFIVGLWLKPSSGSERILLKAANTHSSSQLCEQQSVHLGGVFELQAGASVFVNVTEASQVIHRVGFSSFGLLKLHHHHHH

Supplementary Table 1 | CD40L dimer sequence. The CD40L dimer, purchased from Dr. Zhirui Wang of the University of Colorado Anschutz Medical Campus Protein Core, was designed with two CD40L monomers, a glycine-serine flexible linker and a 6X histidine tag at the C terminal. This sequence was deduced from Hermanrud et al, *Protein Expression and Purification*, 2010.

	Single point attachment	**Multi-point attachment**
Advantages	**Ease** of fabrication	More sophisticated; **less rotational freedom** so more precise spatial control
Disadvantages	CD40L is free to rotate which may **limit the precision** of the spatial arrangements	Far more **challenging to design** and fabricate with precision

Supplementary Table 2 | Comparing single-point attachment and multi-point attachment of the CD40L-oligonucleotide to the DNA origami nanoparticle.

Conjugation Chemistry	Site Specific Conjugation?	Comments
N terminal labeling (2PCA)	Yes	Site specific and relatively straightforward, but has never been demonstrated with protein-oligo conjugation
C terminal labeling	Yes	Has not been demonstrated with oligo protein conjugation
Lysine labeling	No, 9 lysines	Not site specific enough to warrant trying
Cysteine labeling (SMCC)	No, 2 cysteines	Possible but may interfere with CD40L binding to CD40
His-tag labeling	Yes, although 2XHis-tag is more specific than 6X His-tag	Demonstrated attachment of oligos to proteins using this chemistry, we know that N terminal conjugation does not affect CD40L bioactivity
SNAP tag, yBBR tag, Sor-tag conjugation	Yes	Possible, but requires recombinant production of protein

Supplementary Table 3 | Potential CD40L protein-oligonucleotide conjugation schemes. The ideal conjugation scheme would be site-specific and relatively easy to perform with high-yield.

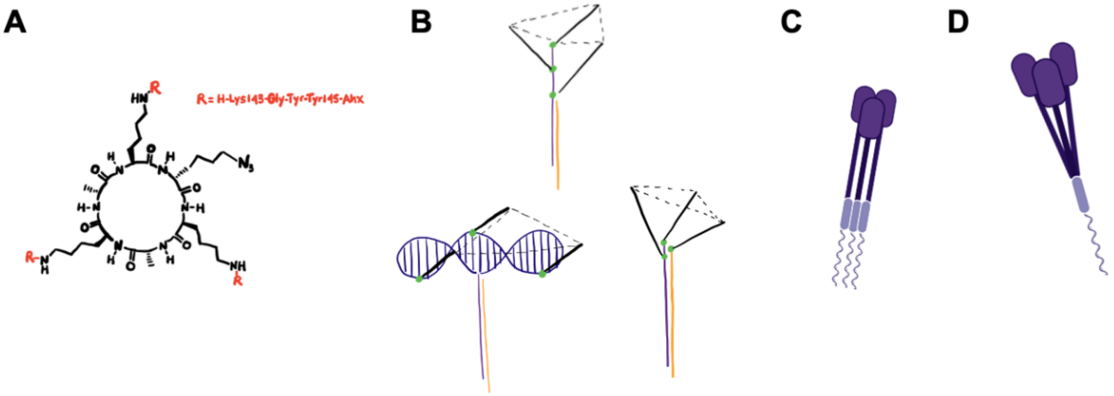

Supplementary Figure 1 | Many different CD40L structures were tested before pursuing the CD40L dimer construct. A) The cyclic CD40L peptide mimic, synthesized by Genscript, with a lysine for facile click chemistry modification (Fournel et al, *Nature Chemical Biology*, 2005). **B)** Various DNA-nanotechnology-based structures were designed in-house to present the KGYY CD40L minimal peptide epitope in a trimer formation that closely mimicked the actual CD40L structure. **C)** Multiple-point attachment of three CD40L monomers to three distinct oligonucleotides, with subsequent hybridization to the DNA origami nanoparticle, was also considered. **D)** Single-point attachment of a CD40L protein to a single oligonucleotide was decided to be the most robust and straightforward method for patterning CD40L on the DNA origami nanoparticles.

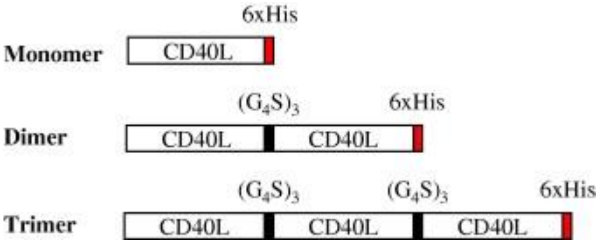

Supplementary Figure 2|CD40L dimer structure. The CD40L dimer protein, purchased from Dr. Zhirui Wang of the University of Colorado Anschutz Medical Campus Protein Core, was designed by Dr. Wang and colleagues to contain two CD40L monomers, a glycine-serine flexible linker and a 6X histidine tag at the C terminal. This figure is taken from Hermanrud et al, *Protein Expression and Purification*, 2010.

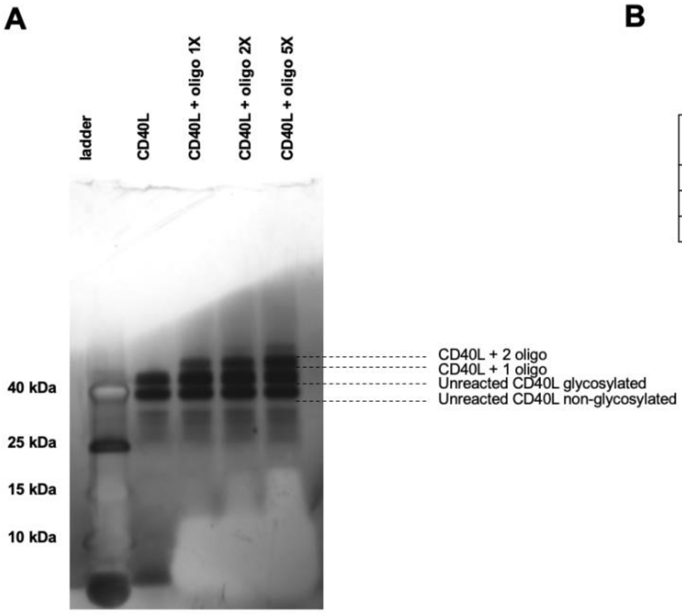

B

Excess oligo in reaction	1 oligo per CD40L protein	2 oligo per CD40L protein
1X	24%	0%
2X	27%	6%
5X	30%	10%

Supplementary Figure 3|Optimizing CD40L-oligonucleotide ratio in bis-sulfone chemical conjugation for optimal production of CD40L-oligonucleotide with one oligonucleotide per protein. The fold excess of oligonucleotide was varied from 1X, 2X and 5X to determine the optimal ratio. **A)** SDS-PAGE gel with silver stain demonstrating the products of the CD40L-oligonucleotide conjugation reactions. **B)** ImageJ analysis of each band intensity to determine the optimal ratio of protein and oligonucleotide for robust production of CD40L with one attached oligonucleotide.

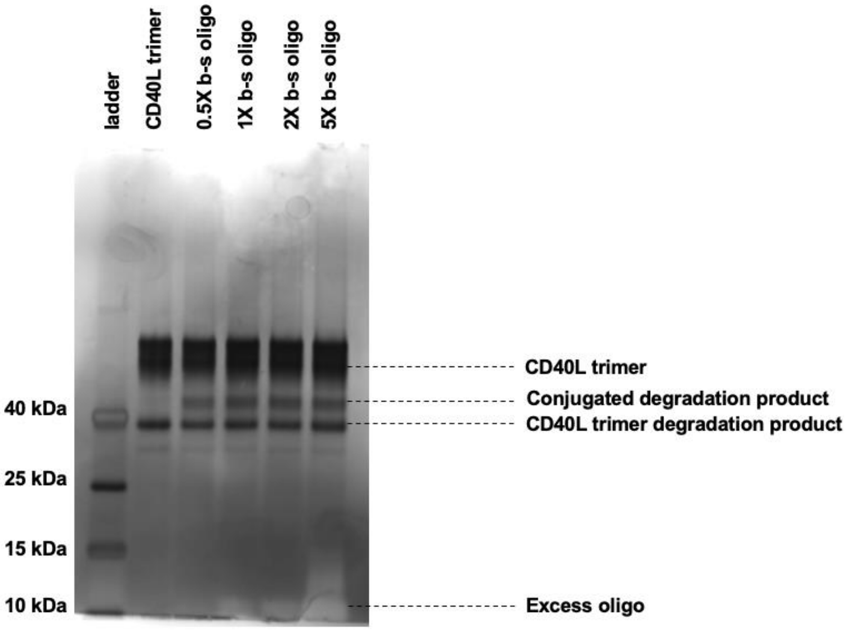

Supplementary Figure 4 | CD40L trimer-oligonucleotide conjugation via bis-sulfone chemical conjugation was not successful. Reaction occurred for 96 hours, followed by SDS-PAGE gel analysis with silver stain of the protein and protein-oligonucleotide products. Even though the CD40L trimer is more physiologically relevant than the CD40L dimer, we could not achieve efficient conjugation and therefore, did not move forward with further optimization and testing of the trimer on the DNA origami nanoparticles.

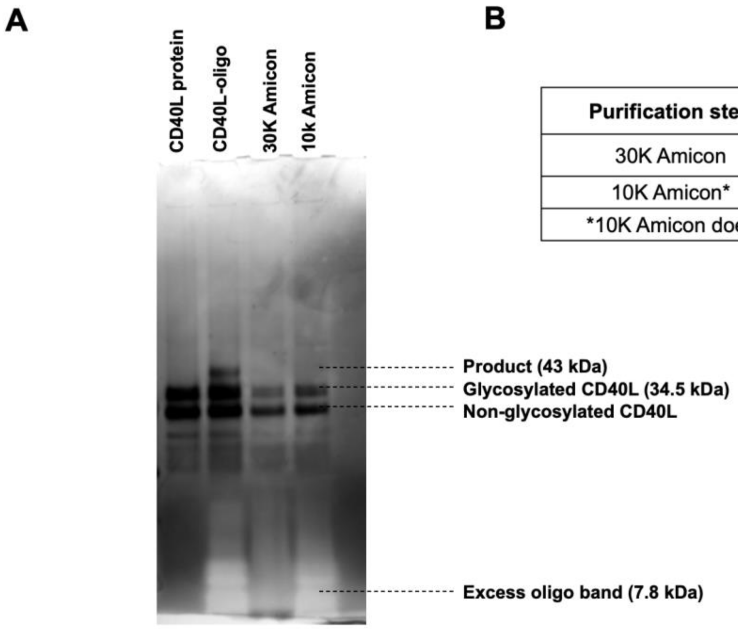

B

Purification step	Estimated yield
30K Amicon	Less than 20%
10K Amicon*	95%
*10K Amicon does not purify out excess oligo	

Supplementary Figure 5 | Purification of CD40L-oligonucleotide via Amicon filtration. A) SDS-PAGE gel coupled with silver stain, demonstrating successful conjugation of CD40L protein to oligonucleotide, as well as a comparison of 30K and 10K Amicon filtration. **B)** Yield of purification was estimated based on the band intensity of the purified product as quantified via ImageJ analysis, compared to the unpurified CD40L-oligonucleotide band. Note the excess oligonucleotide which is still present after filtration through the 10K Amicon filter, as the 7.8 kDa oligonucleotide is very close to the 10 kDa molecular weight cutoff of the filter.

References

[1] Abdi, K., Laky, K., Padhan, K., Petrovas, C., Skinner, J., Kabat, J., Dorward, D. W., Brzostowski, J., Long, E. O., Trinchieri, G., & Varma, R. (2018). Cutting edge: Quantitative determination of cd40l threshold for il-12 and il-23 production from dendritic cells. *J Immunol*, 201(10), 2879–2884.

[2] Afonin, K. A., Dobrovolskaia, M. A., Ke, W., Grodzinski, P., & Bathe, M. (2022). Critical review of nucleic acid nanotechnology to identify gaps and inform a strategy for accelerated clinical translation. *Adv Drug Deliv Rev*, 181, 114081.

[3] Ali, O. A., Emerich, D., Dranoff, G., & Mooney, D. J. (2009a). In situ regulation of dc subsets and t cells mediates tumor regression in mice. *Sci Transl Med*, 1(8), 8ra19.

[4] Ali, O. A., Huebsch, N., Cao, L., Dranoff, G., & Mooney, D. J. (2009b). Infection-mimicking materials to program dendritic cells in situ. *Nat Mater*, 8(2), 151–8.

[5] Altammar, K. A. (2023). A review on nanoparticles: characteristics, synthesis, applications, and challenges. *Front Microbiol*, 14, 1155622.

[6] An, H. J., Kim, Y. J., Song, D. H., Park, B. S., Kim, H. M., Lee, J. D., Paik, S. G., Lee, J. O., & Lee, H. (2011). Crystallographic and mutational analysis of the cd40-cd154 complex and its implications for receptor activation. *J Biol Chem*, 286(13), 11226–35.

[7] Anastassacos, F. M., Zhao, Z., Zeng, Y., & Shih, W. M. (2020). Glutaraldehyde cross-linking of oligolysines coating dna origami greatly reduces susceptibility to nuclease degradation. *J Am Chem Soc*, 142(7), 3311–3315.

[8] Andersen, E. S., Dong, M., Nielsen, M. M., Jahn, K., Subramani, R., Mamdouh, W., Golas, M. M., Sander, B., Stark, H., Oliveira, C. L. P., Pedersen, J. S., Birkedal, V., Besenbacher, F., Gothelf, K. V., & Kjems, J. (2009). Self-assembly of a nanoscale dna box with a controllable lid. *Nature*, 459(7243), 73–76.

[9] Anselmo, A. C. & Mitragotri, S. (2016). Nanoparticles in the clinic. *Bioeng Transl Med*, 1(1), 10–29.

[10] Anselmo, A. C. & Mitragotri, S. (2019). Nanoparticles in the clinic: An update. *Bioeng Transl Med*, 4(3), e10143.

[11] Anselmo, A. C. & Mitragotri, S. (2021). Nanoparticles in the clinic: An update post covid-19 vaccines. *Bioeng Transl Med*, 6(3), e10246.

[12] Baden, L. R., El Sahly, H. M., Essink, B., Kotloff, K., Frey, S., Novak, R., Diemert, D., Spector, S. A., Rouphael, N., Creech, C. B., McGettigan, J., Khetan, S., Segall, N., Solis, J., Brosz, A., Fierro, C., Schwartz, H., Neuzil, K., Corey, L., Gilbert, P., Janes, H., Follmann, D., Marovich, M., Mascola, J., Polakowski, L., Ledgerwood, J., Graham, B. S., Bennett, H., Pajon, R., Knightly, C., Leav, B., Deng, W., Zhou, H., Han, S., Ivarsson, M., Miller, J., Zaks, T., & Group, C. S. (2021). Efficacy and safety of the mrna-1273 sars-cov-2 vaccine. *N Engl J Med*, 384(5), 403–416.

[13] Bai, J., Chiba, A., Murayama, G., Kuga, T., Yahagi, Y., Tabe, Y., Tamura, N., & Miyake, S. (2022). Early cd4. *Sci Rep*, 12(1), 20376.

[14] Bauer, S., Kirschning, C. J., Hacker, H., Redecke, V., Hausmann, S., Akira, S., Wagner, H., & Lipford, G. B. (2001). Human tlr9 confers responsiveness to bacterial dna via species-specific cpg motif recognition. *Proc Natl Acad Sci U S A*, 98(16), 9237–42.

[15] Behler, K. L., Honemann, M. N., Silva-Santos, A. R., Dietz, H., & Weuster-Botz, D. (2022). Phage-free production of artificial ssdna with escherichia coli. *Biotechnol Bioeng*, 119(10), 2878–2889.

[16] Berger, R. M. L., Weck, J. M., Kempe, S. M., Hill, O., Liedl, T., Radler, J. O., Monzel, C., & Heuer-Jungemann, A. (2021). Nanoscale fasl organization on dna origami to decipher apoptosis signal activation in cells. *Small*, 17(26), e2101678.

[17] Bhatia, D., Surana, S., Chakraborty, S., Koushika, S. P., & Krishnan, Y. (2011). A synthetic icosahedral dna-based host-cargo complex for functional in vivo imaging. *Nat Commun*, 2, 339.

[18] Bila, H., Kurisinkal, E. E., & Bastings, M. M. C. (2019). Engineering a stable future for dna-origami as a biomaterial. *Biomater Sci*, 7(2), 532–541.

[19] Bode, C., Zhao, G., Steinhagen, F., Kinjo, T., & Klinman, D. M. (2011). Cpg dna as a vaccine adjuvant. *Expert Rev Vaccines*, 10(4), 499–511.

[20] Bojadzic, D. & Buchwald, P. (2019). Cd40-targeting kgyy. *Diabetologia*, 62(11), 2158–2160.

[21] Botos I, Liu L, W. Y. S. D. D. D. (2009). The toll-like receptor 3:dsrna signaling complex - pubmed. *Biochim Biophys Acta*, 1789(8-10), 667–74.

[22] Braun, J., Loyal, L., Frentsch, M., Wendisch, D., Georg, P., Kurth, F., Hippenstiel, S., Dingeldey, M., Kruse, B., Fauchere, F., Baysal, E., Mangold, M., Henze, L., Lauster, R., Mall, M. A., Beyer, K., Röhmel, J., Voigt, S., Schmitz, J., Miltenyi, S., Demuth, I., Müller, M. A., Hocke, A., Witzenrath, M., Suttorp, N., Kern, F., Reimer, U., Wenschuh, H., Drosten, C., Corman, V. M., Giesecke-Thiel, C., Sander, L. E., & Thiel, A. (2020). Sars-cov-2-reactive t cells in healthy donors and patients with covid-19. *Nature*, 587(7833), 270–274.

[23] Bray, F., Laversanne, M., Weiderpass, E., & Soerjomataram, I. (2021). The ever-increasing importance of cancer as a leading cause of premature death worldwide. *Cancer*, 127(16), 3029–3030.

[24] Brunekreeft, K. L., Strohm, C., Gooden, M. J., Rybczynska, A. A., Nijman, H. W., Grigoleit, G. U., Helfrich, W., Bremer, E., Siegmund, D., Wajant, H., & de Bruyn, M. (2014). Targeted delivery of cd40l promotes restricted activation of antigen-presenting cells and induction of cancer cell death. *Mol Cancer*, 13, 85.

[25] Bush, J., Singh, S., Vargas, M., Oktay, E., Hu, C. H., & Veneziano, R. (2020). Synthesis of dna origami scaffolds: Current and emerging strategies. *Molecules*, 25(15).

[26] Casaletto, J. B. & McClatchey, A. I. (2012). Spatial regulation of receptor tyrosine kinases in development and cancer. *Nat Rev Cancer*, 12(6), 387–400.

[27] Caux, C., Massacrier, C., Vanbervliet, B., Dubois, B., Van Kooten, C., Durand, I., & Banchereau, J. (1994). Activation of human dendritic cells through cd40 cross-linking. *The Journal of experimental medicine*, 180(4), 1263–1272.

[28] Cella, M., Facchetti, F., Lanzavecchia, A., & Colonna, M. (2000). Plasmacytoid dendritic cells activated by influenza virus and cd40l drive a potent th1 polarization. *Nat Immunol*, 1(4), 305–10.

[29] Chambers, P., Pringle, C. R., & Easton, A. J. (1990). Heptad repeat sequences are located adjacent to hydrophobic regions in several types of virus fusion glycoproteins. *J Gen Virol*, 71 (Pt 12), 3075–80.

[30] Chan, D. C., Fass, D., Berger, J. M., & Kim, P. S. (1997). Core structure of gp41 from the hiv envelope glycoprotein. *Cell*, 89(2), 263–73.

[31] Chang, M., Yang, C. S., & Huang, D. M. (2011). Aptamer-conjugated dna icosahedral nanoparticles as a carrier of doxorubicin for cancer therapy. *ACS Nano*, 5(8), 6156–63.

[32] Chen, J. H. & Seeman, N. C. (1991). Synthesis from dna of a molecule with the connectivity of a cube. *Nature*, 350(6319), 631–3.

[33] Cherian, S., Potdar, V., Jadhav, S., Yadav, P., Gupta, N., Das, M., Rakshit, P., Singh, S., Abraham, P., Panda, S., & Team, N. (2021). Sars-cov-2 spike mutations, l452r, t478k, e484q and p681r, in the second wave of covid-19 in maharashtra, india. *Microorganisms*, 9(7).

[34] Chesson, C. B. & Zloza, A. (2017). Nanoparticles: augmenting tumor antigen presentation for vaccine and immunotherapy treatments of cancer. *Nanomedicine (Lond)*, 12(23), 2693–2706.

[35] Chowdhury, A., Hayes, T. L., Bosinger, S. E., Lawson, B. O., Vanderford, T., Schmitz, J. E., Paiardini, M., Betts, M., Chahroudi, A., Estes, J. D., & Silvestri, G. (2015). Differential impact of

in vivo cd8+ t lymphocyte depletion in controller versus progressor simian immunodeficiency virus-infected macaques. *J Virol*, 89(17), 8677–86.

[36] Cohn, H., Bloom, N., Cai, G. Y., Clark, J. J., Tarke, A., Bermúdez-González, M. C., Altman, D. R., Lugo, L. A., Lobo, F. P., Marquez, S., Chen, J. Q., Ren, W., Qin, L., Yates, J. L., Hunt, D. T., Lee, W. T., Crotty, S., Krammer, F., Grifoni, A., Sette, A., Simon, V., Coelho, C. H., & group, P. s. (2023). Mpox vaccine and infection-driven human immune signatures: an immunological analysis of an observational study. *Lancet Infect Dis*.

[37] Comberlato, A., Koga, M. M., Nussing, S., Parish, I. A., & Bastings, M. M. C. (2022). Spatially controlled activation of toll-like receptor 9 with dna-based nanomaterials. *Nano Lett*, 22(6), 2506–2513.

[38] Comberlato, A., Paloja, K., & Bastings, M. M. C. (2019). Nucleic acids presenting polymer nanomaterials as vaccine adjuvants. *Journal of Materials Chemistry B*, 7(41), 6321–6346.

[39] Cong, Y., Pawlisz, E., Bryant, P., Balan, S., Laurine, E., Tommasi, R., Singh, R., Dubey, S., Peciak, K., Bird, M., Sivasankar, A., Swierkosz, J., Muroni, M., Heidelberger, S., Farys, M., Khayrzad, F., Edwards, J., Badescu, G., Hodgson, I., Heise, C., Somavarapu, S., Liddell, J., Powell, K., Zloh, M., Choi, J. W., Godwin, A., & Brocchini, S. (2012). Site-specific pegylation at histidine tags. *Bioconjug Chem*, 23(2), 248–63.

[40] Cooper, C. & Mackie, D. (2011). Hepatitis b surface antigen-1018 iss adjuvant-containing vaccine: a review of heplisav™ safety and efficacy. *Expert Rev Vaccines*, 10(4), 417–27.

[41] Corbett, K. S., Edwards, D. K., Leist, S. R., Abiona, O. M., Boyoglu-Barnum, S., Gillespie, R. A., Himansu, S., Schäfer, A., Ziwawo, C. T., DiPiazza, A. T., Dinnon, K. H., Elbashir, S. M., Shaw, C. A., Woods, A., Fritch, E. J., Martinez, D. R., Bock, K. W., Minai, M., Nagata, B. M., Hutchinson, G. B., Wu, K., Henry, C., Bahl, K., Garcia-Dominguez, D., Ma, L., Renzi, I., Kong, W. P., Schmidt, S. D., Wang, L., Zhang, Y., Phung, E., Chang, L. A., Loomis, R. J., Altaras, N. E., Narayanan, E., Metkar, M., Presnyak, V., Liu, C., Louder, M. K., Shi, W., Leung, K., Yang, E. S., West, A., Gully, K. L., Stevens, L. J., Wang, N., Wrapp, D., Doria-Rose, N. A., Stewart-Jones, G., Bennett, H., Alvarado, G. S., Nason, M. C., Ruckwardt, T. J., McLellan, J. S., Denison, M. R., Chappell, J. D., Moore, I. N., Morabito, K. M., Mascola, J. R., Baric, R. S., Carfi, A., & Graham, B. S. (2020). Sars-cov-2 mrna vaccine design enabled by prototype pathogen preparedness. *Nature*, 586(7830), 567–571.

[42] Dan, J. M., Mateus, J., Kato, Y., Hastie, K. M., Yu, E. D., Faliti, C. E., Grifoni, A., Ramirez, S. I., Haupt, S., Frazier, A., Nakao, C., Rayaprolu, V., Rawlings, S. A., Peters, B., Krammer, F., Simon, V., Saphire, E. O., Smith, D. M., Weiskopf, D., Sette, A., & Crotty, S. (2021). Immunological memory to sars-cov-2 assessed for up to 8 months after infection. *Science*, 371(6529).

[43] Danaei, M., Dehghankhold, M., Ataei, S., Hasanzadeh Davarani, F., Javanmard, R., Dokhani, A., Khorasani, S., & Mozafari, M. R. (2018). Impact of particle size and polydispersity index on the clinical applications of lipidic nanocarrier systems. *Pharmaceutics*, 10(2).

[44] Dietz, H., Douglas, S. M., & Shih, W. M. (2009). Folding dna into twisted and curved nanoscale shapes. *Science*, 325(5941), 725–30.

[45] Dobrovolskaia, M. A. & Bathe, M. (2021). Opportunities and challenges for the clinical translation of structured dna assemblies as gene therapeutic delivery and vaccine vectors. *WIREs Nanomedicine and Nanobiotechnology*, 13(1), e1657.

[46] Dong, R., Aksel, T., Chan, W., Germain, R. N., Vale, R. D., & Douglas, S. M. (2021). Dna origami patterning of synthetic t cell receptors reveals spatial control of the sensitivity and kinetics of signal activation. *Proc Natl Acad Sci U S A*, 118(40).

[47] Douglas, S. M., Bachelet, I., & Church, G. M. (2012). A logic-gated nanorobot for targeted transport of molecular payloads. *Science*, 335(6070), 831–4.

[48] Douglas, S. M., Chou, J. J., & Shih, W. M. (2007). Dna-nanotube-induced alignment of membrane proteins for nmr structure determination. *Proc Natl Acad Sci U S A*, 104(16), 6644–8.

[49] Douglas, S. M., Dietz, H., Liedl, T., Hogberg, B., Graf, F., & Shih, W. M. (2009a). Self-assembly of dna into nanoscale three-dimensional shapes. *Nature*, 459(7245), 414–8.

[50] Douglas, S. M., Marblestone, A. H., Teerapittayanon, S., Vazquez, A., Church, G. M., & Shih, W. M. (2009b). Rapid prototyping of 3d dna-origami shapes with cadnano. *Nucleic Acids Res*, 37(15), 5001–6.

[51] Drexler, E. K., Peterson, C., & Pergamit, G. (1991). Unbounding the future: The nanotechnology revolution. *William Morrow and Company Inc.: New York, NY, USA*.

[52] Du, R. R., Cedrone, E., Romanov, A., Falkovich, R., Dobrovolskaia, M. A., & Bathe, M. (2022). Innate immune stimulation using 3d wireframe dna origami. *ACS Nano*, 16(12), 20340–20352.

[53] Elgueta, R., Benson, M. J., de Vries, V. C., Wasiuk, A., Guo, Y., & Noelle, R. J. (2009). Molecular mechanism and function of cd40/cd40l engagement in the immune system. *Immunol Rev*, 229(1), 152–72.

[54] Elshabrawy, H. A., Coughlin, M. M., Baker, S. C., & Prabhakar, B. S. (2012). Human monoclonal antibodies against highly conserved hr1 and hr2 domains of the sars-cov spike protein are more broadly neutralizing. *PLoS One*, 7(11), e50366.

[55] Endo, M., Xing, X., Zhou, X., Emura, T., Hidaka, K., Tuesuwan, B., & Sugiyama, H. (2015). Single-molecule manipulation of the duplex formation and dissociation at the g-quadruplex/i-motif site in the dna nanostructure. *ACS Nano*, 9(10), 9922–9.

[56] Endo, M., Yang, Y., & Sugiyama, H. (2013). Dna origami technology for biomaterials applications. *Biomater Sci*, 1(4), 347–360.

[57] Engelen, W. & Dietz, H. (2021). Advancing biophysics using dna origami. *Annu Rev Biophys*, 50, 469–492.

[58] Engelhardt, F. A. S., Praetorius, F., Wachauf, C. H., Brüggenthies, G., Kohler, F., Kick, B., Kadletz, K. L., Pham, P. N., Behler, K. L., Gerling, T., & Dietz, H. (2019). Custom-size, functional, and durable dna origami with design-specific scaffolds. *ACS Nano*, 13(5), 5015–5027.

[59] Fang, T., Alvelid, J., Spratt, J., Ambrosetti, E., Testa, I., & Teixeira, A. I. (2021). Spatial regulation of t-cell signaling by programmed death-ligand 1 on wireframe dna origami flat sheets. *ACS Nano*, 15(2), 3441–3452.

[60] Feynman, R. P. (1959). There's plenty of room at the bottom. *Engineering and science*, 23(5).

[61] Fitzgerald-Bocarsly, P., Dai, J., & Singh, S. (2008). Plasmacytoid dendritic cells and type i ifn: 50 years of convergent history. *Cytokine Growth Factor Rev*, 19(1), 3–19.

[62] Folegatti, P. M., Ewer, K. J., Aley, P. K., Angus, B., Becker, S., Belij-Rammerstorfer, S., Bellamy, D., Bibi, S., Bittaye, M., Clutterbuck, E. A., Dold, C., Faust, S. N., Finn, A., Flaxman, A. L., Hallis, B., Heath, P., Jenkin, D., Lazarus, R., Makinson, R., Minassian, A. M., Pollock, K. M., Ramasamy, M., Robinson, H., Snape, M., Tarrant, R., Voysey, M., Green, C., Douglas, A. D., Hill, A. V. S., Lambe, T., Gilbert, S. C., Pollard, A. J., & Group, O. C. V. T. (2020). Safety and immunogenicity of the chadox1 ncov-19 vaccine against sars-cov-2: a preliminary report of a phase 1/2, single-blind, randomised controlled trial. *Lancet*, 396(10249), 467–478.

[63] Fournel, S., Wieckowski, S., Sun, W., Trouche, N., Dumortier, H., Bianco, A., Chaloin, O., Habib, M., Peter, J.-C., Schneider, P., Vray, B., Toes, R. E., Offringa, R., Melief, C. J. M., Hoebeke, J., & Guichard, G. (2005). C3-symmetric peptide scaffolds are functional mimetics of trimeric cd40l. *Nature Chemical Biology*, 1(7), 377–382.

[64] Friedrich, T. C., Valentine, L. E., Yant, L. J., Rakasz, E. G., Piaskowski, S. M., Furlott, J. R., Weisgrau, K. L., Burwitz, B., May, G. E., León, E. J., Soma, T., Napoe, G., Capuano, S. V., Wilson, N. A., & Watkins, D. I. (2007). Subdominant cd8+ t-cell responses are involved in durable control of aids virus replication. *J Virol*, 81(7), 3465–76.

[65] Fu, Xiaoyi, P. F. L. J. Y. Q. Z. F. X. M. K. G. M. H.-M. K. G. Z. X.-B. (2020). Aptamer-funcapttionalized dna nanostructures for biological applications. *Top Curr Chem (Cham.)*, 2(21).

[66] Gao, Y., Chen, X., Tian, T., Zhang, T., Gao, S., Zhang, X., Yao, Y., Lin, Y., & Cai, X. (2022). A lysosome-activated tetrahedral nanobox for encapsulated sirna delivery. *Adv Mater*, 34(46), e2201731.

[67] Garcia-Beltran, W. F., Lam, E. C., St Denis, K., Nitido, A. D., Garcia, Z. H., Hauser, B. M., Feldman, J., Pavlovic, M. N., Gregory, D. J., Poznansky, M. C., Sigal, A., Schmidt, A. G., Iafrate, A. J., Naranbhai, V., & Balazs, A. B. (2021). Multiple sars-cov-2 variants escape neutralization by vaccine-induced humoral immunity. *Cell*, 184(9), 2523.

[68] Geers, D., Shamier, M. C., Bogers, S., den Hartog, G., Gommers, L., Nieuwkoop, N. N., Schmitz, K. S., Rijsbergen, L. C., van Osch, J. A. T., Dijkhuizen, E., Smits, G., Comvalius, A., van Mourik, D., Caniels, T. G., van Gils, M. J., Sanders, R. W., Oude Munnink, B. B., Molenkamp, R., de Jager, H. J., Haagmans, B. L., de Swart, R. L., Koopmans, M. P. G., van Binnendijk, R. S., de Vries, R. D., & GeurtsvanKessel, C. H. (2021). Sars-cov-2 variants of concern partially escape humoral but not t-cell responses in covid-19 convalescent donors and vaccinees. *Sci Immunol*, 6(59).

[69] Goyal, G., Prabhala, P., Mahajan, G., Bausk, B., Gilboa, T., Xie, L., Zhai, Y., Lazarovits, R., Mansour, A., Kim, M. S., Patil, A., Curran, D., Long, J. M., Sharma, S., Junaid, A., Cohen, L., Ferrante, T. C., Levy, O., Prantil-Baun, R., Walt, D. R., & Ingber, D. E. (2022). Ectopic lymphoid follicle formation and human seasonal influenza vaccination responses recapitulated in an organ-on-a-chip. *Adv Sci (Weinh)*, 9(14), e2103241.

[70] Grifoni, A., Weiskopf, D., Ramirez, S. I., Mateus, J., Dan, J. M., Moderbacher, C. R., Rawlings, S. A., Sutherland, A., Premkumar, L., Jadi, R. S., Marrama, D., de Silva, A. M., Frazier, A., Carlin, A. F., Greenbaum, J. A., Peters, B., Krammer, F., Smith, D. M., Crotty, S., & Sette, A. (2020). Targets of t cell responses to sars-cov-2 coronavirus in humans with covid-19 disease and unexposed individuals. *Cell*, 181(7), 1489–1501.e15.

[71] Hahn, J., Wickham, S. F., Shih, W. M., & Perrault, S. D. (2014). Addressing the instability of dna nanostructures in tissue culture. *ACS Nano*, 8(9), 8765–75.

[72] Halley, P. D., Lucas, C. R., McWilliams, E. M., Webber, M. J., Patton, R. A., Kural, C., Lucas, D. M., Byrd, J. C., & Castro, C. E. (2016). Daunorubicin-loaded dna origami nanostructures circumvent drug-resistance mechanisms in a leukemia model. *Small*, 12(3), 308–20.

[73] Han, D., Pal, S., Nangreave, J., Deng, Z., Liu, Y., & Yan, H. (2011). Dna origami with complex curvatures in three-dimensional space. *Science*, 332(6027), 342–6.

[74] Han, S., Liu, W., Yang, S., & Wang, R. (2019). Facile and label-free electrochemical biosensors for microrna detection based on dna origami nanostructures. *ACS Omega*, 4(6), 11025–11031.

[75] Harrison, S. C. (2008). Viral membrane fusion. *Nat Struct Mol Biol*, 15(7), 690–8.

[76] He, C., Yang, J., Hong, W., Chen, Z., Peng, D., Lei, H., Alu, A., He, X., Bi, Z., Jiang, X., Jia, G., Yang, Y., Zhou, Y., Yu, W., Tang, C., Huang, Q., Yang, M., Li, B., Li, J., Wang, J., Que, H., Chen, L., Ren, W., Wan, D., Wang, W., Shen, G., Zhao, Z., Yang, L., Wang, Z., Su, Z., Wei, Y., Cen, X., Tanaka, Y., Song, X., Lu, S., Peng, X., Lu, G., & Wei, X. (2022). A self-assembled

trimeric protein vaccine induces protective immunity against omicron variant. *Nat Commun*, 13(1), 5459.

[77] Hellmeier, J., Platzer, R., Eklund, A. S., Schlichthaerle, T., Karner, A., Motsch, V., Schneider, M. C., Kurz, E., Bamieh, V., Brameshuber, M., Preiner, J., Jungmann, R., Stockinger, H., Schütz, G. J., Huppa, J. B., & Sevcsik, E. (2021). Dna origami demonstrate the unique stimulatory power of single pmhcs as t cell antigens. *Proc Natl Acad Sci U S A*, 118(4).

[78] Heo, M. B., Kim, S. Y., Yun, W. S., & Lim, Y. T. (2015). Sequential delivery of an anticancer drug and combined immunomodulatory nanoparticles for efficient chemoimmunotherapy. *Int J Nanomedicine*, 10, 5981–92.

[79] Hermanrud, C. E., Lucas, C. L., Sykes, M., Huang, C. A., & Wang, Z. (2011). Expression and purification of soluble murine cd40l monomers and polymers in yeast pichia pastoris. *Protein Expr Purif*, 76(1), 115–20.

[80] Hoffmann, M., Hofmann-Winkler, H., Krüger, N., Kempf, A., Nehlmeier, I., Graichen, L., Arora, P., Sidarovich, A., Moldenhauer, A. S., Winkler, M. S., Schulz, S., Jäck, H. M., Stankov, M. V., Behrens, G. M. N., & Pöhlmann, S. (2021). Sars-cov-2 variant b.1.617 is resistant to bamlanivimab and evades antibodies induced by infection and vaccination. *Cell Rep*, 36(3), 109415.

[81] Igyártó, B. Z., Jacobsen, S., & Ndeupen, S. (2021). Future considerations for the mrna-lipid nanoparticle vaccine platform. *Curr Opin Virol*, 48, 65–72.

[82] Jabbari, A., Sameiyan, E., Yaghoobi, E., Ramezani, M., Alibolandi, M., Abnous, K., & Taghdisi, S. M. (2023). Aptamer-based targeted delivery systems for cancer treatment using dna origami and dna nanostructures. *Int J Pharm*, 646, 123448.

[83] Jackson, L. A., Anderson, E. J., Rouphael, N. G., Roberts, P. C., Makhene, M., Coler, R. N., McCullough, M. P., Chappell, J. D., Denison, M. R., Stevens, L. J., Pruijssers, A. J., McDermott, A., Flach, B., Doria-Rose, N. A., Corbett, K. S., Morabito, K. M., O'Dell, S., Schmidt, S. D., Swanson, P. A., Padilla, M., Mascola, J. R., Neuzil, K. M., Bennett, H., Sun, W., Peters, E., Makowski, M., Albert, J., Cross, K., Buchanan, W., Pikaart-Tautges, R., Ledgerwood, J. E., Graham, B. S., Beigel, J. H., & Group, m.-. S. (2020). An mrna vaccine against sars-cov-2 - preliminary report. *N Engl J Med*, 383(20), 1920–1931.

[84] Jiang, Q., Song, C., Nangreave, J., Liu, X., Lin, L., Qiu, D., Wang, Z. G., Zou, G., Liang, X., Yan, H., & Ding, B. (2012). Dna origami as a carrier for circumvention of drug resistance. *J Am Chem Soc*, 134(32), 13396–403.

[85] Johansson, M., Denardo, D. G., & Coussens, L. M. (2008). Polarized immune responses differentially regulate cancer development. *Immunol Rev*, 222, 145–54.

[86] Joshi, S. B., Dutch, R. E., & Lamb, R. A. (1998). A core trimer of the paramyxovirus fusion protein: parallels to influenza virus hemagglutinin and hiv-1 gp41. *Virology*, 248(1), 20–34.

[87] Kang, Y., Zhang, W., Yu, Q., Gao, L., Quan, J., Gu, F., Wu, Y., Tian, Y., Wu, Z., Shao, S., Zhou, H., Duan, S., Zhou, Y., Zhang, L., Gao, X., Tian, H., & Yao, W. (2023). Self-assembled nanoparticles based on dna origami and a nitrated t helper cell epitope as a platform for the development of personalized cancer vaccines. *Cancer Immunol Immunother*, 72(8), 2741–2755.

[88] Karikó, K., Muramatsu, H., Welsh, F. A., Ludwig, J., Kato, H., Akira, S., & Weissman, D. (2008). Incorporation of pseudouridine into mrna yields superior nonimmunogenic vector with increased translational capacity and biological stability. *Mol Ther*, 16(11), 1833–40.

[89] Karupiah, G. (1998). Type 1 and type 2 cytokines in antiviral defense. *Vet Immunol Immunopathol*, 63(1-2), 105–9.

[90] Ke, Y., Douglas, S. M., Liu, M., Sharma, J., Cheng, A., Leung, A., Liu, Y., Shih, W. M., & Yan, H. (2009). Multilayer dna origami packed on a square lattice. *J Am Chem Soc*, 131(43), 15903–8.

[91] Ke, Y., Ong, L. L., Sun, W., Song, J., Dong, M., Shih, W. M., & Yin, P. (2014). Dna brick crystals with prescribed depths. *Nat Chem*, 6(11), 994–1002.

[92] Keech, C., Albert, G., Cho, I., Robertson, A., Reed, P., Neal, S., Plested, J. S., Zhu, M., Cloney-Clark, S., Zhou, H., Smith, G., Patel, N., Frieman, M. B., Haupt, R. E., Logue, J., McGrath, M., Weston, S., Piedra, P. A., Desai, C., Callahan, K., Lewis, M., Price-Abbott, P., Formica, N., Shinde, V., Fries, L., Lickliter, J. D., Griffin, P., Wilkinson, B., & Glenn, G. M. (2020). Phase 1-2 trial of a sars-cov-2 recombinant spike protein nanoparticle vaccine. *N Engl J Med*, 383(24), 2320–2332.

[93] Keestra, A. M., de Zoete, M. R., Bouwman, L. I., & van Putten, J. P. (2010). Chicken tlr21 is an innate cpg dna receptor distinct from mammalian tlr9. *J Immunol*, 185(1), 460–7.

[94] Kern, N., Dong, R., Douglas, S. M., Vale, R. D., & Morrissey, M. A. (2021). Tight nanoscale clustering of fcgamma receptors using dna origami promotes phagocytosis. *Elife*, 10.

[95] Kick, B., Praetorius, F., Dietz, H., & Weuster-Botz, D. (2015). Efficient production of single-stranded phage dna as scaffolds for dna origami. *Nano Lett*, 15(7), 4672–6.

[96] Klein, W. P., Thomsen, R. P., Turner, K. B., Walper, S. A., Vranish, J., Kjems, J., Ancona, M. G., & Medintz, I. L. (2019). Enhanced catalysis from multienzyme cascades assembled on a dna origami triangle. *ACS Nano*, 13(12), 13677–13689.

[97] Klinman, D. M., Sato, T., & Shimosato, T. (2016). Use of nanoparticles to deliver immunomodulatory oligonucleotides. *Wiley Interdiscip Rev Nanomed Nanobiotechnol*, 8(4), 631–7.

[98] Knappe, G. A., Wamhoff, E. C., & Bathe, M. (2023). Functionalizing dna origami to investigate and interact with biological systems. *Nat Rev Mater*, 8(2), 123–138.

[99] Kornbluth, R. S., Adase, C., Hamilton, V. S., & Studer, S. (2019). Cd40 ligand (cd40l) multitrimer antigen fusion protein (magavax) as a vaccine design for high-level cd8+ t cell responses. *The Journal of Immunology*, 202(1 Supplement), 196.6–196.6.

[100] Kornbluth, R. S., Stempniak, M., & Stone, G. W. (2012). Design of cd40 agonists and their use in growing b cells for cancer immunotherapy. *Int Rev Immunol*, 31(4), 279–88.

[101] Kreiter, S., Vormehr, M., van de Roemer, N., Diken, M., Lower, M., Diekmann, J., Boegel, S., Schrors, B., Vascotto, F., Castle, J. C., Tadmor, A. D., Schoenberger, S. P., Huber, C., Tureci, O., & Sahin, U. (2015). Mutant mhc class ii epitopes drive therapeutic immune responses to cancer. *Nature*, 520(7549), 692–6.

[102] Kumar, V., Palazzolo, S., Bayda, S., Corona, G., Toffoli, G., & Rizzolio, F. (2016). Dna nanotechnology for cancer therapy. *Theranostics*, 6(5), 710–25.

[103] Kuse, N., Zhang, Y., Chikata, T., Nguyen, H. T., Oka, S., Gatanaga, H., & Takiguchi, M. (2022). Long-term memory cd8. *Nat Commun*, 13(1), 5251.

[104] Kwon, P. S., Ren, S., Kwon, S. J., Kizer, M. E., Kuo, L., Xie, M., Zhu, D., Zhou, F., Zhang, F., Kim, D., Fraser, K., Kramer, L. D., Seeman, N. C., Dordick, J. S., Linhardt, R. J., Chao, J., & Wang, X. (2020). Designer dna architecture offers precise and multivalent spatial pattern-recognition for viral sensing and inhibition. *Nat Chem*, 12(1), 26–35.

[105] Kyriakidis, N. C., López-Cortés, A., González, E. V., Grimaldos, A. B., & Prado, E. O. (2021). Sars-cov-2 vaccines strategies: a comprehensive review of phase 3 candidates. *NPJ Vaccines*, 6(1), 28.

[106] Laczkó, D., Hogan, M. J., Toulmin, S. A., Hicks, P., Lederer, K., Gaudette, B. T., Castaño, D., Amanat, F., Muramatsu, H., Oguin, T. H., Ojha, A., Zhang, L., Mu, Z., Parks, R., Manzoni, T. B., Roper, B., Strohmeier, S., Tombácz, I., Arwood, L., Nachbagauer, R., Karikó, K., Greenhouse, J., Pessaint, L., Porto, M., Putman-Taylor, T., Strasbaugh, A., Campbell, T. A., Lin, P. J. C., Tam, Y. K., Sempowski, G. D., Farzan, M., Choe, H., Saunders, K. O., Haynes, B. F., Andersen, H., Eisenlohr, L. C., Weissman, D., Krammer, F., Bates, P., Allman, D., Locci, M., & Pardi, N. (2020). A single immunization with nucleoside-modified mrna vaccines elicits strong cellular and humoral immune responses against sars-cov-2 in mice. *Immunity*, 53(4), 724–732.e7.

[107] Lahoud, M. H., Ahmet, F., Zhang, J. G., Meuter, S., Policheni, A. N., Kitsoulis, S., Lee, C. N., O'Keeffe, M., Sullivan, L. C., Brooks, A. G., Berry, R., Rossjohn, J., Mintern, J. D., Vega-Ramos, J., Villadangos, J. A., Nicola, N. A., Nussenzweig, M. C., Stacey, K. J., Shortman, K., Heath, W. R., & Caminschi, I. (2012). Dec-205 is a cell surface receptor for cpg oligonucleotides. *Proc Natl Acad Sci U S A*, 109(40), 16270–5.

[108] Lai, N., Min, Q., Xiong, E., Liu, J., Zhang, L., Yasuda, S., & Wang, J.-Y. (2019). A tetrameric form of cd40 ligand with potent biological activities in both mouse and human primary b cells. *Molecular Immunology*, 105, 173–180.

[109] Le Bert, N., Tan, A. T., Kunasegaran, K., Tham, C. Y. L., Hafezi, M., Chia, A., Chng, M. H. Y., Lin, M., Tan, N., Linster, M., Chia, W. N., Chen, M. I., Wang, L. F., Ooi, E. E., Kalimuddin, S., Tambyah, P. A., Low, J. G., Tan, Y. J., & Bertoletti, A. (2020). Sars-cov-2-specific t cell immunity in cases of covid-19 and sars, and uninfected controls. *Nature*, 584(7821), 457–462.

[110] Lee, E. Y., Lee, C. K., Schmidt, N. W., Jin, F., Lande, R., Curk, T., Frenkel, D., Dobnikar, J., Gilliet, M., & Wong, G. C. L. (2016). A review of immune amplification via ligand clustering by self-assembled liquid-crystalline dna complexes. *Adv Colloid Interface Sci*, 232, 17–24.

[111] Lee, H. H., Kalhor, R., Goela, N., Bolot, J., & Church, G. M. (2019). Terminator-free template-independent enzymatic dna synthesis for digital information storage. *Nat Commun*, 10(1), 2383.

[112] Leleux, J. A., Pradhan, P., & Roy, K. (2017). Biophysical attributes of cpg presentation control tlr9 signaling to differentially polarize systemic immune responses. *Cell Rep*, 18(3), 700–710.

[113] Li, A. W., Sobral, M. C., Badrinath, S., Choi, Y., Graveline, A., Stafford, A. G., Weaver, J. C., Dellacherie, M. O., Shih, T. Y., Ali, O. A., Kim, J., Wucherpfennig, K. W., & Mooney, D. J. (2018a). A facile approach to enhance antigen response for personalized cancer vaccination. *Nat Mater*, 17(6), 528–534.

[114] Li, S., Jiang, Q., Liu, S., Zhang, Y., Tian, Y., Song, C., Wang, J., Zou, Y., Anderson, G. J., Han, J. Y., Chang, Y., Liu, Y., Zhang, C., Chen, L., Zhou, G., Nie, G., Yan, H., Ding, B., & Zhao, Y. (2018b). A dna nanorobot functions as a cancer therapeutic in response to a molecular trigger in vivo. *Nat Biotechnol*, 36(3), 258–264.

[115] Liedl, T., Hogberg, B., Tytell, J., Ingber, D. E., & Shih, W. M. (2010). Self-assembly of three-dimensional prestressed tensegrity structures from dna. *Nat Nanotechnol*, 5(7), 520–4.

[116] Liu, D., Chen, X., Jiang, D., Wang, C., Xia, Q., & Yang, Y. (2023). Structural properties and surface modification decided pharmacokinetic behavior and bio-distribution of dna origami frameworks in mice. *Small*, 19(40), e2302932.

[117] Liu, S., Jiang, Q., Zhao, X., Zhao, R., Wang, Y., Liu, J., Shang, Y., Zhao, S., Wu, T., Zhang, Y., Nie, G., & Ding, B. (2021). A dna nanodevice-based vaccine for cancer immunotherapy. *Nat Mater*, 20(3), 421–430.

[118] Liu, S., Su, W., Li, Z., & Ding, X. (2015). Electrochemical detection of lung cancer specific micrornas using 3d dna origami nanostructures. *Biosens Bioelectron*, 71, 57–61.

[119] Luan, N., Li, T., Wang, Y., Cao, H., Yin, X., Lin, K., & Liu, C. (2022). Th2-oriented immune serum after sars-cov-2 vaccination does not enhance infection. *Front Immunol*, 13, 882856.

[120] Lucas, C. R., Halley, P. D., Chowdury, A. A., Harrington, B. K., Beaver, L., Lapalombella, R., Johnson, A. J., Hertlein, E. K., Phelps, M. A., Byrd, J. C., & Castro, C. E. (2022). Dna origami nanostructures elicit dose-dependent immunogenicity and are nontoxic up to high doses in vivo. *Small*, (pp. e2108063).

[121] Ma, D. Y. & Clark, E. A. (2009). The role of cd40 and cd154/cd40l in dendritic cells. *Semin Immunol*, 21(5), 265–72.

[122] Ma, X., Zou, F., Yu, F., Li, R., Yuan, Y., Zhang, Y., Zhang, X., Deng, J., Chen, T., Song, Z., Qiao, Y., Zhan, Y., Liu, J., Zhang, J., Peng, Z., Li, Y., Lin, Y., Liang, L., Wang, G., Chen, Y., Chen, Q., Pan, T., He, X., & Zhang, H. (2020). Nanoparticle vaccines based on the receptor binding domain (rbd) and heptad repeat (hr) of sars-cov-2 elicit robust protective immune responses. *Immunity*, 53(6), 1315–1330.e9.

[123] Ma, Y., Lu, Z., Jia, B., Shi, Y., Dong, J., Jiang, S., & Li, Z. (2022). Dna origami as a nanomedicine for targeted rheumatoid arthritis therapy through reactive oxygen species and nitric oxide scavenging. *ACS Nano*, 16(8), 12520–12531.

[124] Madhi, S. A., Baillie, V., Cutland, C. L., Voysey, M., Koen, A. L., Fairlie, L., Padayachee, S. D., Dheda, K., Barnabas, S. L., Bhorat, Q. E., Briner, C., Kwatra, G., Ahmed, K., Aley, P., Bhikha, S., Bhiman, J. N., Bhorat, A. E., du Plessis, J., Esmail, A., Groenewald, M., Horne, E., Hwa, S. H., Jose, A., Lambe, T., Laubscher, M., Malahleha, M., Masenya, M., Masilela, M., McKenzie, S., Molapo, K., Moultrie, A., Oelofse, S., Patel, F., Pillay, S., Rhead, S., Rodel, H., Rossouw, L., Taoushanis, C., Tegally, H., Thombrayil, A., van Eck, S., Wibmer, C. K., Durham, N. M., Kelly, E. J., Villafana, T. L., Gilbert, S., Pollard, A. J., de Oliveira, T., Moore, P. L., Sigal, A., Izu, A., Group, N.-S., & Group, W.-V. C. (2021). Efficacy of the chadox1 ncov-19 covid-19 vaccine against the b.1.351 variant. *N Engl J Med*, 384(20), 1885–1898.

[125] Majikes, J. M., Ferraz, L. C. C., & LaBean, T. H. (2017). ph-driven actuation of dna origami via parallel i-motif sequences in solution and on surfaces. *Bioconjug Chem*, 28(7), 1821–1825.

[126] Malashkevich, V. N., Schneider, B. J., McNally, M. L., Milhollen, M. A., Pang, J. X., & Kim, P. S. (1999). Core structure of the envelope glycoprotein gp2 from ebola virus at 1.9-a resolution. *Proc Natl Acad Sci U S A*, 96(6), 2662–7.

[127] Mao, C., LaBean, T. H., Relf, J. H., & Seeman, N. C. (2000). Logical computation using algorithmic self-assembly of dna triple-crossover molecules. *Nature*, 407(6803), 493–6.

[128] Mateus, J., Grifoni, A., Tarke, A., Sidney, J., Ramirez, S. I., Dan, J. M., Burger, Z. C., Rawlings, S. A., Smith, D. M., Phillips, E., Mallal, S., Lammers, M., Rubiro, P., Quiambao, L., Sutherland, A., Yu, E. D., da Silva Antunes, R., Greenbaum, J., Frazier, A., Markmann, A. J.,

Premkumar, L., de Silva, A., Peters, B., Crotty, S., Sette, A., & Weiskopf, D. (2020). Selective and cross-reactive sars-cov-2 t cell epitopes in unexposed humans. *Science*, 370(6512), 89–94.

[129] McMahan, K., Yu, J., Mercado, N. B., Loos, C., Tostanoski, L. H., Chandrashekar, A., Liu, J., Peter, L., Atyeo, C., Zhu, A., Bondzie, E. A., Dagotto, G., Gebre, M. S., Jacob-Dolan, C., Li, Z., Nampanya, F., Patel, S., Pessaint, L., Van Ry, A., Blade, K., Yalley-Ogunro, J., Cabus, M., Brown, R., Cook, A., Teow, E., Andersen, H., Lewis, M. G., Lauffenburger, D. A., Alter, G., & Barouch, D. H. (2021). Correlates of protection against sars-cov-2 in rhesus macaques. *Nature*, 590(7847), 630–634.

[130] Mills, A., Aissaoui, N., Finkel, J., Elezgaray, J., & Bellot, G. (2023). Mechanical dna origami to investigate biological systems. *Adv Biol (Weinh)*, 7(3), e2200224.

[131] Min, Y., Roche, K. C., Tian, S., Eblan, M. J., McKinnon, K. P., Caster, J. M., Chai, S., Herring, L. E., Zhang, L., Zhang, T., DeSimone, J. M., Tepper, J. E., Vincent, B. G., Serody, J. S., & Wang, A. Z. (2017). Antigen-capturing nanoparticles improve the abscopal effect and cancer immunotherapy. *Nat Nanotechnol*, 12(9), 877–882.

[132] Minari, J., Mochizuki, S., & Sakurai, K. (2008). Enhanced cytokine secretion owing to multiple cpg side chains of dna duplex. *Oligonucleotides*, 18(4), 337–44.

[133] Minev, D., Guerra, R., Kishi, J. Y., Smith, C., Krieg, E., Said, K., Hornick, A., Sasaki, H. M., Filsinger, G., Beliveau, B. J., Yin, P., Church, G. M., & Shih, W. M. (2019). Rapid in vitro production of single-stranded dna. *Nucleic Acids Res*, 47(22), 11956–11962.

[134] Monferrer, A., Kretzmann, J. A., Sigl, C., Sapelza, P., Liedl, A., Wittmann, B., & Dietz, H. (2022). Broad-spectrum virus trapping with heparan sulfate-modified dna origami shells. *ACS Nano*, 16(12), 20002–20009.

[135] Moss, P. (2022). The t cell immune response against sars-cov-2. *Nat Immunol*, 23(2), 186–193.

[136] Mueller, S., Coleman, J. R., & Wimmer, E. (2009). Putting synthesis into biology: a viral view of genetic engineering through de novo gene and genome synthesis. *Chem Biol*, 16(3), 337–47.

[137] Nanda, J. S. & Lorsch, J. R. (2014). Labeling a protein with fluorophores using nhs ester derivitization. *Methods Enzymol*, 536, 87–94.

[138] Nelde, A., Bilich, T., Heitmann, J. S., Maringer, Y., Salih, H. R., Roerden, M., Lübke, M., Bauer, J., Rieth, J., Wacker, M., Peter, A., Hörber, S., Traenkle, B., Kaiser, P. D., Rothbauer, U., Becker, M., Junker, D., Krause, G., Strengert, M., Schneiderhan-Marra, N., Templin, M. F., Joos, T. O., Kowalewski, D. J., Stos-Zweifel, V., Fehr, M., Rabsteyn, A., Mirakaj, V., Karbach, J., Jäger, E., Graf, M., Gruber, L. C., Rachfalski, D., Preuß, B., Hagelstein, I., Märklin, M., Bakchoul, T., Gouttefangeas, C., Kohlbacher, O., Klein, R., Stevanović, S., Rammensee, H. G., & Walz, J. S. (2021). Sars-cov-2-derived peptides define heterologous and covid-19-induced t cell recognition. *Nat Immunol*, 22(1), 74–85.

[139] Niemeyer, C. M. (2010). Semisynthetic dna-protein conjugates for biosensing and nanofabrication. *Angew Chem Int Ed Engl*, 49(7), 1200–16.

[140] Njongmeta, L. M., Bray, J., Davies, C. J., Davis, W. C., Howard, C. J., Hope, J. C., Palmer, G. H., Brown, W. C., & Mwangi, W. (2012). Cd205 antigen targeting combined with dendritic cell recruitment factors and antigen-linked cd40l activation primes and expands significant antigen-specific antibody and cd4(+) t cell responses following dna vaccination of outbred animals. *Vaccine*, 30(9), 1624–35.

[141] Oberhardt, V., Luxenburger, H., Kemming, J., Schulien, I., Ciminski, K., Giese, S., Csernalabics, B., Lang-Meli, J., Janowska, I., Staniek, J., Wild, K., Basho, K., Marinescu, M. S., Fuchs, J., Topfstedt, F., Janda, A., Sogukpinar, O., Hilger, H., Stete, K., Emmerich, F., Bengsch, B., Waller, C. F., Rieg, S., Sagar, Boettler, T., Zoldan, K., Kochs, G., Schwemmle, M., Rizzi, M., Thimme, R., Neumann-Haefelin, C., & Hofmann, M. (2021). Rapid and stable mobilization of cd8. *Nature*, 597(7875), 268–273.

[142] Ohto, U., Shibata, T., Tanji, H., Ishida, H., Krayukhina, E., Uchiyama, S., Miyake, K., & Shimizu, T. (2015). Structural basis of cpg and inhibitory dna recognition by toll-like receptor 9. *Nature*, 520(7549), 702–5.

[143] Oishi, M. & Saito, K. (2020). Simple single-legged dna walkers at diffusion-limited nanointerfaces of gold nanoparticles driven by a dna circuit mechanism. *ACS Nano*, 14(3), 3477–3489.

[144] Oktay, E., Alem, F., Hernandez, K., Girgis, M., Green, C., Mathur, D., Medintz, I. L., Narayanan, A., & Veneziano, R. (2023). Dna origami presenting the receptor binding domain of sars-cov-2 elicit robust protective immune response. *Commun Biol*, 6(1), 308.

[145] Oldenburg, M., Kruger, A., Ferstl, R., Kaufmann, A., Nees, G., Sigmund, A., Bathke, B., Lauterbach, H., Suter, M., Dreher, S., Koedel, U., Akira, S., Kawai, T., Buer, J., Wagner, H., Bauer, S., Hochrein, H., & Kirschning, C. J. (2012). Tlr13 recognizes bacterial 23s rrna devoid of erythromycin resistance-forming modification. *Science*, 337(6098), 1111–5.

[146] Palluk, S., Arlow, D. H., de Rond, T., Barthel, S., Kang, J. S., Bector, R., Baghdassarian, H. M., Truong, A. N., Kim, P. W., Singh, A. K., Hillson, N. J., & Keasling, J. D. (2018). De novo dna synthesis using polymerase-nucleotide conjugates. *Nat Biotechnol*, 36(7), 645–650.

[147] Pan, Q., Nie, C., Hu, Y., Yi, J., Liu, C., Zhang, J., He, M., Chen, T., & Chu, X. (2020). Aptamer-functionalized dna origami for targeted codelivery of antisense oligonucleotides and doxorubicin to enhance therapy in drug-resistant cancer cells. *ACS Appl Mater Interfaces*, 12(1), 400–409.

[148] Pati, R., Shevtsov, M., & Sonawane, A. (2018). Nanoparticle vaccines against infectious diseases. *Front Immunol*, 9, 2224.

[149] Peciak, K., Laurine, E., Tommasi, R., Choi, J. W., & Brocchini, S. (2019). Site-selective protein conjugation at histidine. *Chem Sci*, 10(2), 427–439.

[150] Peng, Y., Mentzer, A. J., Liu, G., Yao, X., Yin, Z., Dong, D., Dejnirattisai, W., Rostron, T., Supasa, P., Liu, C., López-Camacho, C., Slon-Campos, J., Zhao, Y., Stuart, D. I., Paesen, G. C., Grimes, J. M., Antson, A. A., Bayfield, O. W., Hawkins, D. E. D., Ker, D. S., Wang, B., Turtle, L., Subramaniam, K., Thomson, P., Zhang, P., Dold, C., Ratcliff, J., Simmonds, P., de Silva, T., Sopp, P., Wellington, D., Rajapaksa, U., Chen, Y. L., Salio, M., Napolitani, G., Paes, W., Borrow, P., Kessler, B. M., Fry, J. W., Schwabe, N. F., Semple, M. G., Baillie, J. K., Moore, S. C., Openshaw, P. J. M., Ansari, M. A., Dunachie, S., Barnes, E., Frater, J., Kerr, G., Goulder, P., Lockett, T., Levin, R., Zhang, Y., Jing, R., Ho, L. P., Cornall, R. J., Conlon, C. P., Klenerman, P., Screaton, G. R., Mongkolsapaya, J., McMichael, A., Knight, J. C., Ogg, G., Dong, T., Consortium, O. I. N. C.-. R. T. c., & Investigators, I. (2020). Broad and strong memory cd4. *Nat Immunol*, 21(11), 1336–1345.

[151] Polack, F. P., Thomas, S. J., Kitchin, N., Absalon, J., Gurtman, A., Lockhart, S., Perez, J. L., Pérez Marc, G., Moreira, E. D., Zerbini, C., Bailey, R., Swanson, K. A., Roychoudhury, S., Koury, K., Li, P., Kalina, W. V., Cooper, D., Frenck, R. W., Hammitt, L. L., Türeci, �., Nell, H., Schaefer, A., Ünal, S., Tresnan, D. B., Mather, S., Dormitzer, P. R., Şahin, U., Jansen, K. U., Gruber, W. C., & Group, C. C. T. (2020). Safety and efficacy of the bnt162b2 mrna covid-19 vaccine. *N Engl J Med*, 383(27), 2603–2615.

[152] Ponnuswamy, N., Bastings, M. M. C., Nathwani, B., Ryu, J. H., Chou, L. Y. T., Vinther, M., Li, W. A., Anastassacos, F. M., Mooney, D. J., & Shih, W. M. (2017). Oligolysine-based coating protects dna nanostructures from low-salt denaturation and nuclease degradation. *Nat Commun*, 8, 15654.

[153] Praetorius, F., Kick, B., Behler, K. L., Honemann, M. N., Weuster-Botz, D., & Dietz, H. (2017). Biotechnological mass production of dna origami. *Nature*, 552(7683), 84–87.

[154] Pulendran, B. & Ahmed, R. (2006). Translating innate immunity into immunological memory: implications for vaccine development. *Cell*, 124(4), 849–63.

[155] Ranjbar, R. & Hafezi-Moghadam, M. S. (2016). Design and construction of a dna origami drug delivery system based on mpt64 antibody aptamer for tuberculosis treatment. *Electron Physician*, 8(2), 1857–64.

[156] Rauscher, H., Sokull-Klüttgen, B., & Stamm, H. (2013). The european commission's recommendation on the definition of nanomaterial makes an impact. *Nanotoxicology*, 7(7), 1195–7.

[157] Reynisson, B., Alvarez, B., Paul, S., Peters, B., & Nielsen, M. (2020). Netmhcpan-4.1 and netmhciipan-4.0: improved predictions of mhc antigen presentation by concurrent motif deconvolution and integration of ms mhc eluted ligand data. *Nucleic Acids Res*, 48(W1), W449–w454.

[158] Riou, C., Keeton, R., Moyo-Gwete, T., Hermanus, T., Kgagudi, P., Baguma, R., Valley-Omar, Z., Smith, M., Tegally, H., Doolabh, D., Iranzadeh, A., Tyers, L., Mutavhatsindi, H., Tincho, M. B., Benede, N., Marais, G., Chinhoyi, L. R., Mennen, M., Skelem, S., du Bruyn, E., Stek, C., de Oliveira, T., Williamson, C., Moore, P. L., Wilkinson, R. J., Ntusi, N. A. B., Burgers, W. A., & network, S. A. c. i. (2022). Escape from recognition of sars-cov-2 variant spike epitopes but overall preservation of t cell immunity. *Sci Transl Med*, 14(631), eabj6824.

[159] Rock, K. L. & Shen, L. (2005). Cross-presentation: underlying mechanisms and role in immune surveillance. *Immunol Rev*, 207, 166–83.

[160] Rodda, L. B., Netland, J., Shehata, L., Pruner, K. B., Morawski, P. A., Thouvenel, C. D., Takehara, K. K., Eggenberger, J., Hemann, E. A., Waterman, H. R., Fahning, M. L., Chen, Y., Hale, M., Rathe, J., Stokes, C., Wrenn, S., Fiala, B., Carter, L., Hamerman, J. A., King, N. P., Gale, M., Campbell, D. J., Rawlings, D. J., & Pepper, M. (2021). Functional sars-cov-2-specific immune memory persists after mild covid-19. *Cell*, 184(1), 169–183.e17.

[161] Rosier, B. J. H., Markvoort, A. J., Gumí Audenis, B., Roodhuizen, J. A. L., den Hamer, A., Brunsveld, L., & de Greef, T. F. A. (2020). Proximity-induced caspase-9 activation on a dna origami-based synthetic apoptosome. *Nat Catal*, 3(3), 295–306.

[162] Rothemund, P. W. (2006). Folding dna to create nanoscale shapes and patterns. *Nature*, 440(7082), 297–302.

[163] Sadoff, J., Gray, G., Vandebosch, A., Cárdenas, V., Shukarev, G., Grinsztejn, B., Goepfert, P. A., Truyers, C., Fennema, H., Spiessens, B., Offergeld, K., Scheper, G., Taylor, K. L., Robb, M. L., Treanor, J., Barouch, D. H., Stoddard, J., Ryser, M. F., Marovich, M. A., Neuzil, K. M., Corey, L., Cauwenberghs, N., Tanner, T., Hardt, K., Ruiz-Guiñazú, J., Le Gars, M., Schuitemaker, H., Van Hoof, J., Struyf, F., Douoguih, M., & Group, E. S. (2021). Safety and efficacy of single-dose ad26.cov2.s vaccine against covid-19. *N Engl J Med*, 384(23), 2187–2201.

[164] Sahin, U. & Tureci, O. (2018). Personalized vaccines for cancer immunotherapy. *Science*, 359(6382), 1355–1360.

[165] Saliba, D. G., Céspedes-Donoso, P. F., Bálint, �., Compeer, E. B., Korobchevskaya, K., Valvo, S., Mayya, V., Kvalvaag, A., Peng, Y., Dong, T., Tognoli, M. L., O'Neill, E., Bonham, S., Fischer, R., Kessler, B. M., & Dustin, M. L. (2019). Composition and structure of synaptic ectosomes exporting antigen receptor linked to functional cd40 ligand from helper t cells. *Elife*, 8.

[166] Scheible, M. B., Ong, L. L., Woehrstein, J. B., Jungmann, R., Yin, P., & Simmel, F. C. (2015). A compact dna cube with side length 10 nm. *Small*, 11(39), 5200–5205.

[167] Scheuerpflug, A., Ahmetlic, F., Bauer, V., Riedel, T., Rocken, M., & Mocikat, R. (2020). The role of dendritic cells for therapy of b-cell lymphoma with immune checkpoint inhibitors. *Cancer Immunol Immunother*.

[168] Schmidt, N. W., Jin, F., Lande, R., Curk, T., Xian, W., Lee, C., Frasca, L., Frenkel, D., Dobnikar, J., Gilliet, M., & Wong, G. C. (2015). Liquid-crystalline ordering of antimicrobial peptide-dna complexes controls tlr9 activation. *Nat Mater*, 14(7), 696–700.

[169] Schuller, V. J., Heidegger, S., Sandholzer, N., Nickels, P. C., Suhartha, N. A., Endres, S., Bourquin, C., & Liedl, T. (2011). Cellular immunostimulation by cpg-sequence-coated dna origami structures. *ACS Nano*, 5(12), 9696–702.

[170] Seeman, N. C. (1982). Nucleic acid junctions and lattices. *J Theor Biol*, 99(2), 237–47.

[171] Sekine, T., Perez-Potti, A., Rivera-Ballesteros, O., Strålin, K., Gorin, J. B., Olsson, A., Llewellyn-Lacey, S., Kamal, H., Bogdanovic, G., Muschiol, S., Wullimann, D. J., Kammann, T., Emgård, J., Parrot, T., Folkesson, E., Rooyackers, O., Eriksson, L. I., Henter, J. I., Sönnerborg, A., Allander, T., Albert, J., Nielsen, M., Klingström, J., Gredmark-Russ, S., Björkström, N. K., Sandberg, J. K., Price, D. A., Ljunggren, H. G., Aleman, S., Buggert, M., & Group, K. C.-. S. (2020). Robust t cell immunity in convalescent individuals with asymptomatic or mild covid-19. *Cell*, 183(1), 158–168.e14.

[172] Shaw, A., Benson, E., & Högberg, B. (2015). Purification of functionalized dna origami nanostructures. *ACS Nano*, 9(5), 4968–75.

[173] Shaw, A., Hoffecker, I. T., Smyrlaki, I., Rosa, J., Grevys, A., Bratlie, D., Sandlie, I., Michaelsen, T. E., Andersen, J. T., & Högberg, B. (2019). Binding to nanopatterned antigens is dominated by the spatial tolerance of antibodies. *Nature nanotechnology*, 14(2), 184–190.

[174] Shaw, A., Lundin, V., Petrova, E., Fordos, F., Benson, E., Al-Amin, A., Herland, A., Blokzijl, A., Hogberg, B., & Teixeira, A. I. (2014). Spatial control of membrane receptor function using ligand nanocalipers. *Nat Methods*, 11(8), 841–6.

[175] Shen, H., Ackerman, A. L., Cody, V., Giodini, A., Hinson, E. R., Cresswell, P., Edelson, R. L., Saltzman, W. M., & Hanlon, D. J. (2006). Enhanced and prolonged cross-presentation following endosomal escape of exogenous antigens encapsulated in biodegradable nanoparticles. *Immunology*, 117(1), 78–88.

[176] Shi, L., Peng, P., Du, Y., & Li, T. (2017). Programmable i-motif dna folding topology for a ph-switched reversible molecular sensing device. *Nucleic Acids Res*, 45(8), 4306–4314.

[177] Shih, W. M. (2015). Exploiting weak interactions in dna self-assembly. *Science*, 347(6229), 1417–8.

[178] Shin, J. S. & Pierce, N. A. (2004). A synthetic dna walker for molecular transport. *J Am Chem Soc*, 126(35), 10834–5.

[179] Si, L., Meng, K., Tian, Z., Sun, J., Li, H., Zhang, Z., Soloveva, V., Fu, G., Xia, Q., Xiao, S., Zhang, L., & Zhou, D. (2018). Triterpenoids manipulate a broad range of virus-host fusion via wrapping the hr2 domain prevalent in viral envelopes. *Sci Adv*, 4(11), eaau8408.

[180] Sigl, C., Willner, E. M., Engelen, W., Kretzmann, J. A., Sachenbacher, K., Liedl, A., Kolbe, F., Wilsch, F., Aghvami, S. A., Protzer, U., et al. (2021). Programmable icosahedral shell system for virus trapping. *Nature materials*, 20(9), 1281–1289.

[181] Smith, L. K., Boukhaled, G. M., Condotta, S. A., Mazouz, S., Guthmiller, J. J., Vijay, R., Butler, N. S., Bruneau, J., Shoukry, N. H., Krawczyk, C. M., & Richer, M. J. (2018). Interleukin-10 directly inhibits cd8(+) t cell function by enhancing n-glycan branching to decrease antigen sensitivity. *Immunity*, 48(2), 299–312 e5.

[182] Smolková, B., MacCulloch, T., Rockwood, T. F., Liu, M., Henry, S. J. W., Frtús, A., Uzhytchak, M., Lunova, M., Hof, M., Jurkiewicz, P., Dejneka, A., Stephanopoulos, N., & Lunov, O. (2021). Protein corona inhibits endosomal escape of functionalized dna nanostructures in living cells. *ACS Appl Mater Interfaces*, 13(39), 46375–46390.

[183] Spies, B., Hochrein, H., Vabulas, M., Huster, K., Busch, D. H., Schmitz, F., Heit, A., & Wagner, H. (2003). Vaccination with plasmid dna activates dendritic cells via toll-like receptor 9 (tlr9) but functions in tlr9-deficient mice. *J Immunol*, 171(11), 5908–12.

[184] Spriggs, M. K., Fanslow, W. C., Armitage, R. J., & Belmont, J. (1993). The biology of the human ligand for cd40. *Journal of clinical immunology*, 13, 373–380.

[185] Stephanopoulos, N., Liu, M., Tong, G. J., Li, Z., Liu, Y., Yan, H., & Francis, M. B. (2010). Immobilization and one-dimensional arrangement of virus capsids with nanoscale precision using dna origami. *Nano Lett*, 10(7), 2714–20.

[186] Stone, G. W., Barzee, S., Snarsky, V., Santucci, C., Tran, B., Langer, R., Zugates, G. T., Anderson, D. G., & Kornbluth, R. S. (2009). Nanoparticle-delivered multimeric soluble cd40l dna combined with toll-like receptor agonists as a treatment for melanoma. *PLOS ONE*, 4(10), e7334.

[187] Sullivan, N. J., Hensley, L., Asiedu, C., Geisbert, T. W., Stanley, D., Johnson, J., Honko, A., Olinger, G., Bailey, M., Geisbert, J. B., Reimann, K. A., Bao, S., Rao, S., Roederer, M., Jahrling, P. B., Koup, R. A., & Nabel, G. J. (2011). Cd8+ cellular immunity mediates rad5 vaccine protection against ebola virus infection of nonhuman primates. *Nat Med*, 17(9), 1128–31.

[188] Sun, Y., Sun, J., Xiao, M., Lai, W., Li, L., Fan, C., & Pei, H. (2022a). Dna origami-based artificial antigen-presenting cells for adoptive t cell therapy. *Sci Adv*, 8(48), eadd1106.

[189] Sun, Y., Yan, L., Sun, J., Xiao, M., Lai, W., Song, G., Li, L., Fan, C., & Pei, H. (2022b). Nanoscale organization of two-dimensional multimeric pmhc reagents with dna origami for cd8. *Nat Commun*, 13(1), 3916.

[190] Takeuchi, A. & Saito, T. (2017). Cd4 ctl, a cytotoxic subset of cd4. *Front Immunol*, 8, 194.

[191] Tan, A. T., Linster, M., Tan, C. W., Le Bert, N., Chia, W. N., Kunasegaran, K., Zhuang, Y., Tham, C. Y. L., Chia, A., Smith, G. J. D., Young, B., Kalimuddin, S., Low, J. G. H., Lye, D., Wang, L. F., & Bertoletti, A. (2021). Early induction of functional sars-cov-2-specific t cells associates with rapid viral clearance and mild disease in covid-19 patients. *Cell Rep*, 34(6), 108728.

[192] Tang, W., Tong, T., Wang, H., Lu, X., Yang, C., Wu, Y., Wang, Y., Liu, J., & Ding, B. (2023). A dna origami-based gene editing system for efficient gene therapy in vivo. *Angew Chem Int Ed Engl*, 62(51), e202315093.

[193] Tegally, H., Wilkinson, E., Giovanetti, M., Iranzadeh, A., Fonseca, V., Giandhari, J., Doolabh, D., Pillay, S., San, E. J., Msomi, N., Mlisana, K., von Gottberg, A., Walaza, S., Allam, M., Ismail, A., Mohale, T., Glass, A. J., Engelbrecht, S., Van Zyl, G., Preiser, W., Petruccione, F., Sigal, A., Hardie, D., Marais, G., Hsiao, N. Y., Korsman, S., Davies, M. A., Tyers, L., Mudau, I., York, D., Maslo, C., Goedhals, D., Abrahams, S., Laguda-Akingba, O., Alisoltani-Dehkordi, A., Godzik, A., Wibmer, C. K., Sewell, B. T., Lourenço, J., Alcantara, L. C. J., Kosakovsky Pond, S. L., Weaver, S., Martin, D., Lessells, R. J., Bhiman, J. N., Williamson, C., & de Oliveira, T. (2021). Detection of a sars-cov-2 variant of concern in south africa. *Nature*, 592(7854), 438–443.

[194] Thi, T. T. H., Suys, E. J. A., Lee, J. S., Nguyen, D. H., Park, K. D., & Truong, N. P. (2021). Lipid-based nanoparticles in the clinic and clinical trials: From cancer nanomedicine to covid-19 vaccines. *Vaccines (Basel)*, 9(4).

[195] Tikhomirov, G., Petersen, P., & Qian, L. (2017). Fractal assembly of micrometre-scale dna origami arrays with arbitrary patterns. *Nature*, 552(7683), 67–71.

[196] Toubi, E. & Shoenfeld, Y. (2007). Protective autoimmunity in cancer (review). *Oncol Rep*, 17(1), 245–51.

[197] Udomprasert, A. & Kangsamaksin, T. (2017). Dna origami applications in cancer therapy. *Cancer Sci*, 108(8), 1535–1543.

[198] Veneziano, R., Moyer, T. J., Stone, M. B., Wamhoff, E.-C., Read, B. J., Mukherjee, S., Shepherd, T. R., Das, J., Schief, W. R., Irvine, D. J., & Bathe, M. (2020). Role of nanoscale antigen organization on b-cell activation probed using dna origami. *Nature Nanotechnology*, (pp. 1–8).

[199] Veneziano, R., Shepherd, T. R., Ratanalert, S., Bellou, L., Tao, C., & Bathe, M. (2018). In vitro synthesis of gene-length single-stranded dna. *Sci Rep*, 8(1), 6548.

[200] Ventola, C. L. (2017). Cancer immunotherapy, part 2: Efficacy, safety, and other clinical considerations. *P T*, 42(7), 452–463.

[201] Verheyen, T., Fang, T., Lindenhofer, D., Wang, Y., Akopyan, K., Lindqvist, A., Högberg, B., & Teixeira, A. I. (2020). Spatial organization-dependent epha2 transcriptional responses revealed by ligand nanocalipers. *Nucleic Acids Res*, 48(10), 5777–5787.

[202] Vonderheide, R. H. (2020). Cd40 agonist antibodies in cancer immunotherapy. *Annual Review of Medicine*, 71(1), 47–58.

[203] Vonderheide, R. H., Burg, J. M., Mick, R., Trosko, J. A., Li, D., Shaik, M. N., Tolcher, A. W., & Hamid, O. (2013). Phase i study of the cd40 agonist antibody cp-870,893 combined with carboplatin and paclitaxel in patients with advanced solid tumors. *Oncoimmunology*, 2(1), e23033.

[204] Vonderheide, R. H., Flaherty, K. T., Khalil, M., Stumacher, M. S., Bajor, D. L., Hutnick, N. A., Sullivan, P., Mahany, J. J., Gallagher, M., Kramer, A., Green, S. J., O'Dwyer, P. J., Running, K. L., Huhn, R. D., & Antonia, S. J. (2007). Clinical activity and immune modulation in cancer patients treated with cp-870,893, a novel cd40 agonist monoclonal antibody. *J Clin Oncol*, 25(7), 876–83.

[205] Vu, M. N., Kelly, H. G., Kent, S. J., & Wheatley, A. K. (2021). Current and future nanoparticle vaccines for covid-19. *EBioMedicine*, 74, 103699.

[206] Wagar, L. E., Salahudeen, A., Constantz, C. M., Wendel, B. S., Lyons, M. M., Mallajosyula, V., Jatt, L. P., Adamska, J. Z., Blum, L. K., Gupta, N., Jackson, K. J. L., Yang, F., Röltgen, K., Roskin, K. M., Blaine, K. M., Meister, K. D., Ahmad, I. N., Cortese, M., Dora, E. G., Tucker, S. N., Sperling, A. I., Jain, A., Davies, D. H., Felgner, P. L., Hammer, G. B., Kim, P. S., Robinson, W. H., Boyd, S. D., Kuo, C. J., & Davis, M. M. (2021). Modeling human adaptive immune responses with tonsil organoids. *Nat Med*, 27(1), 125–135.

[207] Wagenbauer, K. F., Pham, N., Gottschlich, A., Kick, B., Kozina, V., Frank, C., Trninic, D., Stömmer, P., Grünmeier, R., Carlini, E., Tsiverioti, C. A., Kobold, S., Funke, J. J., & Dietz, H. (2023). Programmable multispecific dna-origami-based t-cell engagers. *Nat Nanotechnol*, 18(11), 1319–1326.

[208] Wagenbauer, K. F., Sigl, C., & Dietz, H. (2017). Gigadalton-scale shape-programmable dna assemblies. *Nature*, 552(7683), 78–83.

[209] Walsh, E. E., Frenck, R. W., Falsey, A. R., Kitchin, N., Absalon, J., Gurtman, A., Lockhart, S., Neuzil, K., Mulligan, M. J., Bailey, R., Swanson, K. A., Li, P., Koury, K., Kalina, W., Cooper, D., Fontes-Garfias, C., Shi, P. Y., Türeci, �., Tompkins, K. R., Lyke, K. E., Raabe, V., Dormitzer, P. R., Jansen, K. U., Şahin, U., & Gruber, W. C. (2020). Safety and immunogenicity of two rna-based covid-19 vaccine candidates. *N Engl J Med*, 383(25), 2439–2450.

[210] Wamhoff, E. C., Knappe, G. A., Burds, A. A., Du, R. R., Neun, B. W., Difilippantonio, S., Sanders, C., Edmondson, E. F., Matta, J. L., Dobrovolskaia, M. A., & Bathe, M. (2023a). Evaluation of nonmodified wireframe dna origami for acute toxicity and biodistribution in mice. *ACS Appl Bio Mater*.

[211] Wamhoff, E. C., Ronsard, L., Feldman, J., Knappe, G. A., Hauser, B. M., Romanov, A., Lam, E., Denis, K. S., Boucau, J., Barczak, A. K., Balazs, A. B., Schmidt, A., Lingwood, D., & Bathe, M. (2023b). Enhancing antibody responses by multivalent antigen display on thymus-independent dna origami scaffolds. *bioRxiv*.

[212] Wang, D., Zhang, G., Zhang, Y., Xin, L., Dong, Y., Liu, Y., & Liu, D. (2017). An addressable 2d heterogeneous nanoreactor to study the enzyme-catalyzed reaction at the interface. *Small*, 13(43).

[213] Wang, W., Chen, S., An, B., Huang, K., Bai, T., Xu, M., Bellot, G., Ke, Y., Xiang, Y., & Wei, B. (2019). Complex wireframe dna nanostructures from simple building blocks. *Nat Commun*, 10(1), 1067.

[214] Wang, Z., Schmidt, F., Weisblum, Y., Muecksch, F., Barnes, C. O., Finkin, S., Schaefer-Babajew, D., Cipolla, M., Gaebler, C., Lieberman, J. A., Oliveira, T. Y., Yang, Z., Abernathy, M. E., Huey-Tubman, K. E., Hurley, A., Turroja, M., West, K. A., Gordon, K., Millard, K. G., Ramos, V., Da Silva, J., Xu, J., Colbert, R. A., Patel, R., Dizon, J., Unson-O'Brien, C., Shimeliovich, I., Gazumyan, A., Caskey, M., Bjorkman, P. J., Casellas, R., Hatziioannou, T., Bieniasz, P. D., & Nussenzweig, M. C. (2021a). mrna vaccine-elicited antibodies to sars-cov-2 and circulating variants. *Nature*, 592(7855), 616–622.

[215] Wang, Z., Song, L., Liu, Q., Tian, R., Shang, Y., Liu, F., Liu, S., Zhao, S., Han, Z., Sun, J., Jiang, Q., & Ding, B. (2021b). A tubular dna nanodevice as a sirna/chemo-drug co-delivery vehicle for combined cancer therapy. *Angew Chem Int Ed Engl*, 60(5), 2594–2598.

[216] Watson, J. D. & Crick, F. H. (1953). The structure of dna. *Cold Spring Harb Symp Quant Biol*, 18, 123–31.

[217] Wibmer, C. K., Ayres, F., Hermanus, T., Madzivhandila, M., Kgagudi, P., Oosthuysen, B., Lambson, B. E., de Oliveira, T., Vermeulen, M., van der Berg, K., Rossouw, T., Boswell, M., Ueckermann, V., Meiring, S., von Gottberg, A., Cohen, C., Morris, L., Bhiman, J. N., & Moore, P. L. (2021). Sars-cov-2 501y.v2 escapes neutralization by south african covid-19 donor plasma. *Nat Med*, 27(4), 622–625.

[218] Wickham, S. F. J., Auer, A., Min, J., Ponnuswamy, N., Woehrstein, J. B., Schueder, F., Strauss, M. T., Schnitzbauer, J., Nathwani, B., Zhao, Z., Perrault, S. D., Hahn, J., Lee, S., Bastings, M. M., Helmig, S. W., Kodal, A. L., Yin, P., Jungmann, R., & Shih, W. M. (2020). Complex multicomponent patterns rendered on a 3d dna-barrel pegboard. *Nature Communications*, 11(1), 5768.

[219] Winfree, E., Liu, F., Wenzler, L. A., & Seeman, N. C. (1998). Design and self-assembly of two-dimensional dna crystals. *Nature*, 394(6693), 539–44.

[220] Woldemeskel, B. A., Garliss, C. C., & Blankson, J. N. (2021). Sars-cov-2 mrna vaccines induce broad cd4+ t cell responses that recognize sars-cov-2 variants and hcov-nl63. *J Clin Invest*, 131(10).

[221] Wu, K., Werner, A. P., Koch, M., Choi, A., Narayanan, E., Stewart-Jones, G. B. E., Colpitts, T., Bennett, H., Boyoglu-Barnum, S., Shi, W., Moliva, J. I., Sullivan, N. J., Graham, B. S., Carfi, A., Corbett, K. S., Seder, R. A., & Edwards, D. K. (2021a). Serum neutralizing activity elicited by mrna-1273 vaccine. *N Engl J Med*, 384(15), 1468–1470.

[222] Wu, X., Liu, Q., Liu, F., Wu, T., Shang, Y., Liu, J., & Ding, B. (2021b). An rna/dna hybrid origami-based nanoplatform for efficient gene therapy. *Nanoscale*, 13(30), 12848–12853.

[223] Yao, G., Zhang, F., Wang, F., Peng, T., Liu, H., Poppleton, E., Šulc, P., Jiang, S., Liu, L., Gong, C., Jing, X., Liu, X., Wang, L., Liu, Y., Fan, C., & Yan, H. (2020). Meta-dna structures. *Nat Chem*, 12(11), 1067–1075.

[224] Yew, N. S., Zhao, H., Przybylska, M., Wu, I. H., Tousignant, J. D., Scheule, R. K., & Cheng, S. H. (2002). Cpg-depleted plasmid dna vectors with enhanced safety and long-term gene expression in vivo. *Mol Ther*, 5(6), 731–8.

[225] Yin, P., Yan, H., Daniell, X. G., Turberfield, A. J., & Reif, J. H. (2004). A unidirectional dna walker that moves autonomously along a track. *Angew Chem Int Ed Engl*, 43(37), 4906–11.

[226] You, C. X., Shi, M., Liu, Y., Cao, M., Luo, R., & Hermonat, P. L. (2012). Aav2/il-12 gene delivery into dendritic cells (dc) enhances ctl stimulation above other il-12 applications: Evidence for il-12 intracrine activity in dc. *Oncoimmunology*, 1(6), 847–855.

[227] Yu, D., Kandimalla, E. R., Bhagat, L., Tang, J. Y., Cong, Y., Tang, J., & Agrawal, S. (2002). 'immunomers'–novel 3'-3'-linked cpg oligodeoxyribonucleotides as potent immunomodulatory agents. *Nucleic Acids Res*, 30(20), 4460–9.

[228] Zeng, Y. C., Young, O. J., Wintersinger, C. M., Anastassacos, F. M., MacDonald, J. M., Isinelli, G., Dellacherie, M. O., Sobral, M., Bai, H., Graveline, A., Vernet, A., Sanchez-Ventura, M., Mulligan, K., Choi, Y.-J., Ferrante, T. C., Keskin, D., Wu, C., Mooney, D., Kwon, I.-C., Ryu, J.-H., & Shih, W. (2023). Optimizing cpg spatial distribution with dna origami for th1-polarized therapeutic vaccination.

[229] Zhang, H., Demirer, G. S., Ye, T., Goh, N. S., Aditham, A. J., Cunningham, F. J., Fan, C., & Landry, M. P. (2019). Dna nanostructures coordinate gene silencing in mature plants. *Proc Natl Acad Sci U S A*, 116(15), 7543–7548.

[230] Zhang, J., Xu, Y., Chen, M., Huang, Y., Song, T., Yang, C., Yang, Y., & Song, Y. (2022). Elucidating the effect of nanoscale receptor-binding domain organization on sars-cov-2 infection and immunity activation with dna origami. *J Am Chem Soc*, 144(46), 21295–21303.

[231] Zhang, Q., Jiang, Q., Li, N., Dai, L., Liu, Q., Song, L., Wang, J., Li, Y., Tian, J., Ding, B., & Du, Y. (2014). Dna origami as an in vivo drug delivery vehicle for cancer therapy. *ACS Nano*, 8(7), 6633–43.

[232] Zhao, J., Mangalam, A. K., Channappanavar, R., Fett, C., Meyerholz, D. K., Agnihothram, S., Baric, R. S., David, C. S., & Perlman, S. (2016). Airway memory cd4(+) t cells mediate protective immunity against emerging respiratory coronaviruses. *Immunity*, 44(6), 1379–91.

[233] Zhao, S., Duan, F., Liu, S., Wu, T., Shang, Y., Tian, R., Liu, J., Wang, Z. G., Jiang, Q., & Ding, B. (2019). Efficient intracellular delivery of rnase a using dna origami carriers. *ACS Appl Mater Interfaces*, 11(12), 11112–11118.

[234] Zhao, S., Tian, R., Wu, J., Liu, S., Wang, Y., Wen, M., Shang, Y., Liu, Q., Li, Y., Guo, Y., Wang, Z., Wang, T., Zhao, Y., Zhao, H., Cao, H., Su, Y., Sun, J., Jiang, Q., & Ding, B. (2021). A dna origami-based aptamer nanoarray for potent and reversible anticoagulation in hemodialysis. *Nat Commun*, 12(1), 358.

[235] Zhao, Y. X., Shaw, A., Zeng, X., Benson, E., Nyström, A. M., & Högberg, B. (2012). Dna origami delivery system for cancer therapy with tunable release properties. *ACS Nano*, 6(10), 8684–91.

[236] Zheng, J., Birktoft, J. J., Chen, Y., Wang, T., Sha, R., Constantinou, P. E., Ginell, S. L., Mao, C., & Seeman, N. C. (2009). From molecular to macroscopic via the rational design of a self-assembled 3d dna crystal. *Nature*, 461(7260), 74–7.

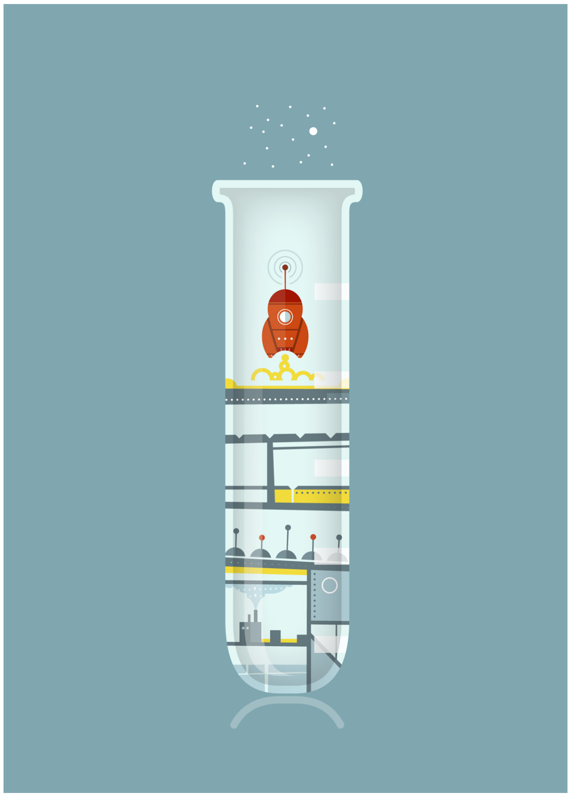

THIS THESIS WAS TYPESET using LaTeX, originally developed by Leslie Lamport and based on Donald Knuth's TeX. The body text is set in 11 point Egenolff-Berner Garamond, a revival of Claude Garamont's humanist typeface. The above illustration, "Science Experiment 02", was created by Ben Schlitter and released under CC BY-NC-ND 3.0. A template that can be used to format a PhD thesis with this look and feel has been released under the permissive MIT (X11) license, and can be found online at github.com/suchow/Dissertate or from its author, Jordan Suchow, at suchow@post.harvard.edu.